

Special Issue Reprint

Modeling and Simulation in Engineering, 3rd Edition

Edited by Camelia Petrescu and Valeriu David

mdpi.com/journal/mathematics



Modeling and Simulation in Engineering, 3rd Edition

Modeling and Simulation in Engineering, 3rd Edition

Guest Editors

Camelia Petrescu Valeriu David



Guest Editors

Camelia Petrescu Valeriu David

Department of Electrical Department of Electrical Engineering Measurements and Materials Technical University of Iasi "Gheorghe Asachi" Technical

Iasi University of Iasi

Romania Iasi

Romania

Editorial Office MDPI AG Grosspeteranlage 5 4052 Basel, Switzerland

This is a reprint of the Special Issue, published open access by the journal *Mathematics* (ISSN 2227-7390), freely accessible at: https://www.mdpi.com/si/mathematics/Model_Simul_Eng_3.

For citation purposes, cite each article independently as indicated on the article page online and as indicated below:

Lastname, A.A.; Lastname, B.B. Article Title. Journal Name Year, Volume Number, Page Range.

ISBN 978-3-7258-5233-8 (Hbk) ISBN 978-3-7258-5234-5 (PDF) https://doi.org/10.3390/books978-3-7258-5234-5

© 2025 by the authors. Articles in this book are Open Access and distributed under the Creative Commons Attribution (CC BY) license. The book as a whole is distributed by MDPI under the terms and conditions of the Creative Commons Attribution-NonCommercial-NoDerivs (CC BY-NC-ND) license (https://creativecommons.org/licenses/by-nc-nd/4.0/).

Contents

About the Editors
Camelia Petrescu and Valeriu David Preface to the Special Issue "Modeling and Simulation in Engineering, 3rd Edition" Reprinted from: <i>Mathematics</i> 2025 , <i>13</i> , 2801, https://doi.org/10.3390/math13172801
Gufran Abass and Suha Shihab Operational Matrix of New Shifted Wavelet Functions for Solving Optimal Control Problem Reprinted from: <i>Mathematics</i> 2023, 11, 3040, https://doi.org/10.3390/math11143040 4
 J. de Curtò, I. de Zarzà and Carlos T. Calafate UWB and MB-OFDM for Lunar Rover Navigation and Communication Reprinted from: <i>Mathematics</i> 2023, 11, 3835, https://doi.org/10.3390/math11183835 18
I. de Zarzà, J. de Curtò, Juan Carlos Cano and Carlos T. Calafate Drone-Based Decentralized Truck Platooning with UWB Sensing and Control Reprinted from: <i>Mathematics</i> 2023, 11, 4627, https://doi.org/10.3390/math11224627 37
Faryal Ali, Zawar Hussain Khan, Khurram Shehzad Khattak, Thomas Aaron Gulliver and Ahmed B. Altamimi A Microscopic Traffic Model Incorporating Vehicle Vibrations Due to Pavement Condition Reprinted from: <i>Mathematics</i> 2023, 11, 4911, https://doi.org/10.3390/math11244911 59
 J. De Curtò and I. De Zarzà Optimizing Propellant Distribution for Interorbital Transfers Reprinted from: Mathematics 2024, 12, 900, https://doi.org/10.3390/math12060900 83
Hangjie Huang and Jinfeng Gao Backstepping and Novel Sliding Mode Trajectory Tracking Controller for Wheeled Mobile Robots Reprinted from: <i>Mathematics</i> 2024, 12, 1458, https://doi.org/10.3390/math12101458 102
Tuan Ngoc Tran Cao, Binh Thanh Pham, No Tan Nguyen, Duc-Lung Vu and Nguyen-Vu Truong Second-Order Terminal Sliding Mode Control for Trajectory Tracking of a Differential Drive Robot Reprinted from: <i>Mathematics</i> 2024, 12, 2657, https://doi.org/10.3390/math12172657 116
A. S. M. Sharifuzzaman Sagar, Samsil Arefin, Eesun Moon, Md Masud Pervez Prince, L. Minh Dang, Amir Haider and Hyung Seok Kim A Gaussian Process-Enhanced Non-Linear Function and Bayesian Convolution–Bayesian Long Term Short Memory Based Ultra-Wideband Range Error Mitigation Method for Line of Sight and Non-Line of Sight Scenarios Reprinted from: <i>Mathematics</i> 2024, 12, 3866, https://doi.org/10.3390/math12233866 129

About the Editors

Camelia Petrescu

Camelia Petrescu received the MSc degree in Electrical Engineering (1982) from the Technical University of Iasi and the Ph.D. degree in Electrical Engineering from Polytechnic University Bucharest, Romania (1994). She is a full professor at the Technical University of Iasi. Her areas of interest include analytical and numerical electromagnetic field analysis, optimization methods, high frequency dielectric heating and electric power quality.

Valeriu David

Valeriu David received the M.S. and Ph.D. degrees in electronic/electric engineering from the "Gheorghe Asachi" Technical University of Iasi, Romania in 1983 and 1998, respectively. He is a professor emeritus at the Technical University of Iasi and a Senior Member of IEEE. His teaching and research activities include electric and electronic measurements, estimation of biomedical and environmental parameters, survey of the electromagnetic environment, and electromagnetic absorbers/shields.





Editorial

Preface to the Special Issue "Modeling and Simulation in Engineering, 3rd Edition"

Camelia Petrescu 1,* and Valeriu David 2

- Department of Electrotechnics, Faculty of Electrical Engineering, Gh. Asachi Technical University of Iași, 700050 Iasi, Romania
- Department of Electrical Measurements and Electrotechnical Materials, Faculty of Electrical Engineering, Gh. Asachi Technical University of Iași, 700050 Iași, Romania; valeriu.david@academic.tuiasi.ro
- * Correspondence: camelia-mihaela.petrescu@academic.tuiasi.ro

1. Introduction

The topic "Modeling and Simulation in Engineering", proposed in 2021 as part of the section "Engineering Mathematics", and later as part of "Control Theory and Mechanics", covers a large array of technical fields, thus arousing much interest among researchers. Two previous editions have already been published, one in 2022 (https://www.mdpi.com/books/book/6451) and one in 2023 (https://www.mdpi.com/books/book/7679).

The purpose of this Special Issue is to offer a platform for ongoing valuable research involving modeling and simulation methods in mathematical physics to present new simulation software applications in engineering or in the design of experiments.

We now have the pleasure of introducing "Modeling and Simulation in Engineering, 3rd Edition", and a fourth one already being launched. This edition comprises eight original research papers that were selected from 18 submitted papers.

2. Description of Published Papers

The paper by A.S.M. Sharifuzzaman Sagar et al. (Contribution 1) proposes a method for error mitigation in UWB (ultra-wide band) range measurements for both line-of-sight (LOS) and non-line-of-sight (NLOS) scenarios. A Gaussian Process-enhanced nonlinear function is proposed for mitigating range bias in LOS cases, while the case of NLOS propagation is identified using a deep learning model. The experimental setup uses State-of-the-Art devices and software (decawave UWB chip, Python as a programming language, PyTorch as the model design framework for the deep learning phase, and NVIDIA GPU in order to accelerate computations). Experiments conducted in various environments and settings proved the effectiveness of the method for range measurements. An uncertainty estimation of the model using the Monte Carlo dropout method was also conducted, showing a very low epistemic and aleatoric uncertainty.

In the paper by Tuan Ngoc Tran Cao et al. (Contribution 2), a second-order TSM (Terminal Sliding Mode) scheme is proposed for the trajectory control of differential drive mobile robots (DDMRs). A solution for the second-order differential equation satisfied by the state variable describing the robot motion is obtained. A cascaded control architecture for the DDMR is proposed using a P-type-only controller for kinematic control. Simulations show a fast convergence to the stable state and fast control of the tracking errors in the DDMR trajectory.

The paper by Hangjie Huang and Jinfeng Gao (Contribution 3) proposes motion controllers for trajectory control of mobile robots. The controllers use the Lyapunov stability theory and the backstepping method. The sliding mode algorithm was used to ensure a fast

and stable convergence to zero of the trajectory tracking error. Simulations carried out in MATLAB/SIMULINK show the superiority of the proposed control algorithms compared to traditional PID controllers, especially in the presence of disturbances.

The paper by J. De Curtò and I. De Zarzà (Contribution 4) studies methods for propellant distribution optimization in different stages of space exploration missions that use chemical and electric propulsion systems. The optimization is based on the Sequential Quadratic Programming (SQP) method suitable for nonlinear processes, with the objective being to minimize the total propellant mass. The authors present a brief description of the mission planner, which must continuously calculate the vehicle speed variation, optimize the propellant distribution, and evaluate the propellant mass. The simulation results show that by integrating electric propulsion for specific mission stages, considerable propellant savings can be achieved. Other simulations were designed to investigate the variable propulsion efficiency and the effect of orbital perturbations during gravitational assists. The authors demonstrate that the propellant mass consumption can be minimized by this hybrid approach that combines chemical and electric propulsion.

The paper by Faryal Ali et al. (Contribution 5) proposes a traffic flow model that takes into account vehicle vibrations due to pavement conditions, defined by the Pavement Condition Index (PCI), calculated using field experiments. The proposed model and an existing Intelligent Driver (ID) model were used in simulations, showing that the proposed model is more suitable for evaluating traffic behavior. The solution to the first-order nonlinear differential equation satisfied by the vehicle speed is used to calculate the distance headway between vehicles in the steady state and also the traffic flow. Simulations show that the proposed model is better suited to predict traffic evolution in real time, thus helping the vehicle-adaptive cruise control system to adjust the speed and following distance by monitoring the traffic density.

In the paper by I. de Zarzà et al. (Contribution 6), the authors propose a dronebased platooning system that uses UWB sensors for distance measurement and control. A multi-objective optimization technique is conceived and used in platoon management in order to optimize travel time, fuel consumption, and traffic safety. An agent-based simulation model is implemented in order to evaluate and compare the proposed system with existing methodologies in platoon management. The drones are used for monitoring and communication, collecting distance and speed data for all vehicles in the platoon. The multi-objective problem is transformed into a single-objective one, using the aggregation of objective functions biased with different weights. Based on the data collected from the drones, the algorithm decides to make a platoon or to split it and find other partners for some vehicles in the convoy. The efficiency of the proposed system is analyzed, proving to be cost-effective due to the small electrical energy consumption of the drones, compared to the economy of the fuel consumption of the heavy trucks. The limited time of drones' operation is also addressed by using multiple drones working in shifts or by using inductive charging platforms along the convoy route. The multi-objective optimization algorithm was written in Python and the simulations of drone platooning were conducted using the open-source software Mesa for agent-based modeling.

The paper by J. de Curtò et al. (Contribution 7) proposes a hybrid communication and navigation system for Earth–Moon communication and rover movement on the Moon's surface. The system uses UWB technology for high-precision positioning and multi-band orthogonal frequency division multiplexing (MB-OFDM) for high-data-rate communication. The proposed model takes into account the potential for interference and the compatibility with Earth-based networks. Various factors are considered in simulations, such as terrain generation, rover movement constraints, obstacle avoidance, and communication channel

modeling. Simulation results show that the proposed communication algorithm ensures efficient navigation and reliable data transfers between rovers and lunar landers.

In the paper by Gufran Abass and Suha Shihab (Contribution 8), a new state parametrization based on the shifted wavelet method is proposed for solving optimal control problems. Simulations are carried out for different test cases, showing that the solutions obtained with the proposed method are more accurate than the other methods presented in the literature. The mathematical derivation of the method is presented in detail and is based on the construction of a new shifted wavelet function with its operational matrix of derivatives.

3. Conclusions

As Guest Editors of the Special Issue Modeling and Simulation in Engineering, 3rd Edition, we would like to express our gratitude to all the authors who submitted their articles for publication in this Special Issue. We also express our gratitude and appreciation to the reviewers for their valuable observations, which helped to improve the submitted papers.

We hope that the papers selected for this Special Issue will attract a significant audience in the scientific community and further stimulate research involving modeling and simulation in mathematical physics and engineering.

Author Contributions: Conceptualization, C.P. and V.D.; writing—original draft preparation, C.P.; writing—review and editing, C.P. All authors have read and agreed to the published version of the manuscript.

Funding: This research received no external funding.

Conflicts of Interest: The authors declare that there are no conflicts of interest.

List of Contributions:

- Sagar, A.S.M.S.; Arefin, S.; Moon, E.; Prince, M.P.; Dang, L.M.; Haider, A.; Kim, H.S. Gaussian Process-Enhanced Non-Linear Function and Bayesian Convolution

 –Bayesian Long Term Short Memory Based Ultra-Wideband Range Error Mitigation Method for Line of Sight and Non-Line of Sight Scenarios. *Mathematics* 2024, 12, 3866.
- Cao, T.N.T.; Pham, B.T.; Nguyen, N.T.; Vu, D.-L.; Truong, N.-V. Second-Order Terminal Sliding Mode Control for Trajectory Tracking of a Differential Drive Robot. *Mathematics* 2024, 12, 2657.
- 3. Huang, H.; Gao, J. Backstepping and Novel Sliding Mode Trajectory Tracking Controller for Wheeled Mobile Robots. *Mathematics* **2024**, 12, 1458.
- 4. De Curtò, J.; De Zarzà, I. Optimizing Propellant Distribution for Interorbital Transfers. *Mathematics* **2024**, *12*, 900.
- 5. Ali, F.; Khan, Z.H.; Khattak, K.S.; Gulliver, T.A.; Altamimi, A.B. A Microscopic Traffic Model Incorporating Vehicle Vibrations Due to Pavement Condition. *Mathematics* **2023**, *11*, 4911.
- 6. de Zarzà, I.; de Curtò, J.; Cano, J.C.; Calafate, C.T. Drone-Based Decentralized Truck Platooning with UWB Sensing and Control. *Mathematics* **2023**, *11*, 4627.
- 7. de Curtò, J.; de Zarzà, I.; Calafate, C.T. UWB and MB-OFDM for Lunar Rover Navigation and Communication. *Mathematics* **2023**, *11*, 3835.
- 8. Abass, G.; Shihab, S. Operational Matrix of New Shifted Wavelet Functions for Solving Optimal Control Problem. *Mathematics* **2023**, *11*, 3040.

Disclaimer/Publisher's Note: The statements, opinions and data contained in all publications are solely those of the individual author(s) and contributor(s) and not of MDPI and/or the editor(s). MDPI and/or the editor(s) disclaim responsibility for any injury to people or property resulting from any ideas, methods, instructions or products referred to in the content.





Article

Operational Matrix of New Shifted Wavelet Functions for Solving Optimal Control Problem

Gufran Abass and Suha Shihab *

Department of Applied Science, University of Technology, Baghdad 10066, Iraq; as.21.06@grad.uotechnology.edu.iq

* Correspondence: suha.n.shihab@uotechnology.edu.iq

Abstract: This paper is devoted to proposing an approximate numerical algorithm based on the use of the state parameterization technique in order to find the solution to the optimal control problem (OCP). An explicit formula for new shifted wavelet (NSW) functions is constructed. A new formula that expresses the first-order derivative of the NSW in terms of their original NSW is established. The development of our suggested numerical algorithms begins with the extraction of a new operational matrix of derivative from this derivative formula. The expansion's convergence study is performed in detail, and some illustrative examples of OCP are displayed. The proposed algorithm is compared with the exact one and some other methods in the literature. This confirms the accuracy and the high efficiency of the presented algorithm.

Keywords: new shifted wavelet functions; optimal control problem; convergence criteria; error analysis

MSC: 49M99

1. Introduction

The dynamics in some mathematical models are represented by a system of ordinary differential equations for a set of dependent functions x(t) when an independent procedure set controls such systems u(t). In this case, the aim is to determine u(t) that optimizes the dynamical system, and this problem is called optimal control. Numerous studies have focused on the approximate solutions of optimal control problems, which can be found in many fields [1–5]. The two general techniques, which are indirect and direct, are used for the approximate solution of optimal control problems. An indirect method transforms the original optimal control problem to a boundary value problem, which can be solved either analytically or numerically.

Direct methods are more suitable techniques and can be quickly and simply utilized to a new optimal control problem. Optimal control in natural methods is seen as a standard optimization problem by searching for the control function u(t) that optimizes the performance index. Different algorithms were used for solving optimal control problems, including the indirect modified pseudospectral method [6], a direct Chebyshev cardinal functions method [7], Cauchy discretization technique [8], the synthesized optimal control technique [9], Legendre functions method [10], Evolutionary Algorithm-Control Input Range Estimation [11], a hybrid of block-pulse function, and orthonormal Taylor polynomials [12]. (See [13–17] for some other articles exploring various optimal control problems.) Wavelet functions have important roles in numerical analysis for solving optimal control problems [18–21]. In particular, the Chebyshev wavelets families are widely applied in contributions to the field of approximation theory. For example, the authors in [22] employed the Boubaker wavelets together with the operation matrix of derivative in order to solve the singular initial value problem. The collocation method is presented in [23] based on the second kind of Chebyshev wavelets for solving calculus of variation problems. The use of the operational matrices of derivatives and integrals has been highlighted in the

field of numerical analysis [24]. This utilization gives special algorithms to obtain accurate approximate solutions of many types of differential and integral equations with flexible computations. An operational matrix of derivatives is extracted based on choosing suitable basis functions in terms of celebrated special functions and expressing the first derivative of these basis functions in terms of their original types.

Motivated by the above discussion, we are mainly interested in presenting new shifted wavelet functions with some important properties. A novel state parameterization method is suggested to solve the optimal control problem. Such a method is used together with NSW as a basis function to parameterize the states variables. The proposed technique is constructed to simultaneously reach the accuracy and efficiency. The rest of the work is organized as follows: Section 2 provides the definition of NSW. In Section 3, the convergence of the NSW is studied. The general exact formula of the NSW differentiation operational matrix is generated in Section 4, and then the suggested algorithm to solve the optimal control problem is illustrated in Section 5. Section six discusses the application of the NSW by considering various examples in the optimal control. Simulation results are also given in Section 7, followed by concluding remarks that are summarized in Section 8.

2. The New Shifted Wavelet Functions

The expression for the special polynomials $M_m(t)$ in the interval [-1, 1] can be defined as below:

$$M_0(t) = 2$$
, $M_1(t) = t$, $M_2(t) = t^2 - 2$, ...

The general recurrence relation for obtaining $M_m(t)$, m = 2, 3, 4, ... is given by:

$$M_{m+1}(t) = tM_{m-1}(t) - M_m(t), m = 1, 2, 3, 4, \dots,$$

with the given initial conditions $M_0(t)$ and $M_1(t)$.

Sometimes, it is convenient to use the half-interval [0, 1] instead of the interval [-1, 1]. In this case, the term shifted is defined and indicated by $Ms_m(t)$. In this work, $Ms_m(t)$ are defined as $Ms_m(t) = M_m(2t-1)$.

Wavelet functions have been used successfully in scientific and engineering fields. The special new shifted wavelet functions can be defined as below:

$$Q_{nm}(t) = \begin{cases} \frac{2^{\frac{k-1}{2}}}{\sqrt{\pi}} Ms_m \left(2^k t - 2n + 1 \right), & \frac{n-1}{2^{k-1}} \le t \le \frac{n}{2^{k-1}}, \\ 0, & \text{otherwise.} \end{cases}$$
 (1)

where $n = 1, 2, ..., 2^k$, k can be assumed to be any positive integer, m is the degree of the shifted polynomials, and t denotes the time for m = 0, 1, ..., M.

Here, $Ms_m(t)$ are called the shifted special polynomials of order m, which are orthogonal with respect to the weight function w(t), and which satisfy the following recursive formula:

$$Ms_m(t) = (2t-1)Ms_{m-1}(t) - Ms_{m-2}(t), m = 2, 3, 4, ...,$$
 (2)

with initial conditions:

$$Ms_0(t) = 2$$
, $Ms_1(t) = 2t - 1$. (3)

3. Convergence Analysis of New Wavelet Functions

A function approximation $f \in C^2[0,1)$, with $|\ddot{f}(t)| \le L$, L > 0 may by expanded in terms of new shifted wavelets as below:

$$f(t) = \sum_{n=1}^{\infty} \sum_{m=0}^{\infty} c_{nm} Q_{nm}(t).$$
 (4)

where:

$$c_{nm} = \langle f(t), Q(t) \rangle.$$
 (5)

In Equation (5), the symbol $\langle .,. \rangle$ is denoted the inner product operator on Hilbert space over the interval [0,1].

If the infinite series in Equation (4) is truncated, then the solution f(t) can be rewritten in matrix form as below:

$$f(t) = \sum_{n=1}^{2^{k-1}} \sum_{m=0}^{M} c_{nm} Q_{nm}(t) = C^{T} \Phi(t),$$
 (6)

where $\Phi(t)$ and C are matrices of $2^{k-1}M \times 1$ dimensions, given by:

$$C = \begin{bmatrix} c_{1,0} \ c_{1,1} \dots c_{1,M} \ c_{2,0} \dots c_{2,M} \ c_{(2^k-1),0} \ \dots c_{(2^k-1),M} \end{bmatrix}$$

and:

$$\Phi(t) = \begin{bmatrix} Q_{1,0} \ Q_{1,1} \dots \ Q_{1,M} \ Q_{2,0} \dots Q_{2,M} \ Q_{(2^k-1),0} \ \dots Q_{(2^k-1),M} \end{bmatrix}^T$$

Note that both k and n are integer numbers, and m is the degree of shifted polynomials. Now, we state and prove a theorem in order to ensure the convergence of the new shifted wavelet expansion of a function.

Theorem 1. Assume that a function $f(t) \in L^2_w([0,1])$ where $w(t) = \frac{1}{\sqrt{1-t}}$, $t \neq \pm 1$, with bounded second derivative $|\ddot{f}(t)| \leq L$, L > 0, f can be expanded as an infinite series of the new shifted wavelets (1), then c_{nm} in (4) converges uniformly to f, i.e., c_{nm} satisfy the inequality:

$$|c_{nm}| \le L \frac{1}{n^{\frac{3}{2}}} 2^{\frac{3}{2}} \left(\frac{\sqrt{\pi}}{(m^2 - 1)} \right).$$
 (7)

Proof. Let:

$$f(t) = \sum_{n=1}^{\infty} \sum_{m=0}^{\infty} c_{nm} Q_{nm}(t).$$

It follows that for $k = 1, 2, 3, ...; n = 1, 2, ..., 2^k, m = 0, 1, ..., M$.

$$c_{nm} = \langle f(t), Q(t) \rangle = \int_{0}^{1} f(t) Q_{nm}(t) w_{k}(t) dt.$$

$$= \int_{0}^{\frac{n-1}{2^{k-1}}} f(t) Q_{nm}(t) w_{k}(t) dt$$

$$+ \int_{\frac{n-1}{2^{k-1}}}^{\frac{n}{2^{k-1}}} f(t) Q_{nm}(t) w_{k}(t) dt +$$

$$\int_{\frac{n}{2^{k-1}}}^{1} f(t) Q_{nm}(t) w_{k}(t) dt.$$

Using Equation (1), one can obtain:

$$c_{nm} = \int_{\frac{n-1}{2k-1}}^{\frac{n}{2k-1}} f(t) \frac{2^{\frac{k-1}{2}}}{\sqrt{\pi}} Ms_m \Big(2^k t - 2n + 1 \Big) w \Big(2^k t - 2n + 1 \Big) dt.$$

If m > 1, by substituting:

$$2^{k}t - 2n + 1 = \cos\theta, \ t = \frac{\cos\theta + 2n - 1}{2^{k}}, \ dt = \frac{-\sin\theta}{2^{k}}d\theta.$$

$$c_{nm} = \frac{2^{\frac{k-1}{2}}}{\sqrt{\pi}} \int_{0}^{\pi} f\left(\frac{\cos\theta + 2n - 1}{2^{k}}\right) 2\cos m\theta \sqrt{\frac{1}{1 - \cos^{2}\theta}} \frac{-\sin\theta}{2^{k}}d\theta.$$

$$c_{nm} = \frac{-2^{\frac{(k+1)}{2}}}{\sqrt{\pi}} \int_{0}^{\pi} f\left(\frac{\cos\theta + 2n - 1}{2^{k}}\right) \cos m\theta \ d\theta.$$

By using method of integration by parts, let:

$$\int_0^{\pi} u dv = uv - \int_0^{\pi} v du, u = f\left(\frac{\cos\theta + 2n - 1}{2^k}\right), du = f\left(\frac{\cos\theta + 2n - 1}{2^k}\right)\left(\frac{-\sin\theta}{2^k}\right), dv = \cos m\theta d\theta, v = \frac{\sin m\theta}{m}, m \neq 1.$$

$$c_{nm} = \frac{-2^{\frac{(k+1)}{2}}}{\sqrt{\pi}} f\left(\frac{\cos\theta + 2n - 1}{2^k}\right)\left(\frac{\sin m\theta}{m}\right)\Big]_0^{\pi} - \frac{2^{\frac{(k+1)}{2}}}{m^2} \int_0^{\pi} f\left(\frac{\cos\theta + 2n - 1}{2^k}\right) \sin m\theta \sin\theta d\theta.$$

Using again the method of integration by parts, let

$$u = \dot{f}\left(\frac{\cos\theta + 2n - 1}{2^k}\right), du = \ddot{f}\left(\frac{\cos\theta + 2n - 1}{2^k}\right)\left(\frac{-\sin\theta}{2^k}\right)d\theta, dv = \sin m\theta \sin\theta d\theta,$$

$$v = \left(\frac{\sin(m - 1)\theta}{m - 1} - \frac{\sin(m + 1)\theta}{m + 1}\right).$$

$$c_{nm} = -\frac{2^{\frac{(k+1)}{2}}}{m2^k\sqrt{\pi}}\dot{f}\left(\frac{\cos\theta + 2n - 1}{2^k}\right)\left(-\frac{\sin(m + 1)\theta}{m + 1} + \frac{\sin(m - 1)\theta}{m - 1}\right)\Big]_0^{\pi} - \frac{2^{\frac{(k+1)}{2}}}{m2^{2k}\sqrt{\pi}}\int_0^{\pi} \ddot{f}\left(\frac{\cos\theta + 2n - 1}{2^k}\right)\sin\theta\left(\frac{\sin(m - 1)\theta}{m - 1} - \frac{\sin(m + 1)\theta}{m + 1}\right)d\theta.$$

We have:

$$c_{nm} = -\frac{2^{\frac{(k+1)}{2}}}{m2^{2k}\sqrt{\pi}} \int_0^{\pi} \ddot{f}\left(\frac{\cos\theta + 2n - 1}{2^k}\right) \sin\theta\left(\frac{\sin(m-1)\theta}{m-1} - \frac{\sin(m+1)\theta}{m+1}\right) d\theta$$

Thus, we obtain:

$$|c_{nm}| = \left| -\frac{2^{\frac{(k+1)}{2}}}{m2^{2k}\sqrt{\pi}} \int_{0}^{\pi} \ddot{f}\left(\frac{\cos\theta + 2n - 1}{2^{k}}\right) \sin\theta\left(-\frac{\sin(m+1)\theta}{m+1} + \frac{\sin(m-1)\theta}{m-1}\right) d\theta \right|$$

$$\leq \frac{2^{\frac{(k+1)}{2}}}{m2^{2k}\sqrt{\pi}} \int_{0}^{\pi} \left| \ddot{f}\left(\frac{\cos\theta + 2n - 1}{2^{k}}\right) - \frac{\sin(m+1)\theta}{m+1} + \frac{\sin(m-1)\theta}{m-1} d\theta \right|$$

$$\leq L^{\frac{2}{m2^{2k}}\sqrt{\pi}} \int_{0}^{\pi} \left| \sin\theta\left(\frac{\sin(m-1)\theta}{m-1} - \frac{\sin(m+1)\theta}{m+1}\right) \right| d\theta.$$

However,

$$\int_0^\pi \left| sin\theta \left(-\frac{sin(m+1)\theta}{m+1} + \frac{sin(m-1)\theta}{m-1} \right) \right| d\theta = \int_0^\pi \left| sin\theta \left(-\frac{sin(m+1)\theta}{m+1} + \frac{sin(m-1)\theta}{m-1} \right) d\theta \right|.$$

$$\leq \int_0^\pi \left| \frac{sin\theta sin(m+1)\theta}{m+1} \right| + \left| sin\theta \left(\frac{sin(m-1)\theta}{m-1} \right) \right| d\theta \leq \frac{2m\pi}{(m^2-1)}.$$

Hence:

$$|c_{nm}| \le L \frac{2^{\frac{(k+1)}{2}}}{m2^{2k}\sqrt{\pi}} \left(\frac{2m\pi}{(m^2-1)}\right).$$
 $|c_{nm}| \le L \frac{2^{\frac{(k+1)}{2}}}{2^{2k}} \left(\frac{2\sqrt{\pi}}{(m^2-1)}\right).$

Since $n \le 2^{k-1}$, we have inequality becoming:

$$|c_{nm}| \le L \frac{1}{n^{\frac{3}{2}}} 2^{\frac{3}{2}} \left(\frac{\sqrt{\pi}}{(m^2 - 1)} \right).$$

Therefore, the wavelets expansion $\sum_{n=1}^{\infty} \sum_{m=0}^{\infty} c_{nm} Q_{nm}(t)$ converges to f(t) uniformly.

Accuracy Analysis

If the function f(t) is expanded in terms of New Shifted Wavelet Functions as in Equations (4) and (5), that is:

$$f(t) = \sum_{n=1}^{\infty} \sum_{m=0}^{\infty} c_{nm} Q_{nm}(t).$$

then it is not possible to perform the computation of an infinite number of terms, and we must thus truncate the series as below:

$$f_M(t) = \sum_{n=1}^{2^{k-1}} \sum_{m=0}^{M-1} c_{nm} Q_{nm}(t).$$

so that:

$$f(t) - f_M(t) = r(t).$$

where r(t) is the residual function defined by:

$$r(t) = \sum_{n=2^{k-1}+1}^{\infty} \sum_{m=M}^{\infty} c_{nm} Q_{nm}(t).$$

We must select the coefficients such that ||r(t)|| is less than some convergence value ϵ , that is:

$$\left(\int_0^1 |f(t)-f_M(t)|^2 w_n(t)dt\right)^{\frac{1}{2}} < \epsilon,$$

for all M greater than some positive integer value M_0 .

The calculation of the accuracy of a numerical method is crucial to describe the applicability and performance in order to solve problems. Theorem 2 discusses the accuracy of the wavelets representation of a function.

Theorem 2. Let f be a continuous function defined on the interval [0, 1) and $|\ddot{f}(t)| < L$, then the accuracy estimation is given by:

$$c_{n,m} = \left(\frac{\sqrt{\pi}L}{2^{-\frac{3}{2}}} \sum_{n=2^{k-1}+1}^{\infty} \sum_{m=M}^{\infty} \frac{1}{n^{\frac{3}{2}}} \left(\frac{1}{(m^2-1)}\right)\right)^{\frac{1}{2}},$$

where:

$$c_{n,m} = \left(\int_0^1 |r(t)|^2 w_n(t) dt\right)^{\frac{1}{2}}.$$

Proof. Since:

$$c_{n,m} = \left(\int_0^1 |r(t)|^2 w_n(t) dt\right)^{\frac{1}{2}}$$

Then:

$$c_{nm}^{2} = \int_{0}^{1} |r(t)|^{2} w_{n}(t) dt.$$

$$= \int_{0}^{1} \sum_{n=2^{k-1}+1}^{\infty} \sum_{m=M}^{\infty} |c_{nm}Q_{nm}(t)|^{2} w_{n}(t) dt.$$

$$= \sum_{n=2^{k-1}+1}^{\infty} \sum_{m=M}^{\infty} |c_{nm}|^{2} \int_{0}^{1} |Q_{nm}(t)|^{2} w_{n}(t) dt.$$

From the orthonormality criterion form Q_{nm} , one can obtain:

$$c_{nm}^2 = \sum_{n=2^{k-1}+1}^{\infty} \sum_{m=M}^{\infty} |c_{nm}|^2.$$

Using the findings from Equation (7):

$$c_{nm}^2 = \frac{\sqrt{\pi}L}{2^{-\frac{3}{2}}} \sum_{n=2^{k-1}+1}^{\infty} \sum_{m=M}^{\infty} \frac{1}{n^{\frac{3}{2}}} \left(\frac{1}{(m^2-1)}\right),$$

or

$$c_{n,m} = \left(\frac{\sqrt{\pi}L}{2^{-\frac{3}{2}}} \sum_{n=2^{k-1}+1}^{\infty} \sum_{m=M}^{\infty} \frac{1}{n^{\frac{3}{2}}} \left(\frac{1}{(m^2-1)}\right)\right)^{\frac{1}{2}}. \square$$

4. Operational Matrix of the NSW

The present section is built to derive an operational matrix of derivatives for the NSW. Based on the NSW vector $\Phi(t)$ mentioned in Equation (1), it can be determined that the operational matrix of integer derivative is as below.

The following theorem is needed hereafter:

Theorem 3. Let $\Phi(t)$ be the NSW vector defined in Equation (1). Then, the first derivative of the vector $\Phi(t)$ can be expressed as:

$$\frac{d\Phi(t))}{dt} = D_{\Phi}\Phi(t),\tag{8}$$

where D_{Φ} is $2^{k-1}(M+1)$ square operation matrix of differentiation and is defined by:

$$D_{\Phi} = \begin{pmatrix} D & O & \cdots & O \\ O & D & \cdots & O \\ \vdots & \vdots & \ddots & \vdots \\ O & O & \cdots & D \end{pmatrix}$$
 (9)

In which D is a square matrix and their elements can be explicitly obtained as below:

$$D_{i,j} = 2^k \begin{cases} i, & i \text{ odd and } j = 0, \\ 2i, & i > j \text{ and } i - j = odd, \\ 0, & otherwise. \end{cases}$$
 (10)

Proof. By using NSW, the *rth* element of vector $Q_{n,m}(t)$ can be rewritten in the following way:

$$Q_r(t) = Q_{n,m}(t) = \frac{2^{\frac{k-1}{2}}}{\sqrt{\pi}} Ms_m \left(2^k t - 2n + 1 \right), \tag{11}$$

For $\frac{n-1}{2^{k-1}} \le t \le \frac{n}{2^{k-1}}$ and $Q_r(t) = 0$ outside the interval $t \in \left[\frac{n-1}{2^{k-1}}, \frac{n}{2^{k-1}}\right]$, where $r = n(m+1) + (m+1), m = 0, 1, \ldots, M, n = 0, 1, 2, \ldots, (2^k - 1)$.

$$Q_{n,m}(t) = \frac{2^{\frac{k-1}{2}}}{\sqrt{\pi}} \left(Ms_m \left(2^k t - 2n + 1 \right) \right) \chi_{\left[\frac{n-1}{2^{k-1}}, \frac{n}{2^{k-1}} \right]}, \tag{12}$$

where

$$\chi_{\left[\frac{n-1}{2^{k-1}},\frac{n}{2^{k-1}}\right]} = \begin{cases} 1, & t \in \left[\frac{n-1}{2^{k-1}},\frac{n}{2^{k-1}}\right], \\ 0, & otherwise. \end{cases}$$

Differentiating Equation (11) with respect to t yields:

$$\frac{d\Phi(t)}{dt} = \frac{2^{\frac{k-1}{2}}}{\sqrt{\pi}} \left[\dot{M} s_m \left(2^k t - 2n + 1 \right) \right], \text{ for } t \in \left[\frac{n-1}{2^{k-1}}, \frac{n}{2^{k-1}} \right]. \tag{13}$$

Hence, the NSW expansion only has those elements in $Q_{n,m}(t)$ that are non-zero in the interval $\left[\frac{n-1}{2^{k-1}},\frac{n}{2^{k-1}}\right]$, that is:

$$Q_r(t), r = n(M+1), n(M+1) + 2, \dots, n(M+1) + (M+1).$$

This enables us to expand $\left(\frac{dQ_{nm}(t)}{dt}\right)$ in terms of the NSW in the form:

$$\frac{d\Phi(t)}{dt} = \sum_{r=n(M+1)+1}^{(n+1)(M+1)} c_r Q_r(t). \tag{14}$$

This implies that the operational matrix $D_{\Phi}(t)$ is a block matrix, as defined in Equation (9), since $\frac{d\Phi(t)}{dt}=0$.

Then, we have $\frac{d\Phi(t)}{dt} = 0$ for r = 1(M+1)+1, 2(M+1)+1, ..., $(2^k-1)(M+1)+1$, As a result, the elements of the first row of matrix D given in Equation (10) are zeros. Now, substitute $\frac{d\dot{M}s_m(t)}{dt}$ back into Equation (13), gives:

$$\frac{dQ_{n,m}(t)}{dt} = \frac{1}{\sqrt{\pi}} 2. \ 2^{k-1} n \begin{cases} \sum_{i=1}^{n-1} M s_{n-2i+1}(t) + \frac{1}{2} M s_0, & if \ n \ odd, \\ \sum_{i=1}^{n-1} M s_{n-2i+1}(t), & if \ n \ even. \end{cases}$$
(15)

Expanding Equation (15) in terms of NSW basis allows us to obtain:

$$\frac{dQ_{n,m}(t)}{dt} = 2.2^k n \begin{cases} \sum_{i=1}^{n-1} Q_{n(M+1)+i}(t) + \frac{1}{2}Q_0, & \text{if } n \text{ odd,} \\ \sum_{i=1}^{n-1} Q_{n(M+1)+i}(t), & \text{if } n \text{ even.} \end{cases}$$

Choosing D(i, j) such that:

$$D_{i,j} = 2^k \begin{cases} i & i \text{ odd, } j = 0, \\ 2i & i > j, i - j = odd, \\ 0 & otherwise. \end{cases}$$

The equation $\frac{dQ_{n,m}(t)}{dt} = DQ_{n,m}(t)$ is hold. \square

5. The NSW Algorithm for Solving Optimal Control Problem

In this section, the task of optimizing systems governed by ordinary differential equations, which leads to the optimal control problems, is investigated as they are arising in many applications in astronautics and aeronautics.

Consider the following process on fixed interval [0, 1]:

$$J = \int_{0}^{1} \mathcal{F}(t, u(t), x(t)) dt, \tag{16}$$

subject to:

$$u(t) = f(t, x(t), \dot{x}(t)), \tag{17}$$

together with the conditions:

$$x(0) = x_0, \ x(1) = x_1.$$
 (18)

where: $x(\bullet):[0, 1] \to \Re$ is the state variable, $u(\bullet):[0, 1] \to \Re$, is the control variable, and the function f is assumed to be real valued continuously differentiable.

First, we assume the solution of the state variables x(t) and $\dot{x}(t)$ in terms of NSW, respectively, is as below:

$$x(t) = \sum_{i=0}^{m} c_i Q_i(t),$$
(19)

$$\dot{x}(t) = \sum_{i=0}^{m} c_i DQ_i(t).$$
 (20)

where $C = [c_0 \ c_1 \dots c_m]^T$ is the unknown parameters vector.

The second step is to obtain the approximation for the control variable by substituting Equations (19) and (20) into Equation (17):

$$u(t) = f\left(t, \sum_{i=0}^{m} c_i Q_i(t), \sum_{i=0}^{m} c_i D Q_i(t)\right).$$
 (21)

Finally, the performance index value J is obtained as a function of the unknown $c_0, c_1, c_2, \ldots, c_m$ as below

$$J = \int_0^1 \mathcal{F}\left(\left(\sum_{i=0}^m c_i Q_i(t)\right)^2, \left(\sum_{i=0}^m c_i D Q_i(t)\right)^2\right) dt.$$

The resulting quadratic mathematical programming problem can be simplified as below:

$$J = \frac{1}{2}C^T \mathcal{H}C,$$

where:

$$\mathcal{H}=2\int_{0}^{1}\mathcal{F}\Big(\big(\Phi(t)\big)^{2},\big(D\Phi(t)\big)^{2}\Big)dt,$$

subject to:

$$FC - b = 0.$$

where:

$$F = \begin{bmatrix} \Phi^T(0) \\ \Phi^T(1) \end{bmatrix}, \quad b = \begin{bmatrix} x_0 \\ x_1 \end{bmatrix}.$$

Using Lagrange multiplier technique to obtain the optimal values of the unknown parameters C^*

$$C^* = \mathcal{H}^{-1} F^T \Big(F \mathcal{H}^{-1} F^T \Big)^{-1} b.$$

6. Test Examples

In this section, the results for the numerical simulation of optimal control problems formulated based on the proposed new shifted wavelet method are presented. Different test cases for m defined in the interval [0, 1] are considered with a single state function and a single control function. Note that the proposed method can be solved problems with multiple controls. The test problems are considered continuous optimal controls, and the analytic solution is known in order to allow the validation of the proposed algorithm by comparing its result with the exact solution.

Example 1. *In the following example, we have one state function*x(t) *and one control function*u(t)*. This problem is concerned with minimization of* [25,26]:

$$minJ = \int_0^1 \left(u^2(t) + x^2(t) \right) dt,$$

subject to:

$$u(t) = \dot{x}(t),$$

with initial conditions x(0) = 0, x(1) = 0.5.

The exact value of the performance index is J = 0.328258821379.

Table 1 shows the values of the coefficients, and Tables 2 and 3 give the values of the state and the control, respectively.

Table 1. The unknown coefficients c_i in Example 1.

c_i	m = 3	m = 4	<i>m</i> = 5
c_0	0.230545711338576	0.236727303476872	0.256199322878168
c_1	0.123366816327231	0.130013877070087	0.160508907830196
c_2	0.006294225322818	0.017822378525363	0.047112195129104
c_3		0.003860998979349	0.026814740481690
c_4			0.005789066578131

Table 2. Approximate and exact values of x(t) for Example 1.

t	m = 3	m = 4	m = 5	x_{exact}
0.2	0.081818181818	0.085725158561	0.0856632657718	0.0856602272147
0.4	0.172727272727	0.174680761099	0.1747677613426	0.1747583001210
0.6	0.272727272727	0.270773784355	0.2708607845984	0.2708700372292
0.8	0.381818181818	0.377911205073	0.3778493122834	0.3778527400206
1	0.5000000000000	0.5000000000000	0.50000000000000	0.50000000000000

Table 3. Approximate and exact values of u(t) for Example 1.

t	m = 3	m = 4	m = 5	u_{exact}
0.2	0.431818181818182	0.433446088794942	0.434113187975870	0.433996647185271
0.4	0.477272727272728	0.459365750528545	0.459887849303989	0.459952039568011
0.6	0.5227272727274	0.504820295983084	0.504298197207639	0.504366922299765
0.8	0.568181818181821	0.569809725158559	0.569142625977633	0.569023820575788
1	0.613636363636367	0.654334038054970	0.656219529904781	0.656517642749666

Table 4 gives the absolute errors $E_m = |J_{exact} - J_m|$ that the NSW method might produce with compression to the following methods:

- The method existing in [25].
- Chebyshev method proposed in [26].

Table 4. A comparison of the results of Example 1.

	E_m				
m	Presented Method	Method in [26]	Method in [25]		
3	0.00033	0.00033	0.0050		
4	0.00000051	0.00000052	0.0034		
5	0.0000000093	0.000000016	0.00021		

Example 2: Consider the second test problem [26]:

$$\min J = \int_{0}^{1} \left(u^{2}(t) + 3x^{2}(t) \right) dt, \tag{22}$$

$$u(t) = \dot{x}(t) - x(t), x(0) = 1, \ x(1) = 0.51314538.$$

The exact solution of (22) is:

$$u(t) = \frac{3e^{-4}}{3e^{-4} + 1}e^{2t} - \frac{3}{3e^{-4} + 1}e^{-2t}, \ x(t) = \frac{3e^{-4}}{3e^{-4} + 1}e^{2t} + \frac{1}{3e^{-4} + 1}e^{-2t} \text{ and } J = 2.791659975.$$

Table 5 shows the values of the coefficients, and Tables 6 and 7 give the values of the state and the control, respectively, whereas Table 8 lists the absolute errors that our method NSW might produce and compares our technique to the method presented in [26]. From these tables, it can be seen that the state and the control variables are accurately approximated by the proposed method.

Table 5. The unknown coefficients c_i in Example 2.

c_i	<i>m</i> = 3	m = 4	<i>m</i> = 5
c_0	0.355507506871318	0.346802467917968	0.353341978261637
c_1	0.011865347625915	0.003658158193373	0.011466719011776
c_2	0.059865632941091	0.047554848792278	0.053850500952116
<i>c</i> ₃		-0.004103594716271	0.0006.7914878500
c_4			0.001195685875318

Table 6. Approximate and exact values of x(t) for Example 2.

t	m = 3	m = 4	m = 5	x_{exact}
0.2	0.72969817542857	0.71547355348770	0.71303748341008	0.7131081208852
0.4	0.54586180114285	0.53874949017242	0.54172690915617	0.5418429752453
0.6	0.44849087714285	0.45560318811329	0.45858060709704	0.4584348199397
0.8	0.43758540342857	0.45181002536944	0.44937395529182	0.4493594610058
1	0.51314538000000	0.51314538000000	0.51314537999999	0.5131453766955

Table 7. Approximate and exact values of u(t) for Example 2.

t	<i>m</i> = 3	m = 4	<i>m</i> = 5	u_{exact}
0.2	-2.56767274857141	-2.71584589378880	-2.78633403260869	-2.79165997531006
0.4	-1.86504367257142	-1.85674597643924	-1.83028754865182	-1.82851756831608
0.6	-1.24888004685713	-1.17657155199105	-1.16048897823791	-1.16185967374545
0.8	-0.71918187142857	-0.66109799850335	-0.68313541022400	-0.68359121816281
1	-0.275949146285715	-0.296100694035280	-0.31768698166747	-0.31616348542896

Table 8 illustrates the fast convergence rate of the proposed method, since the errors decay rapidly by increasing the number of the NSW.

Table 8. Estimated values of J_m for m = 3, 4, 5 for Example 2.

m	J_m	E_m	<i>J_m</i> in [26]	E_m
3	2.79718233539	0.0055	2.7977436304	0.0060
4	2.79237308337	0.00071	2.7960838642	0.0044
5	2.79166202469	0.0000020	2.7960838642	0.0044

Example 3. Consider the third test problem

$$J = \frac{1}{2} \int_0^1 \left(u^2(t) + x^2(1) \right) dt,$$

$$u(t) = \dot{x}(t) - x(t)$$
, $x(0) = 1$, $x(1) = 0.3678794412$ and $J_{exact} = 1$.

Table 9 shows the values of the coefficients while Tables 10 and 11 compare the exact solutions and the approximate solutions of x(t) and u(t), respectively, for $m=3,\,4,\,5$. The absolute errors of J for various values of m are listed in Table 12. From these results, it is worthwhile to note that the approximate solutions obtain by the proposed method completely coincide with the exact solutions.

Table 9. The unknown coefficients c_i in Example 3.

c_i	<i>m</i> = 3	m = 4	<i>m</i> = 5
c_0	0.317388943264860	0.314366203750058	0.314854167521389
c_1	-0.10561159916574	-0.10846146531065	-0.10789004268669
c_2	0.017219482834726	0.012944683617373	0.013407812437593
c_3		-0.00142493307245	-0.00107009805596
c_4			0.00008.870875412

Table 10. Approximate and exact values of x(t) for Example 3.

t	m = 3	m = 4	m = 5	x_{exact}
0.2	0.8238348176509	0.8188954570054	0.8187261332539	0.81873075307798
0.4	0.6725401705963	0.6700704902736	0.6703085019619	0.67032004603563
0.6	0.5461160588363	0.5485857391591	0.5488237508474	0.54881163609402
0.8	0.4445624823709	0.4495018430164	0.4493325192649	0.44932896411722
1	0.3678794412000	0.3678794411999	0.3678794412000	0.36787944117144

Table 11. Approximate and exact values of u(t) for Example 3.

t	m = 3	m = 4	m = 5	u_{exact}
0.2	-1.642484391160	-1.6396030974501	-1.6376087511890	-1.6374615061559
0.4	-1.366837067632	-1.3417286510180	-1.3405383263440	-1.3406400920712
0.6	-1.116060279400	-1.0958912234308	-1.0975575714816	-1.0976232721880
0.8	-0.890154026461	-0.8971514540429	-0.89880715280116	-0.8986579282344
1	-0.689118308818	-0.7405699822088	-0.73541173113306	-0.7357588823428

Table 12. Estimated values of J_m for m = 3, 4, 5 of Example 3.

т	J_m	E_m
3	1.000272934759060	0.00027
4	1.000001904254601	0.0000019
5	1.000000007516538	0.0000000075

Example 4. *Consider the fourth test problem* [26]:

$$\min J = \int_{0}^{1} \left(0.5u^{2}(t) + x^{2}(t) \right) dt,$$

$$u(t) = \dot{x}(t) - 0.5x(t), \ x(0) = 1, \ x(1) = 0.5018480732.$$
(23)

The exact solution of (23) is:

$$u(t) = \frac{2e^{3t} - e^3}{a}$$
, $x(t) = \frac{2e^{3t} + e^3}{a}$, where $a = 2e^{\frac{3t}{2}}(1 + e^3)$ and $J = 0.8641644978$.

Table 13 compares absolute errors of presented method wavelets to the existing method presented in [26] with different values of m, and we see that the absolute errors of the presented method provide good results compares to the existing other method, which indicates a decrease in absolute errors with the increase in the value of m.

Table 13. Estimated values of J_m for m = 3, 4, 5 of Example 4.

m	J_m	E_m	m	J_m in [26]	E _m
3	0.86472880938	0.00056	2	0.8645390446	00037
4	0.86421807235	0.000053	3	0.8644550472	0.00029
5	0.86416456896	0.000000071	4	0.8643546452	0.00019

It is clear that the approximate solution of the performance index when m=8 is in very good agreement with the corresponding exact solution. Table 13 reports the absolute errors of J_m obtained by the proposed method at m=3, 4, 5 in comparison to the method in [26] at m=2, 3, 4. The obtained results show that the approximate solutions are more accurate for the proposed method than the method in [26]. In addition, the fast convergence rate of the proposed method is also illustrated from the absolute errors results, since by increasing the number of the NSW, the errors decay rapidly.

7. Discussion

The NSW coefficients for the state function x(t) and the control function u(t), the NSW approximated values $x_m(t)$ of orders m = 3, 4 and 5, the NSW approximated values $u_m(t)$ of orders m = 3, 4 and 5 and the error estimates E_m for different values of m are reported respectively in Tables 1-4 for Example 1, In Tables 5-8 for Example 2, in Tables 8-12 for Example 3 while in Table 13, the obtained error estimates E_m for different values of m have been calculated. A comparison between the NSW approximation and the exact solution shows that as *m* increases, the errors decay rapidly. One of the important advantages of the use of the NSW method is that the convergence of J_m is faster than some other methods in the literature see [25,26]. Therefore, by proceeding an approximations for the suitable value of m, the results obtained by the proposed method will rapidly tend to the results for the exact solution. The NSW approximation of order five is a very accurate approximation of the exact solution. Examples 2-4 have been solved by many researchers using different approaches, but the results obtained by NSW using state parameterization are the best results. From the results of Examples 2-4, it is clear that our algorithm gives better or comparable results with that of algorithms in [25,26], although the amount of computations in our method is very much less than in their algorithms.

A comparison between the results for the exact solution and for the values of m = 3 shows that the error in the performance index is of the order of 10^{-4} , while for the values m = 5, an agreement of about nine decimal places is obtained in the performance index. The results gradually tend towards the exact results as we systematically proceed to higher order approximations.

Tables 4, 7, 11 and 13 report the absolute errors for the performance index obtained by our method in comparison to the method in [25,26] at m = 3, 4, 5. The obtained results show that the absolute errors are better for the proposed method than those obtained in [25,26]. From such tables, it can be found that the state and the control variables are accurately approximated by the presented method.

8. Conclusions

This paper presents a new technique for obtaining the numerical solutions for optimal control problems. The derivation of the method is based on the construction of a new shifted wavelet with its operational matrix of derivatives. One of the advantages of the proposed technique is adopting a limited number of wavelets basis functions.

Approximate and exact solutions of examples are correspondingly compared. For Example 1, a comparison reports in Table 4 that it is clear that at m = 5, the results obtained by the proposed method are better than those in [25,26], with the absolute error of the performance index 9.3×10^{-9} , 1.6×10^{-8} and 2.1×10^{-4} , respectively. Numerical results for Example 2 were presented in [25] with the best absolute error 4.4×10^{-3} , while in our method, the best absolute method is 2.0×10^{-6} . Absolute errors of Example 4 were also given as 1.9×10^{-4} and 7.1×10^{-8} in [26] and the present work, respectively. The best absolute errors of Example 4 presented in [26] are given in Table 13. As can be seen from Tables 4, 8, 12 and 13, the present method is highly efficient and accurate, and it is quite high, even in the case of a small number of the basis wavelet functions.

Author Contributions: Methodology, G.A.; validation, S.S; formal analysis, G.A. and S.S; resources, G.A.; supervision, S.S. All authors have read and agreed to the published version of the manuscript.

Funding: This research received no external funding.

Data Availability Statement: Not applicable.

Conflicts of Interest: The authors declare no conflict of interest.

Abbreviations

$M_m(t)$	The special polynomials defined in the interval $[-1, 1]$.
$Ms_m(t)$	The shifted special polynomials defined in the interval [0, 1].
$Q_{nm}(t)$	The new shifted special wavelet functions.
$\Phi(t)$	The vector of the basis functions.
w(t)	The weight function.
$\ddot{f}(t)$	The second derivative.
⟨.,.⟩	Inner product operator on Hilbert space.
$f(t) \in L^2_w([0,1])$	means $\int_0^1 \left[f(t) \right]^2 w(t) dt$ finite.
$f \in C^2[0,1)$	f and its first derivative f are continues.
J	Performance index value.
x(t)	State variable.
u(t)	Control variable.
r(x)	Residual function
ϵ	Convergence value greater than zero.
D_Q	Operation matrix of derivative.
\mathfrak{R}	Real numbers.
χ	Delta function.
u_{exact}	Exact values of the control variable.
x_{exact}	Exact values of the state variable.
u_m	Approximate values of the control variable.
x_m	Approximate values of the state variable.
Jexact	Exact value of the performance index.
J_m	Approximate value of the performance index.
${\mathcal F}$	Integrand function.
C	Vector of unknown parameters.
C*	Vector of optimal parameters.
$E_m = J_{exact} - J_m.$	The absolute errors.

References

Zhaohua, G.; Chongyang, L.; Kok, L.; Song, W.; Yonghong, W. Numerical solution of free final time fractional optimal control problems. Appl. Math. Comput. 2021, 405, 126270.

- 2. Hans, G.; Christian, K.; Andreas, M.; Andreas, P. Numerical solution of optimal control problems with explicit and implicit switches. *Optim. Methods Softw.* **2018**, *33*, 450–474.
- 3. Wang, Z.; Yan, L. An Indirect Method for Inequality Constrained Optimal Control Problems. *IFAC Pap. Line* **2017**, *50*, 4070–4075. [CrossRef]
- 4. Yang, C.; Fabien, B. An adaptive mesh refinement method for indirectly solving optimal control problems. *Numer Algor* **2022**, *91*, 193–225. [CrossRef]
- 5. Nave, O. Modification of Semi-Analytical Method Applied System of ODE. Mod. Appl. Sci. 2020, 14, 75. [CrossRef]
- 6. Mohammad, A. A modified pseudospectral method for indirect solving a class of switching optimal control problems. *Proc. Inst. Mech. Eng. Part G J. Aerosp. Eng.* **2022**, 234, 1531–1542.
- 7. Mohammad, H. A new direct method based on the Chebyshev cardinal functions for variable-order fractional optimal control problems. *J. Frankl. Inst.* **2018**, *355*, 4970–4995.
- 8. Mohamed, A.; Mohand, B.; Nacima, M.; Philippe, M. Direct method to solve linear-quadratic optimal control problems. *Numer. Algebra Control. Optim.* **2021**, *11*, 645–663.
- 9. Askhat, D.; Elena, S.; Sergey, K. Approaches to Numerical Solution of Optimal Control Problem Using Evolutionary Computations. *Appl. Sci.* **2021**, *11*, 7096.
- 10. Mirvakili, M.; Allahviranloo, T.; Soltanian, F. A numerical method for approximating the solution of fuzzy fractional optimal control problems in caputo sense using legendre functions. *J. Intell. Fuzzy Syst.* **2022**, *43*, 3827–3858. [CrossRef]
- Viorel, M.; Iulian, A. Optimal Control Systems Using Evolutionary Algorithm-Control Input Range Estimation. Automation 2022, 3, 95–115.
- 12. Marzban, H.R.; Malakoutikhah, F. Solution of delay fractional optimal control problems using a hybrid of block-pulse functions and orthonormal Taylor polynomials. *J. Frankl. Inst.* **2019**, *356*, 8182–8215. [CrossRef]
- 13. Khamis, N.; Selamat, H.; Ismail, F.S.; Lutfy, O.F. Optimal exit configuration of factory layout for a safer emergency evacuation using crowd simulation model and multi-objective artificial bee colony optimization. *Int. J. Integr. Eng.* **2019**, *11*, 183–191. [CrossRef]
- 14. Behzad, K.; Delavarkhalafi, A.; Karbassi, M.; Boubaker, K. A Numerical Approach for Solving Optimal Control Problems Using the Boubaker Polynomials Expansion Scheme. *J. Interpolat. Approx. Sci. Comput.* **2014**, *3*, 1–18.
- 15. Ayat, O.; Mirkamal, M. Solving optimal control problems by using Hermite polynomials. *Comput. Methods Differ. Equ.* **2020**, *8*, 314–329.
- 16. Abed, M.S.; Lutfy, O.F.; Al-Doori, Q.F. Online Path Planning of Mobile Robots Based on African Vultures Optimization Algorithm in Unknown Environments. *J. Eur. Des Syst. Autom.* **2022**, *55*, 405–412. [CrossRef]
- 17. Sayevand, K.; Zarvan, Z.; Nikan, O. On Approximate Solution of Optimal Control Problems by Parabolic Equations. *Int. J. Appl. Comput. Math.* **2022**, *8*, 248. [CrossRef]
- 18. Suman, S.; Kumar, A.; Singh, G.K. A new closed form method for design of variable bandwidth linear phase FIR filter using Bernstein multiwavelets. *Int. J. Electron.* **2015**, *102*, 635–650. [CrossRef]
- 19. Mahdi, S.M.; Lutfy, O.F. Control of a servo-hydraulic system utilizing an extended wavelet functional link neural network based on sine cosine algorithms. *Indones. J. Electr. Eng. Comput. Sci.* **2022**, 25, 847–856. [CrossRef]
- 20. Keshavarz, E.; Ordokhani, Y.; Razzaghi, M. The Taylor wavelets method for solving the initial and boundary value problems of Bratu-type equations. *Appl. Numer. Math.* **2018**, 128, 205–216. [CrossRef]
- 21. Akram, K.; Asadollah, M.; Sohrab, E. Solving Optimal Control Problem Using Hermite Wavelet, Numerical Algebra. *Control. Optim.* **2019**, *9*, 101–112.
- 22. Rabiei, K.; Ordokhani, Y. A new operational matrix based on Boubaker wavelet for solving optimal control problems of arbitrary order. *Trans. Inst. Meas. Control* **2020**, *42*, 1858–1870. [CrossRef]
- 23. Jafari, H.; Nemati, S.; Ganji, R.M. Operational matrices based on the shifted fifth-kind Chebyshev polynomials for solving nonlinear variable order integro-differential equations. *Adv. Differ. Equ.* **2021**, 2021, 435. [CrossRef] [PubMed]
- 24. Vellappandi, M.; Govindaraj, V. Operator theoretic approach to optimal control problems characterized by the Caputo fractional differential equations. *Results Control Optim.* **2023**, *10*, 100194. [CrossRef]
- 25. Kafash, B.; Delavarkhalafi, A. Restarted State Parameterization Method For Optimal Control Problems. *J. Math. Comput. Sci.* **2015**, 14, 151–161. [CrossRef]
- 26. Kafash, B.; Delavarkhalafi; Mkarbass, S. Application of Chebyshev polynomials to derive efficient algorithms for the solution of optimal control problems. *Sci. Iran.* **2012**, *19*, 795–805. [CrossRef]

Disclaimer/Publisher's Note: The statements, opinions and data contained in all publications are solely those of the individual author(s) and contributor(s) and not of MDPI and/or the editor(s). MDPI and/or the editor(s) disclaim responsibility for any injury to people or property resulting from any ideas, methods, instructions or products referred to in the content.





Article

UWB and MB-OFDM for Lunar Rover Navigation and Communication

J. de Curtò 1,2,3,*, I. de Zarzà 1,2,3 and Carlos T. Calafate 1

- Departamento de Informática de Sistemas y Computadores, Universitat Politècnica de València, 46022 València, Spain; dezarza@em.uni-frankfurt.de (I.d.Z.); calafate@disca.upv.es (C.T.C.)
- Informatik und Mathematik, GOETHE-University Frankfurt am Main, 60323 Frankfurt am Main, Germany
- Estudis d'Informàtica, Multimèdia i Telecomunicació, Universitat Oberta de Catalunya, 08018 Barcelona, Spain
- * Correspondence: decurto@em.uni-frankfurt.de

Abstract: This paper presents a comprehensive study of ultra-wideband (UWB) and multi-band orthogonal frequency-division multiplexing (MB-OFDM) technologies for lunar rover navigation and communication in challenging terrains. Lunar missions pose unique challenges, such as signal propagation in the lunar environment, terrain elevation, and rover movement constraints. To address these challenges, we propose a hybrid communication and navigation system that leverages UWB technology for high-precision positioning and MB-OFDM for robust and high-throughput communication. We develop a realistic simulation framework that incorporates terrain elevation, obstacles, and rover movement constraints, along with a simple fading model for communication. Simulation results demonstrate the effectiveness of the proposed system in navigating lunar rovers to their target locations while maintaining reliable communication links with a lunar lander. A novel approach based on game theory for rover navigation is also presented. The study provides valuable insights into the design and optimization of communication and navigation systems for future lunar missions, paving the way for seamless integration of advanced terrestrial technologies in extraterrestrial environments.

Keywords: UWB; MB-OFDM; lunar missions; interplanetary communications; game theory; rover

MSC: 94A12; 93C85; 85-10; 91A40

1. Introduction and Overview

The exploration of the Moon has gained renewed interest in recent years, fueled by ambitious missions from both governmental and private space agencies. These lunar missions aim to establish a permanent human presence, exploit resources, and conduct scientific research. A key aspect of lunar missions is the deployment and operation of rovers, which play a crucial role in the exploration and utilization of the lunar surface. Ensuring reliable and efficient navigation and communication systems for these rovers is of paramount importance for the success of such missions.

Ultra-wideband (UWB) [1–4] technology has emerged as a promising candidate for high-precision positioning and navigation due to its fine time resolution and ability to operate in cluttered environments. Meanwhile, multi-band orthogonal frequency-division multiplexing (MB-OFDM) [5,6] has been demonstrated as an effective communication technique, offering high data rates and robustness against interference and multipath propagation. The integration of UWB and MB-OFDM technologies can provide a comprehensive solution for lunar rover navigation and communication challenges.

In this paper, we investigate the application of UWB and MB-OFDM technologies for lunar rover operations [7–9]. We develop a realistic simulation framework that incorporates

various lunar environment factors, such as terrain elevation, obstacles, and rover movement constraints. The framework also considers the signal propagation characteristics of the lunar environment and incorporates a simple fading model to simulate communication links between rovers and a lunar lander. Through simulations, we demonstrate the effectiveness of the proposed hybrid system in navigating lunar rovers to their target locations while maintaining reliable communication links [10,11]. A technique for rover navigation based on game theory is provided.

The remainder of this paper is organized as follows: Section 2 introduces the main considerations regarding designing a communication network on the Moon. Section 3 provides a brief overview of UWB and MB-OFDM technologies, along with their potential applications in lunar missions. Section 3.2 presents a comparison between UWB technology and THz communication technologies in the context of 5G. Section 4 describes the simulation framework and the various factors considered in modeling the lunar environment, presents the simulation results, and provides a detailed performance analysis of the proposed system. Section 5 discusses an approach based on game theory for rover navigation. Finally, Section 6 concludes the paper and provides potential directions for future research.

2. Lunar Communications: Network Topology and Frequency Bands

Designing a lunar communication network requires considering coverage, latency, and redundancy. In this simplified scenario, we propose a hybrid network consisting of satellite relays and surface infrastructure. Figure 1 shows an illustration of this hybrid architecture, which consists of lunar base stations, orbiting satellites, and Earth-based stations.

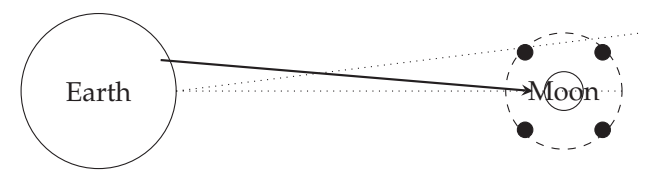


Figure 1. Hybrid lunar communication network architecture with satellite relays and surface infrastructure. This diagram shows Earth, the Moon, a lunar base station, and orbiting satellites. The dashed circle represents satellite orbits, while the filled circles on the orbit represent individual satellites. The dotted lines indicate communication links between Earth, the lunar base station, and the satellites. The FSOC link between Earth and the Moon is represented by a thick arrow.

To provide context for our assumptions and calculations, we present some essential data related to the Moon and its communication with Earth. The Moon's circumference is about 10,921 km, and the average Earth–Moon distance is 384,400 km. In our proposed architecture, we assume that the lunar base and relay satellites have a communication range of 500 km. With N satellites, 11 are needed for full coverage. These satellites can be placed in circular equatorial or polar orbits to ensure continuous coverage. Optical communication systems, such as laser-based free space optical communication (FSOC), can provide high-speed, low-latency communication between Earth and the Moon. In our analysis, we assume that the FSOC system has a data rate of 10 Gbps. Our calculations show a one-way latency of 1.28 s and an 800 s (13.3 min) transmission time for a 1 TB file.

To select suitable frequency bands for lunar communication, we must consider interference potential and Earth-based network compatibility. We examine the S-band (2–4 GHz), X-band (8–12 GHz), and Ka-band (26.5–40 GHz), used for satellite communication. Lower frequency bands offer longer communication ranges but lower data rates, while higher frequency bands support higher data rates but experience higher signal attenuation. In conclusion, lower frequency bands like the S-band may be used for basic communication, while higher frequency bands like the X-band and Ka-band can be used for high-resolution imagery, video communication, and data-intensive applications.

For the lunar surface communication, we focus on the integration of UWB and MB-OFDM technologies. These technologies enable high data rates and precise positioning, facilitating rover navigation and communication in the challenging lunar terrain. In the

following sections, we will delve into the details of the UWB and MB-OFDM systems and their implementation in the lunar environment.

Designing an optimal network topology for lunar communications involves considering multiple factors, including coverage, latency, and redundancy. In this example, we focus on a simple scenario to illustrate the concepts involved. We propose a hybrid network topology that combines satellite-based relay systems and surface-based communication infrastructure.

Assumptions: The Moon's circumference is approximately 10,921 km. The lunar base and relay satellites have a communication range of 500 km on the lunar surface. There are N satellites in orbit providing coverage for the lunar surface. Based on the developed code and the given assumptions, 11 satellites are required for full coverage of the lunar surface. This means that, at any given time, there will be a satellite within communication range (500 km) of any point on the Moon's surface. In reality, achieving full coverage can be more complex due to factors like the Moon's uneven topography and signal attenuation caused by the lunar regolith, but for the sake of this example, we are using a simplified model. To elaborate on the concept, these 11 satellites would be placed in strategically chosen orbits to ensure continuous communication coverage. To achieve this, the satellites could be placed in a constellation configuration, which could involve:

- Circular equatorial orbits: The satellites are placed in circular orbits around the Moon's
 equator, evenly spaced in terms of longitude. This configuration provides continuous
 coverage, as each satellite would cover a specific region of the lunar surface, and their
 combined coverage would span the entire Moon;
- Polar orbits: The satellites are placed in orbits that pass over or near the Moon's poles.
 This configuration can also provide continuous coverage, especially when considering the elliptical or inclined nature of the orbits, which can help to optimize coverage for regions near the poles or at higher latitudes.

Optical communication systems, such as laser-based systems, can provide high-speed, low-latency communication between the Moon and Earth. These systems rely on modulating light signals, often in the infrared spectrum, to transmit data. Let us consider the free space optical communication (FSOC) system for this example, as it is a promising technology for such applications.

Assumptions: The average distance between the Moon and Earth is approximately 384,400 km. The speed of light in a vacuum is approximately 299,792 km/s. We will assume a data rate of 10 gigabits per second (Gbps) for the FSOC system. Based on the developed code and the given assumptions, we calculated the one-way latency and the time required to transmit a 1 TB file using the free space optical communication (FSOC) system for communication between the Moon and Earth. The one-way latency of 1.28 s represents the time it takes for a signal to travel from the Moon to Earth, or vice versa, using the optical communication system. This is the minimum amount of time required for a message to be transmitted between the two points, not taking into account any additional processing delays, encoding, or error correction. This low-latency communication is beneficial for timesensitive operations and real-time control of lunar assets, as it allows for near-instantaneous exchange of information. The calculated time of 800 s (approximately 13.3 min) to transmit a 1 TB file represents a high data rate of 10 Gbps. This high data rate allows for the efficient transmission of large volumes of data, which is crucial for lunar missions that generate significant amounts of scientific data or require high-resolution imagery and video communication. By using FSOC systems, data can be sent back to Earth rapidly, enabling timely analysis and decision making.

To study suitable frequency bands and spectrum allocation strategies for lunar communication systems, we need to consider factors like the potential for interference and compatibility with Earth-based networks. Radio frequency (RF) bands are typically divided into low, medium, and high frequency ranges. Lower frequency bands can penetrate obstacles and provide longer communication ranges, while higher frequency bands can support higher data rates but are more susceptible to signal attenuation.

Let us start by looking at some popular frequency bands used for space communication and their respective characteristics:

- The S-band (2–4 GHz) is commonly used for near-Earth satellite communication, including navigation and weather satellites. It offers moderate data rates and has relatively low signal attenuation;
- The X-band (8–12 GHz) is used for deep space communication, including Mars missions and deep space probes. It provides higher data rates than the S-band, but it is more susceptible to signal attenuation due to its higher frequency;
- The Ka-band (26.5–40 GHz) offers high data rates and is used for high-capacity satellite communication systems. However, it is more susceptible to signal attenuation caused by atmospheric conditions, such as rain.

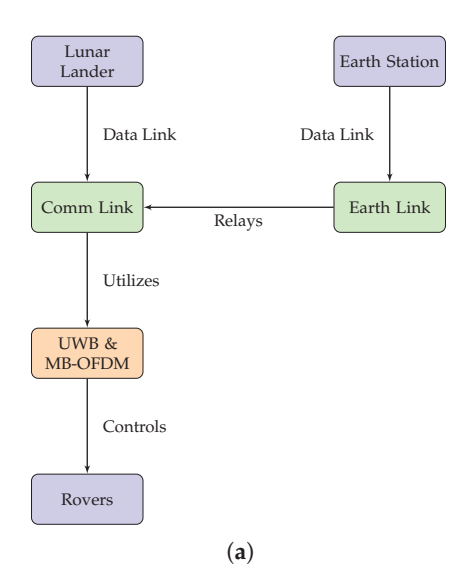
The calculated free space path loss (FSPL) for each frequency band provides insight into the signal attenuation that occurs over the average Moon–Earth distance. FSPL represents the loss in signal power that results solely from the spreading of the electromagnetic wave as it travels through free space. The greater the FSPL is, the more significant the signal attenuation over the given distance will be. Here are the calculated FSPL values for each frequency band: S-band—212.10 dB, X-band—224.14 dB, and Ka-band—234.24 dB. These results indicate that signal attenuation increases with frequency. The S-band experiences the lowest FSPL, while the Ka-band experiences the highest. Lower frequency bands, such as the S-band, are generally more resistant to signal attenuation and can penetrate obstacles more easily, providing longer communication ranges. However, they typically support lower data rates compared to higher frequency bands. Higher frequency bands, such as the X-band and Ka-band, can support higher data rates, which is essential for applications that require the transmission of large volumes of data. However, these bands are more susceptible to signal attenuation, as demonstrated by their higher FSPL values. Additionally, they may experience higher levels of interference due to atmospheric conditions, such as rain.

When selecting a frequency band for lunar communication systems, it is crucial to balance the need for data rate capacity and signal strength. Lower frequency bands, like the S-band, may be suitable for basic communication and telemetry, while higher frequency bands, like the X-band and Ka-band, can be used for high-resolution imagery, video communication, and data-intensive scientific applications.

2.1. Overview of Lunar Missions

An understanding of the general architecture of lunar missions is essential for appreciating the specific challenges and solutions addressed in this paper. Figure 2a presents an overview of a typical lunar mission, while Figure 2b shows a common visual illustration.

In a standard mission, a lunar lander transports one or more rovers to the lunar surface. Upon landing, the rovers are deployed to carry out various tasks, such as scientific investigations or logistical operations. The lander often serves as a relay point for communication between the rovers and Earth-based stations. The critical role of navigation and communication systems, such as UWB and MB-OFDM, is evident in ensuring the success of such complex missions [12–14].



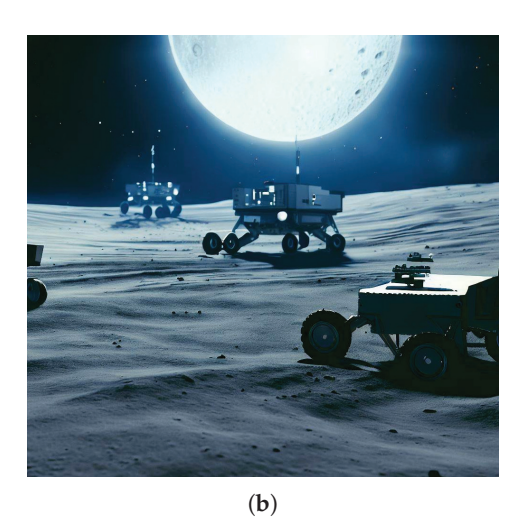


Figure 2. Diagram and visual illustration of a typical lunar mission. (a) General diagram illustrating the components and architecture of a typical lunar mission. (b) Visual illustration of the setup with a lander communicating with several rovers.

2.2. Motivation for Employing UWB and MB-OFDM in Lunar Rover Navigation

UWB and MB-OFDM are pivotal technologies for achieving robust and high-throughput communication between lunar rovers and the lunar lander. These technologies were chosen due to their unique advantages in the context of lunar exploration. Below, we outline the contributions of each:

UWB

- High data rate: UWB can provide extremely high data rates, crucial for transmitting high-definition sensor data;
- **Low power consumption**: UWB's low-power spectral density makes it energy-efficient, prolonging the mission lifespan;
- **Robustness**: UWB is known for its robustness against multi-path fading and interference, which is critical in challenging lunar terrains.

MB-OFDM

- Spectral efficiency: MB-OFDM is highly spectral efficient, making the best use of available frequency bands;
- Flexibility: It allows flexible allocation of resources, which can be dynamically adjusted based on mission requirements;
- Resilience: The technology is resilient to frequency-selective fading, making it ideal for lunar operations.

The integration of UWB and MB-OFDM technologies with the pathfinding algorithm forms one of the cornerstones of this research study. These communication technologies provide the backbone that supports the decision-making capabilities of the pathfinding algorithm and one of the key components of the game-theoretic proposal, enabling rovers to make more informed choices based on real-time data.

- Data transmission: High-speed data transmission enabled by UWB and MB-OFDM ensures that the rovers can receive timely updates, essential for the pathfinding algorithm to operate optimally;
- **Scalability**: The adaptability of MB-OFDM supports the operation of multiple rovers, thereby allowing the pathfinding algorithm to scale its operations;
- Reliability: The robustness of UWB ensures that essential control messages, crucial
 for the pathfinding algorithm, are delivered reliably even in the harshest of conditions.

3. UWB and MB-OFDM

UWB [15] is a radio technology that utilizes a large portion of the radio spectrum, typically exceeding 500 MHz, for the transmission of low-power, short-range signals. The key advantage of UWB is its high time resolution, which enables precise positioning and navigation capabilities. The impulse radio nature of UWB allows it to penetrate obstacles and operate effectively in cluttered environments, making it suitable for lunar missions [16].

UWB signals are characterized by their large fractional bandwidth, given by: $B_f = (f_H - f_L)/f_c$, where f_H and f_L are the highest and lowest frequencies of the UWB signal, respectively, and f_c is the center frequency. According to the Federal Communications Commission (FCC), a signal is considered UWB if its fractional bandwidth is greater than 0.2 or its bandwidth is greater than 500 MHz.

The time difference of arrival (TDoA) method is commonly employed for UWB-based positioning systems. The TDoA measures the difference in arrival times of UWB signals transmitted from multiple anchors to a receiver. By calculating the TDoA values for at least three anchors, the receiver can accurately determine position using trilateration.

A key feature of UWB signals is their extremely short duration, often in the order of nanoseconds. These signals are generated by transmitting a series of pulses with a very low duty cycle, resulting in a wide bandwidth and minimal interference with other narrowband systems. The mathematical representation of a UWB pulse is given by:

$$p(t) = A \cdot \operatorname{rect}\left(\frac{t - t_0}{T_p}\right) \cdot \cos(2\pi f_c(t - t_0)),\tag{1}$$

where A is the amplitude, t_0 is the pulse start time, T_p is the pulse duration, and f_c is the carrier frequency. The rect function is defined as:

$$\operatorname{rect}(x) = \begin{cases} 1, & \text{if } -\frac{1}{2} \le x \le \frac{1}{2}, \\ 0, & \text{otherwise.} \end{cases}$$
 (2)

The wide bandwidth of UWB signals offers several advantages, including high data rates, precise time resolution, and robustness against multipath fading and interference [16,17]. Moreover, UWB systems can coexist with other wireless technologies without causing significant interference, making them suitable for various applications, such as indoor positioning, radar systems, and wireless personal area networks [18,19].

The UWB channel can be modeled as a linear time-variant system with multipath components, each characterized by its path gain, delay, and phase shift. The impulse response of the UWB channel is given by:

$$h(t,\tau) = \sum_{z=1}^{N_p} \alpha_z(t) \cdot \delta(\tau - \tau_z(t)) \cdot e^{-j\phi_z(t)},$$
(3)

where N_p is the number of multipath components, $\alpha_z(t)$ is the path gain, $\tau_z(t)$ is the delay, $\phi_z(t)$ is the phase shift, and $\delta(\cdot)$ is the Dirac delta function. The received UWB signal, r(t), is obtained by convolving the transmitted signal, s(t), with the channel impulse response:

$$r(t) = s(t) * h(t,\tau) + n(t), \tag{4}$$

where n(t) is the additive white Gaussian noise (AWGN) with zero mean and variance σ^2 . To recover the transmitted signal, a UWB receiver typically employs a matched filter or a rake receiver that combines the energy from different multipath components.

3.1. UWB Positioning Techniques

UWB technology is particularly well suited for positioning and localization applications owing to its high time resolution and ability to resolve multipath components. Some common UWB-based positioning techniques include time of arrival (ToA), time difference

of arrival (TDoA), and angle of arrival (AoA). These techniques rely on accurate estimation of the propagation delay or angle of arrival of the UWB signal, which can be achieved using cross-correlation or maximum likelihood estimation methods.

To A is a technique that estimates the distance between a transmitter and a receiver by measuring the time it takes for a UWB signal to travel from the transmitter to the receiver. The distance d can be calculated using the relation: $d = c \cdot t_{\rm prop}$, where c is the speed of light and $t_{\rm prop}$ is the propagation time of the UWB signal. To A-based positioning typically requires the transmitter and receiver to be synchronized, and the accuracy of the distance estimation is directly proportional to the UWB signal's time resolution.

TDoA is a technique that measures the difference in arrival times of a UWB signal at multiple receivers. The position of the transmitter can be estimated by finding the intersection of hyperbolic curves obtained from the time difference measurements. TDoA-based positioning does not require the transmitter and receiver to be synchronized but demands precise time synchronization among the receivers.

AoA is a technique that estimates the transmitter's position by measuring the angle at which the UWB signal arrives at multiple receivers. The position of the transmitter can be estimated by finding the intersection of the lines obtained from the angle measurements. AoA-based positioning typically requires an array of antennas at the receiver to measure the angle of arrival accurately.

3.2. Comparison of UWB and B5G

This section presents a comparative study of the performance of UWB and a specific Beyond 5G technology, focusing on key performance indicators such as latency, data rate, path loss, and distance. To provide a relevant comparison, we consider terahertz (THz) communication [20], which offers ultra-high data rates and low latency. THz communication has been proposed as a promising candidate for Beyond 5G networks, particularly for short-range and high-capacity applications. UWB offers the benefits of high-precision positioning, robustness against multipath fading and interference, and coexistence with other wireless technologies, while THz communication provides ultra-high data rates and low latency.

3.2.1. Latency vs. Distance and Data Rate vs. Distance

Latency is a critical factor in lunar communication systems, as it affects the responsiveness and coordination of rovers, landers, and other nodes in the network. The latency in both UWB and Beyond 5G systems can be modeled as a function of the distance between the transmitter and receiver, taking into account the propagation speed, the processing delay, and the queuing delay.

$$Latency = \frac{Distance}{c} + Processing Delay + Queuing Delay,$$
 (5)

where *c* represents the speed of light in a vacuum.

UWB technology exhibits lower latency as the distance increases within its short-range operating limits owing to its ultra-wide bandwidth and impulse-based transmission. In contrast, Beyond 5G [20] systems may experience higher latency due to the increased overhead from the complex modulation and coding schemes employed to achieve higher data rates. It is important to note that the UWB technology is suitable for short-range communication scenarios (e.g., within a lunar base or between closely spaced rovers), while Beyond 5G technology can be more suitable for longer range communications. The data rate of a communication system is a crucial aspect of its performance, particularly when transmitting large amounts of data, such as high-resolution images and scientific measurements. In UWB systems, the data rate is primarily determined by the available bandwidth and the modulation scheme employed. The Shannon–Hartley theorem, which states the maximum achievable data rate for a given bandwidth and signal-to-noise ratio

(SNR), can provide a rough estimate of the data rate. However, it should be noted that this equation is a theoretical upper bound.

Data Rate =
$$B \times \log_2(1 + SNR)$$
, (6)

where *B* represents the bandwidth and SNR denotes the signal-to-noise ratio. On the other hand, Beyond 5G systems leverage advanced techniques, such as massive multiple-input and multiple-output (MIMO) and beamforming, to achieve high data rates over longer distances. These techniques help improve the SNR, allowing for higher data rates without necessarily increasing the available bandwidth. Our simulation results indicate that Beyond 5G systems can achieve higher data rates compared to UWB, particularly at longer distances. However, this comes at the cost of increased complexity and power consumption, which may be detrimental in the resource-constrained lunar environment.

3.2.2. Path Loss vs. Distance

Path loss is a significant factor in determining the signal strength and communication range in wireless systems. In both UWB and Beyond 5G technologies, path loss can be modeled using the log-distance path loss model:

Path Loss (dB) =
$$PL_{d_0} + 10n \log_{10} \left(\frac{d}{d_0}\right)$$
, (7)

where PL_{d_0} represents the reference path loss at distance d_0 , n is the path loss exponent, and d is the distance between the transmitter and receiver.

UWB systems exhibit lower path loss over short distances due to their wide bandwidth and impulse-based transmission, as depicted in Figure 3. In contrast, Beyond 5G systems may experience higher path loss, especially in the presence of obstacles and multipath propagation. However, advanced techniques, such as beamforming and massive MIMO, can help mitigate these effects.

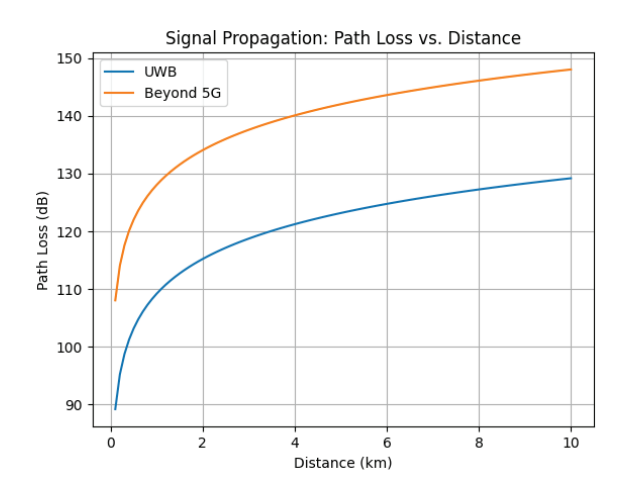


Figure 3. Path loss vs. distance comparison using UWB and B5G.

3.3. MB-OFDM

OFDM [21,22] is widely used in modern communication systems for its robustness against multipath fading and inter-symbol interference. OFDM divides the available frequency band into multiple closely-spaced orthogonal subcarriers, each carrying a modulated data symbol. Multi-band OFDM (MB-OFDM) extends the basic OFDM concept by dividing the available spectrum into several non-overlapping frequency bands, each containing a group of OFDM subcarriers. This approach provides better spectral efficiency, and allows for dynamic frequency allocation to accommodate varying communication requirements. The total number of subcarriers in an MB-OFDM system is given by:

 $N_{total} = N_{bands} * N_{subcarriers_per_band}$, where N_{bands} is the number of frequency bands and $N_{subcarriers_per_band}$ is the number of OFDM subcarriers within each band.

In OFDM, the orthogonality of the subcarriers allows them to be closely spaced, resulting in efficient bandwidth utilization. The time-domain OFDM signal can be represented as:

$$s(t) = \sum_{\alpha=0}^{N-1} \operatorname{Re}\left(X_{\alpha}e^{j2\pi\alpha\Delta ft}\right),\tag{8}$$

where N is the number of subcarriers, Δf is the subcarrier spacing, X_o is the complex data symbol for the o-th subcarrier, and t is time.

In MB-OFDM, each band consists of several orthogonal subcarriers, and data are transmitted by frequency hopping across these bands. This approach provides increased robustness against narrowband interference and improves spectral efficiency by allowing the system to adapt to varying channel conditions. The time-domain MB-OFDM signal can be represented as:

$$s(t) = \sum_{n=0}^{M-1} \sum_{o=0}^{N-1} \operatorname{Re}\left(X_{n,o} e^{j2\pi(n\Delta f_b + o\Delta f)t}\right),\tag{9}$$

where M is the number of bands, Δf_b is the band spacing, and $X_{n,o}$ is the complex data symbol for the o-th subcarrier in the n-th band.

3.3.1. Subcarrier Modulation and Demodulation

Data symbols are modulated onto the subcarriers using a variety of modulation schemes, such as binary phase-shift keying (BPSK), quadrature phase-shift keying (QPSK), or quadrature amplitude modulation (QAM). The choice of modulation scheme depends on the desired trade-off between data rate, power consumption, and error performance. Demodulation is performed using the inverse process, which typically involves fast Fourier transform (FFT) operations to convert the received time-domain signal into frequency-domain data.

3.3.2. Channel Estimation and Equalization

Channel estimation and equalization techniques are employed in MB-OFDM systems to compensate for the effects of channel impairments, such as multipath fading and frequency-selective fading. Common methods for channel estimation include pilot symbol-assisted estimation and decision-directed estimation. Equalization techniques, such as zero forcing (ZF) or minimum mean square error (MMSE) equalizers, are applied to mitigate the effects of channel distortions. In summary, MB-OFDM technology combines the advantages of OFDM with frequency hopping across multiple bands, resulting in improved spectral efficiency and robustness against narrowband interference.

3.4. Theoretical Analysis of RF Interference between UWB and MB-OFDM

RF interference between UWB and MB-OFDM systems poses a critical concern in the implementation of hybrid communication and navigation systems for lunar rovers. In this section, we present a theoretical framework that analyzes this potential interference and discuss possible mitigation techniques.

The key metrics that determine the extent of RF interference are:

- Spectral overlap: frequency ranges where both UWB and MB-OFDM operate;
- 2. Signal-to-interference ratio (SIR): measures the strength of the desired signal relative to interference;
- 3. Adjacent channel leakage ratio (ACLR): represents power leakage into adjacent frequency bands.

Let $P_{\text{UWB}}(f)$ and $P_{\text{MB-OFDM}}(f)$ represent the power spectral densities of the UWB and MB-OFDM systems, respectively. Then, the interference I can be modeled as:

$$I = \int_{-\infty}^{\infty} P_{\text{UWB}}(f) \cdot P_{\text{MB-OFDM}}(f) \, df \tag{10}$$

For an acceptable level of operation, I should be below a certain threshold I_{max} . **Potential mitigation strategies:**

- 1. Dynamic frequency selection (DFS): assign non-overlapping frequency bands when possible;
- 2. Power control: adjust the transmission power based on the proximity of interfering signals;
- 3. Time division multiple access (TDMA): allocate distinct time slots for UWB and MB-OFDM signals.

The theoretical analysis indicates that careful system design, accounting for interference, can enable effective coexistence of UWB and MB-OFDM systems in lunar rover applications.

3.5. Potential Applications in Lunar Missions

The integration of UWB and MB-OFDM technologies provides a comprehensive solution for both navigation and communication in lunar rover operations. By combining the high data rates, precise positioning, and reliable communication offered by UWB and MB-OFDM, the resulting system is highly adaptable to varying channel conditions and challenging environments, such as lunar missions. The use of multiple bands and orthogonal subcarriers enables efficient utilization of the available spectrum, while the inherent robustness against multipath fading and narrowband interference ensures reliable communication links. The high data rates provided by the MB-OFDM UWB system are suitable for transmitting large amounts of information, such as high-resolution images, video streams, and scientific data. Furthermore, the precise positioning capabilities enabled by UWB can assist in navigation and coordination among lunar rovers, landers, and other communication nodes.

Incorporating these technologies in tandem allows for a flexible and reliable communication and navigation system that is well suited to the challenging lunar environment. UWB can provide high-precision positioning and navigation capabilities, enabling rovers to accurately traverse the lunar surface and reach target locations. Simultaneously, MB-OFDM can offer robust communication links, ensuring efficient information exchange between rovers and the lunar lander or other infrastructure. Overall, the integration of UWB and MB-OFDM technologies offers significant advantages for lunar missions, fostering the development of an advanced communication and navigation system for lunar rovers that can effectively navigate and operate in the complex lunar terrain.

4. Simulation Framework and Lunar Environment Modeling

The simulation framework developed in this work (code is available at: https://doi.org/10.24433/CO.5122707.v1, accessed on 1 August 2023) aims to model the behavior of rovers in the lunar environment, focusing on their navigation and communication capabilities. The framework incorporates terrain generation using PERLIN noise, obstacle placement, rover movement, and communication system modeling, including UWB and OFDM technologies to illustrate the applicability of MB-OFDM.

The main components of the simulation framework are:

- Terrain generation using PERLIN noise: a grid-based representation of the lunar surface with varying elevation levels;
- Obstacle placement: random placement of obstacles on the terrain representing rocks and other surface features;
- Rover movement: modeling rover movement based on navigation algorithms, such as A* pathfinding or reinforcement learning (RL) techniques like proximal policy optimization (PPO) [23], considering constraints like terrain elevation and slope;
- Communication system: incorporating UWB positioning, OFDM communication, and simple fading models to estimate signal strength and communication delay.

The A* pathfinding algorithm [24] is an informed search algorithm that efficiently finds the shortest path between a given start and end point in a weighted graph, such as a grid or a graph representing a terrain. It is widely used in various applications, including robotics, video games, and route planning, due to its effectiveness and performance. The A* algorithm combines the benefits of Dijkstra's algorithm, which guarantees the shortest path, and the greedy best-first-search algorithm, which directs the search towards the goal using a heuristic function.

Given a graph G = (V, E), where V is the set of vertices (nodes) and E is the set of edges, let S be the starting node and S be the goal node. The algorithm maintains two sets of nodes, an open set S and a closed set S. The open set initially contains the starting node, while the closed set is initially empty. Each node S is associated with two cost values: the actual cost S in the starting the cost of the path from the starting node to S and the estimated total cost S is the sum of S and a heuristic function S in that estimates the cost from S to the goal node S:

$$f(n) = g(n) + h(n). \tag{11}$$

The A^* algorithm performs the steps until the goal node is reached or the open set is empty. The heuristic function h(n) plays a crucial role in the performance of the A^* algorithm. A good heuristic function should be admissible, meaning it never overestimates the actual cost to reach the goal. A common choice for grid-based graphs is the Euclidean distance or the Manhattan distance. The choice of the heuristic function depends on the problem domain and the constraints imposed by the specific application. Upon termination of the algorithm, if the goal node is reached, the optimal path can be reconstructed by traversing the parent pointers from the goal node to the starting node, in reverse order. If the open set is empty and the goal node is not reached, it implies that there is no valid path between the start and goal nodes. Algorithm 1 illustrates the main steps.

Algorithm 1 A* Pathfinding Algorithm

```
1: Initialize open set O with the starting node s and closed set C as empty
2: while O is not empty do
       Select the node n from the open set O with the lowest estimated total cost f(n) and
   remove it from O
 4:
       if n is the goal node g then
          Reconstruct the optimal path and terminate the algorithm
5:
       end if
 6:
       Add n to the closed set C
 7:
       for each neighbor m of n that is not in the closed set C do
8:
          Calculate the tentative cost for m, g_t(m) = g(n) + c(n, m), where c(n, m) is the
   cost of moving from n to m
          if m is not in the open set O or g_t(m) < g(m) then
10:
              Set g(m) = g_t(m)
11:
              Calculate the estimated total cost for m, f(m) = g(m) + h(m)
12:
              Set the parent of m to n
13.
              if m is not in the open set O then
14:
                 Add m to O
15:
              end if
16:
          end if
17:
       end for
18:
19: end while
```

4.1. Lunar Environment Modeling

Several factors were considered to model the lunar environment accurately and assess the performance of the proposed navigation and communication system. These factors included:

- Terrain elevation: A randomly generated elevation map was created to simulate the uneven lunar surface. Elevation differences impact rover movement and navigation due to slope constraints;
- Obstacle placement: Obstacles in the lunar environment, such as rocks and craters, affect rover navigation and communication. The simulation framework places random obstacles on the terrain and validates rover movement to avoid collisions;
- Rover movement constraints: Rovers on the lunar surface are subject to movement constraints, such as maximum slope and velocity limits. These constraints were incorporated into the simulation framework to ensure realistic rover behavior;
- Communication models: The integration of UWB positioning and MB-OFDM communication, along with a simple fading model, provides a comprehensive communication system for the lunar rovers. These models were employed to estimate communication delay and signal strength between the rovers and the lunar lander.

In Figure 4, we show a conceptual plot of a lander acting as an anchor and communicating with several rovers that are exploring the terrain.

Rover and Lander Positions and Communication Links

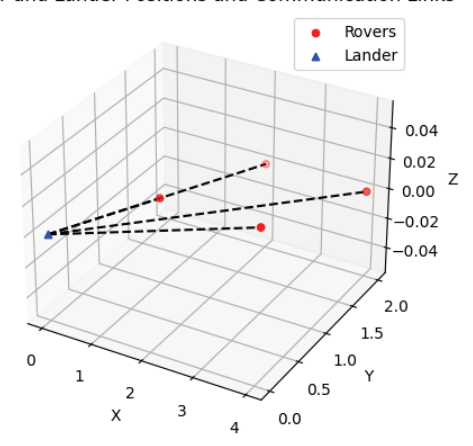


Figure 4. Three-dimensional (3D) representation of a lander acting as anchor and communicating to several rovers.

4.2. Simulation Parameters

To provide a comprehensive evaluation of the proposed system, we consider a set of realistic parameters for UWB, MB-OFDM, terrain generation, and rover movement constraints. For instance, Table 1 provides good default parameters for the simulations.

The parameters were chosen based on a balance between real-world feasibility and the need for extensive simulation testing. The selected parameter values provide a robust testbed for evaluating the system's performance in a lunar environment [25].

Table 1. Summary of good default simulation p	parameters.
--	-------------

Parameter Category	Parameter	Value
UWB	Frequency range Bandwidth Modulation scheme Transmission power	3.1–10.6 GHz 500 MHz BPSK –41.3 dBm/MHz
MB-OFDM	Subcarrier spacing Number of subcarriers Modulation scheme Bandwidth	312.5 kHz 128 64-QAM 20 MHz
Terrain	Noise Scale Octaves Persistence Lacunarity	0.1 4 0.5 2.0
Rover	Maximum speed Turning radius Incline limit	0.5 m/s 0.3 m 30°

4.3. Simulation Results

The simulation was performed using the developed framework incorporating UWB positioning, OFDM communication, terrain generation using PERLIN noise, and rover movement constraints. The results provide insights into the performance of the proposed system in a realistic lunar environment. Several scenarios were simulated with varying terrain, obstacle placements, and rover-target locations; an example is depicted in Figure 5a,b, where we take into account the elevation of the terrain.

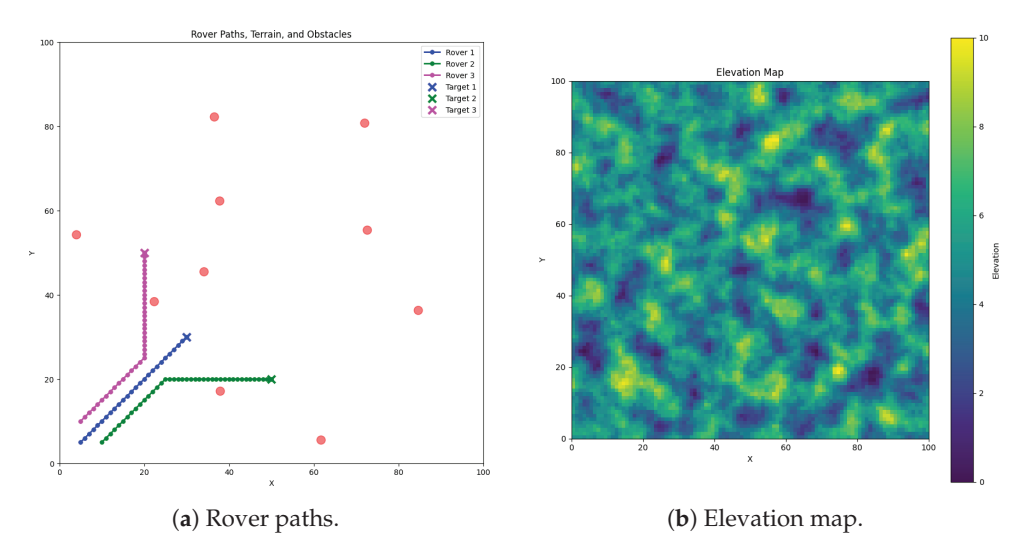


Figure 5. Simulation results. (a) Two-dimensional (2D) representation of a simulated scenario with several rovers following a given path. (b) Corresponding elevation of the terrain for the simulated scenario with PERLIN noise.

The simulation results can be summarized as follows:

- Navigation performance: The rovers were able to navigate to their target locations using the A* pathfinding algorithm, considering terrain elevation, slope constraints, and obstacle avoidance. The generated paths were efficient and safe, ensuring minimal travel time and energy consumption;
- Communication performance: The integrated UWB and OFDM communication system provided reliable and robust communication between the rovers and the lunar lander. The simple fading model allowed for the estimation of signal strength and

- communication delay, demonstrating the effectiveness of the proposed system in maintaining connectivity throughout the mission;
- Robustness and adaptability: The simulation framework demonstrated the ability to handle various scenarios and environmental conditions, proving the adaptability and robustness of the proposed system in the lunar environment.

Figure 6a shows the relationship between signal strength and the distance between the rover and the lunar lander. This plot provides insight into how the signal strength is affected by the distance traveled by the rover. Figure 6b presents the communication delay as a function of the distance between the rover and the lunar lander, showcasing the effectiveness of the proposed communication system in maintaining connectivity throughout the mission.

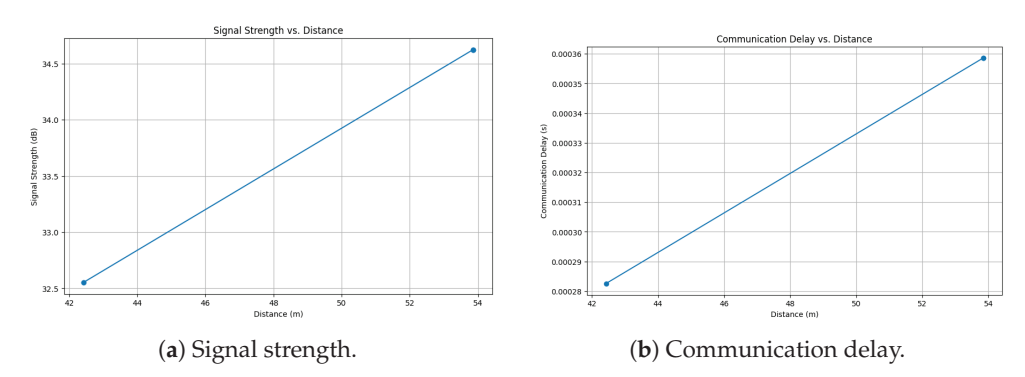


Figure 6. Telecommunication analysis. (a) Signal strength (dB) vs. distance (m) between the rover and the lunar lander. (b) Communication delay (s) vs. distance (m) between the rover and the lunar lander.

Specifically, Figure 6a,b present the telecommunication analysis concerning two key metrics: (a) signal strength in dB vs. distance in meters between the rover and the lunar lander and (b) communication delay in seconds vs. distance in meters between the rover and the lunar lander.

The simulation results in Figure 6a indicate that the signal strength decreases logarithmically with increasing distance between the rover and the lunar lander. This trend is expected due to the path loss experienced by radio signals over distance, especially in the challenging terrain of the lunar surface. The observed behavior is consistent with the FRIIS transmission equation and the effects of multi-path fading.

The results shown in Figure 6b reveal that the communication delay increases linearly with the distance between the rover and the lunar lander. This is attributable to the increased time-of-flight of signals as the distance expands. Additionally, the lunar terrain, characterized by craters and rocky formations, may introduce additional delays due to the diffraction and reflection of signals.

These findings have significant implications for the operational boundaries within which the rover and the lunar lander need to stay to maintain effective communication. The results support the feasibility of our proposed UWB and MB-OFDM hybrid system for lunar applications within the parameters and constraints assumed in our simulations.

5. Game-Theoretic Approach in Lunar Rover Navigation

Navigational strategies for lunar rovers have, for the longest time, leaned heavily on classical pathfinding algorithms, of which A* is emblematic. These algorithms, while adept at determining the shortest path, may not necessarily account for the multifaceted challenges lunar rovers confront, especially in scenarios involving multiple rovers with overlapping objectives. In this intricate web of objectives, one must consider not just the brevity of the path but also the safety of the rover, its speed, and the quality of its communication with the lander. Game theory, a mathematical study of interactions between

rational decision makers, emerges as a potent tool in this context, furnishing a framework that can encapsulate these various objectives.

In the gamified version of our problem, each lunar rover is conceptualized as a player. Mathematically, given n rovers, our set of players can be denoted as $P = \{p_1, p_2, \ldots, p_n\}$. Each player p_0 seeks to optimize its reward function $R(p_0)$, which is influenced by its efficiency in reaching its destination, its adherence to safety protocols, and the integrity of its communication with the lander.

Let S represent the strategy space for a rover. Each rover p_0 selects a strategy $s \in S$. The strategies can be mathematically represented as a vector, with potential strategies including:

- 1. s_1 : minimize the Euclidean distance to the target;
- 2. s_2 : traverse a path that minimizes elevation changes, represented by a function E(s) that gives the elevation change for strategy s;
- 3. s_3 : choose a trajectory that optimizes the communication link with the lander, given by a function C(s) that gives the communication quality for strategy s.

Each strategy combination results in a payoff matrix Π , where each element π_{oz} represents the payoff for player o when players select strategies s_o and s_z , respectively. The payoff is a composite function of:

- T(s): time taken to reach the destination;
- O(s): number of close encounters with obstacles or treacherous terrain;
- C(s): communication quality with the lander.

The payoff function for a rover p_o can be represented as:

$$\Pi(p_o, s) = \alpha T(s) + \beta O(s) + \gamma C(s)$$
(12)

where α , β , and γ are weights representing the importance of time, safety, and communication, respectively.

A NASH equilibrium in our game is a state s^* such that no player has an incentive to deviate from its current strategy, given the strategies chosen by the other players. Formally, for every player p_i :

$$R(p_o, s^*) \ge R(p_o, s) \quad \forall s \in S \tag{13}$$

This equilibrium ensures that each rover's selected strategy is optimal in the context of the choices made by its peers, as illustrated below.

Proposition 1. *In a two-rover scenario where both rovers have the same reward weights* α , β , and γ and they both prioritize safety ($\beta > \alpha$, γ), a strategy s that minimizes the number of close encounters with obstacles (i.e., minimizes O(s)) will be part of the NASH equilibrium.

Proof. Given the two rovers p_1 and p_2 , let us assume p_1 chooses strategy s_1 , which minimizes O(s), and p_2 chooses some other strategy s_2 .

From the given conditions, the payoff for p_1 when choosing s_1 is:

$$\Pi(p_1, s_1) = \alpha T(s_1) + \beta O(s_1) + \gamma C(s_1)$$

Since s_1 minimizes O(s) and $\beta > \alpha$, γ , $\Pi(p_1, s_1)$ will be greater than the payoff from any other strategy.

For rover p_2 , since $\beta > \alpha$, γ , it will also achieve its maximum payoff when it chooses a strategy that minimizes O(s). Thus, the best response for p_2 when p_1 chooses s_1 is to also choose s_1 .

Similarly, if p_2 were to choose s_1 , the best response for p_1 is s_1 .

Therefore, in the defined scenario, both rovers choosing the strategy s_1 that minimizes close encounters with obstacles is a NASH equilibrium. \Box

5.1. System Complexity

The proposed system integrating UWB, MB-OFDM, and a game-theoretic approach for lunar rover navigation is inherently complex due to various factors. The computational aspects become particularly intricate when considering the game-theoretic models described above. Each rover, modeled as a player in a game, must solve a multi-objective optimization problem to find its optimal strategy, which itself is a function of the strategies chosen by other rovers. This introduces the need for solving a NASH equilibrium, adding an additional layer of computational burden. Traditional navigational strategies are also supplemented by a rich set of game-theoretic strategies, requiring complex mathematical modeling and solving of payoff matrices to reach an equilibrium state. Communication-wise, UWB and MB-OFDM demand dynamic bandwidth allocation, channel estimation, and interference mitigation, requiring advanced control algorithms. Furthermore, the time-based localization techniques used in UWB contribute additional complexity. Implementationwise, the system must be robust, lightweight, and energy-efficient, especially considering the harsh conditions of a lunar mission. Despite these complexities, the proposed system aims for a balanced trade-off between performance and operational constraints, ensuring effective lunar exploration.

5.2. Simulation of Simplified Game-Theoretic Approach in Lunar Rover Navigation

To explore the potential advantages of a game-theoretic approach for lunar rover navigation, we implemented a simplified toy example as a case study. This simulation involved multiple rovers in a hypothetical lunar environment and aimed to illustrate the basics of strategy selection and payoff calculations.

The simulation parameters can be seen in Table 2.

Table 2. Simulation parameters for the simplified game-theoretic lunar rover navigation study.

Parameter	Value
Number of players	N=3
Strategy space	$S = \{$ move forward, turn left, turn right, stay, move diagonally $\}$
Payoff function	Payoff $(p,s) = \alpha \times T(s) + \beta \times O(s) + \gamma \times C(s)$
Initial weights	$\alpha = 0.4, \beta = 0.3, \gamma = 0.3$

Each rover was implemented as an object possessing attributes for both position and current strategy. Random values were used to approximate real-world metrics such as time efficiency, obstacle avoidance, and communication strength for the purpose of this simplified simulation. The simulation utilized dynamic weights α , β , and γ to model changing priorities in real-world scenarios. For instance, as a rover approaches an obstacle, it might dynamically adjust the weights to favor obstacle avoidance over time efficiency.

The game was simulated for a total of 100 rounds. During each round, each rover independently selected a strategy at random from the strategy space *S*. The payoffs for the chosen strategies were then calculated, using randomized values as placeholders for the real-world metrics.

The frequency distribution of strategies, as shown in Figure 7, suggests that, in a more deterministic and refined model, we would expect strategies to converge toward a NASH equilibrium. It is important to emphasize that the stochastic elements in this simulation serve primarily as a simplified representation, illustrating the type of sophisticated calculations that would be involved in a complete, real-world model.

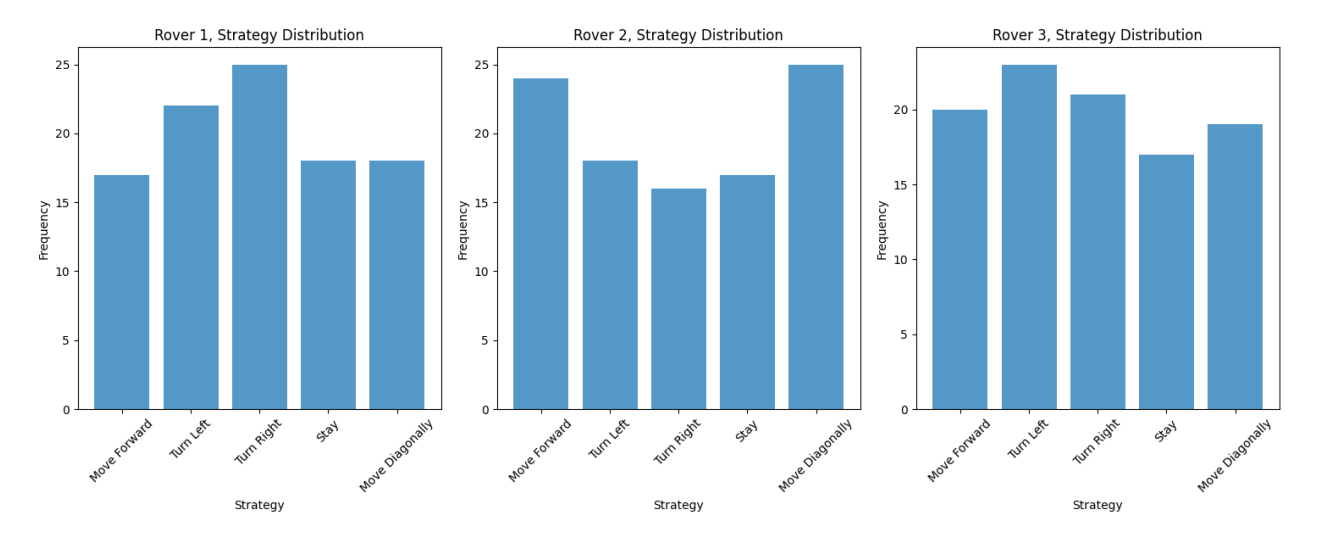


Figure 7. Distribution of strategies in the simplified game-theoretic lunar rover navigation simulation.

6. Conclusions and Future Work

This paper presented a comprehensive simulation framework for evaluating the performance of an integrated UWB and MB-OFDM communication and navigation system in a lunar environment. The framework considered various factors, such as terrain generation, rover movement constraints, obstacle avoidance, and communication channel modeling, to provide a realistic assessment of the proposed system. The simulation results demonstrated the effectiveness and robustness of the integrated UWB and OFDM technologies in ensuring efficient navigation and reliable communication between rovers and the lunar lander. The study's findings have significant implications for the design and deployment of future lunar missions, showcasing the potential of UWB and MB-OFDM technologies in enhancing the capabilities of lunar rovers and landers. Furthermore, the developed simulation framework can be utilized for evaluating other communication and navigation technologies, fostering the development of advanced systems for lunar exploration. Additionally, a novel approach based on game theory for rover navigation was presented.

- Future work could focus on:
- Incorporating more complex communication channel models, including multipath effects, to provide a more accurate representation of the lunar environment;
- Investigating the performance of alternative communication and navigation technologies, such as optical or quantum communication systems, in the lunar context;
- Exploring cooperative strategies among multiple rovers for improved navigation, communication, and mission efficiency;
- Further developing the game-theoretic approach, with the possibility of incorporating sophisticated AI techniques for autonomous navigation;
- Evaluating the impact of rover energy consumption, considering the limited power resources available on the Moon, and developing energy-efficient routing and communication algorithms;
- Integrating real-world lunar terrain data and simulating rover missions in specific regions of the Moon to validate the performance of the proposed system under actual lunar conditions.

By addressing these research directions, the presented framework can contribute to the continuous advancement of communication and navigation technologies for lunar exploration, ultimately enabling more efficient and reliable missions on the Moon.

Author Contributions: Conceptualization, J.d.C. and I.d.Z.; funding acquisition, C.T.C.; investigation, I.d.Z. and J.d.C.; methodology, I.d.Z. and J.d.C.; software, J.d.C. and I.d.Z.; supervision, C.T.C.; writing—original draft, J.d.C.; writing—review and editing, C.T.C., J.d.C., and I.d.Z. All authors have read and agreed to the published version of the manuscript.

Funding: We thank the following funding sources from GOETHE-University Frankfurt am Main; "DePP-Dezentrale Plannung von Platoons im Straßengüterverkehr mit Hilfe einer KI auf Basis einzelner LKW", "Center for Data Science & AI", and "xAIBiology". We acknowledge the support of R&D project PID2021-122580NB-I00, funded by MCIN/AEI/10.13039/501100011033 and ERDF.

Institutional Review Board Statement: Not applicable.

Informed Consent Statement: Not applicable.

Data Availability Statement: Not applicable.

Conflicts of Interest: The authors declare that they have no conflict of interest. The funders had no role in the design of the study, in the collection, analyses, or interpretation of data, in the writing of the manuscript, or in the decision to publish the results.

Abbreviations

The following abbreviations are used in this manuscript:

Ultra-Wideband **UWB** Multi-Band Orthogonal Frequency-Division Multiplexing MB-OFDM Free Space Optical Communication **FSOC** Radio Frequency RF Free Space Path Loss **FSPL** Federal Communications Commission FCC Time of Arrival ToA Time Difference of Arrival TDoA Angle of Arrival AoA Multiple-Input and Multiple-Output **MIMO** Signal-to-Noise Ratio **SNR** Quadrature Amplitude Modulation **QAM** Binary Phase-Shift Keying **BPSK** Quadrature Phase-Shift Keying **QPSK** Fast Fourier Transform FFT ZF Zero Forcing Minimum Mean Square Error **MMSE** Reinforcement Learning RI. Proximal Policy Optimization PPO

References

- 1. Aiello, G.R.; Rogerson, G.D. Ultra-wideband wireless systems. IEEE Microw. Mag. 2003, 4, 36–47. [CrossRef]
- 2. Rahayu, Y.; Rahman, T.A.; Ngah, R.; Hall, P. Ultra wideband technology and its applications. In Proceedings of the 2008 5th IFIP International Conference on Wireless and Optical Communications Networks (WOCN '08), Surabaya, Indonesia, 5–7 May 2008; pp. 1–5.
- 3. Alarifi, A.; Al-Salman, A.; Alsaleh, M.; Alnafessah, A.; Al-Hadhrami, S.; Al-Ammar, M.A.; Al-Khalifa, H.S. Ultra wideband indoor positioning technologies: Analysis and recent advances. *Sensors* **2016**, *16*, 707. [CrossRef] [PubMed]
- 4. Coppens, D.; Shahid, A.; Lemey, S.; Herbruggen, B.V.; Marshall, C.; Poorter, E.D. An overview of UWB standards and organizations (IEEE 802.15.4, FiRa, apple): Interoperability aspects and future research directions. *IEEE Access* 2022, 10, 70219–70241. [CrossRef]
- 5. Scholtz, R.A. Multiple access with time-hopping impulse modulation. In Proceedings of the MILCOM'93-IEEE Military Communications Conference, Boston, MA, USA, 11–14 October 1993; Volume 2, pp. 447–450.
- 6. Batra, A.; Balakrishnan, J.; Dabak, A. Multi-band ofdm: A new approach for uwb. In Proceedings of the 2004 IEEE International Symposium on Circuits and Systems (IEEE Cat. No. 04CH37512), Vancouver, BC, Canada, 23–26 May 2004; Volume 5, p. V.
- 7. Kaiser, T.; Zheng, F.; Dimitrov, E. An overview of ultra-wide-band systems with mimo. *Proc. IEEE* 2009, 97, 285–312. [CrossRef]
- 8. Chen, T.; Govindaraj, S.; Noel, T.; Welch, C.; Zhang, T. Beacon-based localization of the robot in a lunar analog environment. In Proceedings of the 2020 Chinese Control And Decision Conference (CCDC), Hefei, China, 22–24 August 2020; pp. 4297–4304.
- 9. Matthies, L.; Kennett, A.; Kerber, L.; Fraeman, A.; Anderson, R.C. Prospects for very long-range mars rover missions. In Proceedings of the 2022 IEEE Aerospace Conference (AERO), Big Sky, MT, USA, 5–12 March 2022; pp. 1–11.
- 10. Allan, M.; Wong, U.; Furlong, P.M.; Rogg, A.; McMichael, S.; Welsh, T.; Chen, I.; Peters, S.; Gerkey, B.; Quigley, M.; et al. Planetary rover simulation for lunar exploration missions. In Proceedings of the 2019 IEEE Aerospace Conference, Big Sky, MT, USA, 2–9 March 2019; pp. 1–19.

- 11. Zhang, Z.B.; Zuo, W.; Zeng, X.G.; Gao, X.Y.; Ren, X. The Scientific Data and Its Archiving from Chang'e 4 Mission. In Proceedings of the 4th Planetary Data Workshop, Flagstaff, Arizona, 18–20 June 2019; Volume 2151, p. 7032.
- 12. Sravya, R.S.; Sreeja, S. Design and simulation of interplanetary lunar rover. Mater. Today Proc. 2023, in press. [CrossRef]
- 13. Daftry, S.; Chen, Z.; Cheng, Y.; Tepsuporn, S.; Khattak, S.; Matthies, L.; Coltin, B.; Naal, U.; Ma, L.M.; Deans, M. LunarNav: Crater-based Localization for Long-range Autonomous Lunar Rover Navigation. In Proceedings of the 2023 IEEE Aerospace Conference, Big Sky, MT, USA, 4–11 March 2023; pp. 1–15.
- 14. Zhang, P.; Dai, W.; Niu, R.; Zhang, G.; Liu, G.; Liu, X.; Bo, Z.; Wang, Z.; Zheng, H.; Liu, C.; et al. Overview of the Lunar In Situ Resource Utilization Techniques for Future Lunar Missions. *Space Sci. Technol.* **2023**, *3*, 0037. [CrossRef]
- 15. Win, M.Z.; Scholtz, R.A. Ultra-wide bandwidth time-hopping spread-spectrum impulse radio for wireless multiple-access communications. *IEEE Trans. Commun.* **2000**, *48*, 679–689. [CrossRef]
- 16. Nikookar, H.; Prasad, R. UWB Technologies; Springer: Dordrecht, The Netherlands, 2009; pp. 117–133. [CrossRef]
- 17. Sahinoglu, Z.; Gezici, S.; Guvenc, I. *Ultra-Wideband Positioning Systems: Theoretical Limits, Ranging Algorithms, and Protocols*; Cambridge University Press: Cambridge, UK, 2008.
- 18. Fontana, R.J. Recent Applications of Ultra Wideband Radar and Communications Systems; Springer: Boston, MA, USA, 2002; pp. 225–234. [CrossRef]
- 19. Molisch, A.F.; Cassioli, D.; Chong, C.-C.; Emami, S.; Fort, A.; Kannan, B.; Karedal, J.; Kunisch, J.; Schantz, H.G.; Siwiak, K.; et al. A comprehensive standardized model for ultrawideband propagation channels. *IEEE Trans. Antennas Propag.* **2006**, *54*, 3151–3166. [CrossRef]
- 20. Akyildiz, I.F.; Jornet, J.M.; Han, C. Terahertz band: Next frontier for wireless communications. *Phys. Commun.* **2016**, *18*, 292–318. [CrossRef]
- 21. Verdu, S. Multiuser Detection; Cambridge University Press: Cambridge, UK, 1998.
- 22. Skrzypczak, A.; Palicot, J.; Siohan, P. Ofdm/oqam modulation for efficient dynamic spectrum access. *Int. J. Commun. Netw. Distrib. Syst.* **2012**, *8*, 247–266. [CrossRef]
- 23. Schulman, J.; Wolski, F.; Dhariwal, P.; Radford, A.; Klimov, O. Proximal Policy Optimization Algorithms. arXiv 2017, arXiv:1707.06347.
- 24. Russell, S.J.; Norvig, P. Artificial Intelligence: A Modern Approach, 4th ed.; Pearson Education, Inc.: London, UK, 2021.
- 25. Huo, Z.; Zhang, L.; Zeng, Z.; Li, J.; Li, L.; Liu, C. Simulation of Lunar Comprehensive Substructure with Fracture and Imaging of Later LPR Data from Chang'e-4 Mission. *IEEE Trans. Geosci. Remote Sens.* **2023**, *61*, 5104611. [CrossRef]

Disclaimer/Publisher's Note: The statements, opinions and data contained in all publications are solely those of the individual author(s) and contributor(s) and not of MDPI and/or the editor(s). MDPI and/or the editor(s) disclaim responsibility for any injury to people or property resulting from any ideas, methods, instructions or products referred to in the content.





Article

Drone-Based Decentralized Truck Platooning with UWB Sensing and Control

I. de Zarzà 1,2,3, J. de Curtò 1,2,3,*, Juan Carlos Cano 2 and Carlos T. Calafate 2

- Informatik und Mathematik, GOETHE-University Frankfurt am Main, 60323 Frankfurt am Main, Germany; dezarza@em.uni-frankfurt.de
- Departamento de Informática de Sistemas y Computadores, Universitat Politècnica de València, 46022 València, Spain; jucano@disca.upv.es (J.C.C.); calafate@disca.upv.es (C.T.C.)
- 3 Estudis d'Informàtica, Multimèdia i Telecomunicació, Universitat Oberta de Catalunya, 08018 Barcelona, Spain
- * Correspondence: decurto@em.uni-frankfurt.de

Abstract: Truck platooning is a promising approach for reducing fuel consumption, improving road safety, and optimizing transport logistics. This paper presents a drone-based decentralized truck platooning system that leverages the advantages of Ultra-Wideband (UWB) technology for precise positioning, robust communication, and real-time control. Our approach integrates UWB sensors on both trucks and drones, creating a scalable and resilient platooning system that can handle dynamic traffic conditions and varying road environments. The decentralized nature of the proposed system allows for increased flexibility and adaptability compared to traditional centralized platooning approaches. The core platooning algorithm employs multi-objective optimization, taking into account fuel efficiency, travel time, and safety. We propose a strategy for the formation and management of platoons based on UWB sensor data with an emphasis on maintaining optimal inter-vehicle secure distances and compatibility between trucks. Simulation results demonstrate the effectiveness of our approach in achieving efficient and stable platooning while addressing the challenges posed by real-world traffic scenarios. The proposed drone-based decentralized platooning system with UWB technology paves the way for the next generation of intelligent transportation systems that are more efficient, safer, and environment friendly.

Keywords: truck platooning; decentralized control; UWB; drones; V2V communication; connected vehicles

MSC: 93C85; 90C59

1. Introduction

Truck platooning has emerged as a promising approach to improve transportation efficiency, fuel consumption, and road safety. In a platoon, multiple trucks follow seamlessly each other at close distances, leveraging advanced sensing and communication technologies to maintain a constant gap, allowing them to benefit from reduced aerodynamic drag and improved fuel efficiency [1,2]. Traditional platooning systems rely on vehicle-to-vehicle (V2V) communication and centralized control strategies, which can be prone to latency and scalability issues.

Recent advancements in drone technology and Ultra-Wideband (UWB) sensors offer new opportunities to develop innovative solutions for truck platooning. Drones, or Unmanned Aerial Vehicles (UAVs), can serve as mobile monitoring and control platforms, providing real-time data and feedback to optimize formation of platoons and maintenance. Furthermore, UWB technology enables accurate distance measurement and positioning with high precision and robustness, making it well-suited for platooning applications.

In this study, we present a unique contribution in the field of truck platooning systems. We introduce a decentralized strategy, utilizing drones equipped with UWB sensors for precise distance control. The system also incorporates a multi-objective optimization approach, targeting enhancements in fuel efficiency, safety, and travel time.

The incorporation of drones in our proposed platooning system presents several crucial advantages. Firstly, drones equipped with UWB sensors can efficiently provide a bird's eye view of the traffic situation. This aerial perspective not only aids in forming accurate and efficient platoons but also enables real-time monitoring and management of the formed platoons, which is a task that would be challenging from a ground-based viewpoint. Additionally, drones can navigate independently of the traffic flow, bypassing the constraints that ground vehicles face, thereby providing continuous and uninterrupted monitoring. The mobility and agility of drones make them particularly effective in dynamic and rapidly changing environments. In cases of sudden traffic alterations, drones can swiftly react and recalibrate their strategies, ensuring the seamless operation of the platooning system. These attributes position drones as essential components in our proposed truck platooning system, contributing significantly to its efficiency, adaptability, and resilience.

This novel technology can certainly speed up the following use cases:

- 1. Long-haul Freight Transportation: The proposed system greatly benefits long-haul transport, where trucks often cover vast highway distances. Platooning, facilitated by our system, effectively reduces air resistance, leading to significant fuel savings and a consequent reduction in carbon emissions. Furthermore, it promotes road safety and reduces traffic congestion by maintaining optimal inter-vehicle distances.
- Urban Logistics: In response to growing urbanization and associated traffic challenges, our drone-based truck platooning system can be integrated into smart city infrastructure to improve logistics efficiency. This would enhance routing, decrease delivery times, and reduce the environmental impact of city-wide logistics operations.
- 3. Emergency Response: In situations requiring the rapid transportation of supplies and personnel, such as in disaster relief scenarios, our platooning system can enhance the speed and effectiveness of resource allocation and delivery.
- 4. Autonomous Vehicles: The rise of autonomous vehicles presents another valuable application for our platooning system. When integrated with self-driving trucks, our system can offer significant improvements in efficiency and safety, heralding a new era in autonomous transportation.

The transformative potential of the Internet of Things (IoT) in redefining our interaction with the environment is being progressively realized across various sectors. The proposed drone-based decentralized truck platooning system, enabled with UWB sensors, has a spectrum of potential applications. These range from long-haul freight transportation and smart city logistics to emergency response initiatives and military operations. In this novel application of IoT, we envision a transformative potential capable of revolutionizing transportation systems, making them more efficient, sustainable, and secure.

Key aspects of our contribution include the following:

- The implementation of a novel, drone-based, decentralized platooning system, employing UWB sensors for meticulous distance measurement and control.
- The development of a multi-objective optimization technique, effectively forming and managing platoons, thereby optimizing travel time, fuel efficiency, and safety.
- The utilization of an agent-based simulation model to evaluate and compare the performance of our proposed system with existing methodologies in platooning.
- We believe that this distinct combination of technology and strategy will substantially improve current platooning systems.

The rest of this paper is organized as follows: Section 2 reviews related work on truck platooning, drone-based systems, and UWB technology in transportation. Section 3 provides an overview of the proposed system, including agents for trucks and drones, UWB sensing and communication, and decentralized platooning architecture. Section 4

details the strategy for multi-objective optimization and formation of platoons. Section 5 discusses UWB-based positioning and control. Section 6 presents the simulation setup, results, and performance evaluation. Finally, Section 7 concludes the paper and discusses potential future work.

2. Related Work

Truck platooning has been extensively studied in recent years as a means to improve transportation efficiency, reduce fuel consumption, and enhance road safety [1–4]. Most existing platooning systems rely on V2V communication and centralized control strategies, where a lead truck is responsible for coordinating the actions of the following trucks. However, centralized approaches can suffer from latency, scalability, and robustness issues, which have motivated the development of decentralized platooning solutions [5–8].

The use of drones in transportation has been explored for various applications, such as traffic monitoring [9], road infrastructure inspection [10], and vehicle tracking [11]. Drones can provide valuable real-time data [12] and act as mobile communication relays, enabling flexible and efficient control in transportation systems [13]. A few studies have investigated the potential of drones for facilitating truck platooning [14], but the integration of advanced sensing and communication technologies, such as UWB, remains an open research question.

UWB technology has gained significant attention for its potential in high-precision positioning, ranging, and communication applications [15–19]. UWB's ability to provide accurate distance measurements, robustness to multipath effects, and low power consumption make it a suitable candidate for transportation systems. Several studies have explored the use of UWB for vehicle localization, collision avoidance, and V2V communication [20–23]. However, the application of UWB in drone-based decentralized truck platooning remains largely unexplored.

This paper aims to address the gap in the literature by proposing a novel drone-based decentralized platooning system that leverages UWB sensors for distance estimation and control. By integrating the advantages of drone-based monitoring and UWB technology, our proposed system aims to overcome the limitations of existing platooning strategies while improving transportation efficiency, fuel consumption, and safety.

3. System Overview

Before detailing the components of our proposed drone-based decentralized truck platooning system, we present the notation in Table 1 for clarity.

 Table 1. Notation table for the drone-based decentralized truck platooning system.

Symbol	Definition
d_{zo}	Distance between truck z and truck o
v_z	Current speed of truck z
v_z^*	Optimal speed of truck z for fuel efficiency
α	Acceleration factor for responsiveness to distance changes
p_z	Longitudinal position of drone z along the platoon
n	Number of drones in the platoon
N	Number of trucks in the platoon
d_{opt}	Optimal distance between trucks
K_p	Proportional gain in the control algorithm
K_d	Derivative gain in the control algorithm

Our proposed drone-based decentralized truck platooning system consists of two main components: the agents for trucks, and the agents for drones. The system is designed to optimize fuel efficiency, travel time, and safety using UWB technology for precise distance estimation and control, as illustrated in Figure 1.

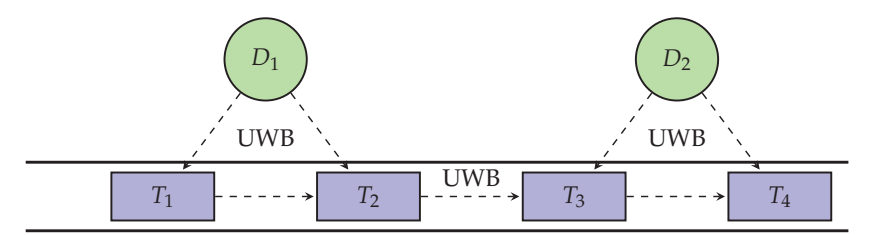


Figure 1. Drone-based decentralized truck platooning with UWB communication. Trucks (T) are monitored and assisted by Drones (D) while maintaining a platoon using UWB communication.

Each truck in the platooning system is equipped with a UWB sensor, which allows it to accurately measure the distance to neighboring trucks. The agents for trucks use a decentralized control algorithm that takes into account the following variables:

- d_{zo} : distance between truck z and truck o;
- v_z : current speed of truck z;
- v_z^{*}: optimal speed of truck z to maximize fuel efficiency;
- α: acceleration factor, which determines the responsiveness of the trucks to changes in distance.

The control algorithm computes the desired acceleration a_z for each truck z as follows:

$$a_z = \alpha \left(\frac{d_{zo} - d_{\text{opt}}}{d_{\text{opt}}}\right) (v_z^* - v_z),\tag{1}$$

where d_{opt} represents the optimal distance between trucks for maximizing fuel efficiency and safety. The acceleration factor α can be tuned to balance the trade-offs between responsiveness and stability in the platooning system.

The drones in our system serve as monitoring and communication facilitators for the platooning system, collecting distance and speed data from the trucks and relaying communication between them. Each drone is equipped with a UWB sensor and a communication module. This allows it to relay messages between the truck agents and estimate their relative distances.

The positioning of the drones is treated in two dimensions: they adjust their longitudinal positions to maintain a balanced distribution across the platoon while maintaining a fixed altitude. This allows them to optimally cover the length of the platoon without the complexity of managing vertical movement. The decentralized coordination algorithm the drones employ accounts for the following variables:

- p_z : longitudinal position of drone z along the platoon;
- *n*: number of drones in the platoon;
- *N*: number of trucks in the platoon.

The coordination algorithm computes the desired position p_z^* along the platoon for each drone z as follows:

$$p_z^* = \frac{z}{n+1}N. (2)$$

In the equation presented, the parameter z represents the index of a given drone within the platoon, which is used to calculate its desired longitudinal position, p_z^* . The index z takes on integer values ranging from 1 to n, where n is the total number of drones in the platoon. This indexing is crucial for determining the precise spacing between drones to ensure balanced coverage. For instance, if there are five drones in a platoon, z would range from 1 to 5. The denominator, n+1, ensures that the drones are evenly spaced along the platoon with the first and last drones positioned at the ends of the convoy. The product of $\frac{z}{n+1}$ and N (the total number of trucks in the platoon) yields the desired longitudinal position of each drone relative to the trucks.

By adjusting their positions to maintain the desired distribution, the drones ensure optimal coverage and efficient communication within the platooning system.

In truck platooning, the primary concern is the management of the convoy along the direction of travel, which is inherently a longitudinal problem. The drones in our system focus on longitudinal positioning to ensure that the platooning dynamics—such as slipstreaming for reduced air resistance and synchronized braking for safety—are optimized. Lateral or vertical movements of drones are less critical to these objectives and introduce unnecessary complexity into the system. Furthermore, by restricting drones to longitudinal adjustments, we simplify the control algorithms and reduce computational overhead, leading to a more efficient and responsive system. The longitudinal focus also aligns with highway driving regulations, where lateral movements are constrained by lane widths and vertical navigation is constrained by airspace regulations. Hence, our system is designed to operate within these practical limitations while delivering the intended benefits of platooning.

3.1. UWB-Based Distance Estimation

The UWB sensors are used to provide accurate and reliable distance measurements between the trucks and the drones. The distance d_{zo} between truck z and truck o can be estimated using the Time of Arrival (ToA) method, as follows:

$$d_{zo} = \frac{c\Delta t_{zo}}{2},\tag{3}$$

where c is the speed of light and Δt_{zo} is the time difference between the transmission and reception of a UWB pulse.

By leveraging UWB technology, our proposed system can achieve precise distance estimation and control, enabling efficient and safe truck platooning.

3.2. Decentralized Platooning Control

The trucks and drones collaborate to create and maintain platoons based on their distance, speed, and truck type. The decentralized platooning control algorithm consists of the following steps:

- 1. Each truck broadcasts its current state, including position, speed, fuel efficiency, and truck type, to the nearby drones using UWB communication.
- 2. The drones collect the state information from the trucks and estimate the distances between them using their UWB sensors.
- 3. The drones share the collected data with neighboring drones, ensuring that all have a consistent view of the platoon.
- 4. Based on the received data, each drone calculates a platooning decision for the trucks in its vicinity, taking into account the distance, speed, and compatibility constraints.
- 5. The drones communicate the platooning decisions to the corresponding trucks, which adjust their speed and position accordingly.
- The trucks continuously update their state information and share it with the drones, allowing the platooning control algorithm to adapt to changes in the environment and traffic conditions.

This decentralized approach enables our platooning system to scale effectively, adapt to dynamic conditions, and maintain optimal performance in terms of fuel efficiency, travel time, and safety.

In the optimization of truck platooning, the determination of each truck's optimal speed and the inter-vehicle distance within a platoon is crucial for enhancing fuel efficiency. These parameters are derived from aerodynamic models that consider factors such as air resistance and vehicle dynamics. While our paper does not delve into the specifics of these calculations, they are based on established principles in the field of transportation engineering. For an in-depth understanding of these models and their application to platooning, we refer readers to [24–26], where these concepts are comprehensively analyzed and discussed.

3.3. Performance Metrics

The performance of our proposed system is evaluated based on the following metrics:

- Fuel efficiency: We calculate fuel efficiency as the ratio of the total distance traveled to the total fuel consumed by each truck in the platoon, which is expressed in liter per km. This is computed by using the real-time data on fuel consumption and distance covered by each truck, which is obtained through the UWB sensors and the truck's onboard diagnostics system. The average fuel efficiency of all trucks in the platoon is then calculated to represent the overall fuel efficiency of the platoon.
- Travel time: This refers to the average time taken by a truck to travel a fixed distance, which is measured in minutes. The UWB sensors provide accurate data on the distance covered and time taken, which is used to calculate the average travel time for each truck and for the platoon as a whole.
- Safety: We consider the average distance between trucks in the platoon as a proxy
 for the safety of the platooning system. This is measured using the UWB sensors,
 which provide precise data on the relative positions and distances between trucks in
 the platoon.

The primary objective of our drone-based decentralized truck platooning system is to optimize these metrics with the ultimate aim of achieving significant cost savings, reducing emissions, and improving road safety.

4. Multi-Objective Optimization and Formation of Platoons

In this section, we describe the multi-objective optimization that our drone-based decentralized truck platooning system aims to solve as well as the algorithm for the formation of platoons that we use to generate platooning decisions based on the collected data.

4.1. Multi-Objective Optimization

Our goal is to optimize the formation of platoons with respect to multiple objectives, including fuel efficiency, travel time, and safety. We formalize this problem as follows:

Let N be the number of trucks, and let $T = \{t_1, t_2, ..., t_N\}$ be the set of trucks. Each truck t_z is characterized by its fuel efficiency f_z , optimal speed v_z , and type c_z . The distance between trucks t_z and t_0 is denoted by d_{z_0} .

The multi-objective optimization can be reformulated as shown below:

minimize
$$\{F(T), T(T), S(T)\}$$
,
subject to $D_{\min} \le d_{zo} \le D_{\max} \quad \forall z, o \in \{1, 2, ..., N\}$, (4)

where F(T) represents the average fuel efficiency of the platoon, T(T) represents the average travel time, S(T) represents the average safety (measured by the distance between trucks), D_{\min} is the minimum allowable distance between trucks to ensure safety, and D_{\max} is the maximum allowable distance between trucks for effective platooning.

In the context of our platooning system, the minimum safe distance between trucks, denoted as D_{\min} , is a critical parameter that ensures the safety of the platoon. This distance is not arbitrarily chosen but is informed by a combination of legal requirements for vehicle spacing, empirical research on stopping distances under various conditions, and industry best practices. For instance, traffic regulations often stipulate a minimum following distance based on factors such as vehicle size, speed, and road conditions. This parameter serves as a constraint in our optimization algorithm, ensuring that the operational safety of the platoon is upheld at all times.

4.2. Algorithm for Formation of Platoons

To solve the multi-objective optimization, we propose an algorithm for the formation of platoons based on the following steps:

- Data Collection: The drones collect the state information from the trucks and estimate
 the distances between them using their UWB sensors. This information is shared
 among the drones to ensure a consistent view of the platoon.
- 2. Compatibility Analysis: For each pair of trucks (t_z, t_0) , the drones evaluate their compatibility based on their fuel efficiency, optimal speed, and truck type. A compatibility score w_{z_0} is calculated as follows:

$$w_{zo} = \alpha \cdot |f_z - f_o| + \beta \cdot |v_z - v_o| + \gamma \cdot \delta(c_z, c_o), \tag{5}$$

where α , β , γ are weight factors, and $\delta(c_z, c_0)$ is a function that returns 1 if $c_z \neq c_0$, and 0 otherwise.

- 3. Formation of Platoons: The drones use the compatibility scores and the distance information to form platoons by minimizing the weighted sum of the objectives. We use a greedy algorithm to achieve this:
 - (a) Initialize an empty set of platoons $P = \{\}$.
 - (b) For each truck $t_z \in T$, find the most compatible truck t_o that is not already in a platoon, i.e., $t_o \notin P$, and satisfies the distance constraint $D_{\min} \le d_{zo} \le D_{\max}$.
 - (c) If such a truck t_0 is found, create a new platoon $p = \{t_z, t_0\}$ and add it to the set of platoons P. Otherwise, create a singleton platoon $p = \{t_z\}$ and add it to P.
 - (d) Continue this process until all trucks are assigned to a platoon.

The weight factors α , β , and γ in the compatibility analysis play important roles in shaping the formation and dynamics of truck platoons. These factors are adjusted based on the relative importance of fuel efficiency, speed alignment, and truck type in the platooning algorithm. For instance, if fuel efficiency is prioritized, α may be set higher than β and γ , reflecting the desire to pair trucks with similar fuel consumption profiles. Conversely, if maintaining a consistent speed is deemed more critical, β would assume a greater value. In our simulations, we propose starting values such as $\alpha=0.5$, $\beta=0.3$, and $\gamma=0.2$, acknowledging that these may be fine-tuned through empirical testing or specific operational requirements.

In our compatibility analysis for truck platooning, the type of each truck is a categorical variable represented by c_z for truck t_z and c_0 for truck t_0 . These variables are indicative of the truck model, which can impact platoon dynamics due to size, aerodynamics, and other characteristics. The calculation of c_z and c_0 is straightforward: each truck type is assigned a unique identifier (such as 'A', 'B', 'C', etc.). Thus, the comparison function $\delta(c_z, c_0)$ evaluates to 1 if the truck types are different (i.e., $c_z \neq c_0$), implying incompatibility, and 0 if they are the same (i.e., $c_z = c_0$), indicating compatibility. This binary approach simplifies the determination of whether two trucks should be considered for platooning based on type without delving into a granular comparison of specific model characteristics, which are beyond the scope of our initial optimization formulation.

The algorithm implemented for platoon formation is designed to iteratively construct a set of platoons in a manner that seeks locally optimal solutions at each step with the goal of achieving a globally optimal set of platoons. The iterative nature of the algorithm comes from its selection process; it chooses the pair of trucks that, at the current iteration, seem to be the most compatible without considering future pairings. This approach does not guarantee a globally optimal set of platoons but is often efficient in terms of computational resources and time, making it suitable for real-time applications where decisions need to be made quickly.

The maximum allowable distance between two trucks in a platoon, denoted as $D_{\rm max}$, is a crucial parameter that balances the benefits of platooning with operational safety and regulatory compliance. This distance is influenced by various factors, including the reaction time of the autonomous systems, the braking capabilities of the trucks, environmental conditions, and legal restrictions on vehicle spacing. For the purposes of our model and simulations, $D_{\rm max}$ is set based on a combination of these factors to ensure that trucks are

close enough to benefit from reduced air resistance and thus improved fuel efficiency while also maintaining a safe buffer to react to unforeseen events.

In practical terms, $D_{\rm max}$ can vary depending on the specific characteristics of the trucks, such as their size, weight, and braking systems, as well as the technology used for communication and control within the platoon. For instance, a commonly used guideline is that trucks maintain a distance that allows for at least one second of reaction time for every ten feet of vehicle length plus an additional second for safety. In highway conditions, where trucks typically travel at higher speeds, this can translate to a $D_{\rm max}$ of approximately 50 to 60 m.

It is essential to note that $D_{\rm max}$ is not a fixed value and can be adjusted based on real-time data and changing conditions. The drone-based system we propose is capable of dynamically recalibrating $D_{\rm max}$ in response to changes in speed, traffic density, weather, and other relevant variables, thereby optimizing the platoon's performance while ensuring safety is not compromised.

4.3. Operational Parameters of Platooning

Given the complexities involved in determining D_{max} , our system includes mechanisms for real-time adjustment and monitoring to maintain optimal inter-vehicle distances. These mechanisms are designed to adapt to varying conditions, including the following:

- Changes in speed: As the platoon's speed increases, the system automatically increases D_{max} to allow for longer reaction times.
- Varying traffic conditions: In denser traffic, D_{max} may be reduced to allow more vehicles to benefit from platooning, provided it remains within safe limits.
- Weather impacts: Adverse weather conditions such as rain or fog will result in an
 increase in D_{max} to account for decreased visibility and potential increases in braking distance.

In summary, D_{max} serves as a flexible boundary within our platooning model, ensuring operational efficiency is matched with the imperative of safety.

4.4. Dynamic Management of Platoons

As the trucks move and their positions change, the formation of platoons may need to be updated to maintain the optimal configuration. To handle this dynamic aspect, the drones continuously monitor the distance between trucks and their compatibility. If the distance between two trucks in a platoon exceeds the maximum allowable distance, or their compatibility score drops significantly, the drones may decide to split the platoon and find new platoon partners for the affected trucks, as defined in the multi-objective optimization in Section 4.2. Figure 2 further illustrates the interconnection between the modules in a sequence diagram.

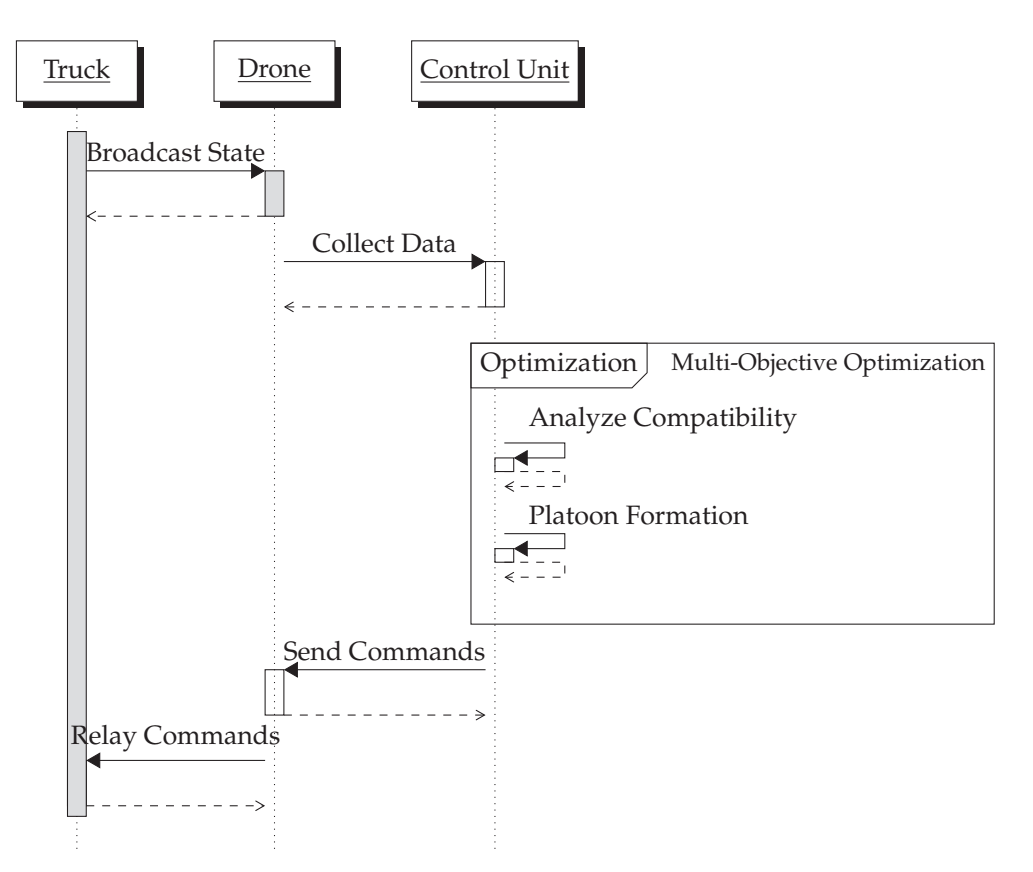


Figure 2. Sequence diagram of the decentralized truck platooning system. Continuous arrows represent synchronous calls, indicating that the sender waits for a response. Dotted arrows, represent asynchronous messages where the sender continues processing without waiting.

5. Positioning and Control Based on UWB

In this section, we discuss the role of Ultra-Wideband (UWB) technology in our drone-based decentralized truck platooning system. UWB sensors provide highly accurate positioning and distance measurements, which are crucial for maintaining the formation of platoons and ensuring safety.

5.1. UWB Positioning and Ranging

UWB technology offers significant benefits for our drone-based decentralized truck platooning system. Unlike other wireless technologies such as Wi-Fi and Bluetooth, UWB operates over a large bandwidth (>500 MHz) and uses short duration pulses, which enables it to provide high-precision distance measurements on the order of centimeters. This precise ranging is critical for maintaining the optimal distances in our platooning system and ensuring safe and efficient operations. In addition, UWB technology can penetrate obstacles such as walls and floors, and it is less prone to interference from other devices. This robustness makes UWB an ideal choice for communication in complex and dynamic environments such as road networks.

The distance measurement with UWB is based on the Time of Flight (ToF) of the signal. The ToF is the time it takes for the signal to travel from the transmitter to the receiver. This time is determined by measuring the difference between the departure and arrival times of the signal as follows:

$$ToF = \frac{t_{arrival} - t_{departure}}{2},$$
 (6)

where $t_{arrival}$ is the time when the signal arrives at the receiver, and $t_{departure}$ is the time when the signal is transmitted. Given the known speed of light c, the distance d between the transmitter and receiver can then be calculated as:

$$d = c \cdot \text{ToF}, \tag{7}$$

Furthermore, UWB signals can also provide directional information, allowing the drones to estimate the orientation of the trucks in addition to their distance. This information can further enhance the safety and efficiency of our platooning system by enabling more sophisticated control strategies. By integrating UWB technology into our system, we can achieve precise distance estimation and control, robust communication, and enhanced situational awareness, all of which contribute to the overall performance and benefits of our drone-based decentralized truck platooning system.

Specifically, the orientation estimation can be derived from the Time Difference of Arrival (TDoA) measurements of UWB signals at multiple receivers installed on the truck. By comparing the arrival times of a UWB pulse at different points on the vehicle, it is possible to infer the angle of arrival, and consequently, the orientation of the truck with respect to the platoon.

The estimation process involves the following steps:

- 1. Signal Emission: UWB transmitters on a truck emit signals that are captured by UWB receivers located on the same and other trucks in the vicinity.
- 2. TDoA Calculation: The receivers use the precise timestamps of the UWB signal arrivals to calculate the TDoA, considering the known geometry of the receivers on the trucks.
- 3. Angle of Arrival (AoA) Determination: Using the TDoA data, the Angle of Arrival of the signals is computed. Given that the speed of radio waves is constant, the differences in arrival times can be directly translated into angle measurements.
- Orientation Computation: By aggregating AoA measurements from multiple pairs
 of receivers, the system computes the truck's orientation with respect to a common
 reference frame used by the platooning system.

The accuracy of orientation estimation is critical for maintaining platoon integrity and ensuring the coordinated movement of trucks. It affects lateral control, alignment within lanes, and the ability to make precise maneuvers. Therefore, our system can also incorporate error correction algorithms and filtering techniques to refine the orientation data. Furthermore, the orientation data can be shared among the platoon members via a secure communication channel to enable collective adjustments and maintain a coherent formation.

5.2. UWB-Based Platoon Control

The drones use the UWB sensors to measure the distance between trucks and maintain the optimal formation of platoons, Algorithm 1 illustrates the procedure. The distance error δd between the actual distance $d_{\rm actual}$ and the desired distance $d_{\rm desired}$ is computed as follows:

$$\delta d = d_{\text{actual}} - d_{\text{desired}}.$$
 (8)

A control signal u is generated based on the distance error δd and is used to adjust the truck's speed to maintain the desired distance:

$$u = K_p \cdot \delta d + K_d \cdot \frac{d(\delta d)}{dt},\tag{9}$$

where K_p is the proportional gain, K_d is the derivative gain, and $\frac{d(\delta d)}{dt}$ is the rate of change of the distance error.

Algorithm 1 UWB-Based Platoon Control

- 1: Initialize the desired distance d_{desired} between trucks
- 2: Initialize the proportional gain K_p and the derivative gain K_d
- 3: while Platoon is moving do
- 4: Measure the actual distance d_{actual} between trucks using UWB sensors
- 5: Compute the distance error $\delta d = d_{\text{actual}} d_{\text{desired}}$
- 6: Calculate the rate of change of the distance error $\frac{d(\delta d)}{dt}$
- 7: Generate the control signal $u = K_p \cdot \delta d + K_d \cdot \frac{d(\delta d)}{dt}$
- 8: Adjust the truck's speed based on the control signal u to maintain the desired distance
- 9: end while

5.3. UWB-Based Drone Coordination

The drones also use the UWB sensors to coordinate their positions and movements, ensuring that they maintain a safe distance from each other and from the trucks. The drones employ a similar control strategy as the trucks, adjusting their speed based on the distance error between their current position and the desired position relative to the trucks, Algorithm 2 illustrates the procedure.

Algorithm 2 UWB-Based Drone Coordination

- 1: Initialize the desired position of the drones relative to the trucks
- 2: Initialize the proportional gain K_p and the derivative gain K_d
- 3: while Drones are operating do
- 4: Measure the actual position of the drones using UWB sensors
- 5: Compute the position error $\delta p = p_{\text{actual}} p_{\text{desired}}$
- 6: Calculate the rate of change of the position error $\frac{d(\delta p)}{dt}$
- 7: Generate the control signal $u = K_p \cdot \delta p + K_d \cdot \frac{d(\delta p)}{dt}$
- 8: Adjust the drone's speed and direction based on the control signal *u* to maintain the desired position
- 9: end while

UWB systems are indeed limited in range when compared to narrowband alternatives like Wi-Fi; however, their precision in distance measurement is typically superior, which is critical for maintaining the tight formations necessary for effective platooning. The choice of UWB over automotive radars was made considering the emerging potential for UWB in indoor positioning and micro-location contexts where high accuracy is paramount. Additionally, UWB's immunity to multipath interference and its low power consumption make it a promising candidate for vehicular networks. The expected accuracy of UWB in our application is within a few centimeters, which aligns with the requirements for maintaining safe distances between trucks. Regarding the range, current UWB implementations can reliably cover distances up to 250 m, which we consider sufficient for the line-of-sight scenarios typical in highway environments.

The utilization of drones does indeed introduce an additional energy overhead; however, this cost must be weighed against the significant fuel savings afforded by the platooning of trucks. Drones are primarily used in our system for monitoring purposes and real-time decision making, which are tasks that do not require continuous operation, thereby reducing their energy consumption. To estimate the cost effectiveness of our approach, we conducted a preliminary analysis comparing the energy usage of drones to the fuel savings from platooning. Our model considers the energy required for the drones to hover, maneuver, and communicate with the trucks. We assume the drones operate on efficient electric power systems, which are becoming increasingly cost-effective with advancements in battery technology. The drones' operational time is directly correlated with the duration of the trucks' journeys; thus, the longer the platoon is in motion, the greater the cumulative fuel savings, offsetting the drones' energy usage. Moreover, the drone's energy consumption is relatively small compared to the fuel consumption of heavy trucks. For instance, a typical commercial quadcopter drone may consume approximately

100 watts per hour during flight, whereas a truck may consume upwards of 30 liters of fuel per hour under normal operation. Even with a conservative estimate of a 5% increase in fuel efficiency due to platooning, the fuel savings for a unique truck could be in the order of 1.5 liters per hour. For a platoon of trucks, these savings far exceed the energy cost of operating the drones. The cost-effectiveness of our proposed system also factors in the reduced need for onboard sensors and communication equipment on each truck, as these functions are offloaded to the drones. By centralizing these capabilities in drones, we anticipate a reduction in the overall system cost.

Furthermore, the operational endurance of drones is a fundamental factor in the deployment of our proposed truck platooning system. Currently, commercial drones capable of the monitoring tasks required for our system have a flight time ranging from 20 to 30 min on a unique charge under ideal conditions. This is a limitation that we acknowledge; however, our system is designed to mitigate this through several strategies. Firstly, our approach envisions the use of multiple drones operating in shifts to ensure continuous monitoring. The drones can be programmed to return to a charging station or vehicle when their battery levels reach a predetermined threshold, allowing a fresh drone to take over the monitoring task. This can be synchronized with the trucks' operational schedules to minimize any gaps in surveillance. Secondly, we are exploring the integration of inductive charging platforms within the infrastructure of truck platooning routes. These platforms could provide charging points at regular intervals, potentially during mandatory rest periods for drivers or while trucks are queued at checkpoints, allowing drones to recharge without returning to a distant base. Lastly, advancements in battery technology and energy-efficient drone designs are continually extending the flight times of drones. We are optimistic that the endurance of drones will increase in the near term, making them even more viable for extended operations. Furthermore, our ongoing research involves evaluating the use of fixed-wing drones, which offer longer flight times compared to rotary-wing drones, albeit with trade-offs in maneuverability and hovering capability.

Weather conditions, indeed, pose also significant challenges to the operation of drones and, by extension, the efficiency of the platooning system. Adverse weather, particularly storms and heavy rains, can impair the drones' ability to collect data and maintain stable flight. In our system design, we advance the incorporation of several mitigative measures to address these concerns. Firstly, the drones can be equipped with sensors capable of detecting inclement weather conditions, which can trigger an automatic return-to-home function to prevent loss or damage. Additionally, we are investigating the use of drones with weather-resistant features, including waterproof frames and enhanced stability controls, which can operate in a wider range of conditions. Secondly, the decentralized system architecture allows for a flexible response to the temporary unavailability of drones. In the event of adverse weather, the trucks can rely on their onboard sensors and communication systems to maintain platoon cohesion until drone surveillance can be safely resumed. Lastly, predictive algorithms can be developed that utilize weather forecasting data to plan drone operations proactively. This could enable us to schedule drone launches during favorable conditions and avoid times when bad weather is expected, thus maximizing operational efficiency.

5.4. Stability Analysis of Platooning System

The stability of the truck platooning system is a vital attribute that ensures the system's resilience to perturbations and its ability to maintain a coherent structure over time. We define the stability of the system in terms of its ability to return to a steady state after a disturbance such as a sudden change in speed or direction by one of the trucks.

To quantify the stability, we employ a mathematical model that represents the platoon dynamics. We consider a linearized model around a nominal operating point, which is a common approach in control theory for systems operating close to a desired state. The model is given by the following set of differential equations:

$$\dot{x}(t) = Ax(t) + Bu(t), \tag{10}$$

where x(t) is the state vector representing the positions and velocities of trucks in the platoon, A is the state matrix that encodes the interaction between the trucks, B is the input matrix that represents how control inputs (e.g., acceleration) affect the system, and u(t) is the control input vector.

The stability of the system can be assessed by examining the eigenvalues of the state matrix *A*. If all the eigenvalues have negative real parts, the system is said to be stable. This implies that any deviation from the steady state will decay over time, leading to the system returning to equilibrium. The stability criterion is formally stated as follows:

$$\operatorname{Re}(\lambda_o) < 0, \quad \forall o,$$
 (11)

where λ_0 represents the eigenvalues of matrix A.

Additionally, we consider the impact of UWB-based distance measurements on the stability. The measurement errors can introduce perturbations in the control inputs. To account for this, we include a disturbance vector d(t) in our model:

$$\dot{x}(t) = Ax(t) + Bu(t) + Ed(t), \tag{12}$$

where *E* is a matrix that describes how measurement errors propagate through the system. We can analyze the robustness of the system to these disturbances by performing a sensitivity analysis and ensuring that the system's poles remain in the left half of the complex plane under all expected operational conditions.

In practice, ensuring stability in a truck platooning system involves not only a robust theoretical foundation but also the consideration of real-world factors such as truck dynamics, driver reactions, and environmental influences. Therefore, our control algorithms should incorporate adaptive mechanisms that adjust to changes in truck behavior and external conditions.

5.5. Calculation of Fuel Consumption for Trucks

The fuel consumption of trucks in a platoon is a critical factor for assessing the efficiency of the platooning system. To calculate the fuel consumption, we can follow a systematic approach that incorporates various parameters such as the truck's engine characteristics, aerodynamic properties, rolling resistance, and the influence of platooning dynamics.

5.5.1. Baseline Fuel Consumption

Firstly, we can establish a baseline fuel consumption model for a unique truck traveling at a steady speed. This model is based on the engine's specific fuel consumption (SFC), which is a measure of the fuel efficiency of the engine at a given speed and power output. The SFC can be obtained from the engine manufacturer's data or from empirical measurements. The baseline fuel consumption F_b for a truck traveling at speed v is given by:

$$F_b = SFC \cdot P \cdot t, \tag{13}$$

where P is the power output required to overcome aerodynamic drag and rolling resistance at speed v, and t is the travel time.

5.5.2. Aerodynamic Effects

In a platooning scenario, trucks following the lead vehicle benefit from reduced aerodynamic drag due to the slipstream effect. To quantify this reduction, we use coefficients of drag C_d that are adjusted based on the position in the platoon and the inter-vehicle distance. The adjusted fuel consumption F_a for a following truck is computed as:

$$F_a = F_b \cdot (1 - \Delta C_d), \tag{14}$$

where ΔC_d represents the percentage reduction in the coefficient of drag due to platooning.

5.5.3. Rolling Resistance

The rolling resistance also affects fuel consumption, particularly for heavy-duty trucks. The rolling resistance force F_r is a function of the truck's weight W and a coefficient of rolling resistance C_r , which varies with the type of tires and road conditions. The additional fuel consumption F_r due to rolling resistance is calculated by the following:

$$F_r = SFC \cdot P_r \cdot t, \tag{15}$$

where P_r is the power needed to overcome rolling resistance.

5.5.4. Platooning Dynamics

The dynamics of the platoon, such as acceleration and deceleration phases, are also incorporated into the fuel consumption model. The variation in speed results in changes in engine power demand, which in turn affects fuel consumption. The total fuel consumption F_t for a truck in a platoon is thus the sum of the baseline, aerodynamic effects, and rolling resistance, which is adjusted by the platoon dynamics:

$$F_t = F_b + F_a + F_r - \Delta F_d, \tag{16}$$

where ΔF_d accounts for the dynamic fuel savings due to optimized speed variations within the platoon.

6. Simulation and Results

In this section, we present the results of our simulation experiments to evaluate the performance of the proposed drone-based decentralized truck platooning system with UWB sensors. We focus on the effectiveness of the multi-objective optimization in forming platoons and the impact of UWB technology on the accuracy and reliability of distance measurements and platoon control.

6.1. Simulation Setup

Our simulation environment consists of a predefined number of trucks and drones operating on a road network; in our particular case, we operate with 30 trucks and 10 drones. The trucks have various fuel efficiencies, optimal speeds, and types, while the drones are equipped with UWB sensors to measure distances between trucks and coordinate the formation of platoons. The platooning controller utilizes multi-objective optimization to dynamically form and maintain platoons based on the compatibility of trucks. The code is written in python from scratch with corresponding classes implementing the controller and the model for the formation of platoons using drones. We evaluate the performance of our system using the metrics defined in Section 3.3, including fuel efficiency, travel time, and safety; and we also take the platoon formation into consideration, which is the number of platoons formed and their average size.

Our implementation provides a simulation of drone-based platooning using the framework Mesa (v.1.2.1) for agent-based modeling. In the system, drones are responsible for maintaining platoons of trucks on a grid, ensuring that the trucks remain within a certain distance of each other.

We summarize the main components of the architecture:

TruckAgent: Represents a truck in the simulation. Each truck has a fuel efficiency, an
optimal speed, and a type. Trucks are capable of sensing the distance to the nearest
other truck.

- DroneAgent: Represents a drone in the simulation. Drones follow the nearest truck
 if it is beyond a threshold distance and collect sensor data from trucks to report the
 average distance between them. They also help in maintaining the platoons of trucks.
- 3. PlatooningController: Manages the platoons of trucks. It ensures that trucks are in the appropriate platoon based on their distances from each other and certain compatibility criteria.
- 4. DronePlatooningModel: The main model that includes all the agents and manages their interactions. It also collects data during the simulation for analysis.
- 5. Visualization: The code includes functions to visualize the positions of the trucks and drones as well as the areas covered by the drones.

6.2. Results and Analysis

We begin with a simplified simulation, where the experiment aimed to simulate a scenario with trucks and drones to observe truck-platooning behavior and drone-following stability. Setup: The simulation involved 30 trucks and 10 drones on a 100×100 grid. Trucks moved toward random destinations, and drones followed the nearest truck.

Main Findings:

- Truck Platooning: The trucks formed platoons with an average size of 2.53, demonstrating potential for fuel efficiency improvement.
- Drone Following: The drones maintained an average distance of 1.39 units from the nearest truck, showcasing effective following behavior.
- Stability: The drones were generally stable in following the trucks with an average of 1.6 nearest truck changes per drone.

This visualization in Figure 3 provides insight into how the drones are able to follow the trucks and adapt to their movements over time.

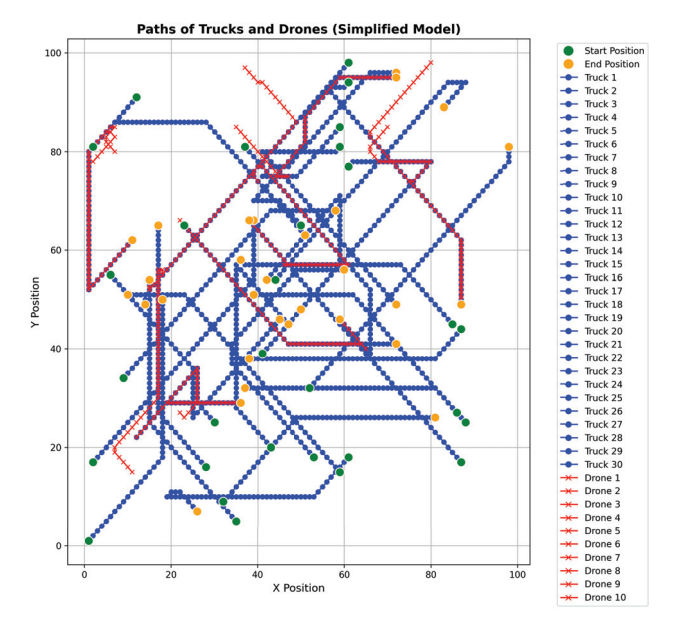


Figure 3. Trajectories of 30 autonomous trucks (in blue) and 10 drones (in red) are depicted over the course of a 50-step simulation within a defined 100 × 100 area. Each truck and drone is represented by a distinct path marked with circles and crosses, respectively, showcasing their individual movements. Green markers indicate starting positions while orange markers denote the final positions after 50 simulation steps. The intersecting and converging paths highlight the dynamic interactions and the emergent platoon formations of the trucks with the drones' paths reflecting their adaptive positioning to effectively monitor and support the platoon system.

Platooning Dynamics:

- The trucks in the simplified model have exhibited platooning behavior throughout the simulation. On average, the size of the platoons (groups of trucks traveling closely together) was approximately 2.53 trucks per platoon.
- A total of 243 platoons were identified over the 50 simulation steps.

Insights: The average platoon size indicates that trucks were often able to form small groups, demonstrating the potential for fuel efficiency improvement and increased road safety, which are key benefits of platooning. The total number of platoons formed suggests active dynamics in platoon formation and dissolution, indicating a responsive system to the changing positions of the trucks.

Proximity to Nearest Truck:

- Average Distance: The drones were, on average, approximately 1.39 units away from the nearest truck. This indicates a relatively close proximity, suggesting effective following behavior.
- Maximum Distance: The maximum observed distance between a drone and the nearest truck was approximately 14.56 units. This could be a moment where the drone was transitioning between trucks or when the trucks were widely spread out.
- Minimum Distance: The minimum observed distance was 0.0 units, meaning there were instances where a drone was exactly at the same position as a truck, showcasing precise following capability.
- Standard Deviation: The standard deviation of the distances was approximately 2.87, indicating some variability in the drones' proximity to the trucks.

Insights: The drones in the simplified model demonstrated an ability to closely follow the trucks, maintaining a generally low average distance to the nearest truck. The variability in distances suggests that there were moments of both very close proximity and relatively farther distances, which could be areas for improvement.

Nearest Truck Changes:

- Average Changes: On average, each drone changed its nearest truck approximately 1.6 times throughout the simulation.
- Maximum Changes: The maximum number of nearest truck changes for a single drone was 4.
- Minimum Changes: The minimum number of nearest truck changes was 1.

Insights: The relatively low average number of nearest truck changes suggests that the drones were fairly stable in following the trucks. However, there is some variability, with certain drones changing their nearest truck more frequently than others. This could be due to the dynamic movement of the trucks and the positioning of the drones.

In the bar plot in Figure 4, you can see the number of nearest truck changes for each drone throughout the 50 simulation steps. The drones are labeled with their IDs, ranging from 30 to 39.

Observations: Most drones have a relatively low number of nearest truck changes, indicating stable following behavior. However, Drone 30 stands out with four nearest truck changes, which is the maximum observed in this simulation. This could be a result of its initial position, movement pattern, or the dynamics of the nearby trucks. Interpretation: A lower number of nearest truck changes suggests that the drone is able to consistently follow a particular truck, which is a desirable behavior for applications such as aerial monitoring or assistance in platooning. On the other hand, a higher number of changes could indicate instability in following or could be a result of the drone effectively adapting to the changing positions of multiple trucks.

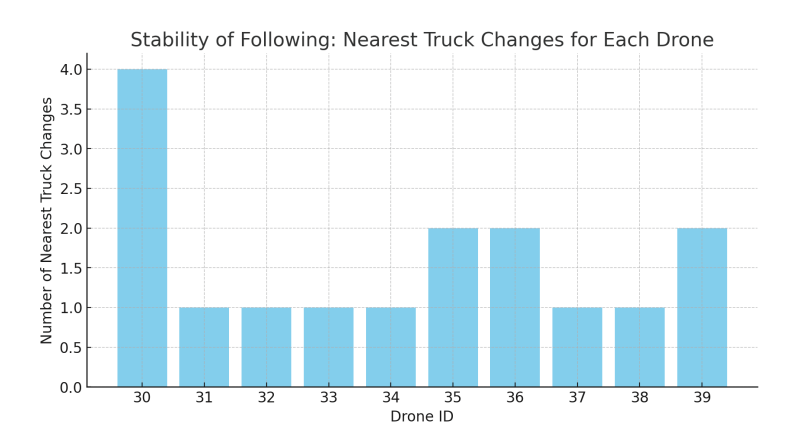


Figure 4. Bar plot that visualizes the number of nearest truck changes for each drone, providing a clear visual representation of the stability in following.

The plot in Figure 5 shows the number of truck platoons formed at each time step. The green line represents the number of platoons. The number of platoons varies over time, reflecting the dynamic nature of truck movements and platoon formations.

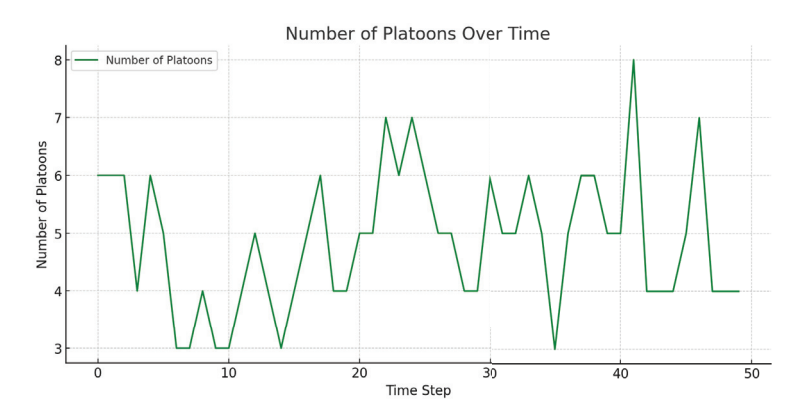


Figure 5. Number of platoons over time along the 50-step simulation.

In the formulation of our truck and drone platooning model, dynamic stability is a primary consideration given the inherent risks associated with the oscillatory modes of a multi-dimensional system. The simplified simulation model incorporates rudimentary movement patterns for trucks and drones, providing a foundational framework upon which stability controls can be built. In our simulations, we implement measures to mitigate the risk of dynamic instability. These include speed synchronization protocols to prevent abrupt relative speed changes and a following algorithm that enables drones to maintain a steady distance from the trucks, thereby providing corrective actions that are both proactive and reactive to the system's state.

Next, we implement the fully fledged system. Here, trucks move around a grid, reporting distances to their nearest neighbor, while whole drones monitor the trucks, calculating the average distance between them, and maintaining platoons of trucks based on their proximity and compatibility. The simulation runs for 50 steps with 30 trucks and 10 drones in a 100×100 grid. After the simulation, it collects and visualizes data on the average distance between trucks and the number of platoons over time. The visualization of drone coverage is also generated, providing insight into how well the drones are able to monitor the trucks on the grid.

The simulation results demonstrate the effectiveness of our drone-based decentralized truck platooning system with UWB sensors. The multi-objective optimization successfully formed platoons based on the compatibility of trucks, resulting in reduced fuel consumption and travel time. The use of UWB sensors for distance measurement and platoon control significantly contributed to the system's performance. The high accuracy and reliability

of the UWB technology ensured that the drones could maintain the desired distance between trucks, preventing incidents and improving safety. Additionally, the UWB sensors enabled the drones to coordinate their positions and movements effectively, ensuring their safe operation within the system. An illustrative example of a particular instance of the simulation is shown in Figure 6 where the number of platoons in operation decided by the controller as a result of the multi-objective optimization is six and the average distance between trucks maintained by the algorithm is 5.11.

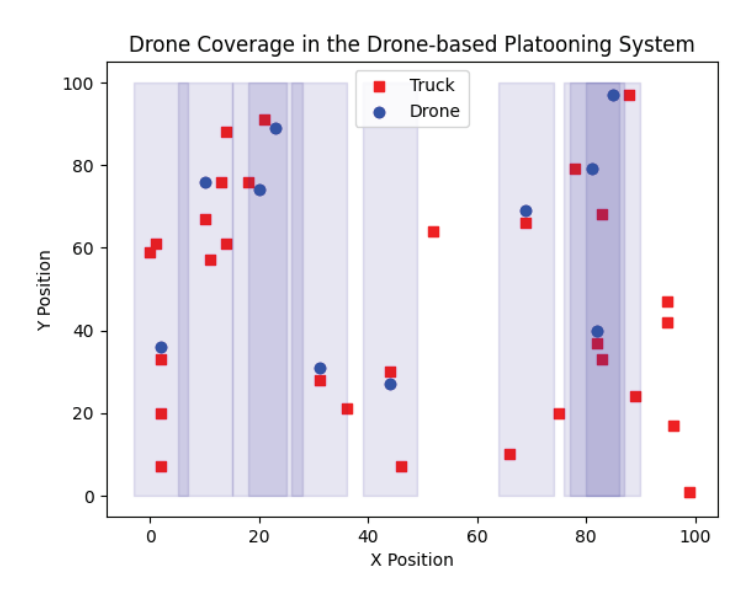


Figure 6. Drone coverage in the drone-based platooning system. This figure illustrates the spatial distribution of trucks and drones in the drone-based platooning system. The trucks are represented by red squares, while the drones are represented by blue circles. The shaded blue rectangles represent an approximation of the effective coverage area within which each drone can reliably communicate with the trucks and measure distances using its UWB sensors. Please note that the rectangular coverage is a simplification; actual coverage patterns may be more complex due to antenna radiation patterns and environmental factors. The *x*-axis represents the horizontal position within the grid, and the *y*-axis represents the vertical position within the grid. This visualization helps demonstrate the effectiveness of drone coverage in managing truck platoons and ensuring optimal distances between trucks are maintained.

We simulated several runs of the drone-based platooning system and calculated the average results for number of platoons over time, see Figure 7a, and the average distance between trucks over time, see Figure 7b.

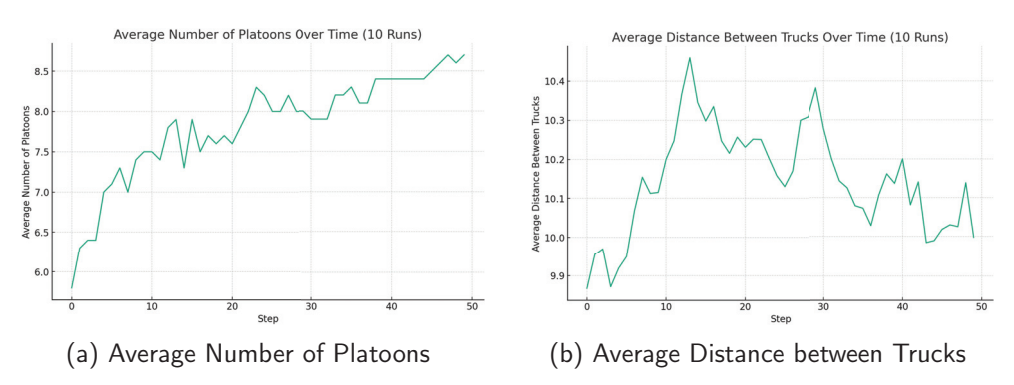


Figure 7. Number of platoons over time in 10 runs. (**a**,**b**) Average distance between trucks over time in 10 runs.

6.3. Simulation Analysis of Fuel Efficiency

To investigate the impact of platooning on fuel efficiency, a simulation was conducted using a model that incorporates various factors such as truck speed, specific fuel consumption (SFC), and aerodynamic effects. The simulation involved 30 trucks over a virtual environment, with each truck moving toward a random destination and consuming fuel based on its speed and whether it was in a platoon. Two key scenarios were analyzed: (1) the average fuel consumed by trucks at different speeds without considering platooning effects, and (2) the fuel efficiency at different truck speeds for varying platooning penetration rates.

Figure 8 presents the results of the first scenario, illustrating the relationship between truck speed and average fuel consumption. As expected, fuel consumption increases with speed due to the higher power requirements for overcoming aerodynamic drag and rolling resistance.

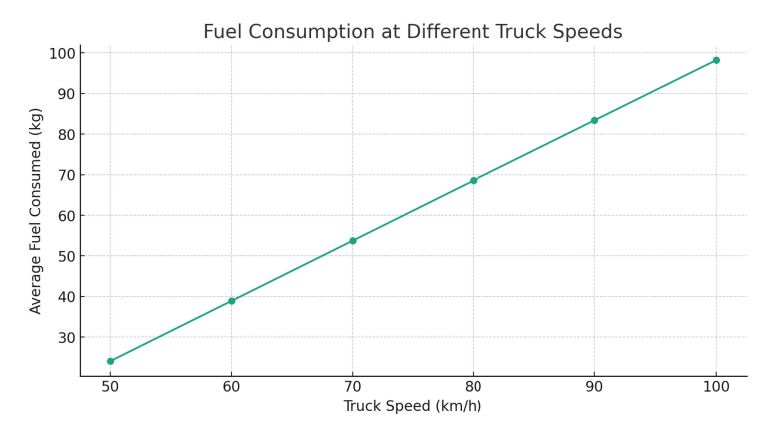


Figure 8. Average fuel consumption of trucks at different speeds.

Figure 9 shows the results of the second scenario, depicting how platooning penetration rates affect fuel efficiency. The graph indicates that higher platooning penetration rates lead to improved fuel efficiency across all speeds tested. This efficiency gain is attributed to the reduced aerodynamic drag when trucks travel in close formation, highlighting the benefits of platooning in reducing fuel consumption.

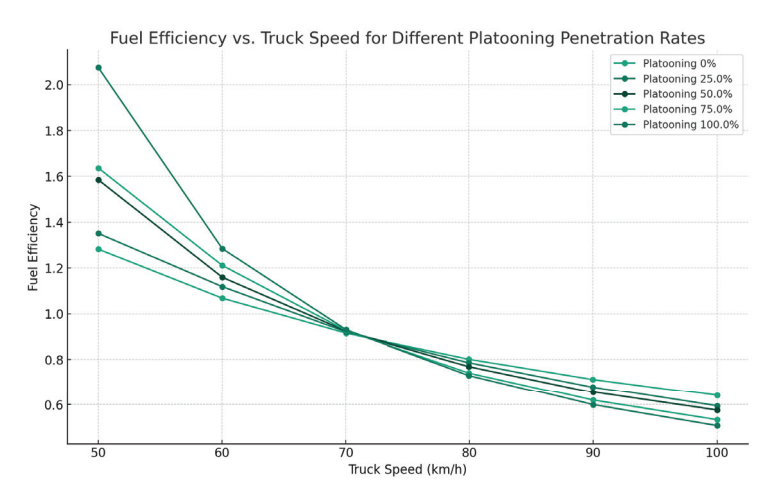


Figure 9. Fuel efficiency at different truck speeds for various platooning penetration rates.

7. Conclusions and Future Work

In this paper, we have introduced an innovative drone-based decentralized truck platooning system leveraging UWB technology. This system is designed to ensure accurate distance estimation and enable the efficient formation of truck platoons. Our system utilizes

a multi-objective optimization strategy to form and maintain platoons based on the compatibility of trucks. This approach is designed to optimize fuel efficiency, travel time, and safety in truck platooning systems. The use of UWB technology is a defining feature of our proposed system, providing highly accurate and reliable distance measurements between vehicles. Such precise measurements are essential for maintaining optimal distances in platooning formations, thereby preventing potential incidents and enhancing safety.

Moving forward, future work will focus on refining and extending the current system. Key areas for future exploration include the following: developing more advanced optimization techniques for efficient platoon formation, establishing reliable and secure communication protocols between drones and trucks, exploring the scalability of the proposed system in more complex scenarios, investigating possible integration with existing or future traffic management systems, and also conducting extensive real-world experiments to validate the system's performance.

Further work could explore the following directions:

- 1. Enhanced algorithms: Investigate more advanced optimization techniques, such as genetic algorithms, reinforcement learning, or swarm intelligence, to further improve the process of formation of platoons and adapt to the dynamic environment.
- 2. Communication protocols: Develop reliable and secure communication protocols [27] between drones and trucks to ensure the robustness and security of the platooning system against potential attacks and failures.
- Scalability: Study the scalability of the proposed system by considering larger numbers of trucks and drones operating in more complex road networks and environments, including urban and rural settings.
- 4. Integration with traffic management systems: Investigate the integration of the proposed platooning system with existing or future traffic management systems to coordinate platoons' movements with other road users and optimize the overall traffic flow.
- Real-world testing: Conduct extensive real-world experiments to validate the performance of the proposed system in practical scenarios and identify potential challenges and limitations that may arise during deployment.

Author Contributions: Conceptualization, J.d.C. and I.d.Z.; funding acquisition, C.T.C. and J.C.C.; investigation, I.d.Z. and J.d.C.; methodology, I.d.Z. and J.d.C.; software, J.d.C. and I.d.Z.; supervision, C.T.C. and J.C.C., writing—original draft, J.d.C. and I.d.Z.; writing—review and editing, C.T.C., J.C.C., J.d.C. and I.d.Z. All authors have read and agreed to the published version of the manuscript.

Funding: We thank the following funding sources from GOETHE-University Frankfurt am Main; 'DePP—Dezentrale Plannung von Platoons im Straßengüterverkehr mit Hilfe einer KI auf Basis einzelner LKW', 'Center for Data Science & AI' and 'HessianAI—AI Biology'. We acknowledge the support of R&D project PID2021-122580NB-I00, funded by MCIN/AEI/10.13039/501100011033 and ERDF.

Institutional Review Board Statement: Not applicable.

Informed Consent Statement: Not applicable.

Data Availability Statement: The data presented in this study are openly available in FigShare at https://doi.org/10.6084/m9.figshare.24549625.

Conflicts of Interest: The authors declare that they have no conflict of interest. The funders had no role in the design of the study, in the collection, analyses, or interpretation of data, in the writing of the manuscript, or in the decision to publish the results.

Abbreviations

The following abbreviations are used in this manuscript:

Ultra-Wideband UWB Vehicle-to-Vehicle V2V Unmanned Aerial Vehicles UAV
Internet of Things IoT
Time of Flight ToF
Time Difference of Arrival TDoA
Angle of Arrival AoA
Specific Fuel Consumption SFC

References

- 1. Lesch, V.; Breitbach, M.; Segata, M.; Becker, C.; Kounev, S.; Krupitzer, C. An overview on approaches for coordination of platoons. *IEEE Trans. Intell. Transp. Syst.* **2022**, 23, 10049–10065. [CrossRef]
- 2. Van de Hoef, S.; Johansson, K.H.; Dimarogonas, D.V. Computing feasible vehicle platooning opportunities for transport assignments. *IFAC-PapersOnLine* **2016**, 49, 43–48. [CrossRef]
- 3. Boysen, N.; Briskorn, D.; Schwerdfeger, S. The identical-path truck platooning problem. *Transp. Res. Part B Methodol.* **2018**, 109, 26–39. [CrossRef]
- 4. Larsson, E.; Sennton, G.; Larson, J. The vehicle platooning problem: Computational complexity and heuristics. *Transp. Res. Part C Emerging Technol.* **2015**, *60*, 258–277. [CrossRef]
- 5. Zeng, Y.; Wang, M.; Rajan, R.T. Decentralized coordination for truck platooning. *Comput. Aided Civ. Infrastruct. Eng.* **2022**, 37, 1997–2015. [CrossRef]
- 6. Elbert, R.; Roeper, F.; Rammensee, M. Decentralized coordination of platoons—A conceptual approach using deep reinforcement learning. In Proceedings of the World Conference on Transport Research—WCTR, Montreal, QC, Canada, 17–21 July 2023.
- 7. de Zarza, I.; de Curto, J.; Calafate, C.T. Decentralized Planning of Platoons in Road Transport using Reinforcement Learning. In Proceedings of the 2023 IEEE 43rd International Conference on Distributed Computing Systems Workshops (ICDCSW), IEEE Computer Society, Hong Kong, China, 18–21 July 2023; pp. 133–138. [CrossRef]
- 8. De Zarza, I.; de Curto, J.; Calafate, C.T. Decentralized Platooning Optimization for Trucks: A MILP and ADMM-based Convex Approach to Minimize Latency and Energy Consumption. In Proceedings of the 2023 IEEE 43rd International Conference on Distributed Computing Systems Workshops (ICDCSW), IEEE Computer Society, Hong Kong, China, 18–21 July 2023; pp. 139–144. [CrossRef]
- 9. Bisio, I.; Garibotto, C.; Haleem, H.; Lavagetto, F.; Sciarrone, A. A systematic review of drone based road traffic monitoring system. *IEEE Access* **2022**, *10*, 101537–101555. [CrossRef]
- 10. Shi, W.; Zhou, H.; Li, J.; Xu, W.; Zhang, N.; Shen, X. Drone assisted vehicular networks: Architecture, challenges and opportunities. *IEEE Netw.* **2018**, *32*, 130–137. [CrossRef]
- 11. Caillouet, C.; Giroire, F.; Razafindralambo, T. Efficient data collection and tracking with flying drones. *Ad Hoc Netw.* **2019**, *89*, 35–46. [CrossRef]
- 12. De Curtò, J.; de Zarzà, I.; Calafate, C.T. Semantic scene understanding with large language models on unmanned aerial vehicles. *Drones* **2023**, *7*, 114. [CrossRef]
- 13. Chung, S.H.; Sah, B.; Lee, J. Optimization for drone and drone-truck combined operations: A review of the state of the art and future directions. *Comp. Operat. Res.* **2020**, *123*, 105004. [CrossRef]
- 14. Chung, S.-H. Applications of smart technologies in logistics and transport: A review. *Transp. Res. Part E Log. Transp. Rev.* **2021**, 153, 102455. [CrossRef]
- 15. de Curtò, J.; de Zarzà, I.; Calafate, C.T. UWB and MB-OFDM for Lunar Rover Navigation and Communication. *Mathematics* **2023**, 11, 3835. [CrossRef]
- 16. Aiello, G.R.; Rogerson, G.D. Ultra-wideband wireless systems. IEEE Microw. Mag. 2003, 4, 36-47. [CrossRef]
- 17. Rahayu, Y.; Rahman, T.A.; Ngah, R.; Hall, P. Ultra wideband technology and its applications. In Proceedings of the 2008 5th IFIP International Conference on Wireless and Optical Communications Networks (WOCN '08), Cairo, Egypt, 28–30 April 2008; pp. 1–5.
- 18. Alarifi, A.; Al-Salman, A.; Alsaleh, M.; Alnafessah, A.; Al-Hadhrami, S.; Al-Ammar, M.A.; Al-Khalifa, H.S. Ultra wideband indoor positioning technologies: Analysis and recent advances. *Sensors* **2016**, *16*, 707. [CrossRef] [PubMed]
- 19. Coppens, D.; Shahid, A.; Lemey, S.; Herbruggen, B.V.; Marshall, C.; Poorter, E.D. An overview of UWB standards and organizations (IEEE 802.15.4, FiRa, apple): Interoperability aspects and future research directions. *IEEE Access* 2022, 10, 70219–70241. [CrossRef]
- 20. Fontana, R.J. Recent Applications of Ultra Wideband Radar and Communications Systems; Springer: Boston, MA, USA, 2002; pp. 225–234. [CrossRef]
- 21. Molisch, A.F.; Cassioli, D.; Chong, C.-C.; Emami, S.; Fort, A.; Kannan, B.; Karedal, J.; Kunisch, J.; Schantz, H.G.; Siwiak, K.; et al. A comprehensive standardized model for ultrawideband propagation channels. *IEEE Trans. Antennas Propag.* 2006, 54, 3151–3166. [CrossRef]
- 22. Macoir, N.; Bauwens, J.; Jooris, B.; Van Herbruggen, B.; Rossey, J.; Hoebeke, J.; De Poorter, E. UWB Localization with battery-powered wireless backbone for drone-based inventory management. *Sensors* **2019**, *19*, 467. [CrossRef]
- 23. Wang, M.; Chen, X.; Jin, B.; Lv, P.; Wang, W.; Shen, Y. A novel V2V cooperative collision warning system using UWB/DR for intelligent vehicles. *Sensors* **2021**, *21*, 3485. [CrossRef]

- 24. Törnell, J.; Sebben, S.; Söderblom, D. Influence of inter-vehicle distance on the aerodynamics of a two-truck platoon. *Int. J. Automot. Technol.* **2021**, 22, 747–760. [CrossRef]
- 25. Törnell, J.; Sebben, S.; Elofsson, P. Experimental investigation of a two-truck platoon considering inter-vehicle distance, lateral offset and yaw. *J. Wind. Eng. Ind. Aerodyn.* **2021**, 213, 104596. [CrossRef]
- 26. Lu, X.Y.; Shladover, S.E. Automated truck platoon control and field test. In *Road Vehicle Automation*; Springer: Berlin, Germany, 2014; pp. 247–261.
- 27. Willemsen, D.M.C.; Schmeitz, A.J.C.; Mascalchi, E. EU ENSEMBLE Project: Specification of an interoperable solution for a support function for platooning. *IEEE Trans. Intell. Transp. Syst.* **2023**, *24*, 5705–5718. [CrossRef]

Disclaimer/Publisher's Note: The statements, opinions and data contained in all publications are solely those of the individual author(s) and contributor(s) and not of MDPI and/or the editor(s). MDPI and/or the editor(s) disclaim responsibility for any injury to people or property resulting from any ideas, methods, instructions or products referred to in the content.





Article

A Microscopic Traffic Model Incorporating Vehicle Vibrations Due to Pavement Condition

Faryal Ali ^{1,*}, Zawar Hussain Khan ¹, Khurram Shehzad Khattak ², Thomas Aaron Gulliver ¹ and Ahmed B. Altamimi ³

- Department of Electrical and Computer Engineering, University of Victoria, Victoria, BC V8W 2Y2, Canada; khanz@uvic.ca (Z.H.K.); agullive@ece.uvic.ca (T.A.G.)
- Department of Computer Systems Engineering, University of Engineering and Technology, Peshawar 25000, Pakistan; khurram.s.khattak@gmail.com
- College of Computer Science and Engineering, University of Ha'il, Ha'il 55476, Saudi Arabia
- * Correspondence: faryalali@uvic.ca

Abstract: A microscopic traffic flow model is developed that incorporates vehicle vibrations due to pavement condition. The Intelligent Driver (ID) model employs a fixed exponent so traffic behavior is the same regardless of the road condition. Thus, it ignores the underlying physics. To address this limitation, the proposed model employs the Pavement Condition Index (PCI) in describing traffic behavior. The performance of both models is evaluated on a 3000 m circular road using the Euler numerical discretization technique. The results show that the performance of the proposed model varies with the pavement condition (PCI), as expected. Furthermore, the traffic flow increases with vehicle speed. The oscillations in speed and density with the proposed model decrease as the PCI increases, and are larger when the speed is higher. Consequently, the results with the proposed model align more closely with reality as they are based on the PCI, and so are a more accurate representation of traffic behavior.

Keywords: traffic exponent; Intelligent Driver model; microscopic traffic flow; Pavement Condition Index; vehicle vibration

MSC: 37M05

1. Introduction

Pavement condition significantly impacts traffic behavior. Pavement deterioration causes traffic accidents, congestion, pollution, and time delays [1]. Moreover, poor roads impact the smooth flow of traffic, resulting in rider discomfort and increased vehicle operating costs [2]. Congestion lowers vehicle speeds so emissions are increased [1]. Further, vehicle speed is reduced by an average of 55% when the road condition is poor compared to when it is excellent, and average emissions increase by 2.49%. Road safety is a primary concern worldwide as road accidents cause 1.3 million fatalities each year [3]. It is also dangerous as uneven pavement and potholes, damaged concrete, cracks, and exposed rebar can cause drivers to lose control, resulting in severe accidents [4]. Efficient traffic forecasting and control are essential to alleviate traffic problems such as congestion and improve road infrastructure [5]. This requires a practical model for traffic prediction.

Traffic models are typically microscopic or macroscopic, and mesoscopic. Macroscopic models focus on speed and density to describe traffic flow [6], while microscopic models focus on individual vehicles and drivers [7]. They incorporate speed, position, and distance and time headway [8,9].

Gazis, Herman, and Rothery proposed a microscopic model commonly known as the GHR model [10]. This model characterizes driver response considering the speed and distance of leading vehicles. However, driver behavior in changing conditions is ignored as speed adjustments are based on a constant and not traffic physics. Newell [11] characterized vehicle behavior in dense traffic and showed that velocity (speed) is impacted by the distance headway. An increase in this headway results in higher speeds and lower density. However, high speeds can produce large acceleration, which is neither safe nor realistic.

Wiedemann [12] and Fritzsche [13] developed similar models based on driver behavior under varying conditions. Their results are employed in the PTV VISSIM and PARAM-ICS simulators, respectively [14]. However, the traffic states have different equations so their models are complex. Wiedemann [15] created an improved model using simulation results for traffic on motorways. However, this model is not stable for a large number of vehicles [16].

An improvement to the Newell model was given in [17], but it neglects speed differences, resulting in acceleration which is very high. Moreover, driver behavior is based on a constant and so traffic physics is ignored. It was shown in [18] that speed differences can be used to accurately characterize speed and time headway in dense traffic. However, average and slow driver behavior are not considered so the results only pertain to aggressive drivers. The model in [19] is widely used because it produces realistic traffic behavior. As a consequence, it is employed in the AIMSUN simulator [14]. However, this model cannot differentiate between acceleration and deceleration and is limited to a small range of parameters [20].

The Intelligent Driver (ID) model was developed in [20] based on driver reaction. This model considers desired velocity (speed) and distance headway to characterize driver behavior [21–23]. Unlike the Gipps model, the ID model provides realistic acceleration and deceleration [14]. As a consequence, it is widely utilized in Adaptive Cruise Control (ACC) and cooperative ACC [24–26]. The ID model is also employed in Simulation of Urban MObility (SUMO) and PTV VISSIM [27]. However, it uses a fixed exponent to characterize traffic. This means that driver behavior is not based on traffic conditions. This is unrealistic as real-world traffic dynamics are influenced by various factors including pavement condition, and this affects driver behavior.

This study introduces a microscopic traffic model that incorporates the pavement condition to accurately represent traffic behavior. The pavement condition is evaluated using the Pavement Condition Index (PCI), which is an indicator of pavement condition and quality, and thus affects driver behavior and traffic flow. It ranges between 0 and 100 [2]. Incorporating the PCI results in a model that provides a more comprehensive and accurate representation of traffic behavior. A flowchart of the methodology employed in this research is given in Figure 1. First, field experiments to determine the impact of vehicle vibrations on the PCI were conducted on the Grand Trunk highway in Peshawar, located in the Khyber Pakhtunkhwa province of Pakistan. This road section spans 7 km and extends from the Chamkani Bus Rapid Transit (BRT) station to Pabbi. Then, the proposed and ID models are implemented using the Euler technique in MATLAB. The results obtained indicate that the proposed model is more suitable for evaluating traffic behavior.



Figure 1. Flowchart of the methodology.

The rest of this paper is organized as follows. In Section 2, traffic flow models are introduced and their stability is analyzed in Section 3. Section 4 outlines the Euler technique and the performance is evaluated in Section 5. The results of this paper are summarized in Section 6.

2. Traffic Models

The ID model is used for microscopic traffic characterization and incorporates factors such as the desired speed v_d , distance to align with leading conditions s, and the difference in speed Δv with the leading vehicle [20]. Driver response is a function of the ratio of average speed v to desired speed v_d , and is expressed as [20]

$$\frac{dv}{dt} = a \left(1 - \left(\frac{v}{v_d} \right)^{\delta} - \left(\frac{H}{s} \right)^2 \right) \tag{1}$$

where a is the maximum acceleration and δ is a fixed acceleration exponent. H is the desired distance headway during traffic alignment to leading conditions and is given by [20]

$$H = J + Tv + \frac{v\Delta v}{2\sqrt{ad}} \tag{2}$$

where *d* is the deceleration or minimum acceleration, *J* is the jam spacing as illustrated in Figure 2, and *T* is the time required by a vehicle to adjust its speed to the speed of the leading vehicle [5]. *H* indicates driver desire to maintain a safe distance from the leading vehicle. This is crucial for ensuring safety on the road and preventing collisions. The ID model employs (1) and (2) for traffic by incorporating driver response and distance headway for the alignment of traffic [5].

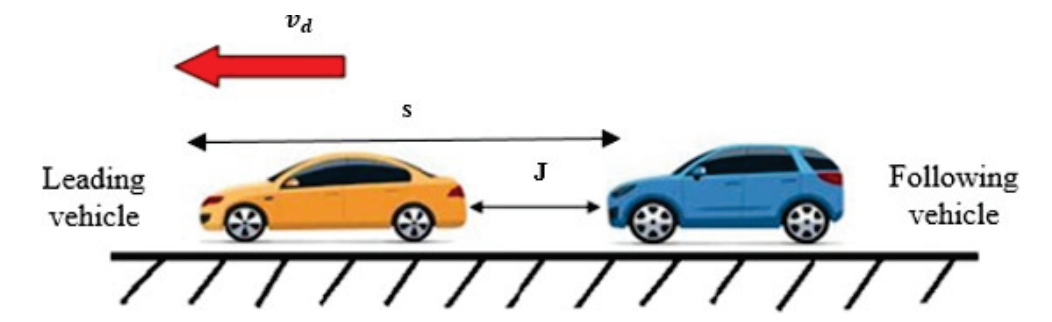


Figure 2. Intelligent Driver (ID) model parameters.

The ID model characterizes driver response to traffic conditions based on a fixed value δ . Thus, driver behavior does not vary based on these conditions, so it is unrelated to traffic physics and results in inadequate and unrealistic traffic characterization.

An acceleration exponent based on the PCI is proposed for the realistic characterization of traffic. Then, δ is a function of vehicle vibrations which are mechanical oscillations. These vibrations are largely generated by the interaction between the road surface and tires, and thus are a major contributor to passenger fatigue and discomfort.

Field experiments were conducted by driving a test vehicle over the road segment in Peshawar, Pakistan, between 12 AM and 2 AM. One lane in each direction was traversed 12 times with speeds of 35 km/h (9.72 m/s), 45 km/h (12.50 m/s), and 55 km/h (15.27 m/s). Thus, for a given speed, a lane was traversed four times. These speeds were selected to represent typical traffic observed on the road segment. Data were collected using an On-Board Diagnostic-II scanner connected to a smartphone with the BotlnckDectr [28] mobile app. This allowed for the recording of various parameters including GPS location, in-vehicle noise, vibration, and time [28]. During the experiments, the smartphone was positioned on the vehicle dashboard. The data were transmitted to the Amazon Web

Services (AWS) cloud. It was then analyzed to obtain the *PCI* of the road segment. The relationships between PCI and vehicle vibrations obtained are

$$\delta = -0.0169PCI + 4.068 \tag{3}$$

$$\delta = -0.0265PCI + 5.037 \tag{4}$$

$$\delta = -0.0251PCI + 5.209 \tag{5}$$

for speeds of approximately 9.72 m/s, 12.50 m/s, and 15.27 m/s, respectively. The PCI ranges from 0 to 100 where 0 corresponds to a poor road condition and 100 to an excellent road condition. Thus, δ and PCI are linearly related. As the pavement condition degrades, the oscillations increase, which reduces passenger comfort, i.e., a higher PCI corresponds to lower vibrations. Substituting (3), (4) and (5) in (1) gives the proposed model for speeds of 9.72 m/s, 12.50 m/s, and 15.27 m/s, respectively

$$\frac{dv}{dt} = a \left(1 - \left(\frac{v}{v_d} \right)^{(-0.0169PCI + 4.068)} - \left(\frac{H}{s} \right)^2 \right) (v_d = 9.72 \text{ m/s})$$
 (6)

$$\frac{dv}{dt} = a \left(1 - \left(\frac{v}{v_d} \right)^{(-0.0265PCI + 5.037)} - \left(\frac{H}{s} \right)^2 \right) (v_d = 12.50 \text{ m/s})$$
 (7)

$$\frac{dv}{dt} = a \left(1 - \left(\frac{v}{v_d} \right)^{(-0.0251PCI + 5.209)} - \left(\frac{H}{s} \right)^2 \right) (v_d = 15.27 \text{ m/s})$$
 (8)

An excellent road condition is required to avoid traffic congestion and accidents and efficiently align to forward vehicles. In this case, there is free flow traffic which corresponds to PCI=100. A poor road condition can result in congestion due to the reduction in vehicle speed. In this case, PCI=0 and vehicle acceleration and deceleration are large so the emissions are high. With the proposed model, alignment is according to the PCI and is more realistic compared with fixed δ .

The traffic density can be expressed as $D = 1/s_e$ [29] where s_e is the distance headway at equilibrium. In this case, $\Delta v = 0$ so substituting (2) in (1) gives for the ID model

$$a\left(1 - \left(\frac{v}{v_d}\right)^{\delta} - \left(\frac{J + Tv}{s_e}\right)^2\right) = 0\tag{9}$$

and rearranging we obtain

$$s_e = (J + Tv) \left(1 - \left(\frac{v}{v_d} \right)^{\delta} \right)^{-\frac{1}{2}} \tag{10}$$

Thus, the fixed δ in the ID model results in a constant distance headway between vehicles at equilibrium regardless of the traffic conditions. In contrast, in the proposed model the distance headway is based on the PCI. The distance headway at equilibrium is obtained by substituting (3), (4), and (5) in (10) which gives

$$s_e = (J + Tv) \left(1 - \left(\frac{v}{v_d} \right)^{(-0.0169PCI + 4.068)} \right)^{-\frac{1}{2}} (v_d = 9.72 \text{ m/s})$$
 (11)

$$s_e = (J + Tv) \left(1 - \left(\frac{v}{v_d} \right)^{(-0.0265PCI + 5.037)} \right)^{-\frac{1}{2}} (v_d = 12.50 \text{ m/s})$$
 (12)

$$s_e = (J + Tv) \left(1 - \left(\frac{v}{v_d} \right)^{(-0.0251PCI + 5.209)} \right)^{-\frac{1}{2}} (v_d = 15.27 \text{ m/s})$$
 (13)

The product of density and speed is traffic flow [8,30] so that

$$F = \frac{v}{s_e} \tag{14}$$

and substituting (10) in (14) gives the flow for the ID model as

$$F = \frac{v}{(J + Tv) \left(1 - \left(\frac{v}{v_d}\right)^{\delta}\right)^{-\frac{1}{2}}}$$
(15)

This is unrealistic as it relies on a fixed exponent. The proposed model considers the PCI to determine traffic flow and so is more realistic. The traffic flow can be expressed as

$$F = \frac{v}{(J + Tv) \left(1 - \left(\frac{v}{v_d}\right)^{(-0.0169PCI + 4.068)}\right)^{-\frac{1}{2}}} (v_d = 9.72 \text{ m/s})$$
(16)

$$F = \frac{v}{(J+Tv)\left(1-\left(\frac{v}{v_d}\right)^{(-0.0265PCI+5.037)}\right)^{-\frac{1}{2}}} (v_d = 12.50 \text{ m/s})$$
(17)

$$F = \frac{v}{(J+Tv)\left(1-\left(\frac{v}{v_d}\right)^{(-0.0251PCI+5.209)}\right)^{-\frac{1}{2}}} (v_d = 15.27 \text{ m/s})$$
(18)

The proposed model indicates that when the road condition is poor, the vehicle vibrations are large and the flow is small, whereas when the road condition is excellent, the vehicle vibrations are small and the flow is large. Further, the proposed model can predict traffic behavior in real-time to help ACC systems better anticipate and adapt to changes in traffic conditions. An ACC system guided by the proposed model can adjust the vehicle speed and following distance in response to the observed traffic density. When the density is high, the ACC can reduce the speed and maintain a safe distance to ensure safety and a smooth traffic flow. Conversely, when the density is low, the ACC can increase the speed while maintaining a safe distance to improve efficiency.

3. Stability Analysis

This section presents an analysis of the stability of traffic models considering an infinitely long road. Identical vehicles are assumed with a constant equilibrium distance headway [31]. Therefore, drivers adjust to forward conditions with minimal acceleration, so there are only small changes in the equilibrium velocity v_e associated with s_e . The corresponding change in distance headway, denoted by a, is also small as is the change in velocity denoted by b. The distance headway can then be expressed as

$$s = s_e + a, \tag{19}$$

and

$$v = v_e(s_e) + b. (20)$$

The temporal change in velocity during traffic alignment over the distance headway is [32]

$$a(t) = \frac{da}{dt} = b_l - b_F,\tag{21}$$

where the subscripts F and l denote the following and leading vehicles, respectively. Given the minor variations in $v_e(s_e)$, the adjustments in headway are negligible. Consequently, b(t) during alignment can be expressed as [31]

$$b(t) = \frac{db}{dt} = f_s a_F + (f_v + f_{\Delta v}) b_F - f_{\Delta v} b_l, \tag{22}$$

where f_v , $f_{\Delta v}$, and f_s denote the partial derivatives w.r.t. velocity, change in velocity, and distance headway, respectively, which are

$$f_v = \frac{\partial f}{\partial v}$$
, $f_{\Delta v} = \frac{\partial f}{\partial \Delta v}$ and $f_s = \frac{\partial f}{\partial s}$.

Using Fourier-Ansatz to express (21) and (22) gives

$$a(t) = \hat{a}e^{\gamma t + ik},\tag{23}$$

$$b(t) = \hat{b}e^{\gamma t + ik},\tag{24}$$

so (23) and (24) can be written as

$$\begin{pmatrix} a(t) \\ b(t) \end{pmatrix} = \begin{pmatrix} \hat{a} \\ \hat{b} \end{pmatrix} e^{\gamma t + ik},$$
 (25)

where $\gamma = \alpha + i\omega$ corresponds to the traffic oscillations during alignment and $i = \sqrt{-1}$. The real part α corresponds to the amplitude change and $\omega = \frac{2\pi}{T}$ is the oscillation frequency with oscillation period T. The parameter k denotes driver delay [31], while \hat{a} and \hat{b} are the changes in velocity and distance headway, respectively.

Substituting (25) in (21) and (22), gives

$$a(t) = b - be^{ik}, (26)$$

$$b(t) = f_s a e^{ik} + (f_v + f_{\Delta v}) b e^{ik} - f_{\Delta v} b.$$
(27)

Model stability requires that the real components of the eigenvalues are negative. The eigenvalues are the solution of

$$\left| j - \begin{pmatrix} \lambda & 0 \\ 0 & \lambda \end{pmatrix} \right| = 0. \tag{28}$$

The Jacobian matrix is

$$j = \begin{pmatrix} j_{11} & j_{12} \\ j_{21} & j_{22} \end{pmatrix},$$

where j_{11} and j_{21} are the gradients of (26) and (27) w.r.t. a and j_{12} and j_{22} are the gradients of (26) and (27) w.r.t. b. We have

$$j = e^{ik} \begin{pmatrix} 0 & e^{-ik} - 1 \\ f_s & (f_v + f_{\Delta v}) - f_{\Delta v} e^{-ik} \end{pmatrix}.$$
 (29)

and substituting this in (28) gives

$$\begin{vmatrix} \lambda & 1 - e^{-ik} \\ -f_s & \lambda - f_v - f_{\Delta v} + f_{\Delta v} e^{-ik} \end{vmatrix} = 0, \tag{30}$$

so that

$$\lambda^2 + \left(-f_v - f_{\Delta v} + f_{\Delta v}e^{-ik}\right)\lambda + f_s\left(1 - e^{-ik}\right) = 0.$$
(31)

Setting
$$M(k) = -f_v - f_{\Delta v} + f_{\Delta v}e^{-ik}$$
 and $N(k) = f_s \left(1 - e^{-ik}\right)$, (24) becomes
$$\lambda^2 + M(k)\lambda + N(k) = 0. \tag{32}$$

Thus, the eigenvalues from (32) are

$$\lambda_{1,2} = -\frac{M(k)}{2} \left(1 \pm \sqrt{1 - \frac{4N(k)}{M^2(k)}} \right),\tag{33}$$

A model is string stable [31] if the real components of the eigenvalues are negative. Under this condition, traffic oscillations diminish over time and the flow becomes stable and smooth [33]. Conversely, a model is considered unstable if traffic oscillations increase and are large as in congestion. In this case, acceleration is high unlike when there is string stability [29]. As the model becomes unstable, $k \to 0$, leading to minimal delay between flow changes (traffic waves) [31].

Approximating M(k) and N(k) using Taylor series for a small delay, i.e., $k \to 0$, gives

$$M(k) = -f_v - if_{\Delta v}k,\tag{34}$$

$$N(k) = if_s k + \frac{f_s}{2}k^2. (35)$$

From [31], at equilibrium

$$f_s = -v_e'(s_e)f_v. (36)$$

where $v'_e(s_e)$ is the equilibrium speed gradient relative to the distance headway. Then, (35) becomes

$$N(k) = -iv'_{e}(s_{e})f_{v} - \frac{v'_{e}(s_{e})}{2}f_{v}.$$
(37)

Let

$$M(k) = x_1 + x_2 k,$$

$$N(k) = y_1 k + y_2 k^2,$$
(38)

where

$$x_{1} = -f_{v},$$

$$x_{2} = -if_{\Delta v},$$

$$y_{1} = -iv'_{e}(s_{e})f_{v} = iv'_{e}(s_{e})x_{1},$$

$$y_{2} = -\frac{v'_{e}(s_{e})}{2}f_{v} = \frac{v'_{e}(s_{e})}{2}x_{1}.$$
(39)

Considering a Taylor series expansion, the square root in (33) can be approximated as

$$\sqrt{1 - \frac{4N(k)}{M^2(k)}} = 1 - \frac{2N(k)}{M^2(k)} - \frac{2N^2(k)}{M^4(k)},\tag{40}$$

which gives

$$\lambda_2 = \frac{-N(k)M^2(k) - N^2(k)}{M^3(k)}. (41)$$

Using (38)

$$\lambda_2 = -\frac{y_1}{x_1}k + \left(\frac{y_1x_2}{x_1^2} - \frac{y_2}{x_1} - \frac{y_1^2}{x_1^3}\right)k^2,\tag{42}$$

and then from (39), we obtain

$$\lambda_2 = -iv_e'(s_e)k + \frac{v_e'(s_e)}{f_v} \left[\frac{-2f_{\Delta v} - f_v}{2} - v_e'(s_e) \right] k^2.$$
 (43)

The real part of (43) represents the rate at which the traffic oscillation amplitude changes, signifying growth or decay. When this real part is negative, the traffic flow is string-stable, since

$$v'_e(s_e) \ge 0 \text{ and } f_v < 0.$$
 (44)

Then, $\left[\frac{-2f_{\Delta v}-f_v}{2}-v_e'(s_e)\right]$ is the string stability criterion [27] which can be expressed as

$$v_e'(s_e) \le -\frac{f_v}{2} - f_{\Delta v}. \tag{45}$$

From (44) and (45), the product of $\left[-\frac{2f_{\Delta v}-f_v}{2}-v_e'(s_e)\right]$ and $\frac{v_e'(s_e)}{f_v}$ indicates that λ_2 has a negative real part. Further, at equilibrium

$$f_v = a \left(-\frac{\delta v_e(s_e)^{\delta - 1}}{v_d^{\delta}} - \frac{2T(J + v_e(s_e)T)}{s_e^2} \right), \tag{46}$$

$$f_{\Delta v} = -\frac{v_e(s_e)}{s_e} \sqrt{\frac{a}{d}} \left(\frac{J + v_e(s_e)T}{s_e} \right). \tag{47}$$

Using (46) and (47), the criterion for string stability from (44) is

$$v_e'(s_e) \le \frac{a\left(\delta(s_e)^2 v_e(s_e)^{\delta-1} + 2TJv_d^{\delta} + 2v_e(s_e)T^2 v_d^{\delta}\right)}{2(s_e)^2 v_d^{\delta}} + \frac{v_e(s_e)\sqrt{ad}(s_e + Tv_e(s_e))}{(s_e)^2 d}$$
(48)

Thus, the velocity with the ID model is determined by δ . A higher value improves stability but may lead to optimistic performance in congestion. Consequently, increasing δ for stability reasons ignores traffic physics and can produce unrealistic results [5]. Changes in velocity during traffic alignment are influenced by driver response and thus pavement condition. Hence, more realistic behavior is obtained using (3), (4), and (5) for δ according to the speed. The stability criteria for the proposed model with speeds 9.72 m/s, 12.50 m/s, and 15.27 m/s are then

$$v'_{e}(s_{e}) \leq \frac{a \left((-0.0169PCI + 4.068)(s_{e})^{2}v_{e}(s_{e})^{(-0.0169PCI + 4.068) - 1} + 2TJv_{d}^{(-0.0169PCI + 4.068)} + \right)}{2v_{e}(s_{e})T^{2}v_{d}^{(-0.0169PCI + 4.068)}} + \frac{2v_{e}(s_{e})T^{2}v_{d}^{(-0.0169PCI + 4.0679)}}{2(s_{e})^{2}v_{d}^{(-0.0169PCI + 4.0679)}} + \frac{v_{e}(s_{e})\sqrt{ad}(s_{e} + Tv_{e}(s_{e}))}{(s_{e})^{2}d}$$

$$(49)$$

$$v_{e}'(s_{e}) \leq \frac{a \left((-0.0265PCI + 5.037)(s_{e})^{2} v_{e}(s_{e})^{(-0.0265PCI + 5.037) - 1} + 2TJ v_{d}^{(-0.0265PCI + 5.037)} + \right)}{2v_{e}(s_{e}) T^{2} v_{d}^{(-0.0265PCI + 5.037)}} + \frac{2v_{e}(s_{e}) T^{2} v_{d}^{(-0.0265PCI + 5.037)}}{2(s_{e})^{2} v_{d}^{(-0.0265PCI + 5.037)}} + \frac{v_{e}(s_{e}) \sqrt{ad}(s_{e} + Tv_{e}(s_{e}))}{(s_{e})^{2} d}$$

$$(50)$$

$$v'_{e}(s_{e}) \leq \frac{a \left((-0.0251PCI + 5.209)(s_{e})^{2}v_{e}(s_{e})^{(-0.0251PCI + 5.209) - 1} + 2TJv_{d}^{(-0.0251PCI + 5.209)} + \right)}{2v_{e}(s_{e})T^{2}v_{d}^{(-0.0251PCI + 5.209)}} + \frac{2v_{e}(s_{e})T^{2}v_{d}^{(-0.0251PCI + 5.209)}}{2(s_{e})^{2}v_{d}^{\delta}} + \frac{v_{e}(s_{e})\sqrt{ad}(s_{e} + Tv_{e}(s_{e}))}{(s_{e})^{2}d}$$

$$(51)$$

respectively. When the pavement is in good condition, vehicles can more easily adjust to changes in traffic ensuring string stability. Conversely, pavement in poor condition results in greater adjustments to changes in traffic which may not result in a smooth flow.

4. The Euler Technique

The Euler technique is used to evaluate the proposed and ID models. It is a simple but effective method to solve systems of differential equations and is widely used in traffic simulators such as SUMO [34] and AIMSUN [35]. This technique divides time into discrete steps and the vehicle position, speed, and acceleration are approximated using the model at each time step. The change in distance w.r.t. time results in a change in speed given by

$$\frac{ds}{dt} = v, (52)$$

and temporal changes in speed lead to changes in acceleration. Denote the right-hand side of (1), (6), (7), and (8) by Y, then

$$\frac{dv}{dt} = Y. (53)$$

For the Euler technique, the position and speed for the ID and proposed models is

$$s_f^{x+1} = s_f^x + \Delta t \times v_f^x \tag{54}$$

$$v_f^{x+1} = v_f^x + \Delta t \times Y_f^x \tag{55}$$

where x is the current time step and x + 1 is the next time step. s_f^x , v_f^x , and Y_f^x are the position, speed, and acceleration, respectively, of the following vehicle in the xth time interval where

$$t = x\Delta t \tag{56}$$

and Δt is the duration of a time step.

5. Performance Evaluation

In this section, the performance of the proposed model and ID models is evaluated on a circular road of length 3000 m. The Euler scheme is employed with time step $\Delta t = 0.50$ s. The proposed model is simulated for 400 s and the ID model for 150 s. Based on (3), (4), and (5) the desired speed v_d for the proposed model is set to 9.72 m/s, 12.50 m/s, and 15.27 m/s. The desired speed for the ID model is 20 m/s [22]. The jam spacing is set to 2.0 m [31], the maximum acceleration is 0.73 m/s², and the minimum acceleration is 1.67 m/s² [20]. The acceleration exponent δ is typically 1 or greater and is often set to 4 [20]. Thus, here $\delta = 1$, 4 and 20. The PCI values considered are PCI = 0, 50 and 100. The maximum normalized density is set to 1/J = 0.50 and the critical density is 0.25 [36]. The maximum flow is obtained at the critical density with speed v_d . Thus, the speed is normalized by v_d and the flow is normalized by $0.25 \times v_d$. The simulation parameters are summarized in Table 1.

Table 1. Simulation Parameters.

Parameter	Values
Desired speed for the proposed model, v_d	9.72 m/s, 12.50 m/s and 15.27 m/s
Desired speed for the $\overline{\text{ID}}$ model, v_d	$20 \mathrm{m/s}$
Time headway for ID and proposed models, T	2.0 s
Critical density	0.25
Jam spacing, J	2.0 m
Maximum density	1/J = 0.50
Maximum acceleration, a	0.73 m/s^2
Vehicle length, <i>L</i>	5.0 m
Acceleration exponent for the ID model, δ	1, 4 and 20
Pavement Condition Index, PCI	0, 50 and 100
Minimum acceleration, d	1.67 m/s^2
Time step, Δt	$0.50 \mathrm{\ s}$

Figure 3 gives the normalized flow for the proposed model with $v_d=9.72$ and PCI=0, 50, and 100. When PCI=0, the flow at 19.0 s is 0.0010. It is 0.0021 at 106.5 s, increasing to 0.0032 at 293.0 s and 0.0035 at 400 s. When PCI=50, the flow at 19.5 s is 0.0010. It is 0.0020 at 162.5 s, increasing to 0.0031 at 288.0 s and 0.0038 at 400 s. When PCI=100, the flow at 21.5 s is 0.0010. It is 0.0025 at 172.0 s, increasing to 0.0033 at 285.5 s and 0.0044 at 400 s.

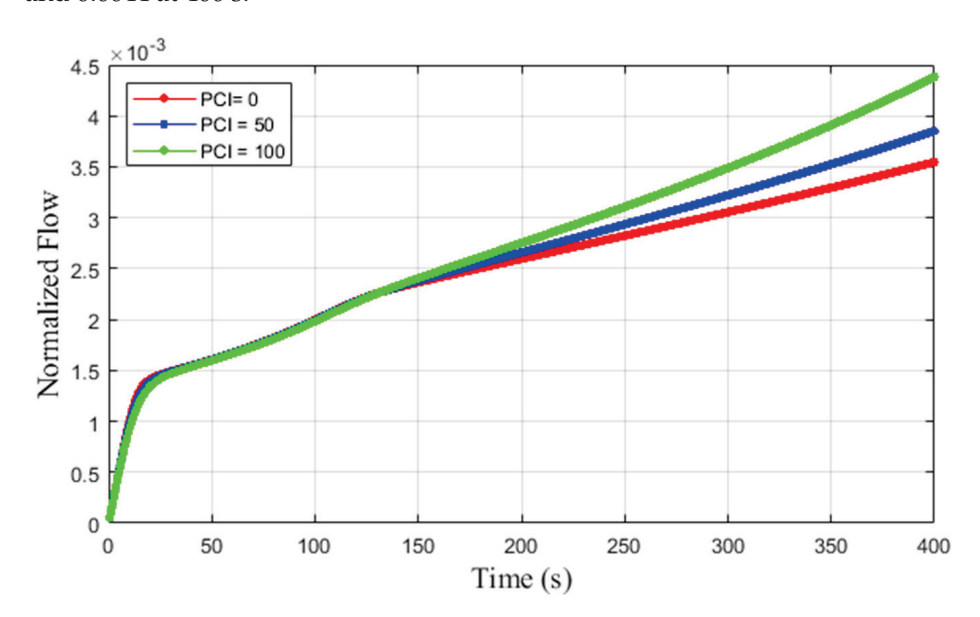


Figure 3. Normalized flow for the proposed model with $v_d = 9.72$ m/s over a 3000 m circular road.

Figure 4 gives the normalized flow for the proposed model with $v_d=12.50~\rm m/s$ and PCI=0, 50, and 100. When PCI=0, the flow at 20.0 s is 0.0012. It is 0.0029 at 156.0 s, increasing to 0.0042 at 268.5 s and 0.0054 at 400 s. When PCI=50, the flow at 22.5 s is 0.0013. It is 0.0033 at 167.0 s, increasing to 0.0045 at 276.0 s and 0.0063 at 400 s. When PCI=100, the flow at 23.5 s is 0.0010. It is 0.0037 at 179.0 s, increasing to 0.0062 at 313.5 s and 0.0110 at 400 s.

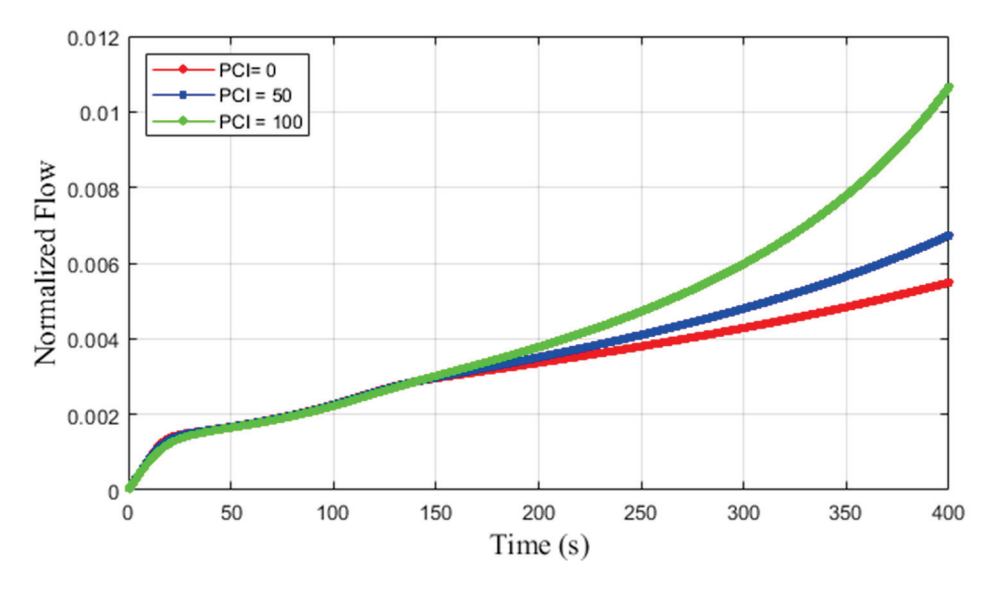


Figure 4. Normalized flow for the proposed model with $v_d = 12.50$ m/s over a 3000 m circular road.

Figure 5 gives the normalized flow for the proposed model with $v_d = 15.27$ m/s and PCI = 0, 50, and 100. When PCI = 0, the flow at 22.0 s is 0.0013. It is 0.0050 at 217.5 s, increasing to 0.0079 at 307.5 s and 0.0140 at 400 s. When PCI = 50, the flow at 25.0 s is

0.0013. It is 0.0052 at 220.5 s, increasing to 0.0110 at 324.0 s and 0.0270 at 400 s. When PCI = 100, the flow at 27.5 s is 0.0010, increasing to 0.0070 at 234.5 s and 0.0770 at 400 s.

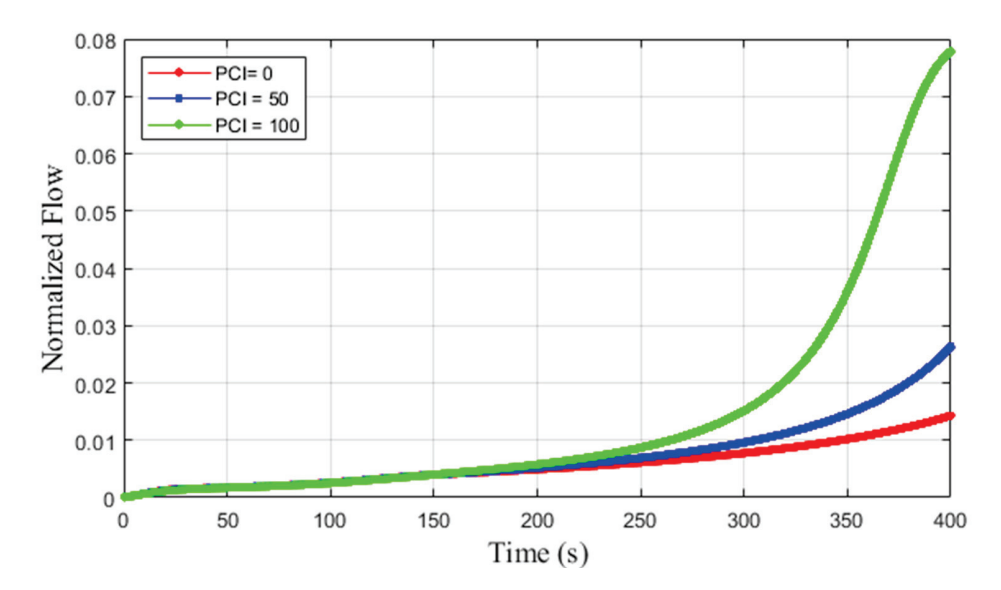


Figure 5. Normalized flow for the proposed model with $v_d = 15.27$ m/s over a 3000 m circular road.

Figure 6 gives the normalized flow for the ID model with $\delta=1$, 4, and 20 and $v_d=20$ m/s. When $\delta=1$, the flow at 31.5 s is 0.0013, increasing to 0.0024 at 94.0 s and 0.0063 at 150 s. When $\delta=4$, the flow at 33.0 s is 0.0017. It is 0.0020 at 80.0 s, increasing to 0.0039 at 116.0 s and 0.0088 at 150 s. When $\delta=20$, at 28.0 s the flow is 0.0012. It is 0.0032 at 100.5 s, increasing to 0.0060 at 130.0 s and 0.0095 at 150 s.

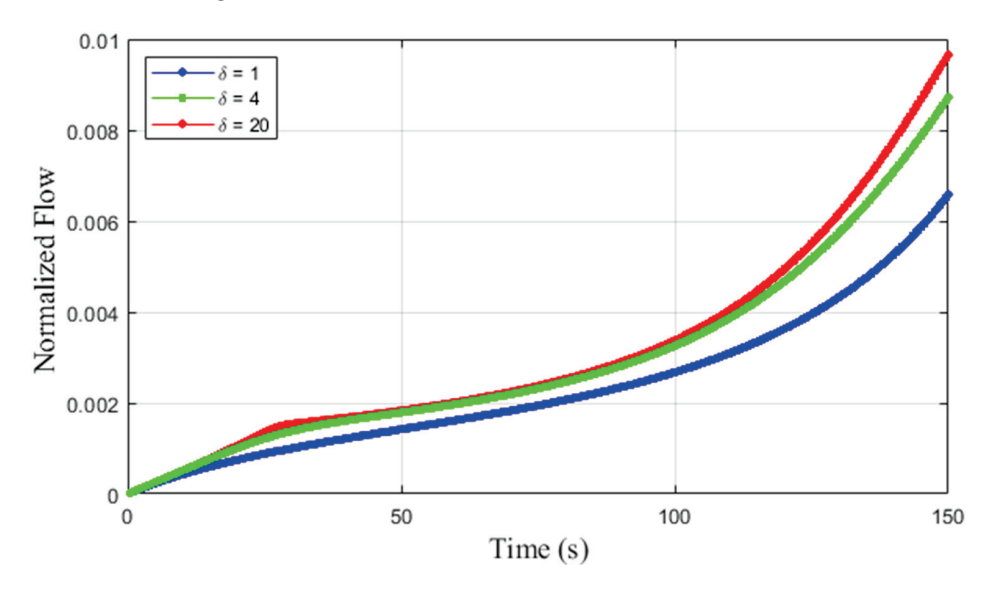


Figure 6. Normalized flow for the ID model with $\delta = 1$, 4, and 20 over a 3000 m circular road.

Figure 7 gives the normalized speed with $v_d = 9.72$ m/s and PCI = 0, 50 and 100 for the proposed model. When PCI = 0, the speed is 0.39 from 0.5 s to 15.0 s, decreasing to 0.23 at 15.5 s, and then increasing to 0.46 at 20.0 s. The speed oscillates between 0.16 and 0.64 from 236.5 s to 399.0 s as indicated in Figure 7a. The speed when PCI = 50 is similar to that when PCI = 0. It is 0.39 from 0.5 s to 15.0 s, decreasing to 0.23 at 15.5 s, and then increasing to 0.46 at 21.0 s. The speed oscillates between 0.21 and 0.58 from 263.0 s to 399.5 s as indicated in Figure 7b. When PCI = 100, the speed is 0.40 from 0.5 s to 15.0 s, decreasing to 0.23 at 15.5 s, and then increasing to 0.46 at 19.5 s. The speed oscillates between 0.32 and 0.48 from 315.0 s to 399.0 s as indicated in Figure 7c. For all PCI values, there are road

segments where the speed is constant such as between -1947.8 m and -426.7 m at 397.5 s when PCI=0, between -1932.3 m and -228.4 m at 392.0 s when PCI=50, and between -1962.4 m and -428.1 m at 393.5 s when PCI=100.

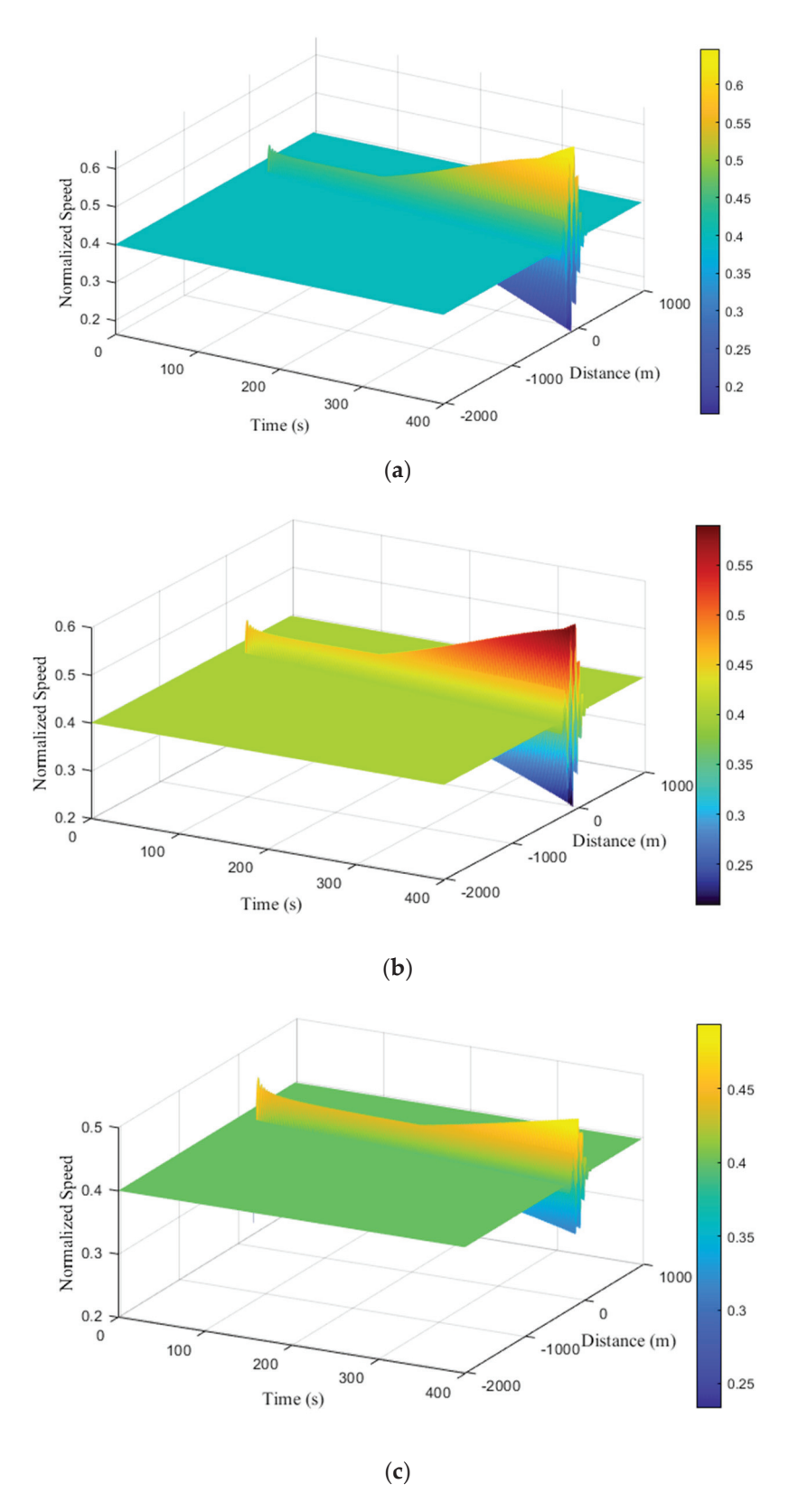


Figure 7. Normalized speed for the proposed model with $v_d = 9.72$ m/s over a 3000 m circular road: (a) PCI = 0; (b) PCI = 50; (c) PCI = 100.

Figure 8 gives the normalized speed with $v_d=12.50~\rm m/s$ and PCI=0, 50, and 100 for the proposed model. When PCI=0, the speed from 0.5 s to 15.0 s is 0.15, decreasing to 0.09 at 15.5 s, and then increasing to 0.18 at 19.5 s. The speed oscillates between 0.06 and 0.27 from 255.0 s to 399.0 s as indicated in Figure 8a. Similarly, when PCI=50 the speed is 0.15 from 0.5 s to 15.0 s, decreasing to 0.09 at 15.5 s, and then increasing to 0.18 at 20.5 s. The speed oscillates between 0.06 and 0.26 from 258.0 s to 399.0 s as indicated in Figure 8b. The speed is also similar when PCI=100. It is 0.15 from 0.5 s to 15.0 s, decreasing to 0.09 at 15.5 s and then increasing to 0.18 at 19.5 s. The speed oscillates between 0.09 and 0.22 from 294.5 s to 399.5 s as indicated in Figure 8c. For all PCI values, there are road segments where the speed is constant such as between $-2022.5~\rm m$ and $-237.5~\rm m$ at 397.0 s when PCI=0, between $-1922.7~\rm m$ and $-245.5~\rm m$ at 395.0 s when PCI=50, and between $-1953.75~\rm m$ and $-230.0~\rm m$ at 390.0 s when PCI=100.

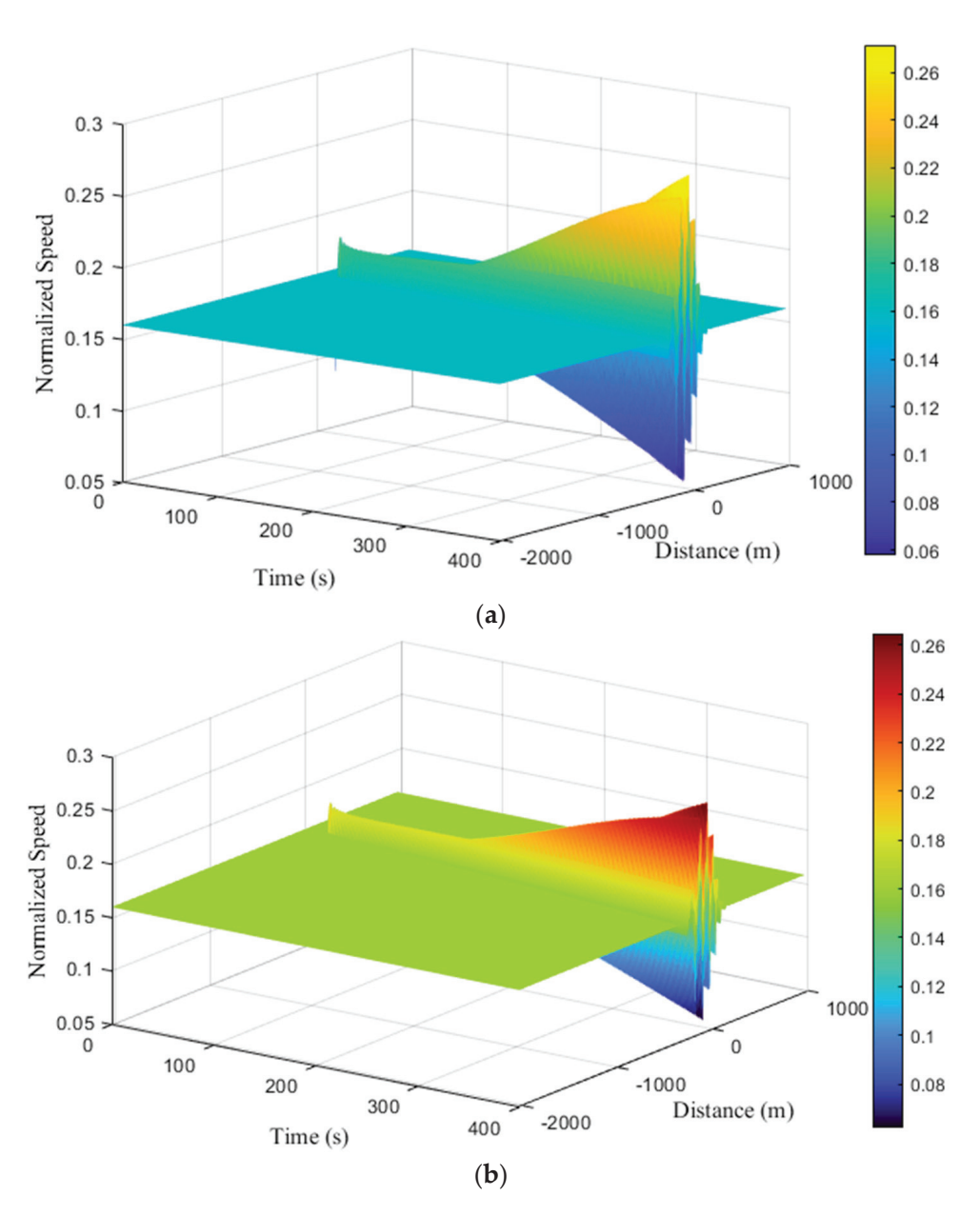


Figure 8. Cont.

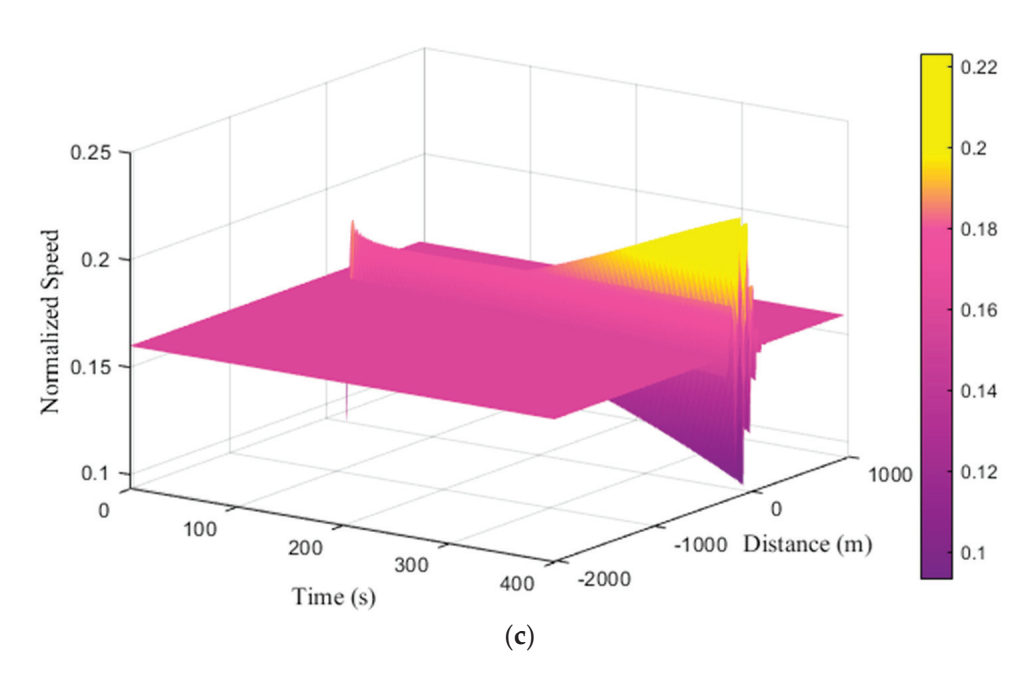


Figure 8. Normalized speed for the proposed model with $v_d = 12.50$ m/s over a 3000 m circular road: (a) PCI = 0; (b) PCI = 50; (c) PCI = 100.

Figure 9 gives the normalized speed with $v_d=15.27~\rm m/s$ and PCI=0, 50, and 100 for the proposed model. When PCI=0, the speed from 0.5 s to 15.0 s is 0.11, decreasing to 0.06 at 15.5 s, and then increasing to 0.13 at 19.5 s. The speed oscillates between 0.04 and 0.20 from 241.0 s to 399.0 s as indicated in Figure 9a. The speed behavior is similar when PCI=50. It is 0.11 from 0.5 s to 15.0 s, decreasing to 0.06 at 15.5 s, and then increasing to 0.14 at 20.5 s. The speed oscillates between 0.04 and 0.20 from 267.5 s to 399.0 s as indicated in Figure 9b. Similar speed behavior also occurs when PCI=100. It is 0.11 from 0.5 s to 15.0 s, decreasing to 0.06 at 15.5 s, and then increasing to 0.13 at 20.5 s. The speed oscillates between 0.05 and 0.18 from 278.5 s to 399.5 as indicated in Figure 9c. For all PCI values, there are road segments where the speed is constant such as between $-1945.4~\rm m$ and $-244.3~\rm m$ at 391.0 s when PCI=0, between $-1911.8~\rm m$ and $-239.7~\rm m$ at 388.5 s when PCI=50, and between $-1817.1~\rm m$ and $-371.4~\rm m$ at 384.0 s when PCI=100.

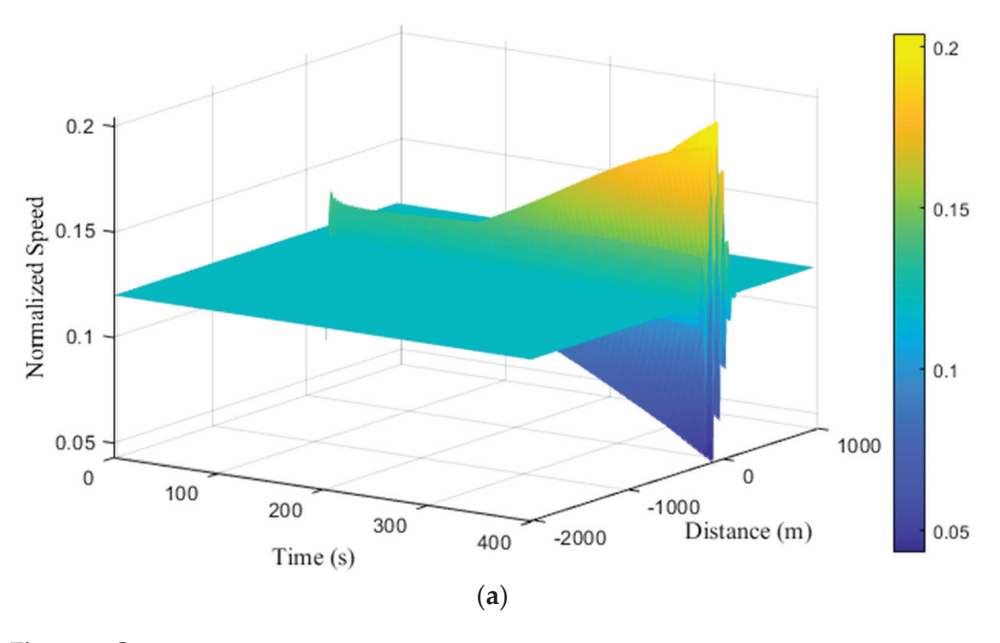


Figure 9. Cont.

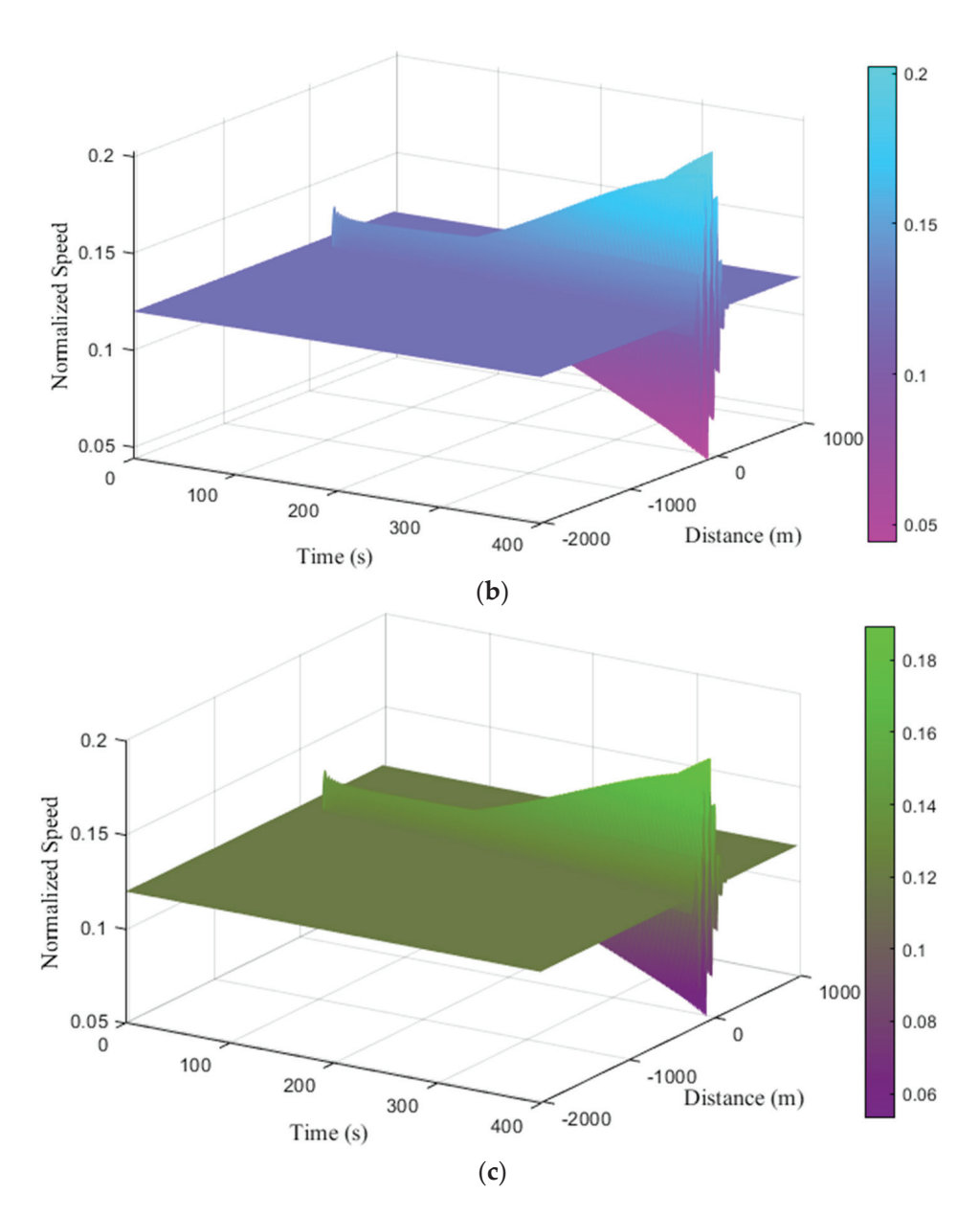


Figure 9. Normalized speed for the proposed model with $v_d = 15.27$ m/s over a 3000 m circular road: (a) PCI = 0; (b) PCI = 50; (c) PCI = 100.

Figure 10 gives the normalized speed for the ID model with $v_d=15.27$ m/s and $\delta=1,4$, and 20. When $\delta=1$, the speed is 0.10 until 15.0 s. It is 0.05 at 15.5 s and then increases to 0.11 at 21.0 s. The speed oscillates between 0.09 and 0.10 from 118.0 s to 149.5 s as indicated in Figure 10a. When $\delta=4$, the speed is 0.09 until 15.0 s, decreasing to 0.05 at 15.5 s, and then increasing to 0.11 at 19.5 s. The speed oscillates between 0.08 and 0.11 from 122.5 s to 149.5 s as indicated in Figure 10b. When $\delta=20$, the speed is 0.1 until 15.0 s, decreasing to 0.05 at 15.5 s, and then increasing to 0.11 at 20.5 s. The speed oscillates between 0.08 and 0.11 from 118.5 s to 150.0 s as indicated in Figure 10c. For all the values of δ , there are road segments where the speed is constant such as between -2590.0 m and -322.0 m at 148.0 s when $\delta=1$, between -2498.0 m and -292.0 m at 147.0 s when $\delta=4$, and between -2594.0 m and -374.0 m at 149.0 s when $\delta=20$.

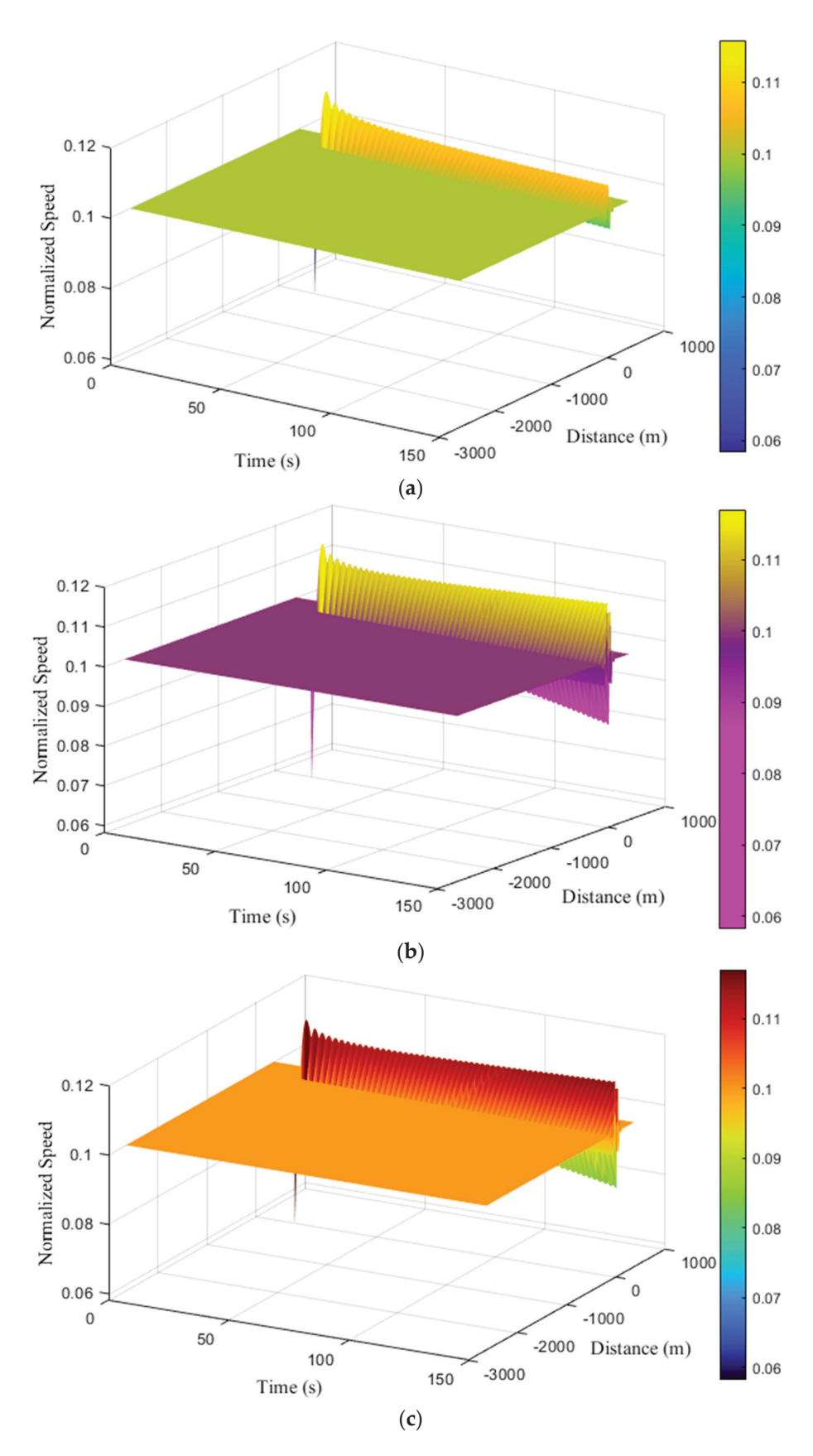


Figure 10. Normalized speed for the ID model over a 3000 m circular road: (a) $\delta = 1$; (b) $\delta = 4$; (c) $\delta = 20$.

Figure 11 gives the normalized density for the proposed model with $v_d=9.72~\rm m/s$ and PCI=0, 50 and 100. When PCI=0, the density is 0.17 until 31.0 s. It is 0.20 at 32.0 s, decreasing to 0.13 at 32.5 s. The density oscillates between 0.13 and 0.21 from 279.5 s to 398.5 s as indicated in Figure 11a. When PCI=50, the density is 0.16 until 31.0 s. It is 0.20 at 32.0 s, decreasing to 0.13 at 33.0 s. The density oscillates between 0.14 and 0.19 from 277.5 s to 399.5 s, and then it varies between 0.16 and 0.23 as indicated in Figure 11b. When PCI=100, the density is 0.16 until 31.0 s. It is 0.20 at 32.0 s, decreasing to 0.13 at 32.5 s. It oscillates between 0.14 and 0.18 from 313.5 s to 398.5 s, and then varies between 0.16 and 0.18 as indicated in Figure 11c.

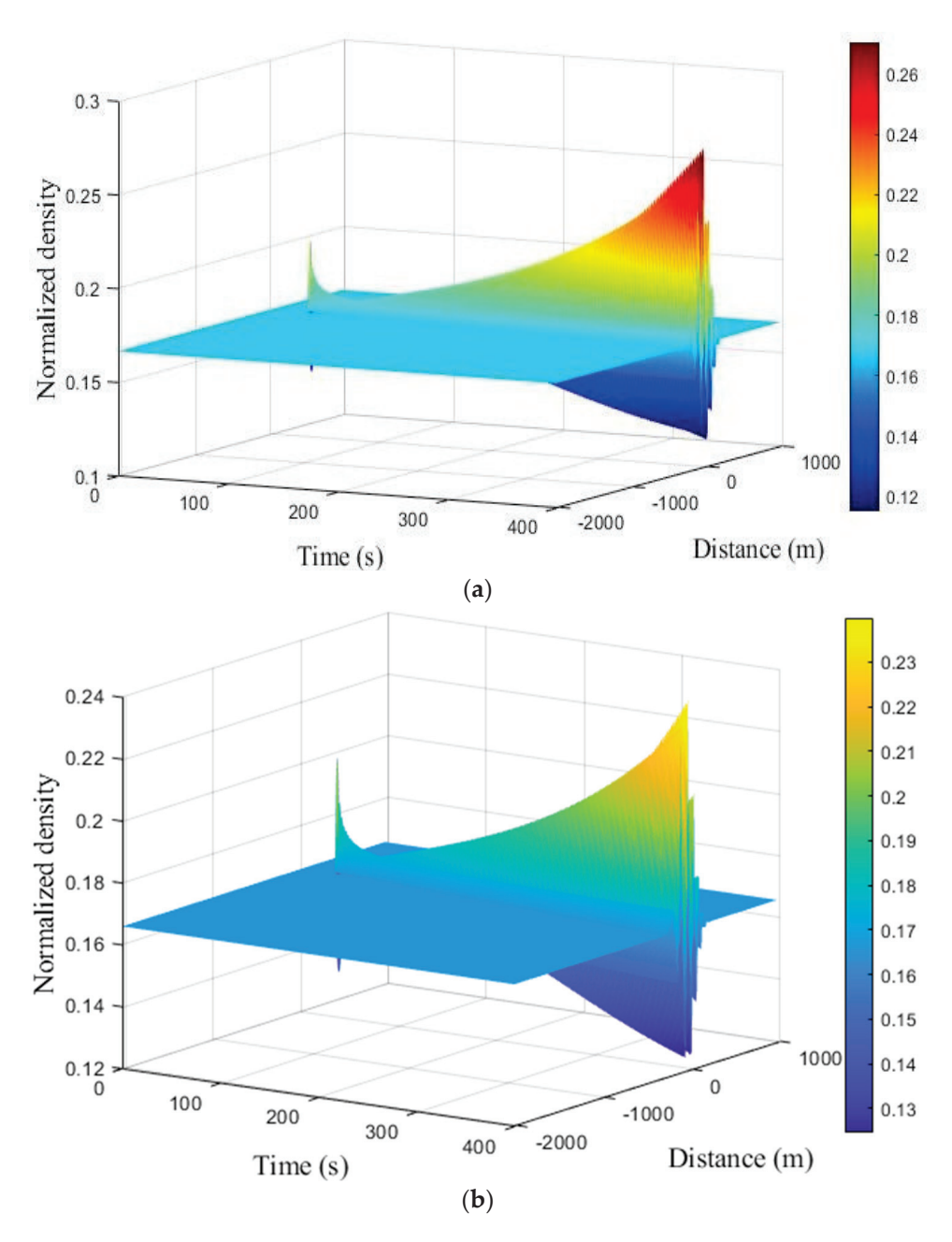


Figure 11. Cont.

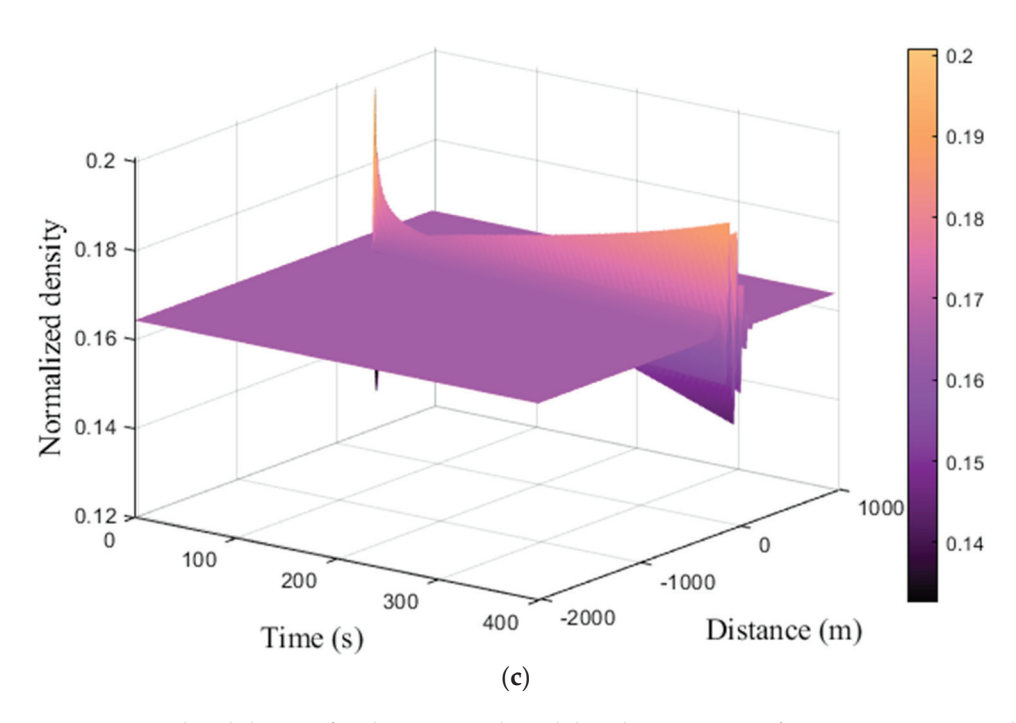


Figure 11. Normalized density for the proposed model with $v_d = 9.72$ m/s over a 3000 m circular road: (a) PCI = 0; (b) PCI = 50; (c) PCI = 100.

Figure 12 gives the normalized density for the proposed model with $v_d=12.50~\rm m/s$ and PCI=0, 50 and 100. When PCI=0, the density is 0.17 until 31.0 s, increasing to 0.20 at 32.0 s and then decreasing to 0.13 at 32.5 s. The density oscillates between 0.13 and 0.21 from 271.5 s to 398.0 s, and then it varies between 0.17 and 0.28 as indicated in Figure 12a. When PCI=50, the density is 0.17 until 31.0 s, increasing to 0.20 at 32.0 s, and then decreasing to 0.13 at 32.5 s. The density oscillates between 0.13 and 0.23 from 269.0 s to 399.0 s, and then it varies between 0.17 and 0.27 as indicated in Figure 12b. When PCI=100, the density is 0.16 until 31.0 s, increasing to 0.20 at 31.5 s, and then decreasing to 0.13 at 32.5 s. From 275.5 s to 398.0 s, the density oscillates between 0.14 and 0.19, and then it varies between 0.16 and 0.21 as indicated in Figure 12c.

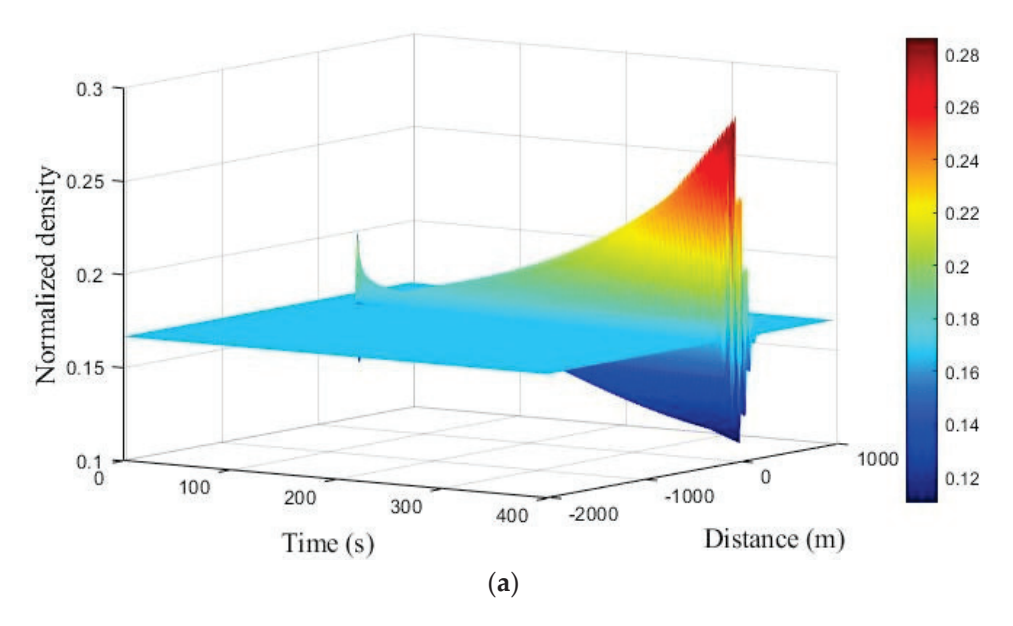


Figure 12. Cont.

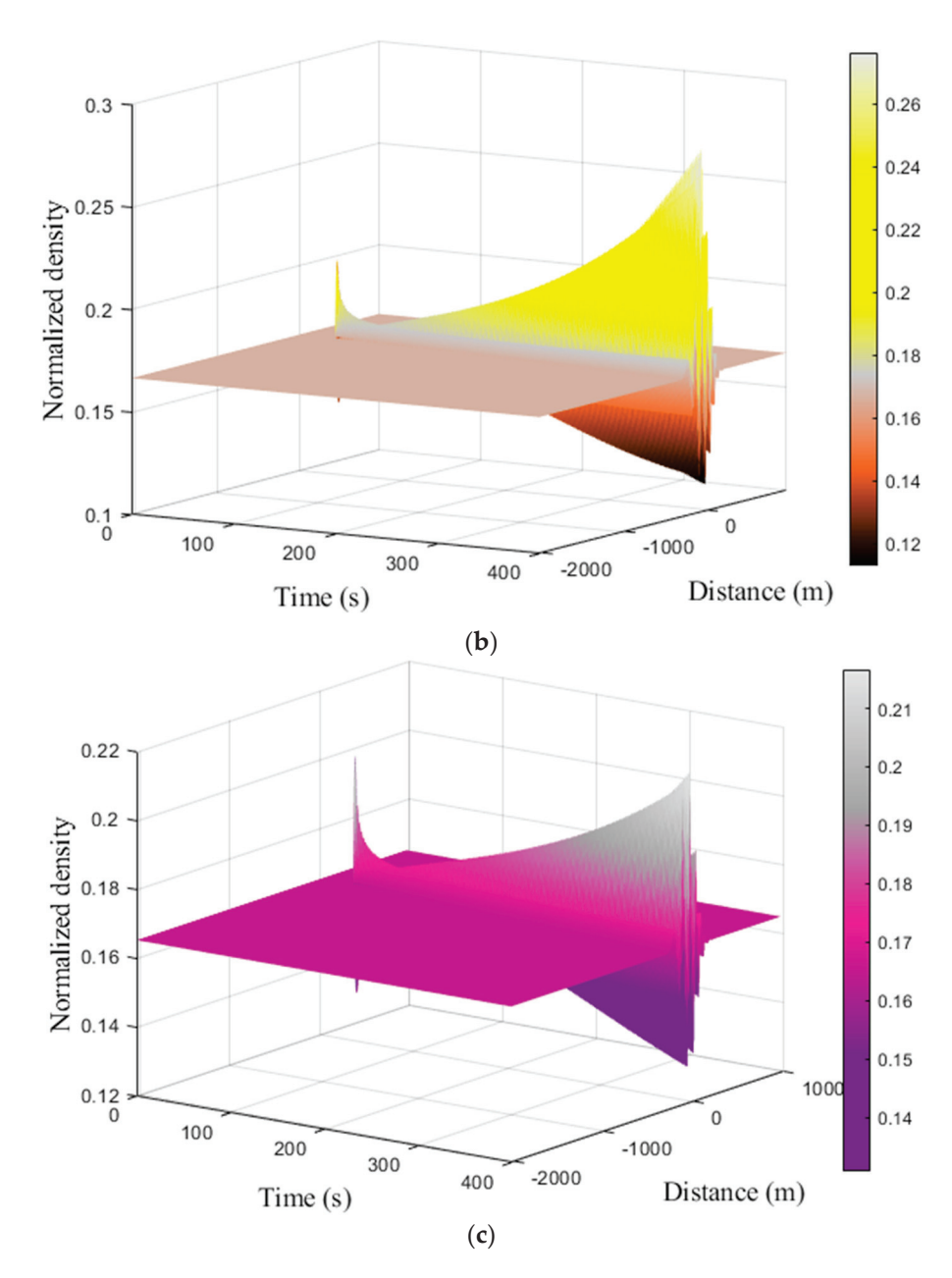


Figure 12. Normalized density for the proposed model with $v_d = 12.50$ m/s over a 3000 m circular road: (a) PCI = 0; (b) PCI = 50; (c) PCI = 100.

Figure 13 gives the normalized density for the proposed model with $v_d=15.27~\rm m/s$ and PCI=0, 50 and 100. When PCI=0, the density is 0.17 until 31.0 s, increasing to 0.20 at 32.0 s, and then decreasing to 0.13 at 33.0 s. The density oscillates between 0.13 and 0.21 from 266.5 s to 398.0 s, and then it varies between 0.17 and 0.28 as indicated in Figure 13a. When PCI=50, the density is at 0.17 until 31.0 s, increasing to 0.20 at 32.0 s, and then decreasing to 0.13 at 33.0 s. The density oscillates between 0.13 and 0.22 from 269.5 s to 398.0 s as indicated in Figure 13b. When PCI=100, the density is 0.16 until 31.0 s, increasing to 0.20 at 32.0 s, and then decreasing to 0.13 at 33.0 s. The density oscillates between 0.13 and 0.20 from 288.5 s to 398.5 s as indicated in Figure 13c.

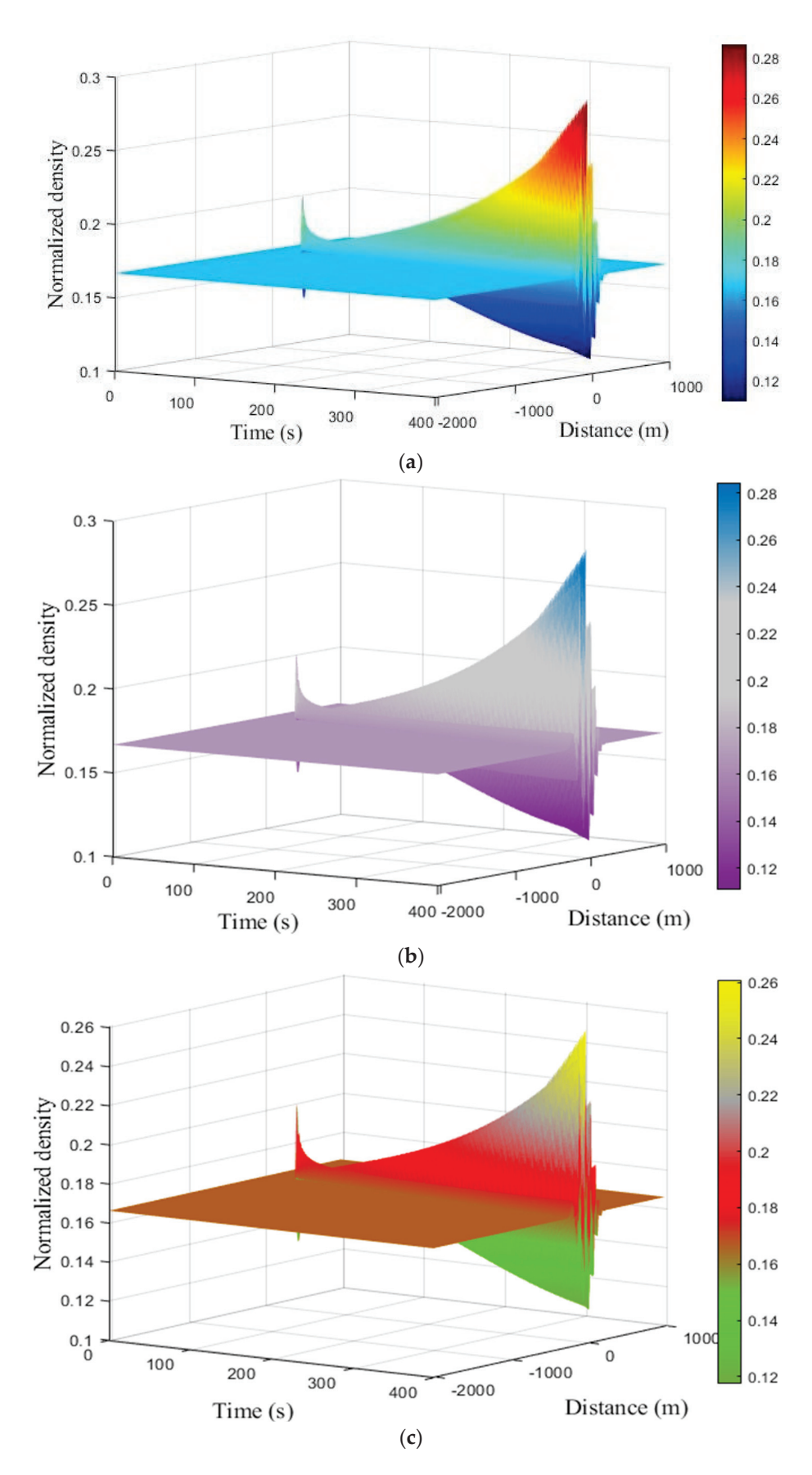


Figure 13. Normalized density for the proposed model with $v_d = 15.27$ m/s over a 3000 m circular road: (a) PCI = 0; (b) PCI = 50; (c) PCI = 100.

Figure 14 gives the normalized density for the ID model with $v_d=15.27$ m/s and $\delta=1,4$, and 20. When $\delta=1$, the density is 0.15 until 31.0 s, increasing to 0.19 at 32.0 s, and then decreasing to 0.12 at 32.5 s. The density oscillates between 0.14 and 0.16 from 123.0 s to 149.0 s, and then it varies between 0.15 and 0.16 as indicated in Figure 14a. When $\delta=4$, the density is 0.16 until 31.0 s, increasing to 0.20 at 32.0 s, and then decreasing to 0.13 at 32.5 s. It oscillates between 0.15 and 0.17 from 102.5 s to 149.0 s as indicated in Figure 14b. When $\delta=20$, the density is 0.16 until 31.0 s, increasing to 0.20 at 32.0 s, and then decreasing to 0.13 at 33.5 s. The density oscillates between 0.15 and 0.17 from 96.5 s to 149.0 s and then it varies between 0.16 and 0.18 as indicated in Figure 14c.

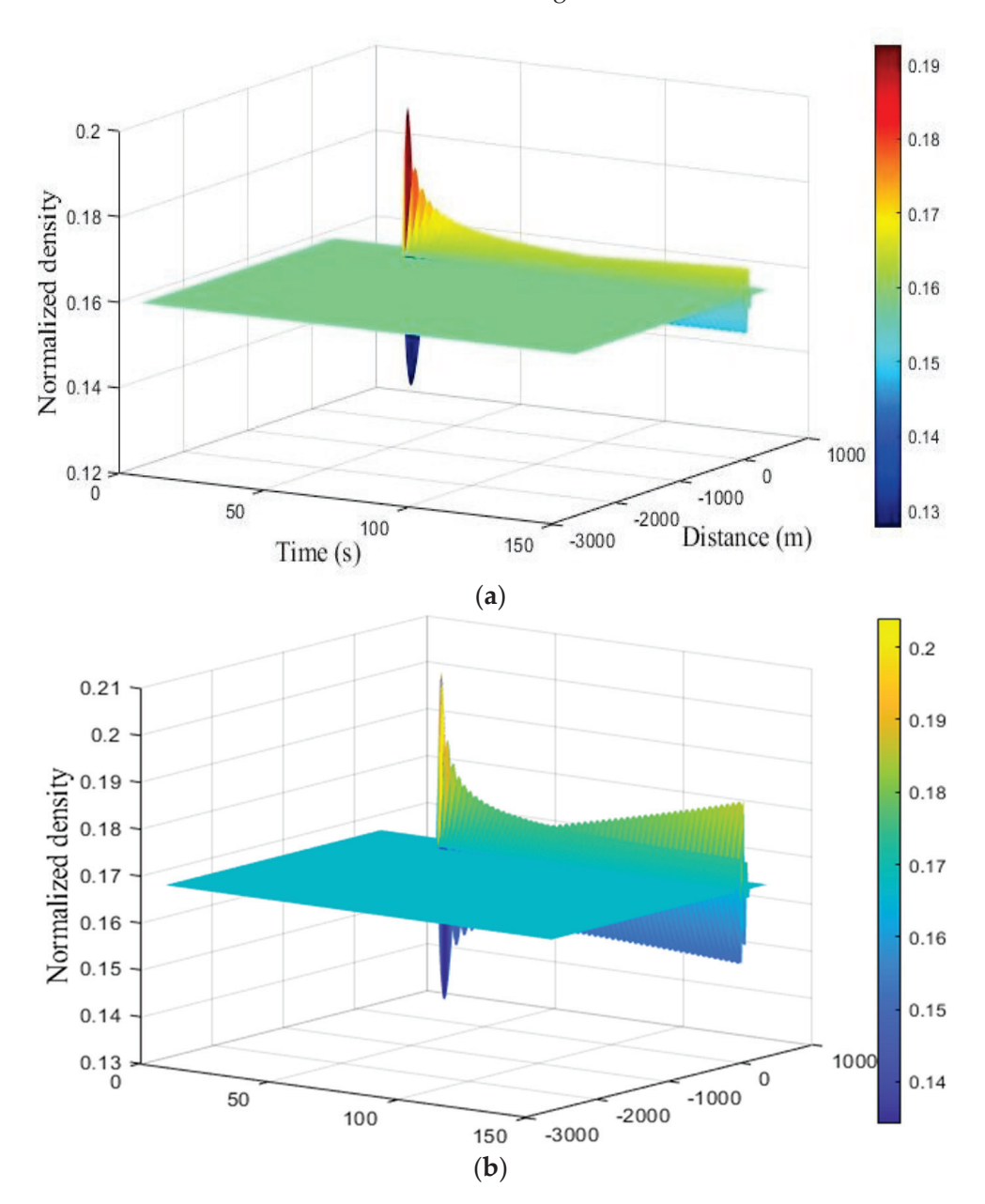


Figure 14. Cont.

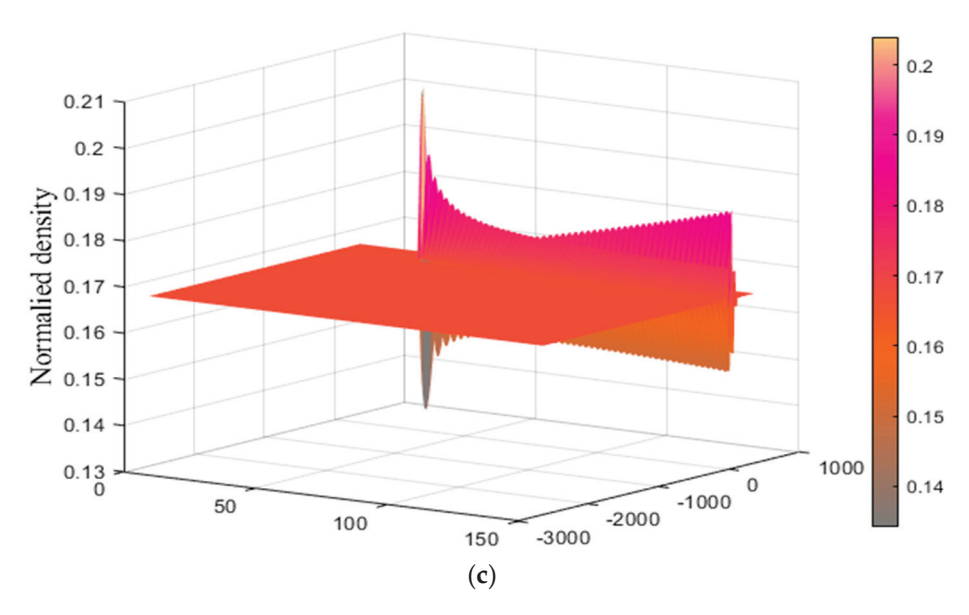


Figure 14. Normalized density behavior for the ID model over a 3000 m circular road: (a) $\delta = 1$; (b) $\delta = 4$; (c) $\delta = 20$.

The results for the proposed model indicate that pavement condition influences traffic flow as expected. In particular, the flow increases with speed as shown in Figures 3–5. The flow with the ID model increases with δ , which is not based on traffic physics. Furthermore, the oscillations in speed and density with the proposed model vary with the PCI and decrease over time as the PCI increases. These results are more realistic as they are based on real parameters such as the PCI. Conversely, the oscillations in speed and density with the ID model are the result of an arbitrary fixed parameter, and they increase over time as δ increases with no justification. This is an inadequate and unrealistic traffic characterization.

6. Conclusions

A microscopic traffic flow model was developed based on pavement condition. The Pavement Condition Index (PCI) was used to characterize traffic behavior. The performance of the proposed model was evaluated and compared with that of the Intelligent Driver (ID) model. The results obtained demonstrate that the proposed model provides realistic traffic flow dynamics. In particular, the traffic flow under excellent pavement conditions (PCI = 100) is high while the flow under poor pavement conditions (PCI = 0) is low, as expected. Conversely, the ID model has a fixed acceleration exponent which does not reflect the relationship between flow and road condition. Furthermore, the oscillations in speed and density with the proposed model vary according to the pavement condition. They are negligible when the PCI is high, which is expected traffic behavior. In contrast, the ID model produces unrealistic speed and density oscillations based on δ . The results given indicate that the proposed model can be used in traffic simulators for realistic and effective traffic prediction.

The proposed model is a deterministic rather than a probabilistic system. Future research can integrate random variables to provide a probabilistic framework. This will allow the model to deal with the uncertainties and variability in complex traffic environments. Furthermore, it can be implemented for road networks to examine challenging traffic situations and propose solutions. Future research can also consider additional parameters. While PCI is a key factor in traffic flow dynamics, it is important to include other factors such as road emergencies to increase the applicability and improve the accuracy and effectiveness in real-world scenarios. This will contribute to the development of more comprehensive and robust models for traffic flow analysis and management.

Author Contributions: Conceptualization, F.A. and Z.H.K.; methodology, F.A.; software, F.A.; validation, F.A., Z.H.K., K.S.K., A.B.A. and T.A.G.; formal analysis, F.A., Z.H.K., K.S.K. and T.A.G.; investigation, F.A., Z.H.K., K.S.K. and T.A.G.; writing—original draft, F.A.; writing—review and editing, F.A., Z.H.K., K.S.K., A.B.A. and T.A.G.; visualization, F.A., Z.H.K., K.S.K., A.B.A. and T.A.G.; funding acquisition, A.B.A., Z.H.K., K.S.K. and T.A.G. All authors have read and agreed to the published version of the manuscript.

Funding: This research was funded by the Scientific Research Deanship at the University of Ha'il, Ha'il, Saudi Arabia through project RG23-186.

Data Availability Statement: No data was generated in this article.

Conflicts of Interest: The authors declare no conflict of interest.

References

- 1. Setyawan, A.; Kusdiantoro, I.; Syafi'i. The effect of pavement condition on vehicle speeds and motor vehicles emissions. *Procedia Eng.* **2015**, *125*, 424–430. [CrossRef]
- 2. Kumar, R.; Suman, S.K.; Prakash, G. Evaluation of pavement condition index using artificial neural network approach. *Transp. Dev. Econ.* **2021**, *7*, 20. [CrossRef]
- Road Traffic Injuries, World Health Organization. Available online: https://www.who.int/news-room/fact-sheets/detail/road-traffic-injuries (accessed on 23 September 2022).
- 4. Accidents Caused by Poor Road Quality and Conditions in DC, Gilman & Bedigian. Available online: https://www.gilmanbedigian.com/accidents-caused-by-poor-road-quality-and-conditions-in-dc/ (accessed on 23 September 2022).
- 5. Ali, F.; Khan, Z.H.; Khan, F.A.; Khattak, K.S.; Gulliver, T.A. A new driver model based on driver response. *Appl. Sci.* **2022**, 12, 5390. [CrossRef]
- 6. Khan, Z.H. Traffic Modelling for Intelligent Transportation Systems. Ph.D. Dissertation, University of Victoria, Victoria, BC, Canada, 2016.
- 7. Henein, C.M.; White, T. Microscopic information processing and communication in crowd dynamics. *Phys. A Stat. Mech. Appl.* **2010**, *389*, 4636–4653. [CrossRef]
- 8. Ali, F.; Khan, Z.H.; Khattak, K.S.; Gulliver, T.A.; Khan, A.N. A microscopic heterogeneous traffic flow model considering distance headway. *Mathematics* **2023**, *11*, 184. [CrossRef]
- 9. Khan, Z.H.; Gulliver, T.A. A macroscopic traffic model based on anticipation. Arab. J. Sci. Eng. 2019, 44, 5151–5163. [CrossRef]
- 10. Gazis, D.C.; Herman, R.; Rothery, R.W. Nonlinear follow-the-leader models of traffic flow. Oper. Res. 1961, 9, 545-567. [CrossRef]
- 11. Newell, G.F. Nonlinear effects in the dynamics of car following. Oper. Res. 1961, 9, 209–229. [CrossRef]
- 12. Wiedemann, R. Simulation des Straßenverkehrsflusses. Ph.D. Dissertation, Instituts für Verkehrswesen, Universität Karlsruhe, Karlsruhe, Germany, 1974.
- 13. Fritzsche, H.T.; Ag, D. A model for traffic simulation. Traffic Eng. Control 1994, 35, 317–321.
- 14. Askari, A.; Farias, D.A.; Kurzhanskiy, A.A.; Varaiya, P. Measuring impact of adaptive and cooperative adaptive cruise control on throughput of signalized intersections. *arXiv* **2017**, arXiv:1611.08973.
- 15. Wiedemann, R. Modelling of RTI-Elements on multi-lane roads. In Proceedings of the DRIVE Conference, Brussels, Belgium, 4–6 February 1991.
- 16. Kovács, T.; Bolla, K.; Gil, R.A.; Fábián, C.; Kovács, L. Parameters of the intelligent driver model in signalized intersections. *Teh. Vjesn.* **2016**, 23, 1469–1474.
- 17. Bando, M.; Hasebe, K.; Nakayama, A.; Shibata, A.; Sugiyama, Y. Dynamical model of traffic congestion and numerical simulation. *Phys. Rev. E* **1995**, *51*, 1035–1042. [CrossRef] [PubMed]
- 18. Helbing, D.; Tilch, B. Generalized force model of traffic dynamics. *Phys. Rev. E* 1998, 58, 133–138. [CrossRef]
- 19. Gipps, P.G. A behavioural car-following model for computer simulation. Transp. Res. Part B 1981, 15, 105–111. [CrossRef]
- 20. Treiber, M.; Hennecke, A.; Helbing, D. Congested traffic states in empirical observations and microscopic simulations. *Phys. Rev. E* **2000**, *62*, 1805–1824. [CrossRef]
- 21. Cao, Z.; Lu, L.; Chen, C.; Chen, X.U. Modeling and simulating urban traffic flow mixed with regular and connected vehicles. *IEEE Access* **2021**, *9*, 10392–10399. [CrossRef]
- 22. Dahui, W.; Ziqiang, W.; Ying, F. Hysteresis phenomena of the intelligent driver model for traffic flow. *Phys. Rev. E* **2007**, *76*, 2–8. [CrossRef] [PubMed]
- 23. Kesting, A.; Treiber, M.; Helbing, D. Enhanced intelligent driver model to access the impact of driving strategies on traffic capacity. *Philos. Trans. R. Soc. Math. Phys. Eng. Sci.* **2010**, *368*, 4585–4605. [CrossRef]
- 24. Schakel, W.J.; Van Arem, B.; Netten, B.D. Effects of cooperative adaptive cruise control on traffic flow stability. In Proceedings of the International IEEE Conference on Intelligent Transportation Systems, Funchal, Portugal, 19–22 September 2010; pp. 759–764.
- 25. Milanés, V.; Shladover, S.E.; Spring, J.; Nowakowski, C.; Kawazoe, H.; Nakamura, M. Cooperative adaptive cruise control in real traffic situations. *IEEE Trans. Intell. Transp. Syst.* **2013**, *15*, 296–305. [CrossRef]

- 26. Wang, M.; Treiber, M.; Daamen, W.; Hoogendoorn, S.P.; van Arem, B. Modelling supported driving as an optimal control cycle: Framework and model characteristics. *Procedia-Soc. Behav. Sci.* **2013**, *80*, 491–511. [CrossRef]
- 27. Derbel, O.; Peter, T.; Zebiri, H.; Mourllion, B.; Basset, M. Modified intelligent driver model for driver safety and traffic stability improvement. *IFAC Proc.* **2013**, *46*, 744–749. [CrossRef]
- 28. Sohail, A.M.; Khattak, K.S.; Iqbal, A.; Khan, Z.H.; Ahmad, A. Cloud-based detection of road bottlenecks using OBD-II telematics. In Proceedings of the International Multitopic Conference, Islamabad, Pakistan, 29–30 November 2019.
- 29. Kessels, F. Traffic Flow Modelling: Introduction to Traffic Flow Theory through a Genealogy of Models; Springer: Cham, Switzerland, 2019.
- 30. Ali, F.; Khan, Z.H.; Khattak, K.S.; Gulliver, T.A. A microscopic traffic flow model characterization for weather conditions. *Appl. Sci.* **2022**, 12, 12981. [CrossRef]
- 31. Treiber, M.; Kesting, A. Traffic Flow Dynamics: Data, Models and Simulation; Springer: Berlin/Heidelberg, Germany, 2013.
- 32. Hallerbach, S.; Xia, Y. Simulation-based identification of critical scenarios for cooperative and automated vehicles. *SAE Int. J. Connect. Autom. Veh.* **2018**, *1*, 93–106. [CrossRef]
- 33. Feng, S.; Zhang, Y.; Li, S.E.; Cao, Z.; Liu, H.X.; Li, L. String stability for vehicular platoon control: Definitions and analysis methods. *Ann. Rev. Control* **2019**, *47*, 81–97. [CrossRef]
- 34. Krajzewicz, D.; Erdmann, J.; Behrisch, M.; Bieker, L. Recent development and applications of SUMO-simulation of urban mobility. *Int. J. Adv. Syst. Meas.* **2012**, *5*, 128–243.
- 35. Casas, J.; Ferrer, J.L.; Garcia, D.; Perarnau, J.; Torday, A. Traffic simulation with Aimsun. In *Fundamentals of Traffic Simulation*; International Series in Operations Research & Management Science, 145; Springer: New York, NY, USA, 2010; pp. 173–232.
- 36. Ahmed, A.; Ngoduy, D.; Adnan, M.; Baig, M.A.U. On the fundamental diagram and driving behavior modeling of heterogeneous traffic flow using UAV-based data. *Transp. Res. Part A Policy Pract.* **2021**, 148, 100–115. [CrossRef]

Disclaimer/Publisher's Note: The statements, opinions and data contained in all publications are solely those of the individual author(s) and contributor(s) and not of MDPI and/or the editor(s). MDPI and/or the editor(s) disclaim responsibility for any injury to people or property resulting from any ideas, methods, instructions or products referred to in the content.





Article

Optimizing Propellant Distribution for Interorbital Transfers

J. De Curtò 1,2,3 and I. De Zarzà 1,3,4,*

- Informatik und Mathematik, GOETHE-University Frankfurt am Main, 60323 Frankfurt am Main, Germany; decurto@em.uni-frankfurt.de
- Escuela Técnica Superior de Ingeniería (ICAI), Universidad Pontificia Comillas, 28015 Madrid, Spain
- 3 Estudis d'Informàtica, Multimèdia i Telecomunicació, Universitat Oberta de Catalunya, 08018 Barcelona, Spain
- Escuela Politècnica Superior, Universidad Francisco de Vitoria, 28223 Pozuelo de Alarcón, Spain
- * Correspondence: dezarza@em.uni-frankfurt.de

Abstract: The advent of space exploration missions, especially those aimed at establishing a sustainable presence on the Moon and beyond, necessitates the development of efficient propulsion and mission planning techniques. This study presents a comprehensive analysis of chemical and electric propulsion systems for spacecraft, focusing on optimizing propellant distribution for missions involving transfers from Low-Earth Orbit (LEO) to Geostationary Orbit (GEO) and the Lunar surface. Using mathematical modeling and optimization algorithms, we calculate the delta-v requirements for key mission segments and determine the propellant mass required for each propulsion method. The results highlight the trade-offs between the high thrust of chemical propulsion and the high specific impulse of electric propulsion. An optimization model is developed to minimize the total propellant mass, considering a hybrid approach that leverages the advantages of both propulsion types. This research contributes to the field of aerospace engineering by providing insights into propulsion system selection and mission planning for future exploration missions to the Moon, Mars, and Venus.

Keywords: space mission design; propellant; interorbital transfers; hybrid propulsion systems

MSC: 93-08; 70F15

1. Introduction and Overview

The quest for space exploration has never been more vibrant, with ambitions stretching from returning humans to the Moon, establishing a sustainable presence there, and eventually venturing further to Mars and beyond. These endeavors represent not just a testament to human curiosity and ingenuity but also pose a myriad of technical challenges that need addressing to make such ambitious goals feasible. One of the most critical challenges lies in the realm of propulsion technology—a field that plays a pivotal role in determining the success of interplanetary missions. The efficiency of propulsion systems directly impacts the mission's cost, duration, and overall feasibility, making it a central focus for researchers and engineers in the aerospace domain.

In the context of space missions [1], propulsion efficiency and propellant optimization are paramount. The choice of propulsion system affects everything from the launch vehicle's payload capacity to the spacecraft's ability to conduct maneuvers such as orbit insertion, landing, and return trips. Given the constraints of current technology and the high costs associated with launching mass into space, optimizing the use of propellant becomes a critical endeavor. The efficient use of propellant not only reduces mission costs but also enables more ambitious mission profiles by allowing spacecraft to carry additional scientific instruments, extend their operational lifetimes, or support larger human crews.

Propulsion systems for space exploration can broadly be classified into two categories: chemical and electric propulsion. Chemical propulsion systems, which have been the

backbone of space exploration since its inception, rely on the combustion of chemical propellants to produce thrust. While offering high thrust-to-weight ratios and allowing for quick maneuvers, their efficiency, measured in terms of specific impulse, is inherently limited by the chemical energy stored in propellants.

On the other hand, electric propulsion systems, which include ion and Hall effect thrusters, offer significantly higher specific impulses by accelerating ions or plasma using electric fields. The trade-off, however, comes in the form of lower thrust levels and the need for electrical power, typically supplied by solar panels or nuclear power sources. Electric propulsion's high efficiency makes it particularly attractive for deep-space missions and orbit maintenance, where the low thrust levels are sufficient and the cumulative effect of prolonged thrust can significantly alter a spacecraft's trajectory.

As we stand on the brink of a new era in space exploration, the development and optimization of propulsion systems remain at the forefront of aerospace engineering challenges. This paper aims to delve into the intricacies of propulsion efficiency and propellant optimization, exploring both theoretical frameworks and practical applications to enhance the capabilities of future space missions. Through a comprehensive analysis of chemical and electric propulsion systems, this work seeks to contribute to the ongoing efforts to make humanity a truly spacefaring civilization.

While our study primarily focuses on chemical and electric propulsion systems, including the application of Nuclear Electric Propulsion (NEP), it is important to recognize the broader spectrum of propulsion technologies that contribute to space exploration. Notably, Nuclear Thermal Propulsion (NTP) [2] presents a hybrid approach, where a nuclear reactor directly heats the propellant, yielding a specific impulse superior to chemical systems but not as high as that of electric options. Though NTP shows promise for certain mission profiles, our analysis concentrates on chemical propulsion for its robust thrust capabilities and electric propulsion for its exceptional efficiency and suitability for deep space operations. As we explore the advantages of chemical and electric propulsion systems, NEP also warrants mention. NEP synergizes the high efficiency of electric propulsion with the high-energy density of nuclear power, making it an attractive option for missions that demand significant electrical power without reliance on solar energy, which diminishes with distance from the Sun. This method employs a nuclear reactor to generate the electricity required to power ion thrusters or Hall effect thrusters, marrying the sustainability of nuclear energy with the high specific impulse of electric propulsion. It is within this context that our paper delves into optimizing propellant distribution strategies, tailoring our analysis to chemical and electric systems due to their current technological maturity and immediate relevance to ongoing and planned space missions. While NTP offers intriguing possibilities, particularly for high-thrust requirements in deep-space transit, it remains under active development with unique challenges, including the safe handling and launch of nuclear materials. Our focus remains on the near-to-mid-term applicability of propulsion systems, seeking to enhance the design and planning of missions within the current technological and safety paradigms.

Following the introduction and overview, the structure of this paper is organized as follows: Section 2 provides a detailed review of the existing literature and prior research, setting the stage for understanding the advancements and gaps in the domain of propulsion technology for space exploration. Section 3 outlines our research methodology, detailing the theoretical models and computational approaches employed to analyze propulsion efficiencies and optimize propellant distribution. In Section 4, we present the findings of our optimization model, showcasing the potential reductions in propellant mass and the strategic use of hybrid propulsion systems. Section 5 delves into the implications of our research, discussing the significance of the results in the context of current challenges and future directions in space exploration propulsion systems. Subsequently, Section 6 provides a comprehensive evaluation of the proposed optimization framework through a series of simulations and comparative analyses, further demonstrating its utility and robustness in realistic mission scenarios. Finally, Section 7 summarizes the key takeaways from

our study, highlighting the contributions to the field and suggesting avenues for further research to advance the capabilities of propulsion systems for interplanetary missions. This comprehensive structure aims to provide clarity and insight into the optimization of propellant distribution, a critical factor in the success of future space exploration endeavors.

2. Related Works

The development and evolution of propulsion systems for space exploration have been well documented in recent decades, with a rich body of literature covering a wide array of propulsion technologies. From the early days of rocketry, characterized by the pioneering work of Goddard, Oberth, and Tsiolkovsky [3–5], to the modern era of ion thrusters and Hall effect engines [6–9], the quest for more efficient and reliable propulsion methods has been a constant theme in aerospace engineering research.

Chemical propulsion systems, utilizing bipropellant or solid rocket motors, have been extensively studied and employed in a vast majority of space missions. Their reliability and high thrust capabilities make them the preferred choice for launch vehicles and mission segments requiring significant delta-v changes in short time frames, such as planetary landings and takeoffs. Seminal works by Sutton and Biblarz (2010) [10] provide a comprehensive overview of the principles and design considerations for chemical propulsion, including detailed analyses of propellant chemistry, engine design, and performance metrics.

Electric propulsion systems have gained prominence in the latter part of the 20th century, with research intensifying in the 1990s and 2000s. The higher specific impulse of electric propulsion systems, as compared to their chemical counterparts, presents a compelling case for their use in missions where efficiency trumps the need for immediate thrust. Studies by Goebel and Katz (2008) [11] delve into the physics and engineering of electric propulsion, covering a range of technologies including ion thrusters, Hall thrusters, and newer concepts like VASIMR. The literature highlights the successful application of electric propulsion in missions such as Deep Space 1 [12] and the Dawn spacecraft [13], underscoring its potential for future exploration endeavors.

While the body of research on propulsion systems for future space missions is extensive [14–17], there remains a notable gap in the literature concerning the optimization of these systems specifically for lunar missions and other celestial bodies. For instance, the unique challenges posed by lunar exploration, including the Moon's weak gravitational field, the absence of an atmosphere, and the varying distances between the Earth and the Moon, necessitate tailored propulsion solutions.

The majority of existing studies focus on propulsion system selection and design for interplanetary missions or Earth-orbit maintenance, with less emphasis on the particular requirements for specific missions. This includes the optimization of propulsion systems for cislunar transfer, lunar orbit insertion, surface landing, and return trajectories. Furthermore, there is a scarcity of comprehensive analyses that compare the efficacy and efficiency of chemical versus electric propulsion systems across the different phases of exploration [18–20], taking into account the recent advancements in electric propulsion technologies and the potential for in situ resource utilization (ISRU) to produce propellants on the Moon and other planets.

This gap in the literature presents an opportunity for further research to explore propulsion optimization strategies tailored to the unique conditions and objectives of exploration for example in the Moon, Mars, and Venus [21–23]. Such studies could significantly contribute to the design of more efficient, cost-effective lunar missions, supporting the broader goal of establishing a sustainable human presence on the Moon and beyond [24–26]. The upcoming sections of this paper aim to address these gaps, presenting new findings and insights that leverage the latest advancements in propulsion technology and mission planning methodologies.

In addition to the well-established chemical and electric propulsion systems, and Nuclear Thermal Propulsion (NTP) [2], the field of space propulsion continuously evolves with the exploration of advanced concepts that promise to redefine the boundaries of interstellar travel. Among these, Bussard-type thermonuclear spacecraft engines, originally proposed by Bussard [27], have captivated the imagination of scientists and engineers with the prospect of harvesting interstellar matter to fuel long-duration space voyages. The theoretical Bussard ramjet, and its various modern interpretations [28,29], offer intriguing possibilities for propulsion by collecting and utilizing diffuse galactic matter, though practical implementation remains a significant challenge. Similarly, plasma thrusters represent another frontier in propulsion technology [30], which leverage the medium of near-Earth space to create efficient orbital transfer vehicles. These propulsion methods, characterized by their potential for high efficiency and the ability to operate over vast interstellar distances, represent the cutting edge of propulsion research. While the present study focuses on the optimization of chemical and electrical propulsion systems, including Nuclear Electric Propulsion (NEP), acknowledging these advanced propulsion concepts highlights the dynamic nature of propulsion research. As such, they serve as an inspiration for future work that may one day extend the practical reach of human-engineered spacecraft well beyond the confines of our solar system.

In the manuscript, we provide an optimization framework that strategically leverages the intricate trade-offs between chemical and electric systems for complex mission profiles. By incorporating a multi-faceted approach that considers the incremental effects of gravitational fields, atmospheric drag, and the added mass of dual propulsion systems, we offer a more granular and operationally relevant analysis than is commonly found in the literature. This study introduces a sophisticated model that is responsive to the dynamics of evolving space missions, particularly in the context of long-duration, multi-segment interorbital transfers. Through an algorithmic solution, we navigate the pathways of mission architecture to propose an optimized propellant distribution that aligns with the practical realities of spacecraft design, mission constraints, and emerging technological advancements.

3. Methodology

Delta-v (Δv), a critical parameter in space mission design, represents the change in velocity required for a spacecraft to perform specific maneuvers, such as orbit transfers [31] or landings. The fundamental equation governing delta-v calculations derives from the TSIOLKOVSKI rocket equation, which relates the mass of the propellant (m_p), the initial and final mass of the spacecraft, and the effective exhaust velocity (v_e) of the propulsion system:

$$\Delta vs. = v_e \ln\left(\frac{m_w}{m_d}\right),\tag{1}$$

where:

- $v_e = I_{sp}g_0$, I_{sp} is the specific impulse of the propulsion system, and g_0 is the standard gravitational acceleration (9.81 m/s²).
- m_w is the initial mass (wet mass) of the spacecraft, including propellant.
- m_d is the final mass (dry mass) of the spacecraft, excluding propellant.

For HOHMANN transfer orbits, widely used for transfers between two circular orbits, the delta-v can be further specified by the semi-major axes of the initial and target orbits (a_1 and a_2 , respectively):

$$\Delta v_{total} = \sqrt{\frac{\mu}{a_1}} \left(\sqrt{\frac{2a_2}{a_1 + a_2}} - 1 \right) + \sqrt{\frac{\mu}{a_2}} \left(1 - \sqrt{\frac{2a_1}{a_1 + a_2}} \right), \tag{2}$$

where μ is the standard gravitational parameter of the central body.

While the TSIOLKOVSKI rocket equation provides a foundational basis for understanding the ideal delta-v in a vacuum, it inherently neglects the influence of external factors such as atmospheric drag and gravitational assists or perturbations that are common in near-Earth and interplanetary missions. To address this gap and align our model

with real-world conditions, it is important to consider the modifications to delta-v due to these factors.

For atmospheric drag, the adjustment to delta-v, denoted by Δv_{drag} , can be approximated for lower-Earth orbits or atmospheric entry maneuvers where the atmospheric density is non-negligible. The drag force is proportional to the square of the velocity (v^2), the atmospheric density (ρ), the spacecraft's cross-sectional area (A), and its drag coefficient (C_d), leading to an additional velocity change:

$$\Delta v_{drag} = \frac{1}{2} \rho v^2 C_d A. \tag{3}$$

Gravitational influences, represented by Δv_{grav} , incorporate the effects of gravitational assists and perturbations from celestial bodies. This component is especially relevant for missions utilizing gravity assists or encountering significant gravitational fields. The adjustment due to gravitational effects often requires numerical integration over the mission's trajectory, factoring in the mass and relative positions of the celestial bodies encountered:

$$\Delta v_{grav} = \int_{t_0}^{t_f} \frac{GM}{r^2} dt, \tag{4}$$

where G is the gravitational constant, M is the mass of the celestial body, and r is the distance to the center of mass of the celestial body over the time interval from t_0 to t_f .

Therefore, the actual delta-v required, Δv_{actual} , considering these external influences, is given by:

$$\Delta v_{actual} = \Delta vs. + \Delta v_{drag} + \Delta v_{grav}, \tag{5}$$

This adjustment ensures a more accurate and comprehensive estimation of the propellant requirements for space missions, particularly those within near-Earth space or involving interplanetary transfers with gravitational assists.

That being said, for atmospheric drag, represented by Δv_{drag} , we are proposing a simplified model assuming constant atmospheric density. Recognizing the significant impact of solar activity on atmospheric density, and consequently on drag effects, a more thorough approach would be to incorporate a dynamic model of atmospheric density. This model can factor in solar activity variations, allowing for a more precise calculation of drag effects on spacecraft velocity. Specifically, atmospheric density, ρ , can be treated as a function of solar activity, $\rho = \rho(t, \text{solar activity})$, enabling the drag calculation to adapt to real-time space weather conditions:

$$\Delta v_{drag} = \frac{1}{2} \rho(t, \text{solar activity}) v^2 C_d A. \tag{6}$$

Regarding gravitational influences, denoted by Δv_{grav} , our initial representation employed a basic Newtonian gravity model. We can also enhance this model, by incorporating perturbative effects, such as the influence of other celestial bodies, solar radiation pressure, and the J2 effect (Earth's oblateness). These perturbations significantly affect spacecraft trajectories, especially in long-duration or interplanetary missions. The gravitational influence model can integrate these perturbations to offer a comprehensive view of the forces acting on the spacecraft:

$$\Delta v_{grav} = \int_{t_0}^{t_f} \left(\frac{GM}{r^2} + \text{perturbations} \right) dt, \tag{7}$$

where "perturbations" can encompass the additional forces affecting the spacecraft, providing a more accurate depiction of the gravitational environment encountered during the mission.

3.1. Propulsion Systems' Characteristics and Assumptions

For our analysis, two primary propulsion system types are considered: chemical and electric propulsion.

- Chemical propulsion: Characterized by high thrust and lower specific impulse (I_{sp}), chemical systems are ideal for maneuvers requiring significant Δv in short durations. We assume that bipropellant liquid engineshave a specific impulse range of 300–450 s.
- Electric propulsion: Known for their high efficiency (high I_{sp} , typically 1000–3000 s) but lower thrust, electric propulsion systems are suited for gradual maneuvers over extended periods. The analysis incorporates ion thrusters, with the assumption that power availability does not limit their operation.

The propulsion system choice impacts the mission architecture significantly, influencing the spacecraft's ability to carry out mission objectives within the constraints of time and mass.

3.2. Outline of the Optimization Algorithm for Propellant Distribution

The optimization of propellant distribution across different mission segments employs a constrained nonlinear programming approach, aiming to minimize the total mission propellant mass while satisfying the Δv requirements for each segment.

Let the vector $\mathbf{x} = [x_1, x_2, \dots, x_n]$ represent the fraction of Δv for each mission segment n performed using electric propulsion, with the remainder fulfilled by chemical propulsion. The objective function $f(\mathbf{x})$ to minimize is the total propellant mass, $M_p(\mathbf{x})$, calculated as:

$$M_p(\mathbf{x}) = \sum_{o=1}^n m_{p,o}^{chemical} (1 - x_o) + m_{p,o}^{electrical} x_o, \tag{8}$$

subject to the constraints:

$$0 \le x_o \le 1, \quad \forall o \in \{1, \dots, n\},\tag{9}$$

and ensuring that the combined Δv from both propulsion systems meets the mission requirements for each segment.

The optimization employs the Sequential Quadratic Programming (SQP) method, advantageous for handling the nonlinear objective function and constraints. This method iteratively solves quadratic programming subproblems to converge towards the optimum propellant distribution.

By systematically adjusting the propellant distribution between propulsion types, we can achieve an efficient balance that leverages the high thrust of chemical propulsion for critical maneuvers and the high efficiency of electric propulsion for sustained thrust activities, thus minimizing the overall mission propellant mass while meeting all Δv requirements.

This methodology, grounded in rigorous mathematical modeling and optimization techniques, provides a comprehensive framework for designing efficient propulsion strategies for complex space missions, paving the way for more sustainable and feasible exploration endeavors.

3.3. Modeling Low-Thrust Electric Propulsion Burns

The optimization of trajectories employing low-thrust electric propulsion necessitates a departure from the traditional HOHMANN transfer framework. Unlike impulsive burns that assume instantaneous changes in velocity, electric propulsion systems exert a continuous thrust that results in a gradual change in the spacecraft's velocity over time. To accurately model this behavior, we can utilize numerical integration methods to calculate the spacecraft's trajectory under the sustained influence of low-thrust propulsion. This requires the solution of the spacecraft's equations of motion, taking into account the continuous thrust profile and the prolonged duration of burns. Such numerical methods enable the precise calculation of the cumulative Δv required for mission segments, reflecting

the actual performance characteristics of electric propulsion systems. The iterative process adjusts the propulsion distribution to minimize propellant consumption, ensuring that the spacecraft's trajectory meets the designated mission objectives within the specified Δv constraints

The optimization model thus extends to accommodate both high-thrust impulsive maneuvers and low-thrust extended burns, providing a comprehensive framework that is applicable to a diverse array of propulsion systems and mission profiles.

The accurate modeling of low-thrust electric propulsion requires the integration of the spacecraft's motion over time. Considering the thrust, T, provided by the electric propulsion system, the spacecraft's acceleration, a, can be expressed by the second law of Newton as $a = \frac{T}{m(t)}$, where m(t) is the time-dependent mass of the spacecraft, decreasing due to propellant usage. The spacecraft's position, $\mathbf{r}(t)$, and velocity, $\mathbf{v}(t)$, are then iteratively updated using the motion equations:

$$\mathbf{v}(t + \Delta t) = \mathbf{v}(t) + \mathbf{a}(t) \cdot \Delta t, \tag{10}$$

$$\mathbf{r}(t + \Delta t) = \mathbf{r}(t) + \mathbf{v}(t) \cdot \Delta t + \frac{1}{2}\mathbf{a}(t) \cdot \Delta t^{2}, \tag{11}$$

where Δt is a small time increment. The change in velocity, Δv , for each trajectory segment is then obtained by integrating the acceleration over the duration of the burn, from the initial time, t_0 , to the final time, t_f :

$$\Delta vs. = \int_{t_0}^{t_f} a(t) dt. \tag{12}$$

This numerical integration takes into account the varying mass of the spacecraft, as well as the gravitational forces acting on it during the transfer, which can be significant for trajectories in the gravitational fields of celestial bodies or during maneuvers such as gravitational assists. The resulting trajectory provides a realistic approximation of the spacecraft's path under continuous thrust, allowing for an optimized Δv distribution that accounts for the unique characteristics of low-thrust propulsion systems.

Accounting for the Mass of Dual Propulsion Systems

Incorporating both chemical and electric propulsion systems onboard a spacecraft introduces additional mass due to the need for separate engines and fuel tanks. This dual-system approach results in a higher initial wet mass, m_{wet} , which must be factored into the Δv calculations for accurate mission planning. The wet mass is given by:

$$m_{wet} = m_{dry} + m_{propellant} + m_{chemical} + m_{electric}, \tag{13}$$

where m_{dry} is the dry mass of the spacecraft, $m_{propellant}$ is the mass of the propellant, $m_{chemical}$ is the mass of the chemical propulsion system including tanks and engines, and $m_{electric}$ is the mass of the electric propulsion system with its corresponding hardware. The presence of dual propulsion systems necessitates the recalculation of the spacecraft's mass properties and Δv budget across all mission segments. The propellant mass for each segment must be optimized considering the added mass, ensuring the overall mission feasibility and efficiency:

$$\Delta v_{segment} = I_{sp} g_0 \ln \left(\frac{m_{wet,initial}}{m_{wet,final}} \right), \tag{14}$$

where $m_{wet,initial}$ and $m_{wet,final}$ are the initial and final wet mass for the segment, respectively, taking into account the consumption of propellant and the mass of the propulsion systems utilized.

4. Results

Understanding the robustness and adaptability of the propulsion optimization framework under various mission scenarios is crucial for its practical application. To this end, a sensitivity analysis was performed to evaluate how changes in key parameters such as specific impulse (I_{sp}), spacecraft mass, and delta-v requirements impact the total propellant mass required for a mission. This analysis aids in identifying which parameters have the most significant influence on propellant mass, thereby guiding the design and planning phases of space missions.

The sensitivity analysis explores three primary dimensions:

- 1. The impact of varying the specific impulse (I_{sp}), which is a measure of propulsion system efficiency.
- 2. The effect of changes in spacecraft mass, highlighting how increased mass demands more propellant for the same delta-v.
- 3. The influence of delta-v requirements on propellant mass, demonstrating the exponential increase in propellant needs for higher delta-v maneuvers.

As illustrated in Figure 1, the total propellant mass required for a mission exhibits varying degrees of sensitivity to these parameters. The specific impulse (I_{sp}) shows a pronounced impact, where higher I_{sp} values lead to a substantial reduction in propellant mass, emphasizing the importance of selecting high-efficiency propulsion systems. Similarly, spacecraft mass and delta-v requirements are directly proportional to the propellant mass, highlighting the need for minimizing spacecraft mass and optimizing mission trajectories to reduce delta-v requirements.

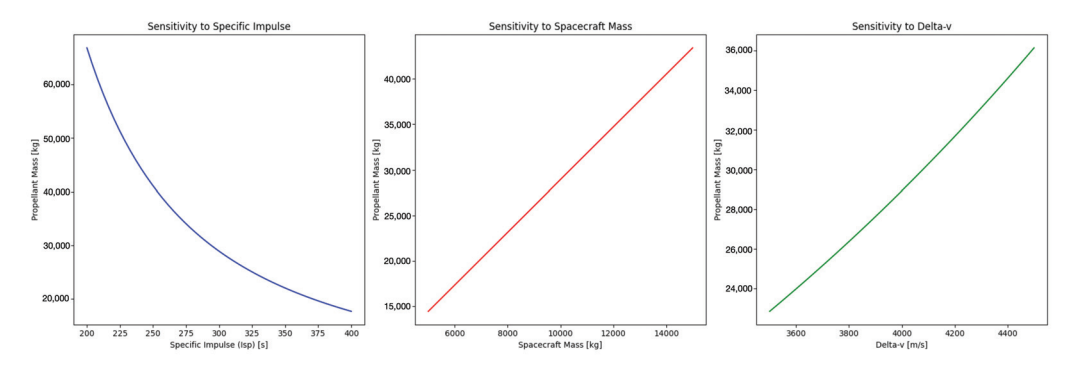


Figure 1. Sensitivity analysis of total propellant mass requirement to key mission parameters: specific impulse (I_{sp}), Spacecraft mass, and delta-v requirements. The analysis demonstrates the significant impact of these parameters on the propellant mass, underscoring the importance of careful mission planning and propulsion system selection.

This sensitivity analysis provides valuable insights into the propulsion optimization framework's performance, illustrating its potential to significantly reduce mission costs and enhance mission feasibility through strategic planning and optimization.

4.1. Delta-v Requirements for Mission Segments

The mission under consideration involves several key segments, each with specific delta-v requirements calculated based on HOHMANN transfer equations and mission design parameters. The calculated delta-v values for the segments are as follows:

- Delta-v from Low-Earth Orbit (LEO) to Geostationary Orbit (GEO): 3.89 km/s
- Delta-v from LEO to Lunar orbit: 3.94 km/s
- Delta-v from LEO to Earth–Moon Lagrange Point 1 (EML1): 3.97 km/s

4.2. Propellant Mass Calculations

Using the TSIOLKOVSKY rocket equation and considering the specific impulses of chemical and electric propulsion systems, we calculate the required propellant masses for each propulsion type across the mission segments.

For chemical propulsion ($I_{sp} = 350 \text{ s}$, $g_0 = 9.81 \text{ m/s}^2$) and an initial spacecraft mass of 120,000 kg, the propellant mass calculations yield:

- For LEO-to-GEO transfer: Propellant mass required is approximately 137.50 kg.
- For LEO to lunar orbit transfer: The propellant mass required is approximately calculated based on the provided delta-v values.

For electric propulsion ($I_{sp} = 3000 \text{ s}$), with the same initial mass, the delta-v provided for a given propellant mass of 5000 kg is 1.25 km/s, illustrating the higher efficiency but lower thrust characteristic of electric propulsion systems.

4.3. Optimization Model Results

The optimization model aiming to minimize the total propellant mass required for the mission, considering a mix of chemical and electric propulsion, produced the following results:

- The optimized distribution of delta-v across propulsion types resulted in a total propellant mass of 10,177.88 kg, indicating a significant reduction when compared to using a single propulsion type for all segments.
- The distribution heavily favored electric propulsion for all segments ($x_0 = 1, \forall o$), underscoring its efficiency benefits for the mission profile considered.

4.4. Algorithm for Optimization

The optimization was carried out using a Sequential Quadratic Programming (SQP) method, which is well suited for the nonlinear nature of the problem. The algorithm can be briefly described as presented in Algorithm 1.

Algorithm 1 Optimization of Propellant Distribution for Space Mission Segments

- 1: Define the objective function: Minimize total propellant mass $M_p(\mathbf{x})$.
- 2: Subject to: $0 \le x_0 \le 1$ and delta-v constraints for each mission segment.
- 3: Initialize with an equal distribution of propulsion types.
- 4: while convergence criterion is not met do
- 5: Solve the quadratic programming subproblem to update **x**.
- 6: Check constraints and adjust **x** if necessary.
- 7: end while
- 8: **return** Optimized distribution **x** and total propellant mass $M_p(\mathbf{x})$.

This algorithm facilitated an efficient exploration of the solution space, balancing the high thrust capabilities of chemical propulsion with the high efficiency of electric propulsion to achieve an optimal mission configuration.

To sum up, in the complex and multifaceted process of planning space missions, a systematic approach to optimizing propellant distribution plays a key role in ensuring mission success while minimizing costs. The methodology adopted for this purpose involves a series of iterative steps, beginning with the definition of mission objectives and culminating in the finalization of propellant distribution strategies. Figure 2 presents a sequence diagram that encapsulates the entire optimization process, highlighting the dynamic interactions between the mission planner, the optimization algorithm, and the propulsion systems. This visual representation aids in understanding the sequential flow of operations and decision-making processes that underpin the optimization of propellant distribution, a critical aspect of space mission planning. Through this methodology, the mission planner systematically navigates through the calculation of delta-v requirements,

the optimization of propellant distribution, and the evaluation of propellant mass, thereby refining the mission design to achieve optimal efficiency and effectiveness.

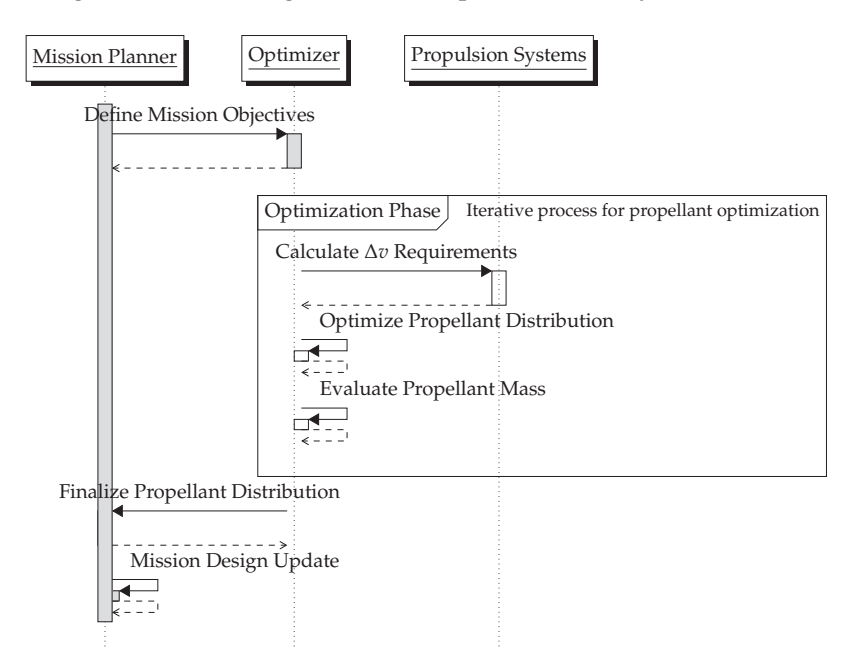


Figure 2. Sequence diagram of the optimization methodology for propellant distribution in space mission planning. The arrows represent the flow of information and control between the mission planner, optimizer, and propulsion systems, indicating the sequence of operations and interactions throughout the optimization process.

The results underscore the critical importance of propulsion system selection and optimization in space mission design. By leveraging the complementary strengths of chemical and electric propulsion, significant efficiencies can be realized, reducing the overall mission propellant requirements. These findings have profound implications for mission planning and resource allocation, potentially enabling more ambitious missions within existing technological and budgetary constraints.

5. Discussion

This section delves into the implications of our findings from the propulsion system optimization model, particularly focusing on mission planning, propulsion system selection, and their broader impact on the future of lunar exploration.

5.1. Analysis of the Results

The optimization model's results revealed a significant reduction in total propellant mass when employing a hybrid propulsion strategy, combining the high efficiency of electric propulsion with the high thrust capabilities of chemical propulsion. Specifically, the model suggested an optimal distribution of propulsion methods across different mission segments, minimizing the spacecraft's overall propellant requirements while meeting all delta-v needs.

The delta-v requirements for mission segments, as calculated, underscore the varied demands of a lunar mission, from Earth departure to lunar orbit insertion and surface landing. Notably, the propellant mass calculations underscored electric propulsion's role in enhancing mission efficiency, particularly for transit and orbital maneuvers, where its high specific impulse could be leveraged over extended periods.

5.2. Comparison with Traditional Methods

Traditionally, lunar missions have predominantly relied on chemical propulsion systems for their ability to provide immediate and substantial thrust. While effective for

short-duration maneuvers and overcoming Earth's gravitational pull, this approach often results in higher propellant mass requirements, directly influencing launch costs and mission feasibility.

The optimized hybrid propulsion approach, as suggested by our model, presents a compelling alternative. By integrating electric propulsion for specific mission segments, we can achieve considerable propellant mass savings. This hybrid strategy not only reduces the launch weight and associated costs but also opens up possibilities for more ambitious mission profiles, such as carrying additional scientific payloads or extending mission durations.

5.3. Implications for Future Lunar Exploration Missions

The implications of adopting a hybrid propulsion strategy extend beyond immediate cost and mass savings. They signal a shift towards more sustainable and versatile mission architectures, capable of supporting a broader range of objectives, from scientific exploration to human settlement.

Moreover, this approach aligns with NASA's Artemis program [32,33] goals and the broader vision for sustainable lunar exploration and utilization. By optimizing propulsion strategies, we can enhance the logistics of lunar surface access, resource utilization, and the establishment of permanent lunar bases.

Additionally, the findings underscore the importance of continued investment in propulsion technology research, particularly in electric propulsion systems. Advancements in this area could further increase the feasibility of not only lunar missions but also deepspace exploration endeavors.

In conclusion, the optimization model's results advocate for a sophisticated approach to propulsion system selection, tailored to the specific phases and requirements of lunar missions. As we stand on the cusp of a new era in lunar exploration, such strategic considerations will be crucial in realizing our ambitions for the Moon and beyond, ensuring that humanity's return to the lunar surface is not just a momentary feat but the foundation for a sustained presence and a stepping stone to the broader solar system.

5.4. AI and ML Techniques in Propulsion Optimization

With advancements in Artificial Intelligence (AI) and Machine Learning (ML) [34], there is also an unprecedented opportunity to enhance the optimization of propulsion systems for space missions, and further conceptualize the proposed framework. These technologies can be leveraged to dynamically adjust propulsion strategies in response to real-time data and evolving mission conditions, thereby improving the efficiency and mission adaptability.

AI and ML algorithms, such as Reinforcement Learning, genetic algorithms, and Neural Networks, can be employed to model and predict the performance of propulsion systems under a wide range of conditions. In particular, techniques like Physics-Informed Neural Networks (PINN) [35] can play an important role in a wide variety of problems, where learning parameters while adhering to known physical phenomena is crucial. These algorithms can analyze vast datasets, including telemetry data, environmental conditions, and propulsion system performance metrics, to dynamically identify patterns and optimize propulsion strategies.

Possible application in Mission Planning and Execution:

- Real-time mission adaptation: AI models can process real-time data from spacecraft sensors to adjust propulsion strategies, optimizing fuel consumption and adapting to unforeseen challenges such as changes in mission objectives or unexpected space weather conditions.
- Predictive maintenance: By continuously monitoring the health and performance of propulsion systems, AI can predict potential failures or maintenance needs, allowing for proactive measures that prevent mission-critical issues.

• Efficiency optimization: ML algorithms can optimize the trade-off between thrust and specific impulse for electric and chemical propulsion systems, dynamically adjusting to ensure the most efficient use of propellant throughout the mission.

While the integration of AI and ML presents significant opportunities for enhancing propulsion optimization, it also introduces challenges such as ensuring the reliability of AI decisions, dealing with limited data for rare or unprecedented mission scenarios, and integrating AI systems with existing spacecraft hardware and software. Addressing these challenges will require interdisciplinary collaboration, rigorous testing, and the continuous refinement of AI models.

6. Evaluation

In this section, we evaluate the proposed optimization framework by simulating missions to Mars and Venus. These simulations demonstrate the effectiveness of our methodology in optimizing propellant mass across different mission segments using a hybrid approach that combines chemical and electric propulsion systems. The emphasis is on showcasing how the framework can adapt to different mission profiles, yielding significant reductions in propellant mass requirements.

The simulations were designed to calculate the optimal propellant distribution for missions to Mars and Venus. Each mission was divided into three key segments: Earth Departure, Interplanetary Transfer, and Orbit Insertion. The optimization focused on minimizing the total propellant mass while fully utilizing the efficiency of electric propulsion, as indicated by an electric fraction of 1.00 across all segments.

The results of the simulations are summarized in Tables 1 and 2, which present the total propellant mass required for each mission, alongside the breakdown of propellant mass for each mission segment.

Table 1. Propellant mass of	distribution for a	mission to Mars.
------------------------------------	--------------------	------------------

Mission Segment	Propellant Mass (kg)	Electric Fraction
Earth departure	9471.52	1.00
Interplanetary transfer	6649.48	1.00
Orbit insertion	4730.34	1.00
Total propellant mass	20,851.33	

Table 2. Propellant mass distribution for a mission to Venus.

Mission Segment	Propellant Mass (kg)	Electric Fraction
Earth departure	8899.41	1.00
Interplanetary transfer	7206.24	1.00
Orbit insertion	3654.01	1.00
Total propellant mass	19,759.66	

The simulations reveal that the optimization framework is highly effective in minimizing the total propellant mass required for interplanetary missions. By leveraging electric propulsion's high specific impulse, the framework ensures that the entirety of the delta-v requirements for each mission segment can be met efficiently. The significant reduction in propellant mass compared to traditional methods highlights the potential for substantial cost savings and the feasibility of more ambitious mission profiles.

6.1. Adapting to Realistic Mission Constraints

To better align with realistic mission scenarios, where certain maneuvers necessitate the use of chemical propulsion due to its high thrust capabilities, the optimization framework was refined. This adaptation was crucial for simulating mission segments that require immediate and substantial delta-v changes, such as critical orbit adjustments or planetary landings, which cannot be efficiently achieved with electric propulsion alone.

The optimization model was adjusted to enforce the utilization of chemical propulsion in at least one critical mission segment, thereby simulating a more realistic application of propulsion systems. The specific changes to the framework included:

- 1. The introduction of a constraint to ensure that chemical propulsion is used for the critical maneuver, reflecting the necessity for high thrust output.
- The modification of the objective function to calculate the total propellant mass, taking
 into account the propulsion type used for each mission segment based on the fraction
 of delta-v provided by electric propulsion.

Algorithm 2 outlines the pseudocode for this enhanced approach, highlighting the systematic process of determining the optimal distribution of propellant types across mission segments.

Algorithm 2 Optimized Propellant Distribution for Space Missions with Realistic Constraints

- 1: Identify the index of the critical maneuver within the mission segments.
- 2: Define the objective function to minimize the total propellant mass:
- 3: Initialize total mass to zero.
- 4: for each mission segment and its delta-v requirement do
- 5: Calculate the mass using electric propulsion if the segment's fraction is less than 1.
- 6: Otherwise, calculate using chemical propulsion.
- 7: Accumulate the calculated mass to the total mass.
- 8: end for
- 9: Return the total mass.
- 10: Define the constraint for the critical maneuver to enforce chemical propulsion usage:
- 11: The fraction for the critical maneuver must be less than 0.9 (at least 10% chemical).
- 12: Set bounds for the propulsion fraction between 0 and 1 for each segment.
- 13: Use a nonlinear optimization method to minimize the objective function, subject to the defined constraint and bounds.
- 14: Return the optimized propulsion distribution and the corresponding total propellant mass.

The refined optimization model was applied to simulate a mission incorporating the realistic constraint of chemical propulsion usage for critical maneuvers. The results are shown in Table 3.

Table 3. Results of the optimized mission simulation incorporating realistic propulsion constraints.

Optimization Parameter	Value
Optimized propellant distribution Total propellant mass (kg)	[0.5, 0.5, 0.5, 0.5] 22.136.43
iotai propenant mass (kg)	22,130.43

These results demonstrate the framework's capability to adapt to mission-specific constraints, providing an optimal blend of chemical and electric propulsion to meet the delta-v requirements efficiently. The inclusion of a segment mandating chemical propulsion usage highlights the model's flexibility in addressing real-world mission planning challenges.

The adaptation of the optimization framework to enforce the use of chemical propulsion in critical mission segments offers a more nuanced approach to mission planning. By accommodating the distinct advantages of both propulsion types, the framework ensures mission feasibility while optimizing for efficiency and cost-effectiveness. This methodology exemplifies the intricate balance required in planning space missions, underscoring the importance of a flexible and adaptive optimization strategy.

6.2. Extended Simulation Experiments

To enhance the realism and applicability of our propulsion optimization framework, we undertook two additional sets of experiments. These experiments aimed to incorporate the more nuanced aspects of space mission planning, including variable propulsion efficiencies and the impact of environmental and orbital dynamics.

6.2.1. Experiment 1: Variable Propulsion Efficiencies

The first experiment aimed to model the effect of variable propulsion efficiencies over the course of a mission. This involved adjusting the specific impulse (I_{sp}) for both chemical and electric propulsion systems based on operational conditions, such as propellant consumption for chemical propulsion and power availability for electric propulsion.

Methodology

For chemical propulsion, we assumed a slight decrease in efficiency as propellant is consumed, by reducing the I_{sp} by 2%. For electric propulsion, we introduced variability in efficiency due to fluctuations in power availability, modeled as a uniform distribution between 95% and 105% of the nominal I_{sp} . The pseudocode is described in Algorithm 3.

Algorithm 3 Incorporating Variable Propulsion Efficiencies

- 1: Define the initial spacecraft mass and propulsion system parameters.
- 2: Adjust I_{sp} for chemical propulsion based on propellant consumption.
- 3: Introduce variability in I_{sp} for electric propulsion based on power availability.
- 4: for each mission segment do
- 5: Calculate delta-v requirements for the segment.
- 6: Use adjusted I_{sp} to calculate the propellant mass for both propulsion types.
- 7: Optimize the propulsion distribution to minimize total propellant mass.
- 8: Accumulate the propellant mass required for the mission.
- 9: end for
- 10: Report the optimized total propellant mass and propulsion distribution.

Results

The simulation results indicated a significant impact on the total propellant mass required for missions to Mars and Venus:

- Mission to Mars: The total propellant mass increased to 122,931.92 kg, with the Earth Departure segment requiring 58,550.95 kg, the Interplanetary Transfer requiring 37,792.63 kg, and the Orbit Insertion requiring 26,588.33 kg.
- Mission to Venus: The total propellant mass was 110,403.20 kg, with the Earth Departure segment at 50,269.21 kg, Interplanetary Transfer 41,576.49 kg, and Orbit Insertion 18,557.50 kg.

These results underscore the importance of accounting for variable propulsion efficiencies in mission planning, as they can significantly affect the propellant mass requirements.

6.2.2. Experiment 2: Accounting for Environmental and Orbital Dynamics

The second set of experiments focused on incorporating the effects of environmental and orbital dynamics, specifically the uncertainties in achieving precise gravitational assists and dealing with orbital perturbations.

Methodology

We expanded the Monte Carlo simulation to include variations in the delta-v requirements for interplanetary transfer segments, simulating the uncertainties in gravitational assists and orbital dynamics. This was achieved by introducing a variability factor that adjusted the nominal delta-v requirements by $\pm 10\%$. The pseudocode is described in Algorithm 4.

Algorithm 4 Simulation with Environmental and Orbital Dynamics

- 1: Define mission profiles with nominal delta-v requirements.
- 2: Incorporate variations in delta-v for interplanetary transfers to simulate gravitational assists and orbital dynamics.
- 3: **for** each iteration of the Monte Carlo simulation **do**
- 4: Adjust delta-v requirements for interplanetary transfer based on simulated variability.
- 5: Recalculate propellant mass requirements using the adjusted delta-v.
- 6: Optimize the propulsion distribution for the new conditions.
- 7: end for
- 8: Aggregate the results from all Monte Carlo iterations.
- 9: Determine the average and variability of the total propellant mass required.
- 10: Report the optimized propulsion distribution and impact of environmental dynamics on propellant mass.

Results

The incorporation of environmental and orbital dynamics into the simulation further adjusted the propellant mass requirements:

- For the mission to Mars, the total propellant mass required was observed to vary significantly across the Monte Carlo simulations, reflecting the impact of orbital dynamics on mission planning.
- Similarly, the mission to Venus showed a notable increase in variability of the total propellant mass, underscoring the challenges in planning missions with precise gravitational assists.

These extended simulation experiments highlight the complex interplay between propulsion system characteristics, spacecraft operational conditions, and environmental dynamics in determining the optimal propellant distribution for space missions. The findings emphasize the need for flexible and robust optimization frameworks that can adapt to a wide range of uncertainties and operational constraints.

By incorporating variable propulsion efficiencies and accounting for environmental and orbital dynamics, we can achieve a more fundamental understanding of propellant mass requirements, thereby enhancing the reliability and feasibility of future space missions.

In summary, our optimization framework employs a hybrid approach, integrating both chemical and electric propulsion systems to minimize the overall propellant mass required for interorbital transfers. The optimization algorithm dynamically determines the optimal distribution of propulsion types across different mission segments by balancing the high thrust capability of chemical propulsion with the high efficiency of electric propulsion. This involves calculating the propellant mass required for each segment and adjusting the propulsion distribution to achieve the lowest total propellant mass, while meeting the delta-v requirements for the mission.

Although our study provides a detailed mathematical framework for this optimization process, we acknowledge the importance of visualizing achieved trajectories to fully understand how the optimization operates in practice. Presently, our analysis focuses on the optimization algorithm and its outcomes without delving into trajectory visualization. Future work could include replicating the optimized mission sequences in advanced aerospace simulation tools such as GMAT (General Mission Analysis Tool) or STK (Systems ToolKit). These simulations would offer a visual representation of where chemical and electric propulsion burns are utilized within a mission, enhancing our understanding of the optimization's practical application. While the incorporation of such simulations is beyond the scope of this current study, we recognize their value in providing comprehensive insights into mission planning and optimization.

6.3. Transitioning Towards High-Fidelity Simulations with GMAT

While the mathematical framework presented in this study serves as a valuable tool for early mission analysis and propellant optimization, it inherently simplifies various complex aspects inherent to space missions. Recognizing these limitations, the path forward in a real mission would be to extended analysis within a framework such as the General Mission Analysis Tool (GMAT) environment. This transition would aim to encapsulate a more comprehensive array of mission dynamics and environmental factors, offering deeper insights into the practical implementation of the mission plans.

GMAT, with its robust simulation capabilities, allows for the detailed modeling of spacecraft trajectories, incorporating gravitational assists, atmospheric drag variations, and the complex gravitational fields of multiple celestial bodies. Such a high-fidelity simulation environment is crucial for validating the initial findings derived from a mathematical optimization framework, ensuring their applicability in real-world mission scenarios. Algorithm 5 illustrates the procedure.

Algorithm 5 Implementation Approach in GMAT for Spacecraft Trajectory Optimization

- 1: Define the spacecraft and its initial conditions including mass and aerodynamic properties.
- 2: Setup the environmental model including gravitational bodies, atmospheric models, and solar radiation pressure.
- 3: Configure the force model to include relevant forces acting on the spacecraft: gravitational forces from Earth, the Moon, and the Sun; solar radiation pressure; and atmospheric drag.
- 4: Establish the propulsion system models for both chemical and electric thrusters, specifying characteristics such as specific impulse and thrust levels.
- 5: Design the mission sequence, detailing each maneuver and its intended propulsion method (chemical or electric).
- 6: Implement impulsive burns and low-thrust arcs, setting initial guesses for maneuver magnitudes and directions.
- 7: Use GMAT's optimization tools to refine the mission plan:
 - 1. Specify the optimization objective (e.g., minimize total propellant mass or mission duration).
 - 2. Define constraints (e.g., maximum allowable thrust or specific impulse values).
 - 3. Initiate the optimization process to iteratively adjust maneuver parameters.
- 8: Analyze the optimized trajectory, examining how chemical and electric burns are integrated and the resulting spacecraft path.
- 9: Validate the results through comparison with known mission profiles or theoretical expectations.
- 10: Document the setup, optimization process, and outcomes for reference in mission planning and further studies.

It is imperative to highlight that this approach, while significantly more detailed, still represents a simulation. Real mission design involves iterative refinements based on simulation results, experimental data, and evolving mission objectives. GMAT simulations offer a platform for such refinements, providing a realistic approximation of spacecraft behavior under a myriad of mission-specific conditions.

Although the implementation of this proposed framework in GMAT is beyond the scope of our current study, it represents a crucial step for future research. Establishing a comprehensive GMAT or STK simulation based on the initial optimization findings will bridge the gap between theoretical analysis and practical mission design.

7. Conclusions

This study embarked on an exploration of propulsion system optimization for lunar missions, with a focus on minimizing propellant mass through a hybrid approach combining chemical and electric propulsion. The methodology employed rigorous mathe-

matical models to calculate delta-v requirements for mission segments and optimize the distribution of propulsion methods to meet these requirements efficiently.

7.1. Summary of Key Findings

The optimization model's results highlight the feasibility and benefits of a hybrid propulsion strategy for lunar exploration missions. Key findings include the following:

- Significant reductions in propellant mass can be achieved by optimizing the distribution between chemical and electric propulsion, depending on the mission segment's specific delta-v requirements.
- The hybrid propulsion approach offers a balanced solution that leverages the high thrust of chemical propulsion for critical maneuvers and the high efficiency of electric propulsion for sustained operations, thereby enhancing the overall mission efficiency.
- This strategy enables more flexible and ambitious mission profiles, potentially allowing for additional payloads, extended mission durations, and reduced launch costs.

7.2. Recommendations for Spacecraft Design and Mission Planning

Based on the study's findings, we recommend the following considerations for future spacecraft design and mission planning:

- Incorporate modular propulsion systems that allow for the strategic use of chemical and electric propulsion according to mission phase requirements.
- Emphasize the development and integration of advanced electric propulsion technologies to further capitalize on their efficiency benefits for long-duration missions.
- Consider the implications of propulsion system selection on spacecraft design, particularly in terms of power requirements, thermal management, and structural integrity.

7.3. Suggestions for Future Research

While this study provides a foundational understanding of propulsion optimization for lunar missions, further research is essential to address the complexities of space exploration. Future research directions include:

- Expanding the optimization model to incorporate more detailed mission parameters, including launch windows, gravitational assists, and variable mission objectives.
- Investigating the potential of emerging propulsion technologies, such as nuclear thermal propulsion or advanced electric propulsion systems, to enhance mission capabilities.
- Exploring the integration of In Situ Resource Utilization (ISRU) technologies with propulsion systems to enable sustainable exploration architectures.
- Conducting case studies of specific mission scenarios to validate and refine the proposed optimization framework.

In conclusion, the pursuit of efficient and optimized propulsion strategies stands as a cornerstone of future lunar exploration efforts. By embracing a holistic approach to propulsion system selection and optimization, we can unlock new possibilities for the sustainable exploration of the Moon and beyond, paving the way for humanity's next giant leap in space.

Author Contributions: Conceptualization, J.D.C. and I.D.Z.; funding acquisition, J.D.C. and I.D.Z.; investigation, I.D.Z. and J.D.C.; methodology, I.D.Z. and J.D.C.; software, J.D.C. and I.D.Z.; supervision, J.D.C. and I.D.Z.; writing—original draft, J.D.C.; writing—review and editing, J.D.C. and I.D.Z. All authors have read and agreed to the published version of the manuscript.

Funding: We thank the following funding sources from GOETHE-University Frankfurt am Main; 'DePP-Dezentrale Plannung von Platoons im Straßengüterverkehr mit Hilfe einer KI auf Basis einzelner LKW', 'Center for Data Science & AI', and 'Hessian.AI-AIBiology'. The work is also developed under UFV R&D pre-competitive project 'OpenMaas: Open Manufacturing as a Service'.

Data Availability Statement: The data presented in this study are openly available in FigShare at https://doi.org/10.6084/m9.figshare.25428211.

Conflicts of Interest: The authors declare that they have no conflicts of interest. The funders had no role in the design of the study, in the collection, analyses, or interpretation of data, in the writing of the manuscript, or in the decision to publish the results.

Abbreviations

The following abbreviations are used in this manuscript:

Nuclear Electric PropulsionNEPNuclear Thermal PropulsionNTPLow-Earth OrbitLEOGeostationary Earth OrbitGEO

ISRU In Situ Resource Utilization

 $\begin{array}{lll} \mbox{Earth-Moon Lagrange Point 1} & \mbox{EML1} \\ \mbox{Specific Impulse} & \mbox{I_{sp}} \\ \mbox{Sequential Quadratic Programming} & \mbox{SQP} \\ \mbox{Artificial Intelligence} & \mbox{AI} \\ \mbox{Machine Learning} & \mbox{ML} \\ \mbox{Physics-Informed Neural Networks} & \mbox{PINN} \\ \end{array}$

References

- 1. de Curtò, J.; de Zarzà, I.; Calafate, C.T. UWB and MB-OFDM for Lunar Rover Navigation and Communication. *Mathematics* **2023**, 11, 3835. [CrossRef]
- 2. Gabrielli, R.A.; Herdrich, G. Review of nuclear thermal propulsion systems. Prog. Aerosp. Sci. 2015, 79, 92–113. [CrossRef]
- 3. Goddard, R.H. A Method of Reaching Extreme Altitudes. In *Smithsonian Miscellaneous Collections*; Smithsonian Institution Press: Washington, DC, USA, 1920.
- 4. Oberth, H. Ways to Spaceflight. In NASA Technical Documents; NASA: Springfield, VA, USA, 1972.
- 5. Tsiolkovsky, K.E. The Exploration of Cosmic Space by Means of Reaction Devices. Sci. Rev. 1903, 5, 60–132.
- 6. Gomez, I.; Aplin, K.L.; Lawrie, A.; Toomer, C.A. Modelling an Ion Thruster for a Small Spacecraft in Very Low Earth Orbit. *J. Phys. Conf. Ser.* **2024**, 2702, 012019. [CrossRef]
- 7. Munro-O'Brien, T.F.; Ryan, C.N. Performance of a low power Hall effect thruster with several gaseous propellants. *Acta Astronaut*. **2023**, 206, 257–273. [CrossRef]
- 8. Tejeda, J.M.; Knoll, A. An oxygen-fuelled Hall Effect Thruster: Channel length, ceramic walls and anode material experimental analyses. *Acta Astronaut*. **2023**, 203, 268–279. [CrossRef]
- 9. Tirila, V.-G.; Demairé, A.; Ryan, C.N. Review of alternative propellants in Hall thrusters. *Acta Astronaut*. **2023**, 212, 284–306. [CrossRef]
- 10. Sutton, G.P.; Biblarz, O. Rocket Propulsion Elements, 8th ed.; John Wiley & Sons: Hoboken, NJ, USA, 2010.
- 11. Goebel, D.M.; Katz, I. Fundamentals of Electric Propulsion: Ion and Hall Thrusters; John Wiley & Sons: Hoboken, NJ, USA, 2008.
- 12. Rayman, M.D.; Varghese, P.; Lehman, D.H.; Livesay, L.L. Results from the Deep Space 1 Technology Validation Mission. *Acta Astronaut*. **2000**, 47, 475–487. [CrossRef]
- 13. Russell, C.T.; Raymond, C.A. The Dawn Mission to Minor Planets 4 Vesta and 1 Ceres. Space Sci. Rev. 2011, 163, 3–23. [CrossRef]
- 14. Cha, P.R.; Rucker, M.A.; Burke, L.M.; Edwards, S.J.; Trent, D.J.; Chappell, M.B. Characterization of In-Space Propulsion Trade Space to Support Initial Human Mars Segment. In Proceedings of the 74th International Astronautical Congress (IAC2023), Baku, Azerbaijan, 2–6 October 2023.
- 15. Burke, L.M.; Oleson, S.R.; Zoloty, Z.C.; Smith, D.; Havens, M. Combined 1-MW Solar Electric and Chemical Propulsion for Crewed Mars Missions. In Proceedings of the ASCEND 2023, Las Vegas, NV, USA, 23–25 October 2023; p. 4789.
- 16. Patel, P.R.; Scheeres, D.J. Rapid and Automatic Reachability Estimation of Electric Propulsion Spacecraft. *J. Astronaut. Sci.* **2023**, 70, 45. [CrossRef]
- 17. Nikitaeva, D.; Thomas, L.D. Propulsion Alternatives for Mars Transportation Architectures. *J. Spacecr. Rocket.* **2023**, *60*, 520–532. [CrossRef]
- 18. Rovey, J.L.; Lyne, C.T.; Mundahl, A.J.; Rasmont, N.; Glascock, M.S.; Wainwright, M.J.; Berg, S.P. Review of multimode space propulsion *Prog. Aerosp. Sci.* **2020**, *118*, 100627.
- 19. Oleson, S.R.; Burke, L.; Dudzinski, L.; Fittje, J.; Mason, L.S.; Packard, T.; Schmitz, P.; Gyekenyesi, J.; Faller, B. A Combined Nuclear Electric and Chemical Propulsion Vehicle Concept for Piloted Mars Opposition Class Missions. In Proceedings of the ASCEND 2020, Virtual, 16–18 November 2020; p. 4055.
- 20. Chai, P.; Qu, M.; Saputra, B. Human Mars Mission In-Space Transportation Sensitivity for Nuclear Electric/Chemical Hybrid Propulsion. In Proceedings of the AIAA Propulsion and Energy 2021 Forum, Virtual, 9–11 August 2021.

- Duchek, M.; Clark, M.; Pensado, A.; Harnack, C.; Machemer, W.; Grella, E.; Qu, M. Hybrid NEP-Chemical Vehicle and Propulsion Technology Study for Crewed Mars Missions. In Proceedings of the 68th JANNAF Propulsion Meeting, Virtual, 7–17 June 2021.
- 22. Levchenko, I.; Goebel, D.M.; Bazaka, K. Electric propulsion of spacecraft. Phys. Today 2022, 75, 38–44. [CrossRef]
- 23. Miao, X.; Zhang, H.; Wang, Q.; Xia, Y.; Sun, W. Optimum design of nuclear electric propulsion spacecraft for deep space exploration. *Energy Rep.* **2022**, *8*, 9629–9641. [CrossRef]
- 24. Bushnell, D.M.; Moses, R.W.; Choi, S.H. *Frontiers of Space Power and Energy*; NASA/TM-20210016143; National Aeronautics and Space Administration: Washington, DC, USA, 2021.
- 25. O'Reilly, D.; Herdrich, G.; Kavanagh, D.F. Electric propulsion methods for small satellites: A review. *Aerospace* **2021**, *8*, 22. [CrossRef]
- Chai, P.; Prasad, A.; McBrayer, K.T.; McCrea, A.C.; Qu, M.; Merrill, R.G. Crewed Mars Mission Mode Options for Nuclear Electric/Chemical Hybrid Transportation Systems. In Proceedings of the ASCEND 2021, Las Vegas, NV, USA, 15–17 November 2021; p. 4136.
- 27. Bussard, R.W. Galactic matter and interstellar flight. Astronaut. Acta 1960, 6, 179-194.
- 28. Blatter, H.; Greber, T. Tau Zero: In the cockpit of a Bussard ramjet. Am. J. Phys. 2017, 85, 915–920. [CrossRef]
- 29. Schattschneider, P.; Jackson, A.A. The Fishback ramjet revisited. Acta Astronaut. 2022, 191, 227–234. [CrossRef]
- 30. Karimov, A.R.; Murad, P.A.; Yamschikov, V.A.; Baranov, D.S. Plasma Accelerator Utilizing the Medium of Near-Earth Space for Orbital Transfer Vehicles. *Appl. Sci.* **2023**, *13*, 13195. [CrossRef]
- 31. Yelnikov, R.V. Use of the Lyapunov functions for calculating the locally optimal control of a thrust vector during low-thrust interorbital transfer. *Cosm. Res.* **2021**, *59*, 212–221. [CrossRef]
- 32. Smith, M.; Craig, D.; Herrmann, N.; Mahoney, E.; Krezel, J.; McIntyre, N.; Goodliff, K. The Artemis Program: An overview of NASA's activities to return humans to the moon. In Proceedings of the 2020 IEEE Aerospace Conference, Big Sky, MT, USA, 7–14 March 2020; pp. 1–10.
- 33. Creech, S.; Guidi, J.; Elburn, D. Artemis: An overview of NASA's activities to return humans to the moon. In Proceedings of the 2022 IEEE Aerospace Conference (AERO), Big Sky, MT, USA, 5–12 March 2022.
- 34. Oche, P.A.; Ewa, G.A.; Ibekwe, N. Applications and challenges of artificial intelligence in space missions. *IEEE Access* **2021**. [CrossRef]
- 35. Raissi, M.; Perdikaris, P.; Karniadakis, G.E. Physics-informed neural networks: A deep learning framework for solving forward and inverse problems involving nonlinear partial differential equations. *J. Comput. Phys.* **2019**, *378*, 686–707. [CrossRef]

Disclaimer/Publisher's Note: The statements, opinions and data contained in all publications are solely those of the individual author(s) and contributor(s) and not of MDPI and/or the editor(s). MDPI and/or the editor(s) disclaim responsibility for any injury to people or property resulting from any ideas, methods, instructions or products referred to in the content.





Article

Backstepping and Novel Sliding Mode Trajectory Tracking Controller for Wheeled Mobile Robots

Hangjie Huang 1 and Jinfeng Gao 2,*

- Qixin Honors School, Zhejiang Sci-Tech University, Hangzhou 310018, China; 2021339930008@mails.zstu.edu.cn
- School of Information Science and Engineering, Zhejiang Sci-Tech University, Hangzhou 310018, China
- * Correspondence: jfgao@zstu.edu.cn

Abstract: A novel variable structure controller based on sliding mode is developed for addressing the trajectory tracking challenge encountered by wheeled mobile robots. Firstly, the trajectory tracking error model under the global coordinate system is established according to the kinematic model of the wheeled mobile robot. Secondly, the novel sliding mode algorithm and backstepping method are introduced to design the motion controller of the system, respectively. Different sliding mode surfaces are formulated to guarantee rapid and stable convergence of the system's trajectory tracking error to zero. Ultimately, comparative simulation trials validate the controller's ability to swiftly and consistently follow the reference trajectory. In contrast to traditional controllers, this controller shows rapid convergence, minimal error, and robustness.

Keywords: wheeled mobile robot (WMR); sliding mode control; trajectory tracking

MSC: 93-10

1. Introduction

In contrast to crawler robots, wheeled mobile robots are distinguished by their uncomplicated design, agility, flexibility, and ease of control [1]. These attributes render them highly promising for advancement in various sectors such as industry and aerospace. Consequently, the difficulties related to motion control in wheeled mobile robots have garnered significant interest among researchers. Nevertheless, the inherent complexities of these robots, such as their high nonlinearity, multivariate nature, and strong coupling, pose significant obstacles to effective motion control.

The illustration in Figure 1 depicts the path tracking of a wheeled mobile robot, with the solid line denoting the intended path and the dashed line indicating the robot's actual tracking path. The visual representation highlights a significant deviation between the intended trajectory and the path executed by the robot [2]. To enhance tracking precision and minimize errors, researchers have introduced various effective strategies for trajectory tracking control.

PID control algorithms are extensively employed as a well-established and effective method for regulating a wide range of dynamic systems. They are also suitable for addressing the trajectory tracking challenge encountered by wheeled mobile robots. For instance, a nonlinear controller is suggested in [3] using the trajectory linearization method (TLC) for an omnidirectional mobile robot. To improve trajectory tracking precision, ref. [4] integrate a neural network framework into the conventional PID control system to estimate the actual model of the system and dynamically optimize parameters. This integration leads to a significant improvement in trajectory tracking accuracy.

Currently, many factories utilize PID control in processing machinery to implement control algorithms. However, accurate modeling of parameters is essential for the successful application of this approach. The ideal model is often theoretical and may change during operation, making real-time adjustment of PID parameters challenging. Consequently, the sliding mode control algorithm has emerged as a viable alternative [5–8]. In [9], a controller is developed based on the position and heading errors of a mobile robot to enable the stable tracking of circular and straight paths despite significant tracking errors and external disturbances. To tackle trajectory tracking challenges in a perturbed single-wheeled mobile robot, two new sliding variables are introduced [10]. This leads to the development of a second-order sliding mode controller with a simple structure and efficient control performance.

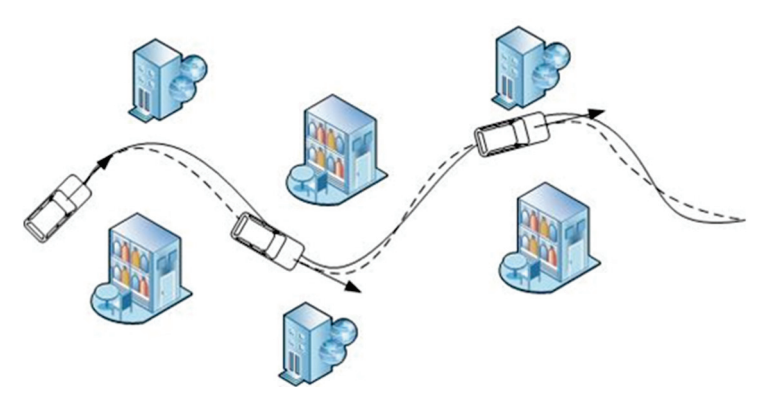


Figure 1. Mobile robot path tracking diagram.

As research progresses, scholars are moving beyond the mere convergence of controllers and are now seeking faster convergence rates and increased control accuracy. They are also moving away from relying on traditional mathematical models. Consequently, scholars have suggested integrating multiple control algorithms to enhance control outcomes. Examples include fuzzy PID control, inverse sliding mode control, and fuzzy adaptive sliding mode control. Sliding mode control is favored for its ability to enhance system convergence speed and mitigate interference. Therefore, combining sliding mode control with other control techniques using a hybrid sliding mode algorithm has shown promise in achieving superior control effects [11,12]. In a study by [13], an adaptive neural network sliding mode control method was introduced to effectively address external disturbances by incorporating adaptive neural network techniques. Another study [14] presents a design for a fuzzy adaptive sliding mode controller that utilizes fuzzy switching to replace the nonlinear switching term. This leads to improved tracking performance and enhanced resistance to interference. The research conducted in [15] integrates the kinematic and dynamic models of a wheeled mobile robot to derive second-order and third-order subsystems. Subsequently, adaptive non-singular fast terminal sliding mode controllers are developed for each subsystem. Furthermore, a novel adaptive sliding mode controller based on the barrier function is proposed in [16]. The barrier function is capable of dynamically adjusting the gain in response to disturbance magnitude, thereby enhancing the robustness of the controller.

The utilization of PID control strategies and sliding mode control techniques is outlined in Table 1. Furthermore, the applications of a hybrid sliding mode algorithm are delineated in Table 2.

Table 1. Typical applications of PID and SMC methods.

Subject	References	Object	Limitations	Proposed Research Directions
PID	[3,4]	Mobile robot	(1) Unable to handle high degree of nonlinearity.(2) Robustness is not enough.	(1) Parameter self-tuning.(2) Combined with intelligent algorithms.
SMC	[5–10]	AGV Mobile robot Mowing robots Intelligent vehicle	 Jitter caused by switching items. Higher accuracy requirements for system modeling. 	 Designing boundary layers or replacing switching functions. Estimation of uncertainty parameters.

Table 2. Typical applications of hybrid sliding mode algorithm.

Subject	References	Object	Highlights]	Highlights of Our Work
Hybrid sliding mode algorithm	[11]	Mobile robot Electro-hydraulic position system WMR NWMRs	Combined with the biofilm potential model. Utilizing the cubic Kalman algorithm and fuzzy compensation. Compensating the sum of perturbations with neural networks. Estimate the unknown parameters in real time. Combining adaptive control and terminal sliding mode control.	(1)	structure, easy application. Continuous switching term to reduce jitter. New sliding mode Surface
	[12]			(2)	
	[13]			(3) (4)	
	[14]				
	[15]				
	[16]		Strong robustness to uncertainties and perturbations.		

Furthermore, aside from the aforementioned control techniques, the predominant approaches for achieving trajectory tracking in wheeled mobile robots include backstepping control methods [17–20] and predictive control methods [21–23]. In the current body of research, the system architecture of mobile robots is commonly presented in two primary forms. One approach involves the kinematic model, which elucidates the correlation between the positional orientation of the robot and the overall velocity of the WMR (wheeled mobile robot). The other method entails the dynamics model, which delineates the connection between the WMR's overall velocity and the disturbance torque acting upon it. The majority of scholarly works predominantly employ a single-loop control configuration, wherein the control law design directly addresses the suppression of positional orientation errors.

Based on the above literature, this study focuses on enhancing trajectory tracking performance for wheeled mobile robots by implementing sliding mode control techniques. By employing the kinematic modeling of mobile robots, the challenge of trajectory tracking is redefined as a systematic error stabilization problem. The paper introduces a sliding mode controller that integrates backstepping methodology, as well as a novel sliding mode controller. Both controllers enable the mobile robot to quickly and accurately track a predefined reference trajectory. The main contributions of this paper are as follows:

- 1. Two distinct design methodologies are employed for the development of the sliding mode controller, each of which holds significant reference value;
- A continuous and differentiable function is used instead of the sign function to reduce the high-frequency oscillations that occur due to the abrupt changes in the sign function at critical points;
- A novel sliding mode surface is suggested by incorporating the Lyapunov function, providing a new direction for future research.

The structure of this document is as follows. In Section 2, the kinematic model and trajectory error model of the wheeled mobile robot are outlined. The design of the backstepping sliding mode controller and the new sliding mode controller is presented in

Section 3. Section 4 verifies the effectiveness of the controllers. Concluding remarks are provided in Section 5.

2. Problem Formulation

The diagram in Figure 2 illustrates the structural configuration of the mobile robot, featuring four wheels, each powered by independent motors. A local coordinate system xoy is established within the framework of the wheeled mobile robot, with designated positional coordinates $[x,y,\theta]^T$. The center of the wheeled mobile robot is denoted as o, the distance between the center and the rear drive wheels in the x-direction is denoted as d, and θ represents the angle between the direction of movement and the x-axis in the horizontal plane. The linear and angular velocities during the movement of the wheeled mobile robot are represented by v and ω , respectively.

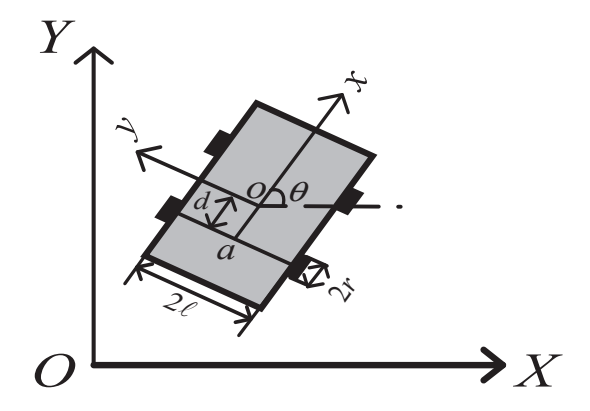


Figure 2. Model diagram of wheeled mobile robot structure.

In order to streamline the kinematic model, it is suggested to set d equal to zero, meaning that the center of mass aligns with the geometric center. The kinematic equations of a wheeled mobile robot can be described as [24]:

$$\begin{bmatrix} \dot{x} \\ \dot{y} \\ \dot{\theta} \end{bmatrix} = \begin{bmatrix} \cos \theta & 0 \\ \sin \theta & 0 \\ 0 & 1 \end{bmatrix} \begin{bmatrix} \nu \\ \omega \end{bmatrix}$$
 (1)

In the local coordinate system xoy, the position error coordinates are defined as $[x_e, y_e, \theta_e]^T$. The position coordinates of the mobile robot in the local coordinate system xoy and the global coordinate system XOY satisfy the following relationship:

$$\begin{cases} x_e = x_r - x \\ y_e = y_r - y \\ \theta_e = \theta_r - \theta \end{cases}$$
 (2)

$$\begin{cases} x_r = x + x_e \cos \theta - y_e \sin \theta \\ y_r = y + x_e \sin \theta + y_e \cos \theta \end{cases}$$
 (3)

By substituting Equation (3) into Equation (2), the positional error coordinates can be derived as shown below:

$$\begin{bmatrix} x_e \\ y_e \\ \theta_e \end{bmatrix} = \begin{bmatrix} \cos \theta & \sin \theta & 0 \\ -\sin \theta & \cos \theta & 0 \\ 0 & 0 & 1 \end{bmatrix} \begin{bmatrix} x_r - x \\ y_r - y \\ \theta_r - \theta \end{bmatrix}$$
(4)

The derivation of (4) gives the differential equation for the trajectory error of the mobile robot:

$$\begin{bmatrix} \dot{x}_e \\ \dot{y}_e \\ \dot{\theta}_e \end{bmatrix} = \begin{bmatrix} y_e \omega + \nu_r \cos \theta_e - \nu \\ -x_e \omega + \nu_r \sin \theta_e \\ \omega_r - \omega \end{bmatrix}$$
 (5)

3. Controller Design

3.1. Sliding Mode Controller Based on Backstepping

The backstepping control design approach is commonly employed in nonlinear systems because of its ability to integrate controller design with Lyapunov stability-based proofs, decompose complex systems into simpler subsystems, and provide a clear structure for the controller [25]. Consequently, this method is utilized to develop the sliding mode control switching function to achieve trajectory tracking control in wheeled mobile robots.

Theorem 1. For any $x \in R$ and x bounded, $\mu(x) = x \sin(\arctan x) \ge 0$, the equality sign holds if and only if x = 0.

Proof of Theorem 1. The situations of cases x=0, x>0 and x<0 were addressed individually. In scenario x=0, there exist $\mu(x)=0$; in cases x>0, it follows that there is a relationship where $\arctan x \in (0,\frac{\pi}{2})$, $\sin(\arctan) \in (0,1)$, $\mu(x)>0$; and when x<0, there is a presence of $\arctan x \in (-\frac{\pi}{2},0)$, $\sin(\arctan) \in (-1,0)$, $\mu(x)>0$. \square

When $x_e = 0$, the Lyapunov function is characterized as follows:

$$V = \frac{1}{2}y_e^2 \tag{6}$$

The derivative of V is computed as

$$\dot{V} = \dot{y}_e y_e = (v_r \sin \theta_e - x_e \omega) y_e = y_e v_r \sin \theta_e \tag{7}$$

Let $\theta_e = -\arctan(v_r y_e)$, and so there is

$$\dot{V} = y_e v_r \sin(-\arctan(y_e v_r)) = -y_e v_r \sin(\arctan(y_e v_r))$$
(8)

According to Theorem 1, $\dot{V} \leq 0$ holds. Therefore, when x_e converges to 0 and θ_e converges to $-\arctan(v_ry_e)$, the systematic error y_e also converges to 0. At the same time, the systematic error θ_e converges to 0.

The sliding mode surface is constructed as follows:

$$s_1 = x_e \tag{9}$$

$$s_2 = \theta_e + \arctan(v_r y_e) \tag{10}$$

The double power convergence rate is utilized to accelerate the convergence of the sliding mode surface towards zero, effectively eliminating tracking errors. This is represented by the following equation:

$$\dot{s}_1 = -\alpha_{11}|s_1|^{\frac{p_{11}}{q_{11}}} \operatorname{sign}(s_1) - \alpha_{12}|s_1|^{\frac{p_{12}}{q_{12}}} \operatorname{sign}(s_1)$$
(11)

$$\dot{s}_{2} = -\alpha_{21}|s_{2}|^{\frac{p_{21}}{q_{21}}} \operatorname{sign}(s_{2}) - \alpha_{22}|s_{2}|^{\frac{p_{22}}{q_{22}}} \operatorname{sign}(s_{2})$$
(12)

where α_{11} , α_{12} , α_{21} , α_{22} > 0; p_{11} < q_{11} ; p_{12} > q_{12} ; p_{21} < q_{21} ; p_{22} > q_{22} , and all are a positive odd number.

The derivation of Equations (11) and (12) and setting $\psi = \arctan(v_r y_e)$ results in the following expressions:

$$\dot{s}_1 = y_e \omega + v_r \cos \theta_e - v \tag{13}$$

$$\dot{s}_2 = \omega_r - \omega + \frac{\partial \psi}{\partial v_r} \dot{v}_r + \frac{\partial \psi}{\partial y_e} (-x_e \omega + v_r \sin \theta_e)$$
 (14)

where $\frac{\partial \psi}{\partial v_r} = \frac{y_e}{1 + (v_r y_e)^2}$, $\frac{\partial \psi}{\partial y_e} = \frac{v_r}{1 + (v_r y_e)^2}$.

By integrating Equations (11) through (14), the backstepping sliding mode controller can be derived:

$$\omega = \omega_r + \frac{\partial \psi}{\partial y_e} v_r \sin \theta_e + \frac{\partial \psi}{\partial v_r} \dot{v}_r + \alpha_{21} |s_2|^{\frac{p_{21}}{q_{21}}} \operatorname{sign}(s_2) + \alpha_{22} |s_2|^{\frac{p_{22}}{q_{22}}} \operatorname{sign}(s_2)$$
 (15)

$$\nu = y_e \omega + \nu_r \cos \theta_e + \alpha_{11} |s_1|^{\frac{p_{11}}{q_{11}}} \operatorname{sign}(s_1) + \alpha_{12} |s_1|^{\frac{p_{12}}{q_{12}}} \operatorname{sign}(s_1)$$
 (16)

3.2. Novel Sliding Mode Controller

We set the slide mode surface function as

$$s_1 = \theta_e \tag{17}$$

$$s_2 = k_1 x_e - k_2 \omega_r y_e \tag{18}$$

where $k_1, k_2 > 0$, $\omega_r \neq 0$, and all are constants.

Derivation of (17) and (18) leads to

$$\dot{s}_1 = \dot{\theta}_e \tag{19}$$

$$\dot{s}_2 = k_1 \dot{x}_e - k_2 \omega_r \dot{y}_e \tag{20}$$

The law of dual power convergence is applicable to Equations (21) and (22):

$$\dot{s}_1 = -\alpha_{11}|s_1|^{\frac{p_{11}}{q_{11}}} \operatorname{sign}(s_1) - \alpha_{12}|s_1|^{\frac{p_{12}}{q_{12}}} \operatorname{sign}(s_1)$$
 (21)

$$\dot{s}_{2} = -\alpha_{21}|s_{2}|^{\frac{p_{21}}{q_{21}}} \operatorname{sign}(s_{2}) - \alpha_{22}|s_{2}|^{\frac{p_{22}}{q_{22}}} \operatorname{sign}(s_{2})$$
(22)

where α_{11} , α_{12} , α_{21} , α_{22} , > 0; $p_{11} < q_{11}$; $p_{12} > q_{12}$; $p_{21} < q_{21}$; $p_{22} > q_{22}$, and all are a positive odd number.

The angular velocity controller for trajectory tracking is derived from Equations (5), (19), and (21):

$$\omega = \omega_r + \alpha_{11}|s_1|^{\frac{p_{11}}{q_{11}}} \operatorname{sign}(s_1) + \alpha_{12}|s_1|^{\frac{p_{12}}{q_{12}}} \operatorname{sign}(s_1)$$
 (23)

When the sliding mode surface $s_1 = \theta_e$ converges to 0 in finite time, $\omega = \omega_r$ is obtained. The trajectory tracking velocity controller is derived from the associative Equations (5), (20), and (22):

$$\nu = y_e \omega_r + \nu_r + \frac{1}{k_1} \left(k_2 \omega_r^2 x_e + \alpha_{21} |s_2|^{\frac{p_{21}}{q_{21}}} \operatorname{sign}(s_2) + \alpha_{22} |s_2|^{\frac{p_{22}}{q_{22}}} \operatorname{sign}(s_2) \right)$$
(24)

3.3. Convergence Time Analysis of the Systems

The presence of two power functions within the sliding mode surface poses challenges for determining the convergence time through analytical methods. As a result, an alternative approach involves establishing an upper bound for the convergence time. Assuming the initial state of the system $s_i(0) > 1$, i = 1, 2, the convergence process can be divided into two distinct time intervals: the first period spans from the initial state $s_i(0)$ to $s_i = 1$, and the second period extends from $s_i = 1$ to the sliding mode surface.

It was initially demonstrated that the sliding mode surface converges to 0 within a finite duration.

Phase I: From the initial state $s_i(0) > 1$ to the stage $s_i = 1$ due to $|s_1| > 1$, $\frac{p_{12}}{q_{12}} > 1$, so in the system the second term of Equation (21) plays a dominant role in the convergence effect; ignoring the first term, the system is:

$$\dot{s}_1 = -\alpha_{12} |s_1|^{\frac{p_{12}}{q_{12}}} \operatorname{sign}(s_1) \tag{25}$$

Determining the duration for the system to reach $s_1 = 1$ from the initial state $s_1(0) > 1$ involves the following calculation:

$$\frac{ds_1}{dt} = -\alpha_{12} s_1^{\frac{p_{12}}{q_{12}}} \tag{26}$$

The definite integral of Equation (26) results in a solution:

$$\int_{s_1(0)}^{s_1=1} s_1^{-\frac{p_{12}}{q_{12}}} ds_1 = \int_0^{t_1} -\alpha_{12} dt$$
 (27)

The duration required to travel from $s_1(0) > 1$ to $s_1 = 1$ can be calculated using Equation (27):

$$t_1 = \frac{-q_{12}}{\alpha_{12}(q_{12} - p_{12})} \left(1 - s_1(0)^{1 - \frac{p_{12}}{q_{12}}}\right) \tag{28}$$

As the initial term of the convergence law within the system is disregarded, the effective convergence duration of the sliding mode surface during the initial phase is shorter than t_1 .

Phase II: The system transitions from state $s_1 = 1$ to the sliding mode surface. And since $|s_1| < 0$, $0 < \frac{p_{11}}{q_{11}} < 1$, the primary term in the system significantly influences the convergence outcome, with the secondary term being disregarded. Consequently, the system can be expressed as

$$\dot{s}_1 = -\alpha \, |s_1|^{\frac{p_{11}}{q_{11}}} \operatorname{sign}(s_1)$$
 (29)

Determining the duration for the system to reach the sliding mode surface from $s_1 = 1$ involves the following calculation:

$$\frac{ds_1}{dt} = -\alpha_{11} s_1^{\frac{p_{11}}{q_{11}}} \tag{30}$$

The definite integral to (30) yields

$$\int_{s_1=1}^{s_1=0} s_1^{-\frac{p_{11}}{q_{11}}} ds_1 = \int_{t_1}^{t_1+t_2} -\alpha_{11} dt$$
 (31)

The duration required for the second stage to converge can be calculated based on Equation (31):

$$t_2 = \frac{-q_{11}}{\alpha_{11}(q_{11} - p_{11})} \tag{32}$$

As the second term of the convergence law within the system is disregarded, the effective convergence duration of the sliding mode surface $s_1 = \theta_e$ during the subsequent phase is shorter than t_2 .

Hence, the time required for the system to reach the sliding mode surface from its initial state does not exceed $t_{s1} = t_1 + t_2$.

When the initial state $s_1(0) < -1$, the time for the system to converge to the sliding mode surface is also divided into two stages: from the initial state to $s_1 = -1$ and $s_1 = -1$ arrives at the sliding mode surface, the analysis and calculation principle is the same as that of the initial state $s_1(0) > 1$ of the system.

Similarly, it can be shown that the sliding mode surface $s_2 = k_1 x_e - k_2 \omega_r y_e$ converges to 0 in a finite time, and the convergence time is denoted as t_{s2} .

3.4. Convergence Time Analysis of the Systems

When $t > t_{s1} + t_{s2}$, s_1 , s_2 converges to 0:

$$\begin{cases} \omega = \omega_r \\ \nu = y_e \omega_r + \nu_r + \frac{1}{k_1} k_2 \omega_r^2 x_e \end{cases}$$
 (33)

The equation denoted as (5) has the potential to be converted into a different form:

$$\begin{cases} \dot{x}_e = y_e \omega_r + \nu_r - \nu \\ \dot{y}_e = -x_e \omega \end{cases}$$
 (34)

The Lyapunov function is selected, as indicated by Equation (35):

$$V_x = \frac{1}{2}x_e^2 (35)$$

The derivation of Equation (35) demonstrates that

$$\dot{V}_{x} = x_{e}\dot{x}_{e} = x_{e}(y_{e}\omega_{r} + \nu_{r} - \nu) = x_{e}\left(y_{e}\omega_{r} + \nu_{r} - y_{e}\omega_{r} - \nu_{r} - \frac{k_{2}\omega_{r}^{2}x_{e}}{k_{1}}\right)
= -\frac{k_{2}\omega_{r}^{2}}{k_{1}}x_{e}^{2} = -\frac{2k_{2}\omega_{r}^{2}}{k_{1}}V_{x} \le 0$$
(36)

Therefore, when $\omega_r \neq 0$, x_e asymptotically converges to 0. The equation represented by (18) can be restated as

$$y_e = (k_1 x_e - s_2) / (k_2 \omega_r) \tag{37}$$

Since x_e converges to 0 asymptotically, the sliding mode surfaces s_1 , s_2 converge to 0 in finite time, and thus y_e also converges to 0 asymptotically. In summary, it can be seen that the trajectory tracking error x_e , y_e converges to 0 asymptotically under the action of the sliding mode controller based on the law of double power convergence, which θ_e converges to zero in a finite time.

3.5. Controller Improvements

In the realm of sliding mode control design, controllers are often conceptualized in an overly idealized manner. One common idealization in sliding mode control involves the utilization of the sign function term, which requires the controller to operate at an infinite switching frequency. However, in practical applications, the control device is typically non-ideal and incapable of achieving infinite switching frequencies. Consequently, the actual motion state of the sliding mode does not precisely align with the pre-defined sliding mode surface, leading to oscillations on either side of the surface, known as jitter vibration.

Jitter vibration poses various risks, such as increased energy consumption, potential damage to system hardware, and other associated hazards. Therefore, investigating methods to suppress jitter vibration in sliding mode control holds significant importance. In this section, we introduce three symbolic functions that can serve as viable alternatives to the sign function. In general, the saturation function, sigmoid function, and hyperbolic tangent function are commonly employed as alternatives to the sign function. The fundamental concept behind the saturation function approach involves the utilization of a continuous saturation function instead of a sign function. This technique involves creating a boundary layer with controlled continuity within the layer and applying normal sliding mode control

outside the layer, thereby mitigating the impact of oscillations. A prevalent representation of the saturation function is depicted as follows:

$$sat(x) = \begin{cases} sign(x), |x| > \Delta \\ \frac{x}{\Delta}, |x| < \Delta \end{cases}$$
 (38)

where Δ is the boundary layer.

Similar to the saturation function, the common sigmoid function is:

$$sigmoid(x) = \frac{1 - e^{-\varepsilon x}}{1 + e^{-\varepsilon x}}$$
(39)

Similarly, the common hyperbolic tangent function is:

$$tanh \eta x = \frac{e^{\eta x} - e^{-\eta x}}{e^{\eta x} + e^{-\eta x}} \tag{40}$$

In this paper, the decision was made to employ the sigmoid function in place of the sign function. By revising Equations (15), (16), (23), and (24), one can derive the enhanced backstepping sliding mode controller (BSMC) and the novel improved sliding mode controller (NSMC):

$$\begin{cases}
\nu = y_e \omega + \nu_r \cos \theta_e + \alpha_{11} |s_1|^{\frac{p_{11}}{q_{11}}} sigmoid(s_1) + \alpha_{12} |s_1|^{\frac{p_{12}}{q_{12}}} sigmoid(s_1) \\
\omega = \omega_r + \frac{\partial \psi}{\partial y_e} \nu_r \sin \theta_e + \frac{\partial \psi}{\partial \nu_r} \dot{\nu}_r + \alpha_{21} |s_2|^{\frac{p_{21}}{q_{21}}} sigmoid(s_2) + \alpha_{22} |s_2|^{\frac{p_{22}}{q_{22}}} sigmoid(s_2)
\end{cases}$$
(41)

$$\begin{cases} v = y_{e}\omega_{r} + \nu_{r} + \frac{1}{k_{1}} \left(k_{2}\omega_{r}^{2}x_{e} + \alpha_{21}|s_{2}|^{\frac{p_{21}}{q_{21}}} sigmoid(s_{2}) + \alpha_{22}|s_{2}|^{\frac{p_{22}}{q_{22}}} sigmoid(s_{2}) \right) \\ \omega = \omega_{r} + \alpha_{11}|s_{1}|^{\frac{p_{11}}{q_{11}}} sigmoid(s_{1}) + \alpha_{12}|s_{1}|^{\frac{p_{12}}{q_{12}}} sigmoid(s_{1}) \end{cases}$$

$$(42)$$

4. Simulation Results

In this section, in order to verify the effectiveness of the controller proposed in this paper, the comparative simulation experiment between BSMC, NSMC and PID utilized MATLAB/SIMULINK as the primary platform. The control structure of the wheeled mobile robot is depicted in Figure 3.

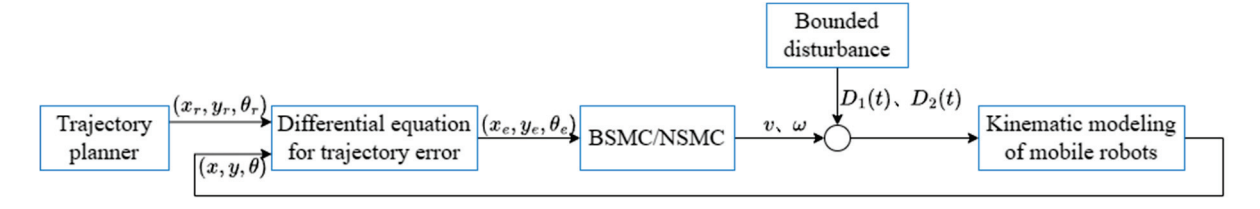


Figure 3. Control structure diagram.

In a simulation test, the initial position of the robot was set to be $[1, 1, -1]^T$, the initial position of the preset trajectory was set to be $[2, 1, 2]^T$, and the set reference velocity was $v_r = 2$ m/s. The controller parameters are shown in Table 3.

Table 3. Controller parameter table.

Parameter	Number	Parameter	Number	Parameter	Number
α_{11}	15	<i>p</i> ₁₂	9	921	9
α_{12}	15	p_{21}	7	922	5
α_{21}	15	p_{22}	13	k_1	10
α_{22}	15	911	9	k_2	15
p_{11}	5	912	5	ε	50

Their comparative simulation results are shown in Figures 4 and 5. The results illustrate that both controllers can effectively track the trajectory and converge the trajectory error. The two controllers exhibit quicker convergence and achieve greater accuracy in convergence compared to the PID controller. In contrast to BSMC, NSMC can converge faster on the systematic errors x_e , y_e , but the systematic error θ_e converges slower than BSMC. The primary distinction between NSMC and BSMC lies in the configuration of the sliding mode surface (Equations (6), (7), (17), and (18)), with different sliding mode surfaces significantly affecting the error convergence process. The design of the sliding mode surface continues to hold considerable importance for its functionality. The simulation results indicate that both BSMC and NSMC have good fast trajectory tracking control capability.

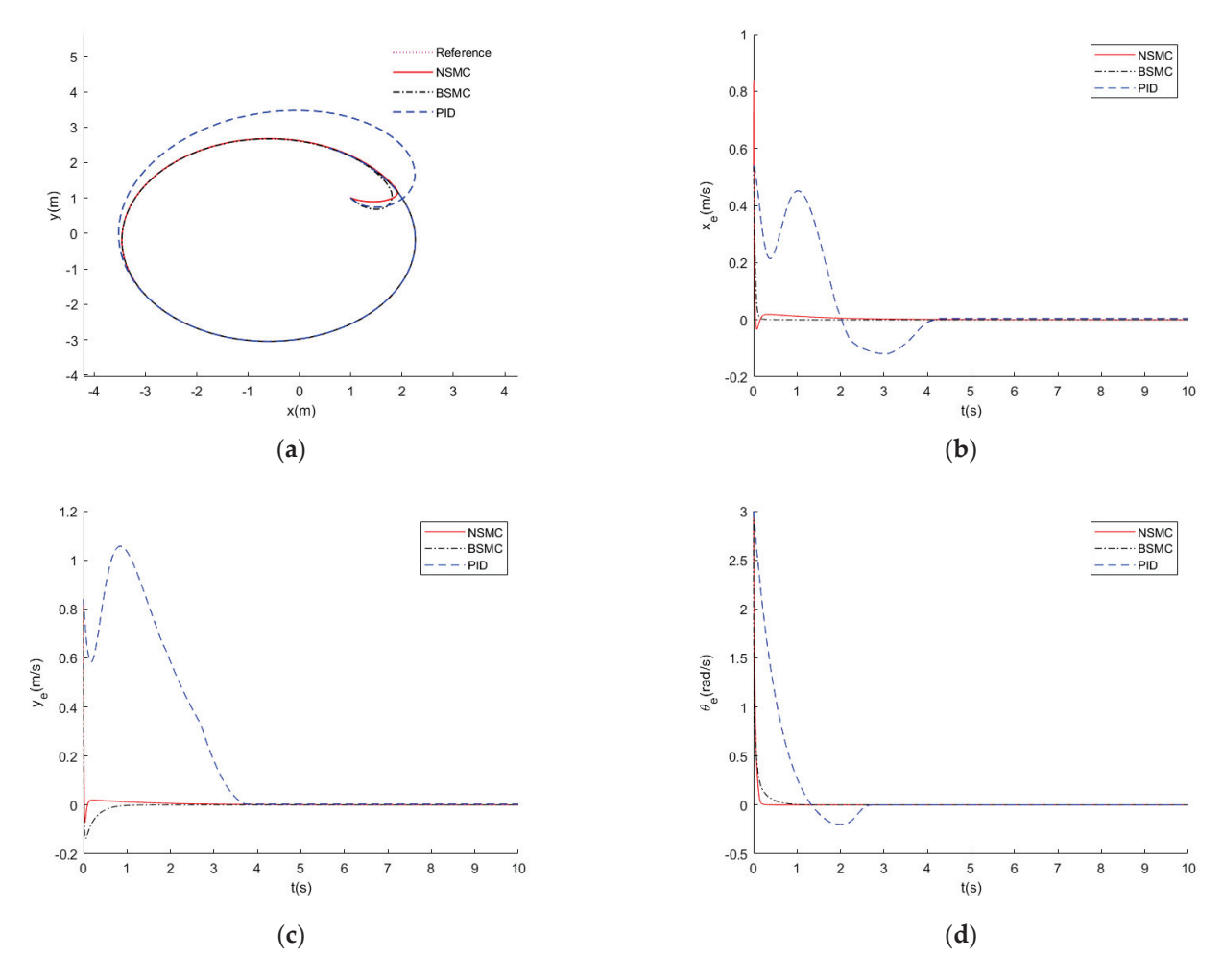


Figure 4. (a) Trajectory tracking diagram; (b) trajectory tracking errors diagram of x_e ; (c) trajectory tracking errors diagram of y_e ; (d) trajectory tracking errors diagram of θ_e .

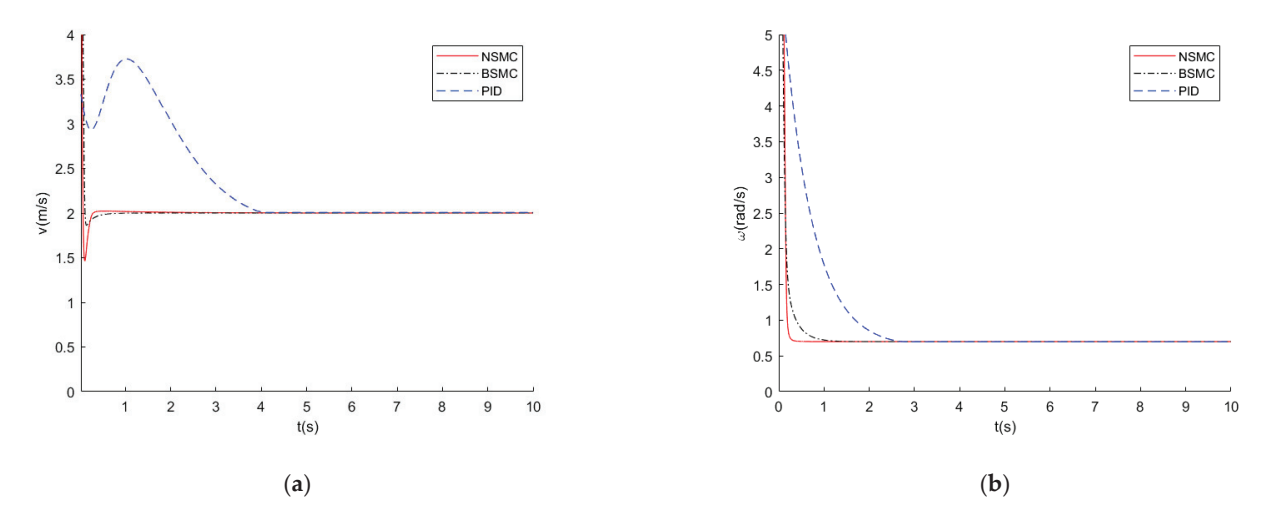


Figure 5. (a) Controller output diagram of v; (b) controller output diagram of ω .

To verify the robustness of the controller to external perturbations and uncertainties, the total set of perturbations was set to be $D_1(t)=0.2\sin t$, $D_2(t)=0.1\sin t$. The remaining parameters were maintained at a constant level, and the aforementioned simulation experiment was replicated, with the outcomes depicted in Figures 6 and 7.

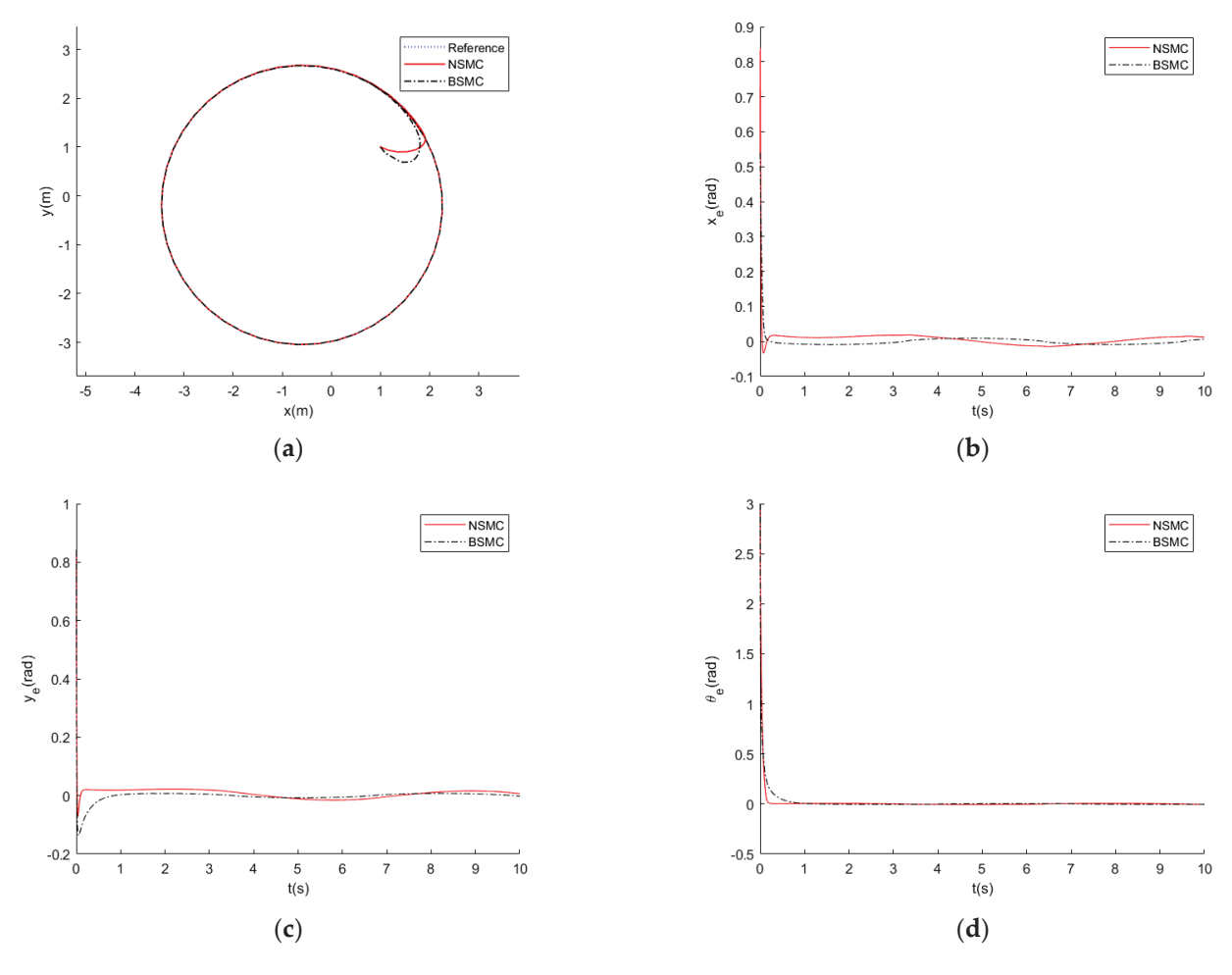


Figure 6. (a) Trajectory tracking diagram with perturbations; (b) trajectory tracking errors diagram of x_e with perturbations; (c) trajectory tracking errors diagram of y_e with perturbations; (d) trajectory tracking errors diagram of θ_e with perturbations.

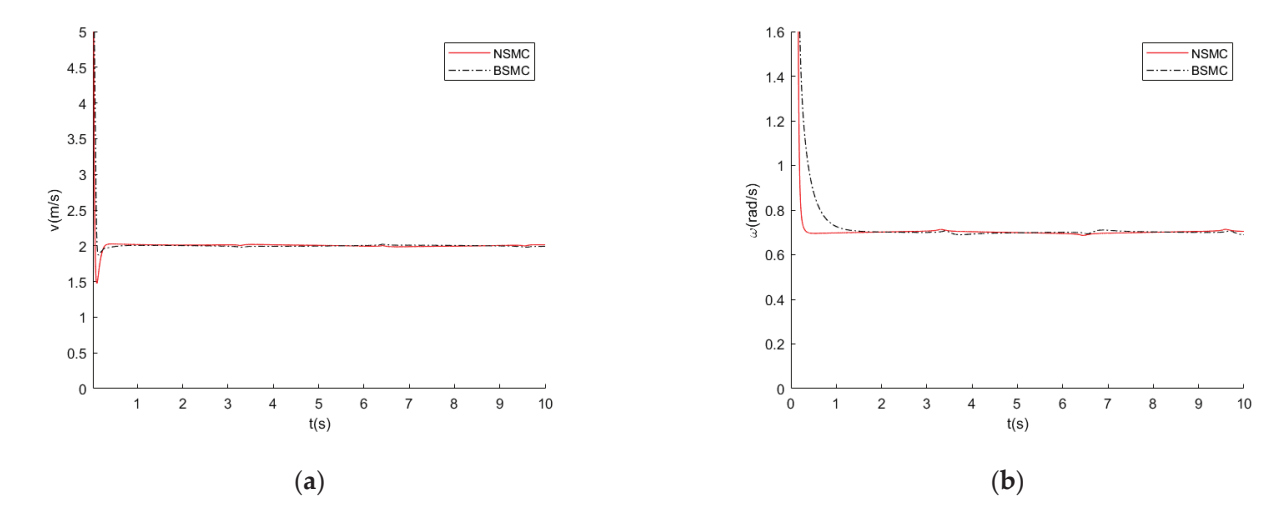


Figure 7. (a) Controller output diagram of v with perturbations; (b) controller output diagram of ω with perturbations.

A comparison of the control effects of NSMC and BSMC is shown in Table 4. The convergence time refers to the moment when the trajectory tracking error decreases to below 0.02 m, and the system approaches a stable state. On the other hand, the maximum error represents the highest value of the trajectory tracking error displayed by the wheeled mobile robot during operation in a steady-state condition. On the contrary, NSMC demonstrates superior convergence speed compared to BSMC, albeit with a slightly lower level of accuracy than BSMC. Traditional PID controllers are unable to achieve trajectory tracking when disturbances are present. The NSMC and BSMC demonstrate effective regulation under various conditions, with or without external disturbances. It can be demonstrated that both controllers exhibit robust performance in the presence of external perturbations. In contrast to conventional PID control methods and traditional sliding mode control, both BSMC and NSMC exhibit enhanced performance in terms of precision of control and rate of convergence.

Table 4. Control effects of NSMC and BSMC.

With or Without	NSMC/BSMC		PID	
Disturbances	Convergence Time	Maximum Error	Convergence Time	Maximum Error
With Without	0.7 s/1.093 s 0.679 s/0.92 s	17 mm/13 mm 10 mm/3 mm	invalid 4.259s	invalid 19 mm

5. Conclusions

This paper focused on the sliding mode trajectory tracking problem of mobile robots. Based on the stability theory of Lyapunov function and the backstepping method, the motion system controllers were designed. The sliding mode algorithm was adopted to make the system trajectory tracking error converge to zero quickly and stably. Simulation results show that the controllers converge quickly, with high accuracy and robustness.

Exploring different dummy variables is a promising research direction in the field of mobile robot trajectory tracking. In our upcoming research, we aim to integrate the dynamics model of wheeled mobile robots to develop robust controllers capable of handling uncertainties. This integration will enhance the precision and applicability of the controller.

Author Contributions: Conceptualization, H.H. and J.G.; methodology, H.H. and J.G.; software, H.H.; validation, H.H.; formal analysis, J.G.; investigation, J.G.; resources, J.G.; data curation, H.H.; writing—original draft preparation, H.H.; writing—review and editing, H.H.; visualization, H.H.; supervision, J.G.; project administration, J.G.; funding acquisition, J.G. All authors have read and agreed to the published version of the manuscript.

Funding: This work is supported by National Natural Science Foundation of China under Grant (62073296), and Zhejiang Province Natural Science Foundation of China under Grant (LZ23F030010).

Data Availability Statement: Data are available on request from the corresponding author.

Acknowledgments: Thank you to the authors (H.H. and J.G.) for their support and contributions to this article.

Conflicts of Interest: The authors declare no conflicts of interest.

References

- 1. Liao, J.; Chen, Z.; Yao, B. Model-based coordinated control of four-wheel independently driven skid steer mobile robot with wheel–ground interaction and wheel dynamics. *IEEE Trans. Ind. Inform.* **2019**, *15*, 1742–1752. [CrossRef]
- 2. Abdelwahab, M.; Parque, V.; Elbab, A.M.F.; Abouelsoud, A.; Sugano, S. Trajectory tracking of wheeled mobile robots using z-number based fuzzy logic. *IEEE Access* **2020**, *8*, 18426–18441. [CrossRef]
- 3. Liu, Y.; Zhu, J.J.; Williams II, R.L.; Wu, J. Omni-directional mobile robot controller based on trajectory linearization. *Robot. Auton. Syst.* **2008**, *56*, 461–479. [CrossRef]
- 4. Rossomando, F.G.; Soria, C.M. Identification and control of nonlinear dynamics of a mobile robot in discrete time using an adaptive technique based on neural PID. *Neural Comput. Appl.* **2015**, *26*, 1179–1191. [CrossRef]
- 5. Yang, J.-M.; Kim, J.-H. Sliding mode control for trajectory tracking of nonholonomic wheeled mobile robots. *IEEE Trans. Robot. Autom.* **1999**, *15*, 578–587. [CrossRef]
- 6. Han, Y.; Cheng, Y.; Xu, G. Trajectory tracking control of AGV based on sliding mode control with the improved reaching law. *IEEE Access* **2019**, *7*, 20748–20755. [CrossRef]
- 7. Song, L.; Huang, J.; Liang, Q.; Nie, L.; Liang, X.; Zhu, J. Trajectory tracking strategy for sliding mode control with double closed-loop for lawn mowing robot based on ESO. *IEEE Access* **2022**, *11*, 1867–1882. [CrossRef]
- 8. Jiang, L.; Wu, Z. Sliding mode control for intelligent vehicle trajectory tracking based on reaching law. *Trans. Chin. Soc. Agric. Mach.* **2018**, 49, 381–386. [CrossRef]
- 9. Chwa, D. Sliding-mode tracking control of nonholonomic wheeled mobile robots in polar coordinates. *IEEE Trans. Control Syst. Technol.* **2004**, *12*, 637–644. [CrossRef]
- 10. Ríos, H.; Mera, M.; Polyakov, A. Perturbed Unicycle Mobile Robots: A Second-Order Sliding-Mode Trajectory Tracking Control. *IEEE Trans. Ind. Electron.* **2024**, *71*, 2864–2872. [CrossRef]
- 11. Yang, X.; Wei, P.; Zhang, Y.; Liu, X.; Yang, L. Disturbance observer based on biologically inspired integral sliding mode control for trajectory tracking of mobile robots. *IEEE Access* **2019**, *7*, 48382–48391. [CrossRef]
- 12. Li, J.; Wang, J.; Peng, H.; Hu, Y.; Su, H. Fuzzy-torque approximation-enhanced sliding mode control for lateral stability of mobile robot. *IEEE Trans. Syst. Man Cybern. Syst.* **2022**, *52*, 2491–2500. [CrossRef]
- 13. Gao, H.; Wang, X.; Hu, J. Adaptive Tracking Control of Mobile Robots based on Neural Network and Sliding Mode Methods. In Proceedings of the 2023 38th Youth Academic Annual Conference of Chinese Association of Automation (YAC), Hefei, China, 27–29 August 2023; pp. 962–967. [CrossRef]
- 14. Feng, H.; Jiang, J.; Chang, X.; Yin, C.; Cao, D.; Yu, H.; Li, C.; Xie, J. Adaptive sliding mode controller based on fuzzy rules for a typical excavator electro-hydraulic position control system. *Eng. Appl. Artif. Intell.* **2023**, *126*, 107008. [CrossRef]
- 15. Zhai, J.-Y.; Song, Z.-B. Adaptive sliding mode trajectory tracking control for wheeled mobile robots. *Int. J. Control* **2018**, 92, 2255–2262. [CrossRef]
- 16. Zheng, Y.; Zheng, J.; Shao, K.; Zhao, H.; Xie, H.; Wang, H. Adaptive trajectory tracking control for nonholonomic wheeled mobile robots: A barrier function sliding mode approach. *IEEE/CAA J. Autom. Sin.* **2024**, *11*, 1007–1021. [CrossRef]
- 17. Dumitrascu, B.; Filipescu, A.; Minzu, V. Backstepping control of wheeled mobile robots. In Proceedings of the 15th International Conference on System Theory, Control and Computing, Sinaia, Romania, 14–16 October 2011; pp. 1–6.
- 18. Ling, Y.; Wu, J.; Lyu, Z.; Xiong, P. Backstepping controller for laser ray tracking of a target mobile robot. *Meas. Control* **2020**, *53*, 1540–1547. [CrossRef]
- 19. Ibari, B.; Benchikh, L.; Bouzgou, K.; Elhachemi, R.H.; Ahmed-Foitih, Z. Backstepping controller with force estimator applied for mobile robot. *Prz. Elektrotechniczny* **2019**, 2019, 18–21. [CrossRef]
- 20. Ye, J. Tracking control for nonholonomic mobile robots: Integrating the analog neural network into the backstepping technique. *Neurocomputing* **2008**, *71*, 3373–3378. [CrossRef]
- 21. Yang, H.; Guo, M.; Xia, Y.; Cheng, L. Trajectory tracking for wheeled mobile robots via model predictive control with softening constraints. *IET Control Theory Appl.* **2018**, 12, 206–214. [CrossRef]
- 22. Yu, S.; Guo, Y.; Meng, L.; Qu, T.; Chen, H. MPC for path following problems of wheeled mobile robots. *IFAC-Pap.* **2018**, *51*, 247–252. [CrossRef]
- 23. Wang, C.; Liu, X.; Yang, X.; Hu, F.; Jiang, A.; Yang, C. Trajectory tracking of an omni-directional wheeled mobile robot using a model predictive control strategy. *Appl. Sci.* **2018**, *8*, 231. [CrossRef]

- 24. Hassan, N.; Saleem, A. Neural network-based adaptive controller for trajectory tracking of wheeled mobile robots. *IEEE Access* **2022**, *10*, 13582–13597. [CrossRef]
- 25. Yin, Q.; Bian, Y.; Du, J.; Zhao, W.; Yang, S. Dual backstepping variable structure switching control of bounded uncertain nonlinear system. *Int. J. Syst. Sci.* **2022**, *53*, 2341–2357. [CrossRef]

Disclaimer/Publisher's Note: The statements, opinions and data contained in all publications are solely those of the individual author(s) and contributor(s) and not of MDPI and/or the editor(s). MDPI and/or the editor(s) disclaim responsibility for any injury to people or property resulting from any ideas, methods, instructions or products referred to in the content.





Article

Second-Order Terminal Sliding Mode Control for Trajectory Tracking of a Differential Drive Robot

Tuan Ngoc Tran Cao ^{1,2}, Binh Thanh Pham ^{1,2}, No Tan Nguyen ¹, Duc-Lung Vu ³ and Nguyen-Vu Truong ^{1,*}

- National Institute of Applied Mechanics and Informatics, Vietnam Academy of Science and Technology, Ho Chi Minh City 700000, Vietnam; ngoctuan@iami.vast.vn (T.N.T.C.); thanhbinh@iami.vast.vn (B.T.P.); tanno@iami.vast.vn (N.T.N.)
- Graduate University of Science and Technology, Vietnam Academy of Science and Technology, Hanoi 10072, Vietnam
- University of Information Technology, Vietnam National University, Ho Chi Minh City 71308, Vietnam; lungvd@uit.edu.vn
- * Correspondence: tnvu@vast.gov.vn

Abstract: This paper proposes a second-order terminal sliding mode (2TSM) approach to the trajectory tracking of the differential drive mobile robot (DDMR). Within this cascaded control scheme, the 2TSM dynamic controller, at the innermost loop, tracks the robot's velocity quantities while a kinematic controller, at the outermost loop, regulates the robot's positions. In this manner, chattering is greatly attenuated, and finite-time convergence is guaranteed by the second-order TSM manifold, which involves higher-order derivatives of the state variables, resulting in an inherently robust as well as fast and better tracking precision. The simulation results demonstrate the merit of the proposed control methods.

Keywords: nonlinear control systems; robust control; terminal sliding-mode control; uncertain systems

MSC: 37N35

1. Introduction

Differential drive mobile robot (DDMR) trajectory tracking has been a popular research topic in recent years [1–16]. Practical approaches [1,2,4,5,8–12] consider the DDMR's dynamics in addition to its kinematics in the control loop in order to attain tracking performance, especially in the presence of disturbances and unmodeled dynamics. These include actuator dynamics, the system's intrinsic nonlinearities, changes in load, working surface/terrain, etc., which are commonly encountered in many industrial applications, such as automated guided vehicles (AGVs), automated forklift robots (AFRs) and so on.

Among these methods, sliding mode control [4,5,10,11,13–15,17,18] has emerged as an attractive alternative due to its simplicity in implementation; more importantly, it has a fast dynamic response as well as strong robustness to external disturbances and parameter variations. The conventional linear SMC method (LSM), however, poses serious drawbacks because of its instinctive chattering phenomenon, which makes it less likely to be efficient for use in the electro-mechanical system control scheme [19–22]. This motivates the further research and development of chattering-free SMC techniques, including the nonlinear terminal sliding mode (TSM), i.e., [19–22], as well as higher-order sliding mode control methods, i.e., [22–25].

The TSM method possesses superior properties in finite-time convergence, excellent tracking precision, and better chattering attenuation in comparison to conventional LSM control systems. Nonetheless, in this particular application, the first-order TSM-based controller would not be able to totally suppress chattering from the torque inputs generated by the robot's dynamic models, making it less favorable to be employed in practical

applications since the aforementioned "chattering" would cause severe damage to the robot's actuating systems.

This paper proposes a second-order TSM control scheme (2TSM) for the DDMR's trajectory tracking problem. Here, by dealing with derivatives of the state variables at a higher order incorporated within the nonlinear 2TSM manifold, the finite-time convergence of tracking errors (i.e., velocity quantities) to zero is guaranteed; singularities, such as those appearing in conventional first-order TSM (i.e., [19]) can be avoided; and the resulting control signals (torque's commands) are continuous, enabling the proposed method to be directly applied in practical applications. This is the original motivation for this work.

The remainder of this paper is organized as follows. Section 2 describes both the kinematic and dynamic models of the DDMR system. The finite-time convergence characteristics of the 2TSM manifold are discussed in Section 3. One of the major contributions of the proposed work relies on the analytical calculation of convergence time, which is crucial and applied for the determination and selection of relevant parameters that govern the system's dynamics when the sliding manifold is reached. The 2TSM-based controller design is presented in Section 4. The simulation results are documented in Section 5, illustrating the outstanding merits of the proposed 2TSM control scheme for DDMR's trajectory tracking in comparison to the LSM and TSM methods. Finally, Section 6 concludes the paper.

2. DDMR's Model

Figure 1 describes the DDMR's position with respect to the following coordinates:

- Global coordinate system: denoted as $\{x, y\}$ to define its exact position on the Descartes plane.
- Robot coordinate system: denoted as $\{x^r, y^r\}$, which refers to the relative local position with respect to the robot's frame. Here, its origin is located at $\{x_A, y_A\}$ (point A). The robot's center of mass, denoted as point C, is assumed to be located along the x^r axis at a distance d from point A.

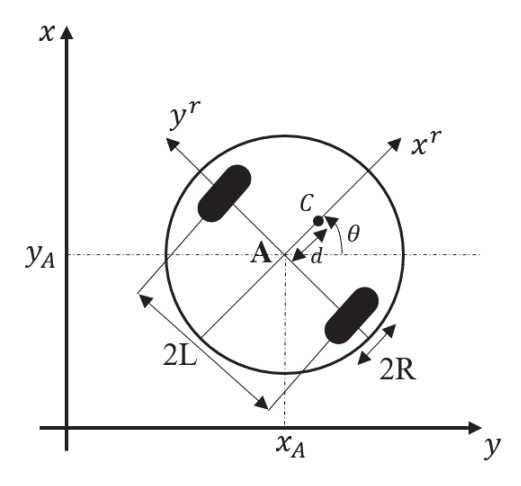


Figure 1. DDMR's coordinates.

Let $\{x_A, y_A\}$, $\{x_A^r, y_A^r\}$ represent the coordinate of point A on the global frame and robot frame, respectively

The definitions of
$$\dot{p} = \begin{bmatrix} \dot{x}_A \\ \dot{y}_A \\ \dot{\theta} \end{bmatrix}$$
 and $\dot{p}^r = \begin{bmatrix} \dot{x}_A^r \\ \dot{y}_A^r \\ \dot{\theta} \end{bmatrix}$ correspond to the velocities of DDMR in

the global frame and robot frame, in which θ refers to the robot's heading angle; thus, $\dot{\theta}$ denotes its derivative with respect to time

The relationship of motion between the two frames is shown as follows:

$$\dot{p} = O(\theta)\dot{p}^r \tag{1}$$

where $O(\theta)$ is the orthogonal rotation matrix

$$O(\theta) = \begin{bmatrix} \cos \theta & -\sin \theta & 0\\ \sin \theta & \cos \theta & 0\\ 0 & 0 & 1 \end{bmatrix}$$
 (2)

With the assumption of no lateral slip, as described in (3), this indicates that the wheels do not slide perpendicularly to their longitudinal axis, i.e.,

$$\dot{y}_A^r = 0 \tag{3}$$

and pure rolling motion, which means the wheels rotate without any slipping or skidding along their contact points with the ground; the linear velocity of each wheel (the velocity of point H) (Figure 2) is expressed by the following equations:

$$\begin{cases} v_{Hr} = v_r = R\dot{\varphi_r} \\ v_{Hl} = v_l = R\dot{\varphi_l} \end{cases}$$
 (4)

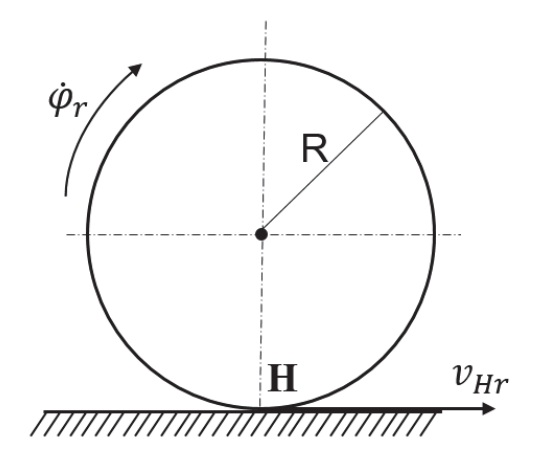


Figure 2. Right wheel of DDMR as an example to describe the velocity quantities of each wheel.

Here,

- $-v_{Hr},v_{Hl}$ represent the linear velocities of point H on the right wheel and left wheel.
- $-v_r, v_l$ denote the linear velocities of the right wheel and left wheel.
- $\dot{\varphi}_r$, $\dot{\varphi}_l$ are the respective angular velocities of the right wheel and left wheel.

2.1. Kinematic Model

Equation (5) formulizes the DDMR's kinematic model [1]:

$$\begin{cases} v = \frac{v_r + v_l}{2} = \frac{R(\dot{\varphi}_r + \dot{\varphi}_l)}{2} \\ \omega = \frac{v_r - v_l}{2I} = \frac{R(\varphi_r - \dot{\varphi}_l)}{2I} \end{cases}$$
 (5)

with v as the linear velocity and ω as the angular velocity of DDMR in the robot frame. As a result,

$$\begin{cases} x_A^{\dot{r}} = \frac{R(\dot{\varphi}_r + \dot{\varphi}_l)}{2} \\ y_A^{\dot{r}} = 0 \\ \dot{\theta} = \omega = \frac{R(\dot{\varphi}_r - \dot{\varphi}_l)}{2L} \end{cases}$$
 (6)

leading to the following expression

$$\dot{p}^r = \begin{bmatrix} \dot{x_A^r} \\ \dot{y_A^r} \\ \dot{\theta} \end{bmatrix} = \begin{bmatrix} R/2 & R/2 \\ 0 & 0 \\ R/2L & -R/2L \end{bmatrix} \begin{bmatrix} \dot{\varphi_r} \\ \dot{\varphi_l} \end{bmatrix}$$
 (7)

From (1), (5), (6), and (7), the following is obtained:

$$\dot{p} = \begin{bmatrix} R/2\cos\theta & R/2\cos\theta \\ R/2\sin\theta & R/2\sin\theta \\ R/2L & -R/2L \end{bmatrix} \begin{bmatrix} \dot{\varphi_r} \\ \dot{\varphi_l} \end{bmatrix}$$
(8)

or

$$\dot{p} = \begin{bmatrix} \cos \theta & 0 \\ \sin \theta & 0 \\ 0 & 1 \end{bmatrix} \begin{bmatrix} v \\ \omega \end{bmatrix} \tag{9}$$

2.2. Dynamic Model

As discussed in [3], (10) formulizes DDMR's respective dynamic model with the consideration of all relevant force components.

$$\begin{cases}
\left(m + \frac{2}{R^2} I_w\right) \dot{v} - m_c d\omega^2 = \frac{1}{R} (\tau_r + \tau_l) \\
\left(I + \frac{2L^2}{R^2} I_w\right) \dot{\omega} + m_c d\omega v = \frac{L}{R} (\tau_r - \tau_l)
\end{cases}$$
(10)

Here, the total equivalent inertia *I* is calculated as follows:

$$I = I_C + 2I_m + 2I_w = m_C d^2 + 2m_a L^2 + 2m_w R^2$$
(11)

with m_w and m_a as the mass of each wheel with and without its actuators, m and m_c as the DDMR's total mass with and without its wheels and actuators, I_w as the wheel's moment of inertia, and τ_r , τ_l as the left and right wheel's actuator torques.

In the state space form, (10) is expressed as

$$\begin{bmatrix} m + \frac{2}{R^2} I_w & 0 \\ 0 & I + \frac{2L^2}{R^2} I_w \end{bmatrix} \begin{bmatrix} \dot{v} \\ \dot{\omega} \end{bmatrix} = \begin{bmatrix} m_c d\omega \\ -m_c d\omega v \end{bmatrix} + \begin{bmatrix} 1/R & 1/R \\ L/R & -L/R \end{bmatrix} \begin{bmatrix} \tau_r \\ \tau_l \end{bmatrix}$$
(12)

3. Finite-Time Convergence Characteristics of 2TSM Manifold

The following theorem describes the finite-time convergence of relevant state variables once the 2TSM manifold is reached.

Theorem 1. The state variable x(t) and its derivative $\dot{x}(t)$ satisfy the following:

$$\ddot{x} + \gamma_1 \dot{x}^\alpha + \gamma_2 x^\beta = 0 \tag{13}$$

where

 $0 < \alpha = \frac{q}{p} < 1$, $\beta = \frac{\alpha}{2-\alpha} = \frac{q}{2p-q}$, p > q are odd positive integers; while $0 < \gamma_1$ and $\gamma_2 = \gamma_1^{\beta+1} \frac{\alpha^{\beta}}{(\beta+1)^{\beta}} (1-\frac{\alpha}{2}) > 0$. Given the set of initial conditions as $x(0) = x_0$ and $\dot{x}(0) = -\gamma_1^{\beta/\alpha} \left(\frac{\alpha}{\beta+1}\right)^{\beta/\alpha} x_0^{1/(2-\alpha)}$. x(t) and its derivative $\dot{x}(t)$ converge to zeros in finite-time $t_{convergence} = \frac{\alpha}{\alpha-\beta} \left(\frac{\gamma_1\alpha}{\beta+1}\right)^{-\beta/\alpha} x_0^{(\alpha-\beta)/\alpha}$.

Proof. Let $y = \dot{x}$; then, the following is obtained $\ddot{x} = y \frac{dy}{dx}$, and Equation (13) converts to the following form:

$$y\frac{dy}{dx} + \gamma_1 y^{\alpha} + \gamma_2 x^{\beta} = 0$$

$$y\frac{dy}{dx} + \gamma_1 y^{\alpha} = -\gamma_2 x^{\beta}$$

$$F(y, \dot{y}) = y\frac{dy}{dx} + \gamma_1 y^{\alpha} = -\gamma_2 x^{\beta}$$
(14)

Let us solve the unforced response of (14)

$$F(y,\dot{y}) = 0$$

$$y^{\frac{dy}{dx}} + \gamma_1 y^{\alpha} = 0$$
(15)

y = 0 is one solution of (15).

In the case of $y \neq 0$, dividing (15) by y^{α} results in the following:

$$y^{1-\alpha}\frac{dy}{dx} = -\gamma_1$$

or

$$\frac{1}{2-\alpha}y^{2-\alpha} = -\gamma_1 x + C$$

$$y^{2-\alpha} = -\gamma_1 (2-\alpha)x + C(2-\alpha)$$

$$y = \left(\underbrace{-\gamma_1 (2-\alpha)}_{M} x + \underbrace{C(2-\alpha)}_{N}\right)^{1/(2-\alpha)}$$

$$y = (Mx + N)^{1/(2-\alpha)}$$
(16)

In the presence of a perturbation $u = -\gamma_2 x^{\beta}$, the forced response, which describes the generalized solution of

$$F(y,\dot{y})=u,$$

takes the following form:

$$y = (Mx + f(x))^{1/(2-\alpha)}$$
(17)

where N = f(x) is the function of x.

When substituting the following expressions:

$$y\frac{dy}{dx} = \frac{M + df/dx}{2 - \alpha} (Mx + f(x))^{\frac{\alpha}{2 - \alpha}} = \frac{M + df/dx}{2 - \alpha} (Mx + f(x))^{\beta}$$

$$\gamma_1 y^{\alpha} = \gamma_1 (Mx + f(x))^{\frac{\alpha}{2-\alpha}} = \gamma_1 (Mx + f(x))^{\beta}$$

into Equation (14), the following is obtained

$$F(y,\dot{y}) = \left(\gamma_1 + \frac{M + \frac{df}{dx}}{2 - \alpha}\right) (Mx + f(x))^{\beta} \equiv -\gamma_2 x^{\beta}$$
 (18)

This implies

- Mx + f(x) would take the form of Mx + f(x) = Kx; as a result, f(x) = (K M)x;
- $\frac{df}{dx} = (K M)$. The below-mentioned equation is satisfied as follows:

$$\left(\gamma_1 + \frac{M + (K - M)}{2 - \alpha}\right) K^{\beta} = -\gamma_2$$

$$\left(\gamma_1 + \frac{K}{2 - \alpha}\right) K^{\beta} = -\gamma_2$$
(19)

Equation (19) indicates that $\gamma_2 > 0$, K < 0; and it is easy to show as follows:

- The minima of $g(K) = \left(\gamma_1 + \frac{K}{2-\alpha}\right)K^{\beta} + \gamma_2$ is located at $K^* = -\gamma_1 \frac{\beta(2-\alpha)}{\beta+1} = -\gamma_1 \frac{\alpha}{\beta+1}$;
- $g\left(K^* = -\gamma_1 \frac{\alpha}{\beta+1}\right) = 0$ and K^* is the only root of Equation (19).

As a result,

$$y = (K^*x)^{1/(2-\alpha)} = \underbrace{-\left[\gamma_1 \frac{\alpha}{\beta+1}\right]^{1/(2-\alpha)}}_{A} x^{1/(2-\alpha)}$$

Consequently, the solution would be the following:

$$y = \dot{x} = Ax^{1/(2-\alpha)} \tag{20}$$

As seen in Equation (20), it is easy to show that the convergence time of the state variable x(t) and its derivative $\dot{x}(t)$ to zero is calculated using the following:

$$t_{convergence} = \frac{2 - \alpha}{1 - \alpha} A^{-1} x^{\frac{1 - \alpha}{2 - \alpha}}(0) = \frac{\alpha}{\alpha - \beta} \left(\frac{\gamma_1 \alpha}{\beta + 1}\right)^{-\beta/\alpha} x_0^{(\alpha - \beta)/\alpha}$$
(21)

This completes the proof.

Remark 1. The solution, as in Equation (20), satisfies the aforementioned initial conditions

$$x(0) = x_0$$
 and $\dot{x}(0) = -\gamma_1^{\beta/\alpha} \left(\frac{\alpha}{\beta+1}\right)^{\beta/\alpha} x_0^{-1/(2-\alpha)}$

Remark 2. The Picard – Lindelöf theorem reconfirms that (20) is a unique solution of $F(y, \dot{y}) = y \frac{dy}{dx} + \gamma_1 y^{\alpha} = -\gamma_2 x^{\beta}$ for the given set of initial values.

Remark 3. With p > q chosen to be odd positive integers, it is easy to see that $(-x)^{\alpha} = -x^{\alpha} = |x|^{\alpha} sign(x)$, $0 < (-x)^{\alpha \pm 1} = x^{\alpha \pm 1} = |x|^{\alpha \pm 1}$ and $0 < (-x)^{\alpha \pm \beta} = x^{\alpha \pm \beta} = |x|^{\alpha \pm \beta}$.

Remark 4. With the convergence time calculated as in (21), it is observed that $t_{convergence}$ is inversely proportional to $\left(\frac{\gamma_1 \alpha}{\beta+1}\right)^{\beta/\alpha}$. In the practice of 2TSM-based controller design to be discussed in Section 4, the selection of these relevant parameters can be accordingly selected for the delivery of efficient control performance and design criterion.

4. TSM-Based Controller Design

4.1. Kinematic Controller

The trajectory tracking error p_e is the difference between the actual posture of a robot,

denoted as $p = \begin{bmatrix} x \\ y \\ \theta \end{bmatrix}$, and the reference of the robot (illustrated in Figure 3), denoted as

$$p_{ref} = \begin{bmatrix} x_{ref} \\ y_{ref} \\ \theta_{ref} \end{bmatrix} = \begin{bmatrix} x_d \\ y_d \\ \theta_d \end{bmatrix}, \text{ i.e.,}$$

$$p_e = \begin{bmatrix} x_e \\ y_e \\ \theta_e \end{bmatrix} = p_{ref} - p = \begin{bmatrix} x_{ref} - x \\ y_{ref} - y \\ \theta_{ref} - \theta \end{bmatrix}$$
(22)

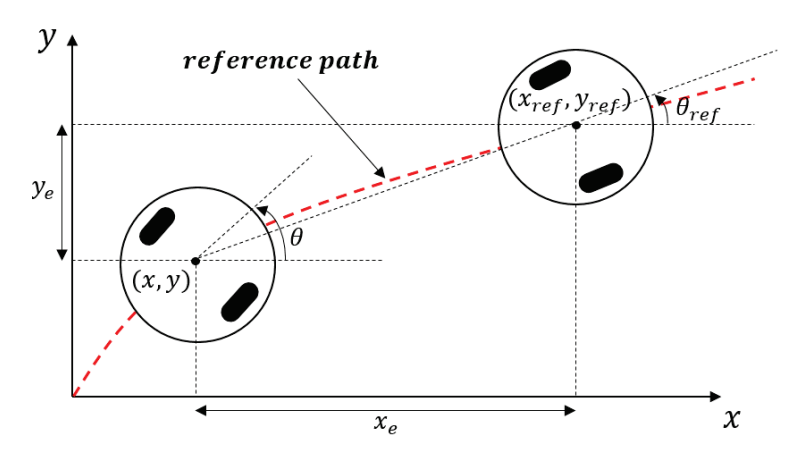


Figure 3. Real robot in the trajectory tracking of the reference robot on Descartes coordinates $\{x,y\}$.

Within this cascaded control architecture (Figure 4), the kinematic controller at the outer-most loop relies on a simple *P*-type-only controller designed as

$$\omega_{ref} = K_w.\theta_e = K_w.\left(\theta_{ref} - \theta\right)$$

$$v_{ref} = K_v.d_e$$
(23)

Here, ω_{ref} and v_{ref} refer to the reference angular velocities; K_w and K_v are proportional gains for angular and linear velocity controllers; and $d_e = (x_e^2 + y_e^2)^{1/2}$ and $\theta_e = tan^{-1}(y_e, x_e)$.

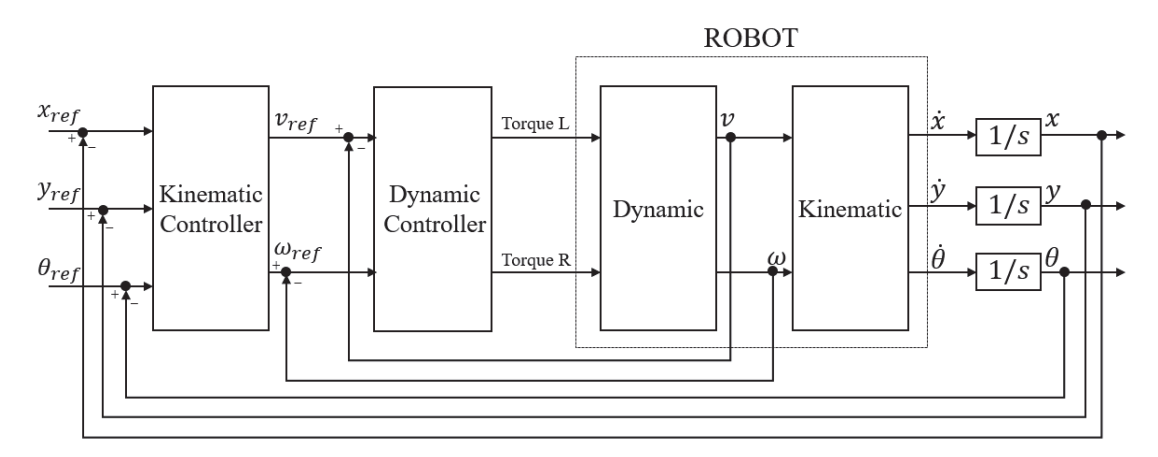


Figure 4. DDMR's trajectory cascaded control architecture.

4.2. Dynamic Controller

With the integration of an unknown bounded disturbance $\rho(t)$ into Equation (12), the following is obtained:

$$M\ddot{q} = V(\dot{q}) + C\tau(t) + \rho(t) \tag{24}$$

where

$$M = \begin{bmatrix} m + \frac{2}{R^2} I_w & 0 \\ 0 & I + \frac{2L^2}{R^2} I_w \end{bmatrix}; \dot{q} = \begin{bmatrix} v \\ \omega \end{bmatrix}; \ddot{q} = \begin{bmatrix} \dot{v} \\ \dot{\omega} \end{bmatrix}.$$

$$V(\dot{q}) = \begin{bmatrix} m_c d\omega^2 \\ m_c dv\omega \end{bmatrix}; C = \begin{bmatrix} \frac{1}{R} & \frac{1}{R} \\ \frac{L}{R} & \frac{-L}{R} \end{bmatrix}; \tau(t) = \begin{bmatrix} \tau_r \\ \tau_l \end{bmatrix}$$

Let and the error $\dot{e}(t)$ calculated as

$$\dot{e}(t) = \dot{q} - \dot{q}_r = [v_e, w_e]^T = [v - v_{ref}, w - w_{ref}]^T$$
 (25)

Then,

$$\ddot{e} = M^{-1}(V(\dot{q}) + C\tau(t) + \rho(t)) - \ddot{q}_r$$
(26)

Here, a second-order terminal sliding mode control (2TSM) scheme is employed to realize the dynamic controller. In order to achieve good performances, such as fast convergences, chattering-free, and better tracking precision, a 2TSM manifold is designed as follows:

$$s = \ddot{e} + \gamma_1 \dot{e}^{\alpha} + \gamma_2 e^{\beta} \tag{27}$$

where $\gamma_1, \gamma_2, \alpha, \beta$ are as specified in Theorem 1.

In this manner, the 2TSM's dynamic controller is designed according to the following Theorem 2.

Theorem 2. The velocity error can converge to zero in finite time if the 2TSM manifold is chosen as (27), and the control law is designed as follows:

$$u = u_{eq} + u_n \tag{28}$$

$$u_{eq} = C^{-1}M(-M^{-1}V + \ddot{q}_r - \gamma_1 \dot{e}^{\alpha} - \gamma_2 e^{\beta})$$
 (29)

$$\dot{u}_n = C^{-1}M(sign(s)(k+\mu)) \tag{30}$$

where $k = Max\{\|M^{-1}\dot{\rho}(t)\|\}$ refers to the bounded disturbance and $\mu > 0$.

Proof. Substituting the error dynamics (26) into the second-order TSM manifold (27) gives the following:

$$s = M^{-1}(V(\dot{q}) + C\tau(t) + \rho(t)) - \ddot{q}_r + \gamma_1 \dot{e}^{\alpha} + \gamma_2 e^{\beta}$$

Substituting Equation (29) into the above yields

$$s = M^{-1}Cu_n + M^{-1}\rho(t)$$

The following Lyapunov function candidate is considered:

$$V = \frac{1}{2}s^T s$$

Differentiating *V* with respect to time, t gives

$$\dot{V} = s^{T} \dot{s}$$

$$= s^{T} \left(M^{-1} C \dot{u}_{n} + M^{-1} \dot{\rho}(t) \right)$$

$$= s^{T} \left(-sign(s)k - sign(s)\mu + M^{-1} \dot{\rho}(t) \right),$$
(31)

i.e.

$$\dot{V} \le -k\|s\| - \mu\|s\| + M^{-1}\dot{\rho}(t) \le -\mu\|s\| = -\mu\sqrt{2V^{1/2}} < 0 \text{ for } \|s\| \ne 0.$$

Therefore, according to the Lyapunov stability criterion, the second-order TSM manifold, as in (27), reaches zero from $s(0) \neq 0$ within a finite time $t_r \leq \frac{\sqrt{2}V^{1/2}(0)}{\mu}$ or $t_r \leq \frac{s(0)}{\mu}$. Once the 2TSM manifold s is reached, e(t) and its derivative $\dot{e}(t)$ (which corresponds to the velocities' error) converge to zero in finite time (Theorem 1), as given by

$$t_e = t_r + \frac{\alpha}{\alpha - \beta} \left(\frac{\gamma_1 \alpha}{\beta + 1} \right)^{-\beta/\alpha} x^{(\alpha - \beta)/\alpha} (t_r)$$
 (32)

This concludes the proof. \Box

Remark 5. As calculated according to Theorem 2, there is no singularity that exists in the 2TSM control law u. In other words, the proposed approach is well regarded as a non-singular second-order terminal sliding mode (2NTSM) control scheme.

Remark 6. u_n satisfying $\dot{u}_n = C^{-1}M(sign(s)(k+\mu))$ is a continuous signal. This implies that the proposed 2TSM control scheme is chattering-free, indicating its suitability and effectiveness to be employed in practical electro-mechanical control systems.

5. Simulation Results

In order to demonstrate the effectiveness and advantages of the proposed second-order TSM, the simulation results are compared with the TSM (as in the previous work in [16]) and the LSM. The physical parameters of DDMR are shown in Table 1. The unknown bounded disturbance is $\rho(t) = \sin(10t) + n$, where n represents random noises with amplitudes of 0.1.

Table 1. The physical parameters of DDMR used in this simulation study.

As described in Figure 1	d	0.15 m
Ü	R	0.25 m
	L	1 m
As described in (11)	m_{c}	70 kg
	m_a	70 kg 5 kg
	m_{w}	1 kg

LSM controller

The LSM manifold and control are designed as follows:

$$s = \dot{e} + 4e = \begin{bmatrix} \dot{e}_1 \\ \dot{e}_2 \end{bmatrix} + \begin{bmatrix} 4 & 0 \\ 0 & 4 \end{bmatrix} \begin{bmatrix} e_1 \\ e_2 \end{bmatrix}$$

$$u_{eq} = C^{-1}M \left(-M^{-1}V + \ddot{q}_r - 4e \right)$$

$$u_n = -C^{-1}M(sign(s)(k+\mu))$$

$$k = Max \left\{ \|M^{-1}\rho(t)\| \right\}, \mu = 0.1$$

TSM controller

The TSM manifold and control are designed as follows:

$$s = \dot{e} + 4e^{3/5} = \begin{bmatrix} \dot{e}_1 \\ \dot{e}_2 \end{bmatrix} + \begin{bmatrix} 4 & 0 \\ 0 & 4 \end{bmatrix} \begin{bmatrix} e_1^{3/5} \\ e_2^{3/5} \end{bmatrix}$$

$$u_{eq} = C^{-1}M \Big(-M^{-1}V + \ddot{q}_r - 4e^{3/5} \Big)$$

$$u_n = -C^{-1}M (sign(s)(k + \mu))$$

$$k = Max \Big\{ \|M^{-1}\rho(t)\| \Big\}, \ \mu = 0.1$$

• Second-order TSM controller

The 2TSM manifold and control are designed as follows:

$$s = \ddot{e} + \gamma_1 \dot{e}^{3/5} + \gamma_2 e^{3/7} = \begin{bmatrix} \ddot{e}_1 \\ \ddot{e}_2 \end{bmatrix} + \gamma_1 \begin{bmatrix} \dot{e}_1^{3/5} \\ \dot{e}_2^{3/5} \end{bmatrix} + \gamma_2 \begin{bmatrix} e_1^{3/7} \\ e_2^{3/7} \end{bmatrix}$$
$$\gamma_1 = 4, \ \gamma_2 = 3.49$$

$$\begin{split} u_{eq} &= C^{-1} M \Big(- M^{-1} V + \ddot{q}_r - 4 \dot{e}^{3/5} - 3.49 \dot{e}^{3/7} \Big) \\ \dot{u}_n &= - C^{-1} M (sign(s)(k + \mu)) \\ k &= Max \Big\{ \| M^{-1} \dot{\rho}(t) \| \Big\}, \; \mu = 0.1 \end{split}$$

The simulation results are shown in Figures 5–9. Figures 6–8 depict the output tracking errors. Figure 5 shows the control input signals of two actuators (Torque 1—left actuator; Torque 2—right actuator).

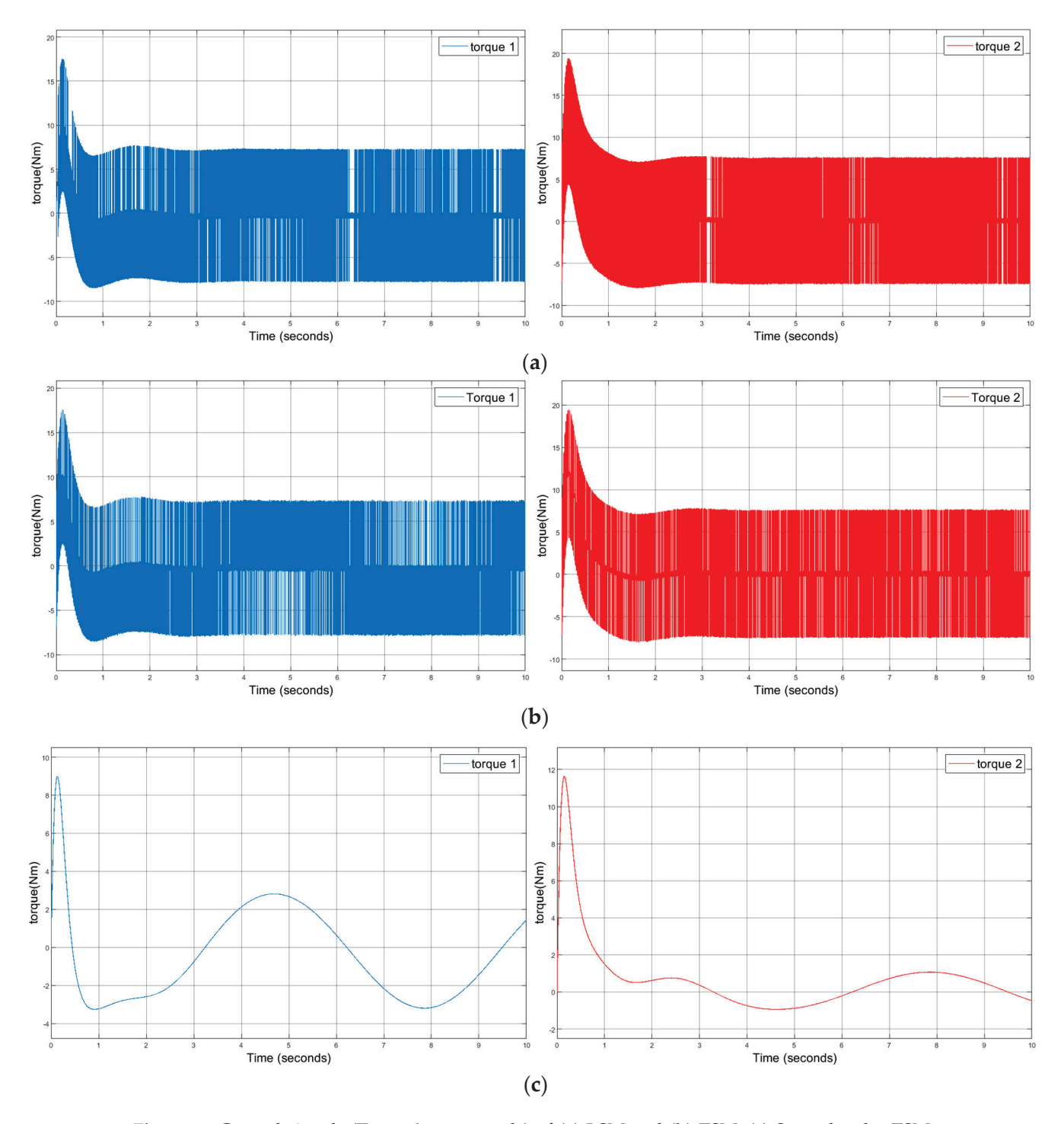


Figure 5. Control signals (Torque's commands) of (a) LSM and (b) TSM. (c) Second-order TSM controllers.

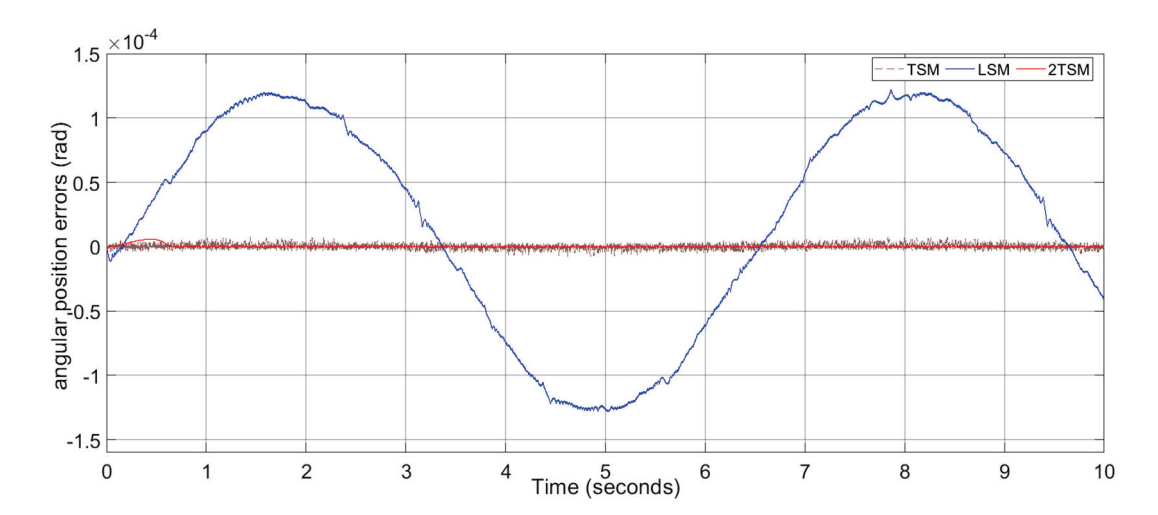


Figure 6. Angular positions' tracking errors.

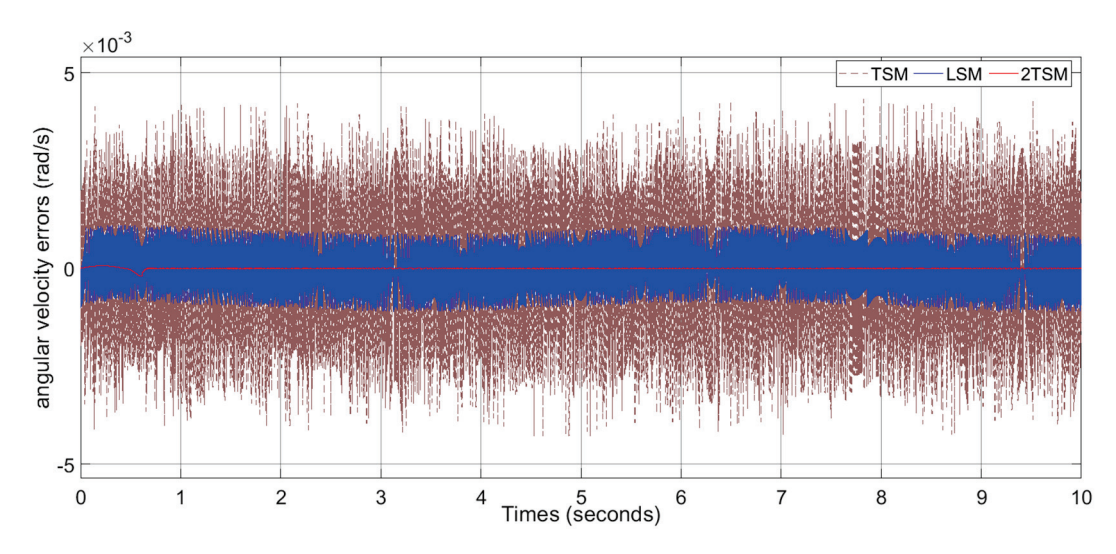


Figure 7. Tracking errors of angular velocity (rad/s).

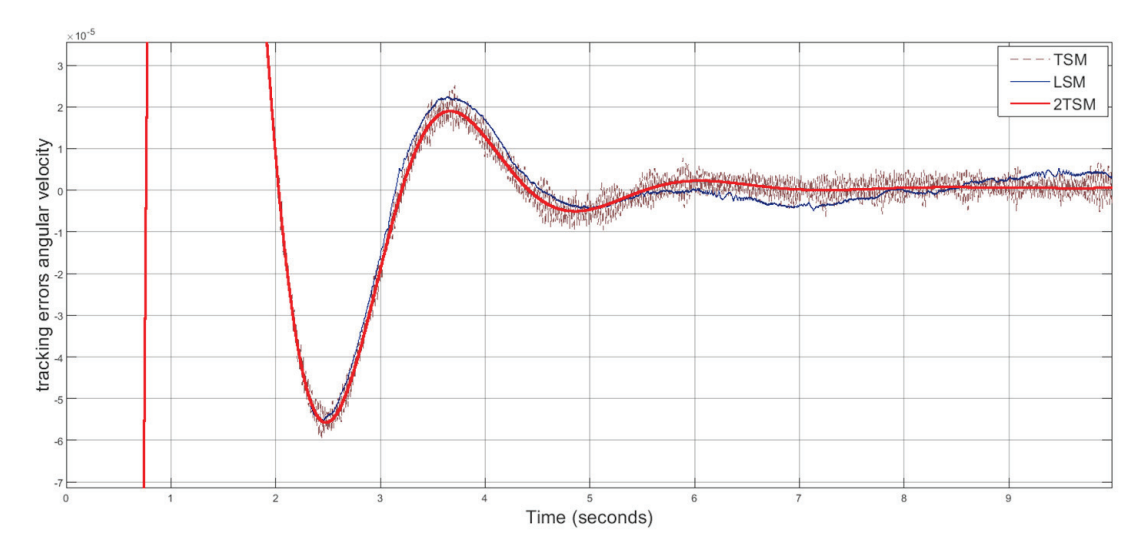


Figure 8. Tracking errors of DDMR's trajectory (distance to reference trajectory) of LSM, TSM, and 2TSM.

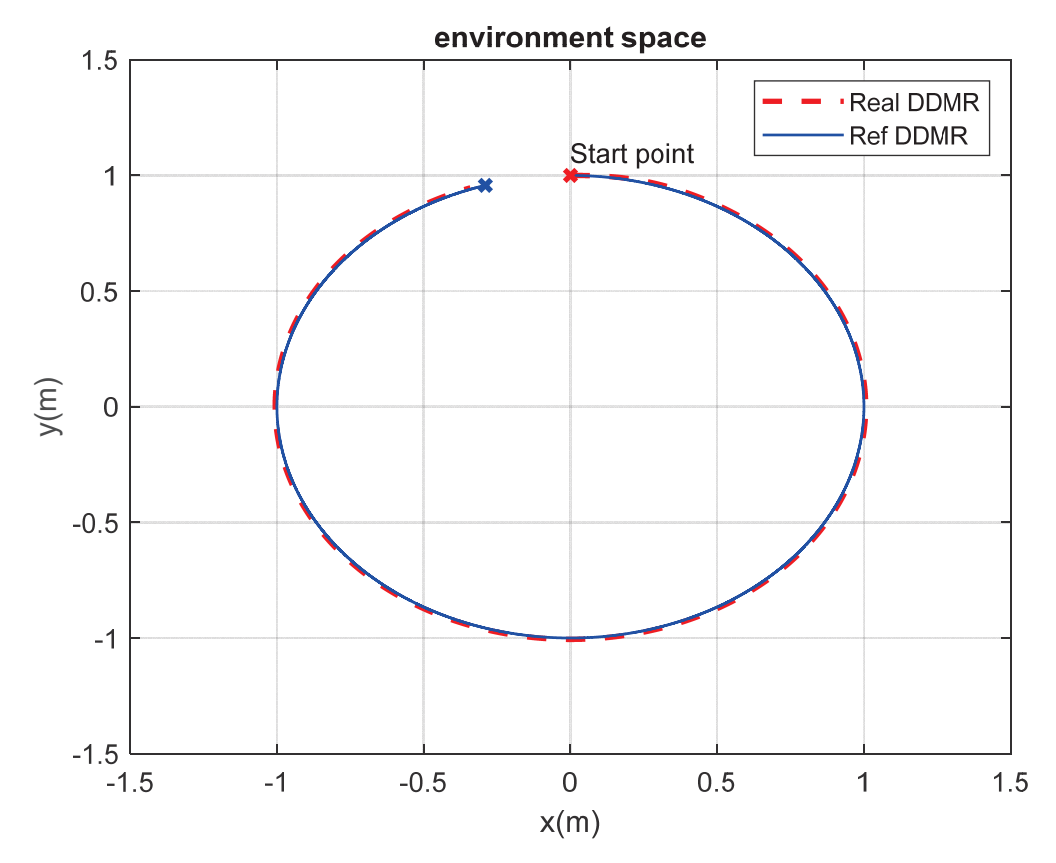


Figure 9. Trajectory tracking performance of 2TSM-based controller on the Descartes coordinates $\{x,y\}$ with units of meters $\{m\}$.

It can be seen that the 2TSM controller outperforms conventional LSM and TSM counterparts in various measures, including faster response and better tracking precision as well as chattering-free, non-singular control signals, which make it suitable to directly apply in practical applications. Here, the finite-time convergence of 2TSM allows us to directly manipulate a variety of tuning parameters as in conventional first-order TSM approaches (i.e., [19,20]).

6. Conclusions

This paper proposes a second-order terminal sliding mode control scheme for the trajectory tracking of differential drive mobile robots. The main advantages of the presented 2TSM approach lie in the faster dynamic response and better tracking precision with chattering free control signals while avoiding singularities in the control law, as demonstrated. More importantly, this paper contributes to the converging characteristics of the analysis and calculation of the finite-time convergence of relevant state variables (velocity errors and angular position errors) to zero once the 2TSM sliding manifold is reached. This facilitates the direct manipulation of various tuning parameters of the 2TSM control scheme in a similar manner as that of conventional, well-known first-order TSM control methods (i.e., [19,20]).

Author Contributions: Methodology, B.T.P.; software, D.-L.V.; Formal analysis, N.T.N.; investigation, T.N.T.C.; supervision, N.-V.T. All authors have read and agreed to the published version of the manuscript.

Funding: This research was funded by Vietnam Academy of Science and Technology (VAST01.06/20-21).

Data Availability Statement: The data presented in this study is available on request from the corresponding authors, and the dataset was jointly completed by the team, so the data is not publicly available.

Conflicts of Interest: The authors declare no conflict of interest.

References

- 1. Dudek, G.; Jenkin, M. Computational Principles of Mobile Robotics, 2nd ed.; Cambridge University Press: Cambridge, UK, 2010.
- 2. Rached, H. Dynamic Modelling of Differential-Drive Mobile Robots using Lagrange and Newton-Euler Methodologies: A Unified Framework. *Adv. Robot. Autom.* **2013**, *2*, 107.
- 3. Fukao, T.; Nakagawa, H.; Adachi, N. Adaptive tracking control of a nonholonomic mobile robot. *IEEE Trans. Robot. Autom.* **2000**, *16*, 609–615. [CrossRef]
- 4. Yang, L.; Pan, S. A Sliding mode control method for trajectory tracking control of wheeled mobile robot. *J. Phys. Conf. Ser.* **2018**, 1074, 26–28. [CrossRef]
- 5. Lee, J.K.; Park, J.B.; Choi, Y.H. Tracking Control of Nonholonomic Wheeled Mobile Robot Based on New Sliding Surface with Approach Angle. *IFAC Proc. Vol.* **2013**, *46*, 38–43. [CrossRef]
- 6. Sousa, R.L.S.; do Nascimento Forte, M.D.; Nogueira, F.G.; Torrico, B.C. Trajectory tracking control of a nonholonomic mobile robot with differential drive. In Proceedings of the 2016 IEEE Biennial Congress of Argentina (ARGENCON), Buenos Aires, Argentina, 15–17 June 2016; pp. 1–6.
- 7. Kanayama, Y.; Kimura, Y.; Miyazaki, F.; Noguchi, T. A stable tracking control method for an autonomous mobile robot. In Proceedings of the IEEE International Conference on Robotics and Automation, Cincinnati, OH, USA, 13–18 May 1990; Volume 1, pp. 384–389.
- 8. Sun, S. Designing approach on trajectory-tracking control of mobile robot. *Robot. Comput.-Integr. Manuf.* **2005**, 21, 81–85. [CrossRef]
- 9. Martins, F.N.; Celeste, W.C.; Carelli, R.; Silho, M.; Bastos, T. An adaptive dynamic controller for autonomous mobile robot trajectory tracking. *Control Eng. Pract.* **2008**, *16*, 1354–1363. [CrossRef]
- 10. Solea, R.; Filipescu, A.; Nunes, U. Sliding-mode control for trajectory-tracking of a Wheeled Mobile Robot in presence of uncertainties. In Proceedings of the 2009 7th Asian Control Conference, Hong Kong, China, 27–29 August 2009; pp. 1701–1706.
- 11. Cen, H.; Singh, B.K. Nonholonomic Wheeled Mobile Robot Trajectory Tracking Control Based on Improved Sliding Mode Variable Structure. *Wirel. Commun. Mob. Comput.* **2021**, 2021, 2974839. [CrossRef]
- 12. Huang, J.; Wen, C.; Wang, W.; Jiang, Z.P. Adaptive output feedback tracking control of a nonholonomic mobile robot. *Automatica* **2014**, *50*, 821–831. [CrossRef]
- 13. Yang, J.; Kim, J. Sliding mode control for trajectory tracking of nonholonomic wheeled mobile robots. *IEEE Trans. Robot. Autom.* **1999**, *15*, 578–587. [CrossRef]
- 14. Chwa, D. Sliding-mode tracking control of nonholonomic wheeled mobile robots in polar coordinates. *IEEE Trans. Control Syst. Technol.* **2004**, 12, 637–644. [CrossRef]
- 15. Zhai, J.Y.; Song, Z.B. Adaptive sliding mode trajectory tracking control for wheeled mobile robots. *Int. J. Control.* **2019**, 92, 2255–2262. [CrossRef]
- 16. Cao, T.; Pham, B.; Tran, H.; Gia, L.; Nguyen, N.; Truong, N. Non-singular terminal sliding mode control for trajectory tracking of a differential drive robot. *E3S Web Conf.* **2024**, 496, 02005. [CrossRef]
- 17. Zheng, J.; Wang, H.; Man, Z.; Jin, J.; Fu, M. Robust Motion Control of a Linear Motor Positioner Using Fast Non-singular Terminal Sliding Modet. *IEEE/ASME Trans. Mechatron.* **2015**, *20*, 1743–1752. [CrossRef]
- 18. Sun, Z.; Xie, H.; Zheng, J.; Man, Z.; He, D. Path-following control of Mecanum-wheels omnidirectional mobile robots using nonsingular terminal sliding mode. *Mech. Syst. Signal* **2021**, *147*, 107128. [CrossRef]
- 19. Feng, Y.; Yu, X.; Han, F. On nonsingular terminal sliding-mode control of nonlinear systems. *Automatica* **2013**, *49*, 1715–1722. [CrossRef]
- 20. Feng, Y.; Zheng, J.; Yu, X.; Truong, N.V. Hybrid Terminal Sliding-Mode Observer Design Method for a Permanent-Magnet Synchronous Motor Control System. *IEEE Trans. Ind. Electron.* **2009**, *56*, 3424–3431. [CrossRef]
- 21. Feng, Y.; Yu, X.; Man, Z. Non-singular terminal sliding mode control of rigid manipulators. *Automatica* **2002**, *38*, 2159–2167. [CrossRef]
- 22. Feng, Y.; Han, X.; Wang, Y. Second-order terminal sliding mode control of uncertain multivariable systems. *Int. J. Control* **2007**, *80*, 856–862. [CrossRef]
- 23. Feng, Y.; Zhou, M.; Yu, X.; Han, F. Full-order sliding mode control of rigid robotics manipulators. *Asian Control J.* **2019**, 21, 1228–1236. [CrossRef]
- 24. Nguyen, N.; Pham, B.; Hoang, T.; Nguyen, T.; Nguyen, L.; Truong, N. Efficient sensorless speed estimation of electrical servo drives using a full order nonsingular terminal sliding mode observer. *Math. Probl. Eng.* **2021**, 2021, 8175848. [CrossRef]
- 25. Shi, H.; Feng, Y. High order terminal sliding mode flux observer for induction motors. *Acta Autom. Sin.* **2012**, *38*, 288–294. [CrossRef]

Disclaimer/Publisher's Note: The statements, opinions and data contained in all publications are solely those of the individual author(s) and contributor(s) and not of MDPI and/or the editor(s). MDPI and/or the editor(s) disclaim responsibility for any injury to people or property resulting from any ideas, methods, instructions or products referred to in the content.





Article

A Gaussian Process-Enhanced Non-Linear Function and Bayesian Convolution–Bayesian Long Term Short Memory Based Ultra-Wideband Range Error Mitigation Method for Line of Sight and Non-Line of Sight Scenarios

A. S. M. Sharifuzzaman Sagar ¹, Samsil Arefin ², Eesun Moon ³, Md Masud Pervez Prince ⁴, L. Minh Dang ^{5,6}, Amir Haider ^{1,*} and Hyung Seok Kim ^{1,*}

- Department of Artificial Intelligence and Robotics, Sejong University, Seoul 05006, Republic of Korea; sharifsagar80@sejong.ac.kr
- School of Mechatronics Engineering, China University of Mining and Technology, Xuzhou 221116, China; fs22050004e@cumt.edu.cn
- Department of Computer Science, Columbia University, New York, NY 10027, USA; eesun.moon@columbia.edu
- Department of Industrial Design Engineering, Zhejiang University, Hangzhou 310058, China; 22351419@zju.edu.cn
- Institute of Research and Development, Duy Tan University, Da Nang 550000, Vietnam; danglienminh@duytan.edu.vn
- $^{\rm 6}$ $\,$ Faculty of Information Technology, Duy Tan University, Da Nang 550000, Vietnam
- * Correspondence: amirhaider@sejong.ac.kr (A.H.); hyungkim@sejong.ac.kr (H.S.K.)

Abstract: Relative positioning accuracy between two devices is dependent on the precise range measurements. Ultra-wideband (UWB) technology is one of the popular and widely used technologies to achieve centimeter-level accuracy in range measurement. Nevertheless, harsh indoor environments, multipath issues, reflections, and bias due to antenna delay degrade the range measurement performance in line-of-sight (LOS) and non-line-of-sight (NLOS) scenarios. This article proposes an efficient and robust method to mitigate range measurement error in LOS and NLOS conditions by combining the latest artificial intelligence technology. A GP-enhanced non-linear function is proposed to mitigate the range bias in LOS scenarios. Moreover, NLOS identification based on the sliding window and Bayesian Conv-BLSTM method is utilized to mitigate range error due to the non-line-of-sight conditions. A novel spatial-temporal attention module is proposed to improve the performance of the proposed model. The epistemic and aleatoric uncertainty estimation method is also introduced to determine the robustness of the proposed model for environment variance. Furthermore, moving average and min-max removing methods are utilized to minimize the standard deviation in the range measurements in both scenarios. Extensive experimentation with different settings and configurations has proven the effectiveness of our methodology and demonstrated the feasibility of our robust UWB range error mitigation for LOS and NLOS scenarios.

Keywords: error mitigation; Bayesian inference; deep learning; sensors; UWB

MSC: 37M10

1. Introduction

Accurate positioning is one of the main courses of research in various engineering fields, and it has received a lot of attention in recent years owing to its inherent academic importance [1,2]. Applications across a wide range of industries, including telecommunications, intelligent machines, and medical/rescue operations, might greatly benefit from this technology, as could autonomous driving [3–5]. Despite this, precise location in line-of-sight (LOS) and non-line-of-sight (NLOS) scenarios for indoor environments remains a

research challenge. Multipath effects, reflections, refractions, and other propagation events can cause errors in the location estimate process [6,7].

Localization has been accomplished via various technologies, such as sensor nodes, acoustics, simultaneous localization and mapping, inertial measurement units, and ultrawideband (UWB) communications. UWB is a potential technology for accurate positioning because of a variety of desired qualities, namely low energy consumption, centimeter-level range accuracy, susceptibility to multipath effects, and a certain obstacle penetrating capacity [8]. UWB has been intensively studied in recent years by academics and industry for indoor and relative positioning [9,10]. On the other hand, the precision of UWB localization degrades when the signal propagates through the obstruction and is subject to antenna calibration issues, and NLOS situations result in a positive bias in range measurements. Most of the UWB-based localization technology uses Time Difference of Arrival (TDoA), Time of Arrival (TOA), and two-way ranging (TWR) methods. The TWR methods are the most common and robust methods because no anchor synchronization is needed to get precise ranging measurements.

TWR is very significant when clock synchronization is not obtainable or not used in a positioning method. The distance between two devices is calculated by measuring the Time of Flight (ToF) between them. Instead of utilizing direct timestamps, the TWR technique calculates the distance between two devices using a sequence of time intervals. This is due to the fact that the duration of a particular time is the same across all devices, independent of their individual clock references. However, a clock will drift from its original state even if it is properly calibrated due to the inherent faults of clock oscillators in the actual physical world [11]. These clock drifts result in inaccurate measurements of the time periods given, particularly whenever the application needs centimeter-level precision. This is because a 1 ns ToF inaccuracy may result in a range measurement error of 30 cm [12]. As a result, various TWR approaches exist in the literature to reduce the inaccuracy in range caused by clock drifts. One of the best and most used methods is the asymmetric TWR method, which reduces errors due to clock and frequency drift. However, the asymmetric TWR method also has an error due to antenna delay and NLOS conditions.

The term "NLOS" generally refers to a scenario in which the direct route between a transceiver and a receiver is impeded. Consequently, the signals travel via a penetrated, reflected, or diffracted route before reaching the receiver, increasing the travel time and decreasing signal intensity. As a result, the distance calculated using either time or signal strength is affected. NLOS is a prevalent issue with wireless positioning technologies, including WiFi, ZigBee, Bluetooth, and UWB. Compared to other approaches, UWB presents a more serious difficulty due to its operating range and the needed precise indoor or relative positioning [13]. As a result, NLOS detection and mitigation has become a major topic in the area of UWB-based positioning systems [14]. Most of the proposed NLOS mitigation methods in the research involve likelihood ratio tests, channel impulse response (CIR)based techniques, and machine learning algorithms. Moreover, the recent literature has proposed support vector machines, Gaussian processes, deep learning, and representation learning models to mitigate NLOS effects. However, to mitigate range error in LOS and NLOS conditions, different parameters such as antenna delay and NLOS environment characteristics play a vital role in mitigating range error. These approaches generally mitigate the LOS- or NLOS-induced range measurement errors before positioning or mitigate the influence of range errors using specific positioning techniques. Although it is commonly understood that perfect range error mitigation is impossible, these solutions ignore the impact of residual range errors and antenna delay calibration on positioning. Furthermore, current NLOS detection and mitigation approaches classify the propagation state as either LOS or NLOS without further information about the NLOS's characteristics. We present a novel range error mitigation method for both LOS and NLOS conditions before the positioning to address these issues. The following are the primary contributions of this paper:

- 1. A GP-enhanced non-linear function and exponential moving average and min-max removing algorithms are proposed to mitigate range bias in the LOS environment.
- A Conv-BLSTM deep learning model-based NLOS identification method is proposed to identify the NLOS propagation through different materials for indoor environments, such as wood, the human body, concrete walls, and metals.
- A novel spatial-temporal attention module is proposed to effectively process the data's features.
- The Monte Carlo (MC) dropout-based uncertainty estimation model is introduced to estimate the proposed model's uncertainty to demonstrate the proposed model's robustness.

The rest of the paper is structured as follows: Section 2 presents the related works associated with this research, Section 3 describes the data preparation method for the proposed algorithms, Section 4 presents the proposed algorithms to mitigate range bias in LOS and NLOS scenarios, Section 5 describes the experimental setting and a discussion on the results, and the conclusion is drawn in Section 6.

2. Related Works

This section divides the existing range error mitigation into two categories based on the LOS and NLOS environments. LOS error mitigation includes antenna calibration, power calibration, and bias compensation due to radio signal strength. The second category involves identifying the NLOS situation and range error mitigation to enable precise range measurement.

2.1. LOS Range Error Mitigation

LOS range error sources include clock drift, power calibration, antenna delay, and bias caused by the signal power. Several approaches are found in the literature to correct clock drift in the UWB-range measurement devices. Fofana et al. developed a dynamic correction methodology that uses artificial delay between messages to calculate clock drift coefficients, which is utilized to limit clock drift in the two-way ranging method. The authors obtained an accuracy of twenty millimeters, enabling range traffic to be included in regular traffic [15]. Adrien et al. developed an open-source framework called Decaduino to enable range measurement using UWB chips. The authors used delay transmission and introduced artificial delay between messages through UWB devices. The authors achieved 15 cm accuracy in range measurements, which is very precise compared to other wireless range measurement technologies [16]. Martel et al. introduced a digital low pass filter to correct clock skew evaluation during TWR range measurements. The proposed method achieves very good results, with an 18 cm mean error and 1.77 cm standard deviation in range measurements [17]. Dotlic et al. proposed three calculating approaches for significantly minimizing systematic localization mistakes caused by clock offsets in comparable localization systems with a low frame exchange rate. The error reduction mechanism is based on the receiver's carrier frequency offset estimation, which is a necessary component of frame reception in many UWB-based systems [18]. Decawave instructed calibrating the antenna and power spectrum of the Decawave's DW1000 chips, but their calibrating method must be implemented manually, which is a big constraint for real-time and commercial applications [12]. Qiang et al. proposed Kalman filter-based range bias estimation and mitigation for both LOS and NLOS environments [19]. Their approach achieves good results by reducing the error to a millimeter level; however, the Kalman filter is computationally expensive for small microcontroller devices and is not suitable for energy-constrained devices. Therefore, a new antenna calibration method and bias mitigation method should be implemented to enable real-time application.

2.2. NLOS Range Error Mitigation

NLOS range error mitigation for UWB-based solutions includes effective NLOS identification and NLOS range bias mitigation. Traditional NLOS identification methods can be

divided into range, location, and channel-based methods [20,21]. Range-based approaches employ the probability density function (PDF) or variation of range estimations to differentiate LOS from NLOS [21] conditions. Channel-based approaches distinguish NLOS from LOS by utilizing CIR, which is accomplished via the use of two widely used functions, the PDF and the cumulative distribution function (CDF) [22]. However, determining a suitable distribution function and determining the proper threshold can be difficult [23]. It is also uncertain how to establish the threshold. Location-based approaches detect NLOS conditions during the location estimate process and might utilize the obtained location information to identify NLOS conditions. The location-based approach is expected to be useful in the scenario wherein redundant range estimates are accessible since it compares the location estimates provided with various sets of range estimations [24], but it is useless when there are no redundant range estimates or when numerous range estimates correspond to NLOS conditions. In order to solve the above-mentioned issues, researchers used different machine learning approaches for NLOS identification. Henk et al. proposed support vector machines to detect non-line-of-sight conditions and mitigate range error in the non-line-of-sight environment [25]. Nguyen et al. introduced relevance vector machine algorithms to mitigate range error in non-line-of-sight environments [26]. Sang et al. used different available machine learning techniques to identify the NLOS and multipath conditions in an indoor environment and compare the performance of the different machine learning algorithms [27]. However, one thing should be noted: wireless signal propagation is different in different materials, and most researchers did not consider these facts.

3. Data Preparation

The range measurements were done in five distinct locations to cover a broad range of LOS and NLOS scenarios: a wide-space area where the obstacles were metal, a human body obstacle between an anchor and a tag [28], an indoor office area where the obstacles were wood, and concrete walls as obstacles. Furthermore, additional measurements were taken across several rooms to investigate the through-the-wall impact. Figure 1 shows the box chart range error of different common obstacles found in the indoor environment. We can see that the propagation through the wall and partial metal obstacles induced large range error compared to the propagation through the wood and human obstacles. Due to the nature of the obstacles and radio signals, range error information from different propagation channels can be beneficial to mitigate the range error for different environments. Therefore, range measurements were taken under various conditions, which can be used to mitigate range error across different environments and allow a representation learning approach to acquire a domain-independent model.

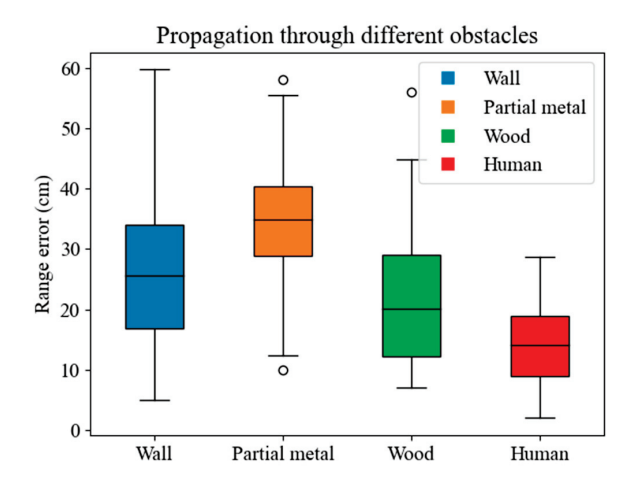


Figure 1. Range measurement error represented in the box chart for four different NLOS propagation scenarios, which can be found indoors. The square box represents the mean, and the dashes represent the maximum and minimum range error observed during the data acquisition.

We utilized an embedded Decawave DW1000 (Qorvo Inc., Greensboro, NC, USA) UWB chip with a NodMCU-BU01 module. As ground truth, a measurement ruler was used to measure the precise distance between the anchor and the tag. To produce both LOS and NLOS data, the tag was placed in different environments loaded with obstacles.

Figure 1 shows the boxplot range error for different propagation scenarios in our acquired data. It can be seen that the range error is very high during partial metal propagation. The mean range error also varies for different propagation materials.

4. Materials and Methods

In this section, we propose the range error mitigation of UWB devices for both LOS and NLOS environments. We propose a Gaussian process model and an unscented Kalman filter along with min-max removing, and a moving average filter is used to reduce the standard deviation of the acquired LOS range measurement. The NLOS identification for different obstacles and NLOS range error mitigation model was developed using the deep learning method. Since the UWB devices are low-power and energy-constrained devices connected to the microcontroller module, the range error mitigation method must be implemented in the microcontroller or edge devices to provide real-time range error mitigation before calculating the positioning. This study mainly focuses on implementing the proposed method in low-level microcontroller devices to minimize inference time and latency. The overall structure of the proposed range error mitigation of the UWB module can be seen in Figure 2.

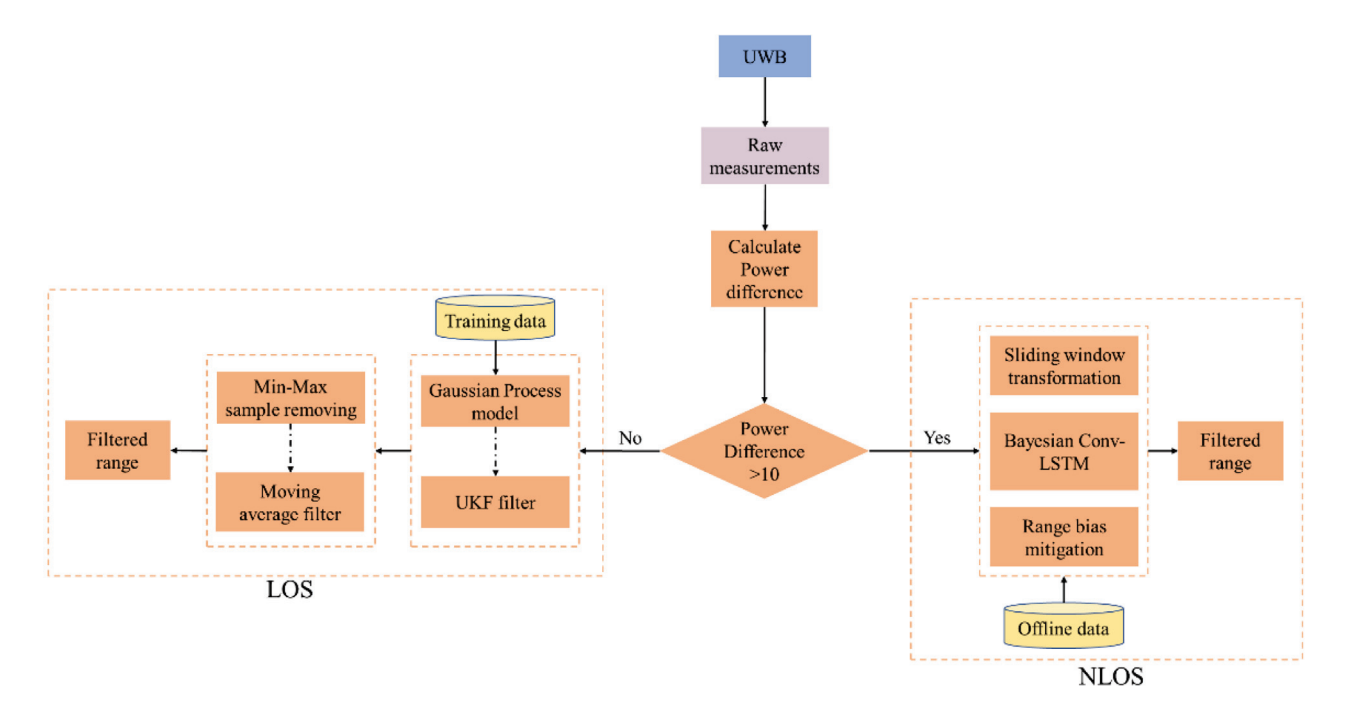


Figure 2. The overall system architecture of the proposed UWB range measurement error mitigation for both LOS and NLOS environments.

4.1. LOS Range Mitigation

4.1.1. System Model

We consider an asynchronous Double-Sided (DS)-TWR UWB system comprising two nodes: a transmitter (Tx) and a receiver (Rx). The range measurement process involves the exchange of UWB signals, with the Time of Flight (ToF) of the signals being critical for range estimation. The ToF, denoted as T_{ToF} , is the time taken by the UWB signal to travel from the Tx to the Rx. In an ideal scenario without any errors, the true range R between the nodes is related to T_{ToF} by

$$R = c \times T_{\text{ToF}},\tag{1}$$

where *c* is the speed of light.

The actual measured ToF, denoted as T'_{ToF} , is affected by various errors, such as environmental noise (N_{env}). This includes multipath effects, interference from other signals, and atmospheric conditions. Chip imperfections (N_{chip}) include errors due to hardware imperfections in the UWB transceivers. Antenna delay (δ_{ant}) includes the inherent delay in the Tx and Rx antennas. The observed ToF can thus be modeled as

$$T'_{\text{ToF}} = T_{\text{ToF}} + \frac{N_{\text{env}} + N_{\text{chip}} + \delta_{\text{ant}}}{c}$$
 (2)

4.1.2. Problem Formulation

The objective is to accurately estimate the true range R from the observed T'_{ToF} while mitigating the errors. The estimation problem can be formulated as follows:

1. Range estimation with error mitigation: we have to find an estimator \hat{R} such that

$$\hat{R} = \operatorname{argmin}_{R} \mathbb{E} \left[\left(R - \left(c \times T_{\text{ToF}}' \right) \right)^{2} \right]$$
(3)

where $\mathbb{E}[\cdot]$ denotes the expectation operator, signifying the minimization of the mean squared error between the true range and the estimated range.

2. Error correction modeling: we can model the combined errors as a stochastic process, which can be learned and predicted:

$$N_{\text{total}} = N_{\text{env}} + N_{\text{chip}} + \delta_{\text{ant}}$$
 (4)

Using a Gaussian process model, we can correct initial range as follows:

$$R_{\text{GP}} = c \cdot \left(T'_{\text{ToF}} - \frac{\mathcal{GP}(m(T'_{\text{ToF}}), k(T'_{\text{ToF}}, T''_{\text{ToF}}))}{c} \right)$$
 (5)

where GP(m,k) directly models the $N_{\rm total}$ as a function of observed $T'_{\rm ToF}$, using a mean function m and a covariance function k that learns from historical data of $T'_{\rm ToF}$ and the total error.

The initial correction from the GP model can be fine-tuned using a statistical filter by incorporating dynamic system behavior and residual error correction as follows:

$$\hat{R} = c \cdot \left(\mathcal{UKF} \left(X_{k|k-1}^{(i)} \right) - \frac{\hat{N}_{\text{resediual}}}{c} \right)$$
 (6)

where \hat{R} denotes the final corrected range estimate. The UKF considered the state represented by sigma points $X_{k|k-1}^{(i)}$, which have been adjusted from the R_{GP} . The residual error $\hat{N}_{residual}$ includes those components of N_{total} not mitigated by the initial GP correction.

4.1.3. Proposed Method

The GPA-UKF method is designed to enhance the accuracy of ultra-wideband (UWB) range measurements, which are often subject to errors due to antenna delays and environmental factors. The method synergizes the state estimation capabilities of the UKF with the error correction proficiency of GP models. This integration mitigates the non-linear and uncertain nature of UWB systems, yielding a more accurate and reliable range estimation.

A GP model is first utilized to predict and correct the total error ($N_{\rm total}$) affecting the ToF measurements. This total error encompasses various sources, including environmental noise ($N_{\rm env}$), chip imperfections ($N_{\rm chip}$), and antenna delay ($\delta_{\rm ant}$).

A Gaussian process can be defined using mean function m(x) and covariance function k(x, x'), where x and x' represent points in the input space, such as T'_{TOF} as follows:

$$m(x) = \mathbb{E}[f(x)] k(x, x') = \mathbb{E}[(f(x) - m(x))(f(x') - m(x'))]$$
(7)

The GP model, denoted as GP(m,k), captures the distribution over the possible functions f(x) that fit the observed data. In our scenario, the function f predicts the total error N_{total} as a function of the observed T'_{ToF} . The GP model learns the function f that maps T'_{ToF} to N_{total} . This learning process involves maximizing the likelihood of the observed data under the GP model as follows:

$$\mathcal{L}(\theta \mid \mathbf{T}'_{\text{ToF}}, \mathbf{N}_{\text{total}}) = \log p(\mathbf{N}_{total} \mid \mathbf{T}'_{ToF}, \theta)$$
 (8)

where θ represents the GP hyperparameters, and \mathbf{T}'_{ToF} and \mathbf{N}_{total} are vectors of observed ToF measurements and their corresponding error.

The trained GP model can predict the error \hat{N}_{total} for a new ToF measurement, T'_{ToF} . The initial range correction is then performed by adjusting the observed ToF for the predicted error as follows:

$$R_{\rm GP} = c \cdot \left(T_{\rm ToF}' - \frac{GP(m(T_{\rm ToF}'), k(T_{\rm ToF}', T_{\rm ToF}''))}{c} \right)$$
(9)

where R_{GP} is the initial corrected range measurement.

The UKF, known for its efficacy in non-linear systems, is employed to fine-tune the initial correct range measurements from the GP model, considering the system's dynamics and measurement noise. We can first define a state transition function as below:

$$x_{k+1} = f(x_k, w_k) \tag{10}$$

where x_k denotes the state at time k, f is the non-linear state transition function, and w_k represents the process noise.

We utilize sigma points to approximate the distribution of the system's state. Sigma points are selected to represent the possible states of the system. They are determined around the current state estimate and spread according to the state covariance. Mathematically, for a state vector x of dimension n, the sigma points $X^{(i)}$ are computed as follows.

$$X^{(0)} = \overline{x}$$

$$X^{(i)} = \overline{x} + (\sqrt{(n+\lambda)P})_i \text{ for } i = 1, \dots, n$$

$$X^{(i)} = \overline{x} - (\sqrt{(n+\lambda)P})_{i-n} \text{ for } i = n+1, \dots, 2n$$
(11)

where \overline{x} is the mean state estimate, P is the state covariance matrix, λ is a scaling parameter, and $\sqrt{(n+\lambda)P})_i$ represents the ith column of the matrix square root of $(n+\lambda)P$. These sigma points are then propagated through the non-linear state transition function f and measurement function h:

$$X_{k|k-1}^{(i)} = f(X_{k-1|k-1}^{(i)}, w_{k-1})$$

$$Z_{k}^{(i)} = h(X_{k|k}^{(i)}, v_{k})$$
(12)

where $X_{k|k-1}^{(i)}$ are the propagated sigma points through the state transition, and $Z_k^{(i)}$ are the sigma points transformed by the measurement function.

$$\overline{x}_{k|k} = \sum_{i=0}^{2n} W_i^{(m)} X_{k|k-1}^{(i)}$$
(13)

$$P_{k|k} = \sum_{i=0}^{2n} W_i^{(c)} \left(X_{k|k-1}^{(i)} - \overline{x}_{k|k} \right) \left(X_{k|k-1}^{(i)} - \overline{x}_{k|k} \right)^T$$
(14)

where $W_i^{(m)}$ and $W_i^{(c)}$ are weights for the mean and covariance, respectively.

The Kalman gain, K_k , is then computed to update the state estimate with the measurement Z_k :

$$K_{k} = P_{k|k-1}^{z} (P_{k|k-1}^{\epsilon})^{-1}$$

$$\overline{x}_{k|k} = \overline{x}_{k|k-1} + K_{k} (Z_{k} - \overline{Z}_{k})$$

$$P_{k|k} = P_{k|k-1} - K_{k} P_{k|k-1}^{z} K_{k}^{T}$$
(15)

where $P_{k|k-1}^z$ is the covariance of the predicted measurement, and $P_{k|k-1}^{\epsilon}$ is the measurement noise covariance.

The initial state of the UKF \bar{x}_0 is adjusted based on the corrected range from the GP model output R_{GP} as follows:

$$\overline{x}_0^{adj} = \overline{x}_0 + K_{GP} \cdot (R_{GP} - H \cdot \overline{x}_0) \tag{16}$$

where K_{GP} is an adjustment factor on the initial state estimation, H is the measurement matrix relating the state to the measured range, and \overline{x}_0^{adj} denotes the adjusted initial state.

The final measurement update of the system is then calculated as follows:

$$\widehat{R}_{k|k} = c \cdot \left(\mathcal{UKF} \left(X_{k|k-1}^{(i)} \right) - \frac{\widehat{N}_{\text{residual },k}}{c} \right)$$
(17)

where $\widehat{R}_{k|k}$ is the dynamically refined range estimate at time step k, incorporating the continuous adjustments for residual errors ($\widehat{N}_{\text{residual },k}$) identified through the UKF process after the initial GP corrections.

4.2. NLOS Range Mitigation

4.2.1. System Model

The range measurement in an NLOS environment at time t_k is affected by the nature of the obstruction. The model is expressed as

$$d_{\text{NLOS}} = d + \Delta d_{\text{nlos}} (\text{ obstacle }, t_k) + \varepsilon$$
 (18)

where $d_{\rm NLOS}$ is the observed distance, d is the actual line-of-sight distance, $\Delta d_{\rm nlos}$ represents the range error influenced by the type of obstacle, and ε signifies the combined standard deviation and mean error. The nature of the obstacle influences the NLOS range bias, $\Delta d_{\rm nlos}$. For example, concrete walls and metal cause significant reflections and absorption of UWB signals, leading to large-range errors. Wood and partial obstructions result in less severe but still notable attenuation and multipath effects. The presence of people affects the signal due to absorption and reflection, introducing variability in range measurements. The range error due to NLOS conditions is thus a function of the obstacle type and the measurement duration:

$$\Delta d_{\text{nlos}} = f_{\text{obstacle}} (d, \text{ type }, t_k)$$
 (19)

4.2.2. Problem Formulation

The goal is to develop an estimation process that adapts to the variability introduced by different obstructions, accurately estimating the true range in diverse NLOS conditions. An estimator \hat{d}_{NLOS} is required that minimizes the error across various types of obstructions:

$$\hat{d}_{\text{NLOS}} = \operatorname{argmin}_{d} \mathbb{E} \left[\left(d - \left(d + \Delta d_{\text{nlos}} \left(\text{ obstacle }, t_{k} \right) + \varepsilon \right) \right)^{2} \right]$$
 (20)

The error model needs to characterize the distinct impacts of different materials on signal propagation. This involves analyzing the impact of different materials uniquely affecting UWB range measurements:

$$\Delta d_{\text{nlos}}$$
 (obstacle, t_k) = g_{material} (d , type, t_k , ε) (21)

where g_{material} models the NLOS error based on the type of obstruction, time, and inherent measurement errors.

4.2.3. Proposed Method

1. Sliding window function: the sliding window function is a batch estimation technique requiring constant time and memory since it marginalizes older states [14,15]. Consider the case wherein a device travels until time t_{k1} , at which point it can be understood to be in an NLOS state by doing a thorough batch estimate of its state history. It then travels until time t_{k2} , at which point it adds the new state to its state history. The previous state m is then marginalized out of the optimization problem being addressed at t_{k2} , thereby eliminating them from the challenge. The new states are the remaining states from the preceding window's estimation. The sliding window function is normally used to process time-series data in machine learning and deep learning models. As the UWB device goes from an LOS to NLOS state at different timeslots, we need to use the sliding window function to utilize time-series data to estimate the state of the UWB device at time t_{k1} .

new window of length
$$K = k_2 - m + 1$$
 (22)

$$\underbrace{x_0 \quad x_1 \quad \dots \quad x_{m-1} \quad x_m \quad \dots \quad x_{k_1}}_{\text{old window of length } K = k_1 + 1} \quad x_{k_1 + 1} \quad \dots \quad x_{k_2}$$
(23)

where every state can be represented as an LOS or NLOS state. The Decawave DW1000 UWB chip user manual stated that if the difference between RX_POWER and FP_POWER, i.e., RX_POWER – FP_POWER, is less than 6 dB, the channel is likely to be LOS, based on the thumb rule. Therefore, every state is compared with the defined RX_POWER – FP_POWER = 6 dB value to first differentiate the LOS state from the NLOS state, then machine learning algorithms are used on the NLOS state data to identify the characteristics of the NLOS propagation.

2. Bayesian Conv-LSTM: this study utilizes the cascade of convolution and Bayesian LSTM to classify the NLOS scenarios with high accuracy. Figure 3 shows the overall structure of the proposed method with the attention module. The input data first pass through the convolution layer and then pass through the Bayesian LSTM (BLSTM) layer, followed by the layer output with the softmax activation function to classify the input. A novel spatial—temporal attention module is proposed to extract important input features, improving the model's performance. The spatial attention is placed at the convolution layer's end, and the temporal attention module is placed at the end of the Bayesian LSTM layer to extract important features. A detailed description of the BLSTM layer and the proposed attention module is presented in this section.

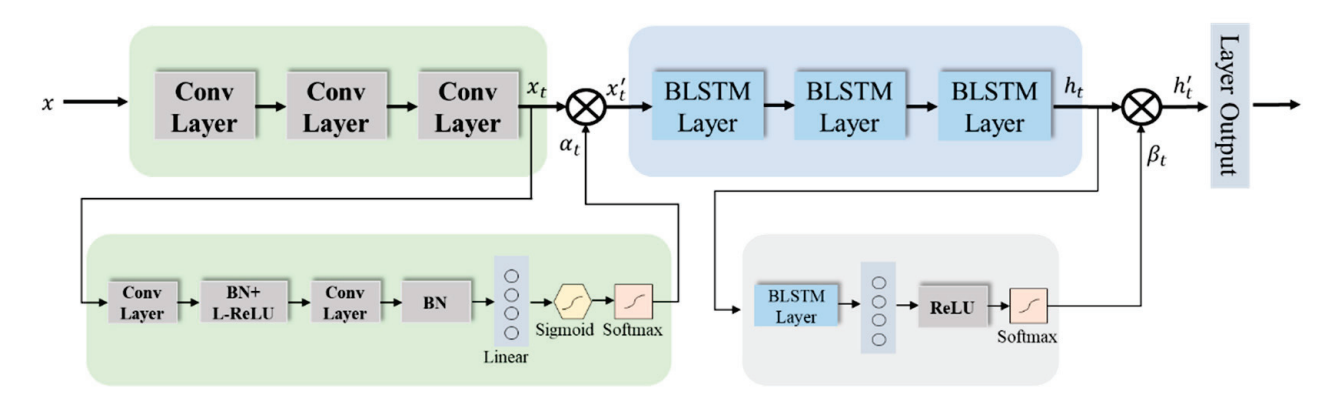


Figure 3. The overall architecture of Conv-BLSTM layer and the proposed attention module.

Bayesian inference in deep learning allows mathematically grounded uncertainty estimation, which can improve the model performance. Grahmani et al. proposed dropout with variational inference to estimate uncertainty in the deep learning model [29]. The uncertainties in the deep learning model can be divided into epistemic and aleatoric uncertainty. The epistemic uncertainty accounts for the lack of a dataset, which can be reduced by providing more observable data to the models during training. The aleatoric uncertainty accounts for the randomness of the data during the acquisition, which cannot be reduced. Moreover, the aleatoric uncertainty can be divided into two parts, such as homoscedastic and heteroscedastic. The homoscedastic uncertainty provides a constant uncertainty estimation regardless of different data points. On the other hand, the heteroscedastic uncertainty varies according to the input data, which is very useful in understanding the noise variance during data acquisition. Therefore, this study considers the epistemic and heteroscedastic aleatoric uncertainty estimation to determine the proposed model's uncertainties in predicting the NLOS class.

A Bayesian neural network replaces the deterministic weights' parameters with a distribution using the Bayesian rule. For example, the posterior over deep learning weights for a given dataset (X, Y) can be defined as p(W|X, Y) in a Bayesian neural network. We can also derive the model likelihood, which contains Gaussian observation noise as follows:

$$p(y|f^{w}(x)) = N(f^{w}(x), \sigma^{2}), \tag{24}$$

where f^w represents the random output from a Bayesian neural network, and σ represents the Gaussian observation noise. However, it is known that the exact posterior of the Bayesian neural network is intractable, but it can be approximated using different approximation methods such as Bayes by backpropagation and the MC dropout method. This study uses the MC dropout method, which performs dropout to generate random predictions to trace the simple distribution over the weights. The objective function to trace simple distribution can be defined as follows:

$$L(\theta, p) = -\frac{1}{N} \sum_{i=1}^{N} log p(y_i | f^{\hat{W}_i}(x_i)) + \frac{1-p}{2N} ||\theta||^2), \tag{25}$$

where θ is the simple distribution, N is the data points, p is the dropout and $log p\left(y_i \middle| f^{\hat{W}_i}(x_i)\right)$ is the Log-likelihood, which can be more simplified as follows:

$$-log p\left(y_{i}|f^{\hat{W}_{i}}(x_{i})\right) \propto \frac{4}{2\sigma^{2}}||y_{i}-f^{\hat{W}_{i}}(x_{i})||^{2} + \frac{1}{2}log\sigma^{2}.$$
 (26)

The predictive variance can also be approximated using the following equation:

$$Var(y) \approx \sigma^2 + \frac{1}{T} \sum_{t=1}^{T} f^{\hat{W}_t}(x)^T f^{\hat{W}_t}(x_t) - E(y)^T E(y).$$
 (27)

As mentioned earlier, σ represents the noise in deep learning. It can be tuned to estimate the uncertainty of the model and data during prediction. As this study considers the estimation of the data-dependent heteroscedastic uncertainty, the objective can be modeled as data-dependent using the following equation:

$$L_{RNN}(\theta) = \frac{1}{N} \sum_{i=1}^{N} \frac{1}{2\sigma(x_i)^2} ||y_i - f(x_i)||^2 + \frac{1}{2} log\sigma(x_i)^2.$$
 (28)

The above equation can be integrated with Bayesian neural network objective functions as follows:

$$L_{BRNN}(\theta) = \frac{1}{N} \sum_{i=1}^{N} \frac{1}{2\hat{\sigma}_{i}^{2}} ||y_{i} - \hat{y}_{i}||^{2} + \frac{1}{2} log \hat{\sigma}_{i}^{2},$$
 (29)

where \hat{y} and $\hat{\sigma}$ represent the predictive mean and noise variance. The predictive uncertainty of a model can be then estimated using the following equation:

$$Var(y) \approx \frac{1}{T} \sum_{t=1}^{T} \hat{y}_t^2 - \left(\frac{1}{T} \sum_{t=1}^{T} \hat{y}_t\right)^2 + \frac{1}{T} \sum_{t=1}^{T} \hat{\sigma}_t^2.$$
 (30)

3. The proposed attention model: this study utilizes the cascade of convolution and Bayesian LSTM to classify the NLOS scenarios with high accuracy. Figure 3 shows the overall structure of the proposed method with the attention module. The input data first pass through the convolution layer and then pass through the Bayesian LSTM (BLSTM) layer, followed by the layer output with the softmax activation function to classify the input. A novel spatial–temporal attention module is proposed to extract important input features, improving the model's performance. The spatial attention is placed at the convolution layer's end, and the temporal attention module is placed at the end of the Bayesian LSTM layer to extract important features. A detailed description of the BLSTM layer and the proposed attention module is presented in this section.

$$\alpha_t = \tau(\sigma\left(W(BN(Conv_2^{3\times3}(\delta\left(BN\left(Conv_1^{3\times3}(X)\right)\right)))))),\tag{31}$$

Temporal attention is used to extract important features from a window frame because the distribution of valuable information is not equal among the window frames. The output from the Bayesian LSTM layer is passed through the Bayesian LSTM layer, fully connected layer, and ReLU activation function in series. Lastly, softmax normalization is used to generate the temporal weight.

$$\beta_t = \tau(\delta(W(\mathcal{L}(X)))), \tag{32}$$

Then, the output from the Bayesian LSTM network and temporal attention weights are incorporated to predict the class score for all window frames, which can be illustrated as follows:

$$w = \sum_{t=1}^{T} \beta_t * p_t \tag{33}$$

where *T* represents the length of the window frame.

4.3. Min-Max Removing and Moving Average Filter

To improve the ranging accuracy affected by the standard deviation in UWB range measurements, we implement a method involving the removal of outliers followed by smoothing through a moving average filter. Specifically, for an update rate of 100Hz in UWB range samples, we initially select the first 50 samples to identify and remove the maximum and minimum values. This process of outlier exclusion enhances the accuracy of the subsequent data processing step.

Following outlier removal, we employ a moving average filter, a technique commonly utilized to process various collected datasets or signals. This filter computes an average from a set number of input samples (M), producing a single output for each iteration. As the length of the filter increases, the resulting output exhibits greater smoothness, effectively diminishing any quick fluctuations. In our application, after excluding the 2 extreme samples, the remaining 48 samples are used within the moving average filter to refine the range measurements. The formula used in our approach is detailed below:

$$MA = \frac{\ddot{d}_1 + \ddot{d}_2 + \cdots + \ddot{d}_{48}}{48}.$$
 (34)

5. Results

In this section, we perform an experimental evaluation of our proposed LOS and NLOS range error mitigation method. We also calculate and compare the accuracy with the available methods found in the literature.

5.1. Experimental Setting

Decawave's UWB chip DWS1000 device was used throughout the data preparation and experimental part. The DWS1000 was connected with the STM32F103C8-based development board to program, debug, and perform range acquisition. NodMCU-BU01 is an STM32-based development board with better SPI communication speed with a 32.768 kHz crystal oscillator. The asymmetric double-sides TWR method was used to acquire range as this method yields better results than the symmetric method.

Experimental data for both LOS and NLOS conditions were taken in the indoor environment. LOS data were taken in an environment where the LOS range can be obtained close to the infield environment. NLOS data were taken in a 15×15 m room furnished with a wooden table, metal door, and other office appliances. Range measurements, along with the power difference of the first path and receive power, were taken at a 5 m distance. NLOS data were taken for four scenarios: the human body, partial metal obstacles, wood objects, and concrete walls, to train the machine learning models to identify the NLOS scenarios. Initially, 50,000 samples were taken for every scenario, then 20,000 samples were selected based on the power difference criteria. These samples are then divided into standard 70–30 train and test data divisions to train the machine learning models.

Table 1 provides the experimental parameters used to train the proposed model in this study. The training was conducted on an Ubuntu 20.04 operating system using Python 3.10 as the programming language and PyTorch 2.0.1 as the model design framework. The training utilized an Nvidia RTX 3080 GPU to accelerate computations. The learning rate for the model was set to 0.0001, and an Adam optimizer was used to adjust the weights during training to ensure efficient convergence.

Table 1. Experimental parameters used in this study to train the model.

Parameters	Settings
Operating system	Ubuntu 20.04
Programming language	Python 3.10
Model design framework	PyTorch 2.0.1
ĞPU	Nvidia RTX 3080
Learning rate (α)	0.0001
Optimizer	Adam

5.2. Quantitative Results

In order to evaluate the proposed method for LOS range measurement improvement, a quantitative analysis of UWB range error mitigation across varying environmental conditions, such as a park, a walking street, an indoor ground, and a lab, was performed. Measurements were taken at three different baseline distances (300 cm, 400 cm, and 500 cm), with subsequent analysis on both measured and mitigated values to assess the precision and accuracy of the proposed method. These results are tabulated across three primary metrics: original (cm), measured (cm), and mitigated (cm), with the Root Mean Squared Error (RMSE) serving as a statistical measure of the differences between values predicted by a model or an estimator and the values observed.

Table 2 presents the results from employing our proposed method for mitigating UWB range errors in an indoor ground environment. The experimental scenario can be seen in Figure 4. Initially, at a baseline distance of 300 cm, the uncorrected measured distance between two UWB devices stood at 268.097 cm. Post-application of our mitigation technique, the distance measured adjusted to 295.177 cm, more closely aligning with the actual distance and resulting in an RMSE of 4.823 cm. Notably, as the baseline distance expanded

to 400 cm and then to 500 cm, the effectiveness of our technique in reducing RMSE became increasingly evident, dropping to 2.444 cm and 0.153 cm, respectively. These results not only underscore the significant impact of environmental factors and measurement noise on initial UWB distance measurements but also demonstrate the substantial precision improvements introduced by our mitigation method across various distances. Consequently, this method proves to be highly effective for correcting range measurements, significantly enhancing the accuracy of UWB devices under diverse conditions and at extended ranges, offering promising implications for its application in precision-critical UWB applications.

Table 2. Summary of indoor ground environmental impact on our proposed model showing measured, mitigated, and RMSE errors.

Environment	Original (cm)	Measured (cm)	Mitigated (cm)	RMSE (cm)
	300	268.097	295.177	4.823
Indoor Ground	400	376.866	402.444	2.444
	500	481.257	499.847	0.153



Figure 4. Experiment with line of sight for indoor ground environment.

Table 3 shows the results of applying our proposed method to address UWB range errors under lab conditions. The detailed scenario is shown in Figure 5. Initially, for a 300 cm baseline distance, the uncorrected distance recorded between two UWB devices was 285.510 cm. Following the error mitigation process, this value was refined to 296.796 cm, achieving an RMSE of 3.204 cm. As the baseline distance was extended to 400 cm and 500 cm, the precision of our proposed method was further highlighted. RMSE values were observed to decrease to 3.063 cm and 1.895 cm, respectively, showcasing a consistent improvement in accuracy across increasing distances. Thus, our methodology emerges as a robust solution for refining range measurements, significantly improving the accuracy of UWB devices in lab settings.

Table 3. Summary of lab environmental impact on our proposed model showing measured, mitigated, and RMSE errors.

Environment	Original (cm)	Measured (cm)	Mitigated (cm)	RMSE
	300	285.510	296.796	3.204
Lab	400	389.976	403.063	3.063
	500	492.287	501.895	1.895



Figure 5. Experiment with line of sight for lab environment.

The data presented in Table 4 illustrate the application of our proposed method for UWB range errors in Park A, across three baseline distances. At 300 cm, the original distance measured was 263.110 cm. After applying the mitigation process, the error was significantly reduced, achieving an RMSE of 2.999 cm. The experimental scenario is given in Figure 6. However, as the distance increased to 400 cm and 500 cm, the RMSE values increased to 6.674 cm and 7.041 cm, respectively. These results suggest that while the mitigation technique is capable of substantially reducing range errors at shorter distances, its efficacy is less pronounced at longer ranges, possibly due to environmental factors specific to Park A. Despite these challenges, the technique demonstrates a significant improvement in UWB measurement accuracy, especially in outdoor environments where precision is critical.

Table 4. Summary of Park A's environmental impact on our proposed model showing measured, mitigated, and RMSE errors.

Environment	Original (cm)	Measured (cm)	Mitigated (cm)	RMSE
	300	263.110	297.001	2.999
Park A	400	382.083	406.674	6.674
	500	498.694	507.041	7.041



Figure 6. Experiment with line of sight for Park A environment.

Table 5 showcases the effectiveness of a calibration and mitigation approach tailored for ultra-wideband (UWB) range measurements in Park B, encompassing three distinct baseline distances. The detailed scenario is shown in Figure 7. At the initial distance of 300 cm, the original measurement was recorded at 256.612 cm, with the estimated value post-calibration reaching 293.415 cm. Following the mitigation process, an RMSE of 6.585 cm was observed, indicating a notable improvement in accuracy, albeit with some remaining discrepancies. As the distance extended to 400 cm and further to 500 cm, the mitigation technique demonstrated increased efficacy, with RMSEs decreasing to 4.601 cm and 1.487 cm, respectively. This pattern suggests a significant enhancement in the precision of UWB devices with distance, particularly after calibration and mitigation. The decreasing trend in RMSE with longer distances highlights the potential of the applied methodology to effectively address range errors, especially in outdoor settings like Park B, where environmental variables can impact measurement accuracy. Consequently, this approach evidences considerable promise for refining UWB range measurements, ensuring higher accuracy and reliability across varied distances in outdoor environments.

Table 5. Summary of Park B's environmental impact on our proposed model showing measured, mitigated, and RMSE errors.

Environment	Original (cm)	Measured (cm)	Mitigated (cm)	RMSE
	300	256.612	293.415	6.585
Park B	400	362.322	395.399	4.601
	500	463.113	498.513	1.487

Figure 8 shows the training and validation plot for the accuracy and loss of NLOS identification, respectively. It can be seen that the proposed model converges well with the acquired dataset. The accuracy and loss were stable after 60 epochs and achieved a training accuracy of 99.14% and a validation accuracy of 98.78%.



Figure 7. Experiment with line of sight for Park B environment.

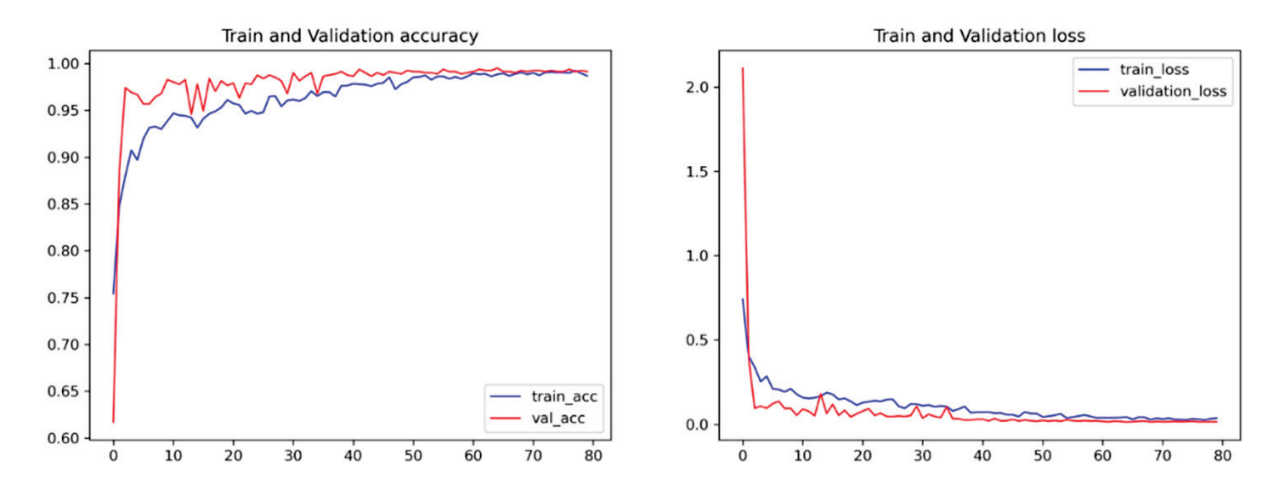


Figure 8. The training and validation accuracy of the proposed model, along with their losses.

We utilized standard multiclass classification evaluation metrics to evaluate the proposed model. In each classification test, we computed the true positive (TP, accurate detection), true negative (TN, correct rejection), false negative (FN, omission error), and false positive (FP, commission error). Using the given formula in [30], we obtained the average classification accuracy (A), average recall (R), average precision (P), and F-1 score (F). Different machine learning methods were implemented on the dataset to evaluate the performance of the proposed model using the following metrics:

$$A = \frac{TP + TN}{TP + TN + FP + FN} \tag{35}$$

$$R = \frac{TP}{TP + FN} \tag{36}$$

$$P = \frac{TP}{TP + FP} \tag{37}$$

$$F = 2 * \frac{R * P}{R + P} \tag{38}$$

Table 6 shows the proposed model's precision, recall, and F-1 score in classifying different NLOS environments. The precision for all classes is 99 or above except for the wood, where the precision is calculated to be 92.1. The model achieves good recall for all the classes, where two classes acquired 99 and one class acquired 100. However, the F-1 score of the proposed model also achieved 100 for the wall and pedestrian environments and 96 for the wood and partial metal environments. The average accuracy achieved from the testing was 98.78.

Class Name	Precision	Recall	F-1 Score	Accuracy
Wall	100.0	99.2	100.0	
Partial metal	99.0	94.5	96.3	00.70
Wood	92.1	100.0	96.0	98.78
Pedestrian	100.0	99.0	100.0	

Figure 9 shows the accuracy comparison of various machine learning models for NLOS classification, including LSTM, Conv + LSTM, CNN, CNN + CRFz, random forest, XGBoost, LightGBM, support vector machine (SVM), Naïve Bayes, decision trees, MLP, and the proposed model. The proposed model achieved the highest accuracy of 98.78%, significantly outperforming CNN + CRF (95.87%), LSTM (95.41%), and other models like LightGBM (94.24%), SVM (94.81%), decision trees (93.18%), XGBoost (92.88%), and random forest (91.53%). These results highlight the robustness of the proposed approach in effectively capturing features and adapting to challenging NLOS environments.

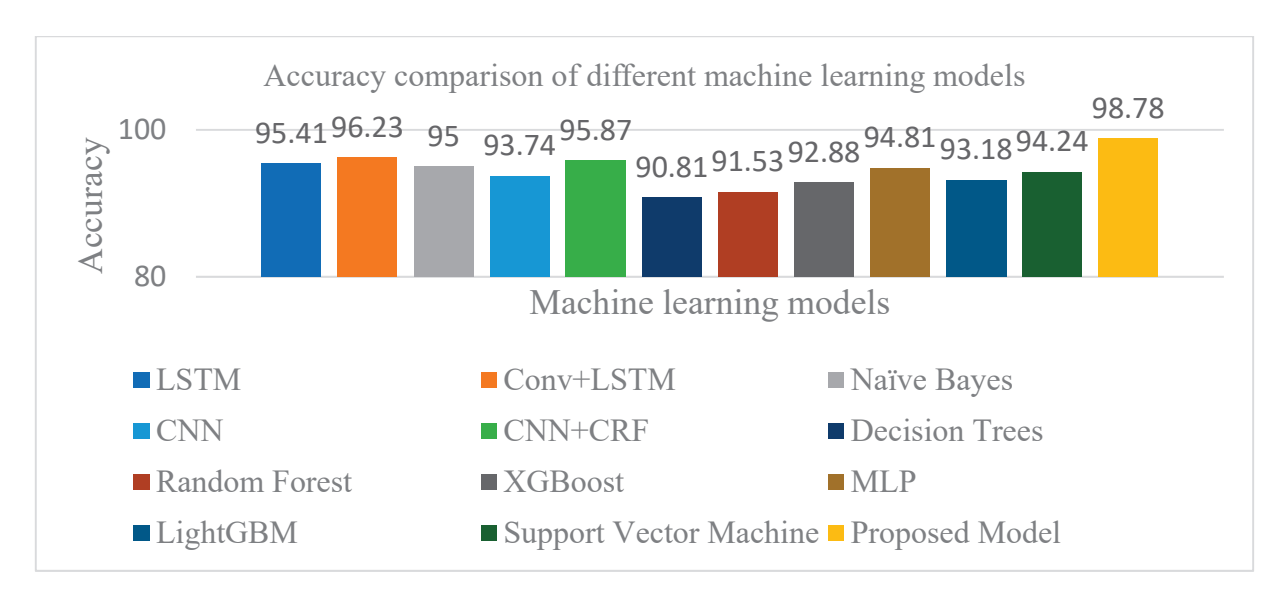


Figure 9. The comparison of different models for NLOS identification in UWB devices.

Table 7 shows the performance of the proposed model with different attention mechanisms, along with their accuracy and processing time. The baseline model, without any attention, achieved an accuracy of 96.32% and a processing time of 5.0 ms per sample. Adding Squeeze-and-Excitation (SE) Attention slightly improved the accuracy to 96.34%, with the processing time increasing to 6.2 ms. Self-Attention, on the other hand, resulted in a lower accuracy of 95.12% and a higher processing time of 9.5 ms, as it was not well suited for the data. Multi-head Attention improved the accuracy to 96.83%, with a processing time of 12.0 ms, by capturing diverse features more effectively.

Table 7. Performance comparison of our proposed model with different attention combinations.

Accuracy	Processing Time
96.32	5.0
96.34	6.2
95.12	9.5
96.83	12.0
98.78	15.8
	96.32 96.34 95.12 96.83

The best performance was achieved with our proposed spatial–temporal attention, which reached an accuracy of 98.78% by extracting both spatial and temporal information. While its processing time was the highest at 15.8 ms per sample, the significant improvement in accuracy makes it worth the trade-off.

Figure 10 presents an analysis of our proposed system's accuracy on human obstacles, wherein we compared original distances with measured and mitigated values across three scenarios: 300 cm, 400 cm, and 500 cm. Table 8 presents our findings, showing close approximations of actual distances and effective error correction, as indicated by RMSE values of 6.533, 7.856, and 5.899, respectively. These results highlight the system's precision and reliability in real-world NLOS scenarios.



Figure 10. Experiment with non-line-of-sight conditions with human obstacle.

Table 8. Summary of human obstacle's impact on our proposed model showing measured, mitigated, and RMSE errors.

Obstacle	Original (cm)	Measured (cm)	Mitigated (cm)	RMSE
	300	243.183	293.467	6.533
Human	400	339.414	395.144	4.856
	500	452.802	494.101	5.899

Figure 11 shows the system's NLOS mitigation accuracy through a comparison of original, measured, and mitigated distances for wood obstacles with various ranges such as 300 cm, 400 cm, and 500 cm. Table 9 illustrates the system's proficiency in estimating the distance of obstacles with a high degree of accuracy, as demonstrated by the close alignment of measured distances with the original. The mitigation process effectively reduces measurement errors, achieving RMSE values of 8.967, 4.176 for the wood piece, and 4.084 for the largest obstacle. These results emphasize the system's effectiveness and reliability in diverse detection scenarios.



Figure 11. Experiment with non-line-of-sight conditions with wood obstacle.

Table 9. Summary of wood obstacle's impact on our proposed model showing measured, mitigated, and RMSE errors.

Obstacle	Original (cm)	Measured (cm)	Mitigated (cm)	RMSE
	300	248.913	296.033	3.967
Wood	400	359.549	395.824	4.176
	500	450.282	495.916	4.084

Figure 12 shows our proposed system's performance on partial metal obstacles, wherein we compared original, measured, and mitigated distances across various ranges. The data reveal the system's precision in closely approximating the true distances of obstacles, with the measured and mitigated values illustrating the system's adeptness at error correction. Notably, the RMSE values of 6.986 for a 300 cm partial metal obstacle, 5.894 for a 400 cm partial metal object, and 4.634 for a 500 cm obstacle highlight the system's consistent accuracy and reliability in a range of scenarios, confirming its effectiveness in real-world applications. The detailed results can be seen in Table 10.



Figure 12. Experiment with non-line-of-sight conditions with partial metal obstacle.

Table 10. Summary of partial metal obstacle's impact on our proposed model showing measured, mitigated, and RMSE errors.

Obstacle	Original (cm)	Measured (cm)	Mitigated (cm)	RMSE
	300	235.914	293.014	6.986
Partial metal	400	345.278	394.106	5.894
	500	439.492	495.366	4.634

Figure 13 demonstrates the system's proficiency in detecting obstacles, showcasing a comparison between original, measured, and mitigated distances for a series of obstacles, with a focus on a wall at 400 cm. This comparison clearly illustrates the system's ability to accurately guess distances, with mitigated measurements closely mirroring the original ones. The RMSE values of 5.935 for the 300 cm wall obstacle, 7.579 for the 400 cm wall obstacle, and 4.195 for the 500 cm wall obstacle shown in Table 11 underscore the system's precise error correction capabilities across various sizes of obstacles. These findings affirm the system's robustness and accuracy in obstacle detection within diverse environments.



Figure 13. Experiment with non-line-of-sight conditions with wall obstacle.

Table 11. Summary of wall obstacle's impact on our proposed model showing measured, mitigated, and RMSE errors.

Obstacle	Original (cm)	Measured (cm)	Mitigated (cm)	RMSE
	300	256.324	294.065	5.935
Wall	400	363.507	393.421	6.579
	500	462.064	495.805	4.195

5.3. Uncertainty Estimation

This study utilized the MC dropout method to train the model with variational inference and also calculated the epistemic and aleatoric uncertainty. Different dropout rates were used and tested to determine the best dropout rates for the proposed model. It was observed that the higher dropout rates reduced the accuracy but yielded better model diversity, and the lower dropout rates increased the accuracy but yielded lower model diversity. We found that our proposed model's dropout rate of 0.50 was optimal; therefore, the dropout rate of 0.50 was used throughout the whole training and experimental procedures. The proposed model's epistemic uncertainty and aleatoric uncertainty can be found in Figure 14. Figure 14a represents the epistemic uncertainty over the prediction one class. The ideal uncertainty would be very close or identical to the prediction of the relevant class. However, we found that epistemic uncertainty is still present in the prediction process. As stated earlier, epistemic uncertainty represents the lack of data during training, which can be minimized by providing more training data. A mean epistemic uncertainty of

0.00408 was calculated for the proposed model, which was very low. Figure 14b represents the aleatoric uncertainty, which was calculated using the proposed model. It can be seen that the aleatoric uncertainty is very low compared to the epistemic uncertainty. Therefore, it can be said that the inherent noise of the data was smaller, and model performance can be improved by providing more data. A mean aleatoric uncertainty of 0.00534 was calculated for the proposed model, which demonstrates that the aleatoric uncertainty is very low for the acquired dataset and robust to environment variance.

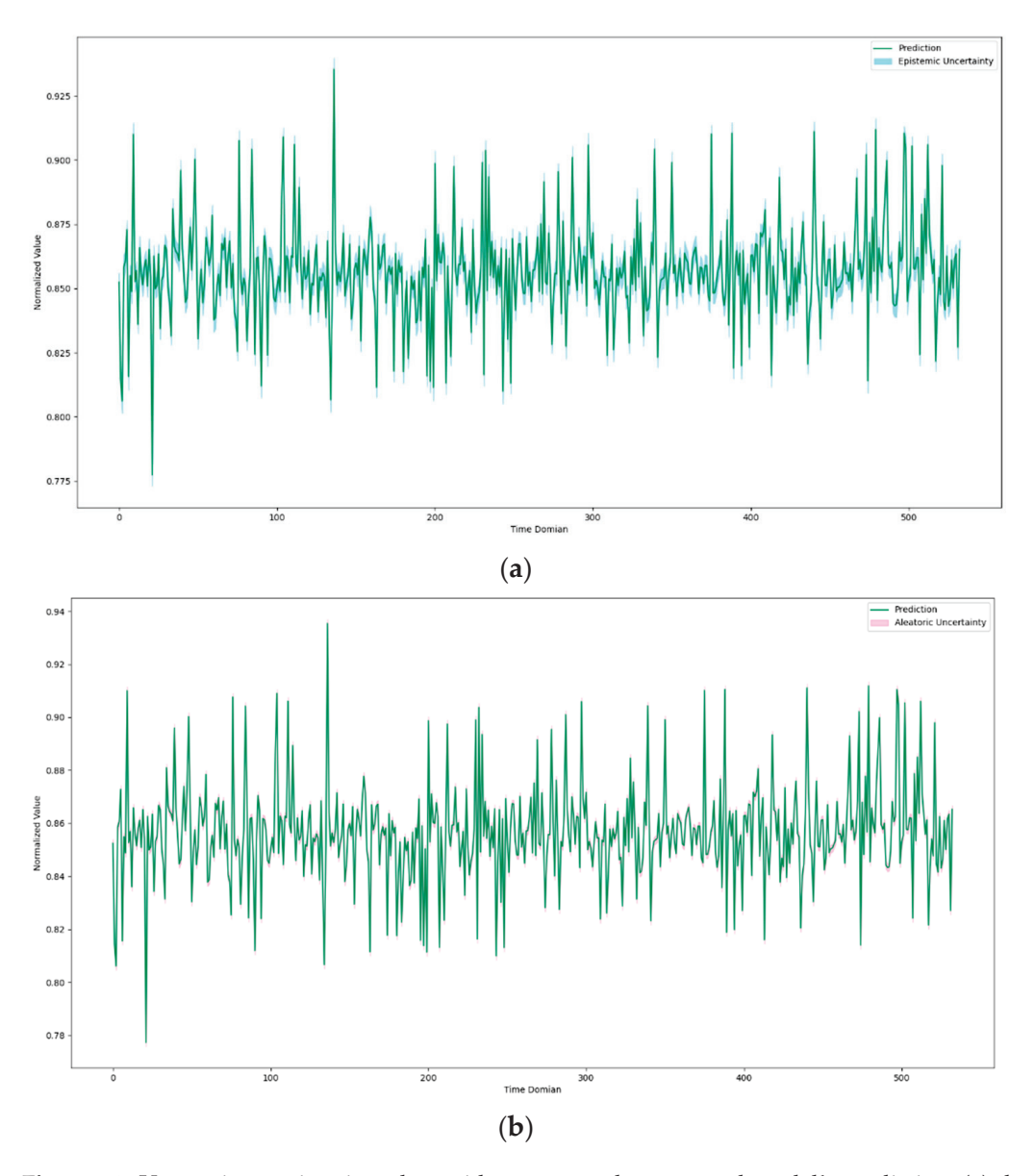


Figure 14. Uncertainty estimation plots with respect to the proposed model's prediction; (a) the epistemic uncertainty of the proposed model, (b) the aleatoric uncertainty or inherent noise of data calculated using the proposed model.

5.4. Discussion

The proposed NLOS identification is also compared with the different NLOS identification solutions that exist in the literature. Two evaluation metrics are utilized to compare the proposed NLOS identification method with other methods. Yu et al. proposed a fuzzy comprehensive evaluation (FCE)-based method to provide NLOS identification and mitigation solutions [14]. They achieved an accuracy of 96.41% with a recall of 93.90% in identifying NLOS scenarios using UWB devices. Jiang et al. proposed a CNN-based method to

identify the NLOS environment for UWB devices [31]. They found that a CNN cascaded with the stacked LSTM method, which achieved a higher accuracy of 82.14%, can provide better accuracy than the LSTM method. Dong et al. proposed Fresnel zones and simple prior knowledge-based methods to provide NLOS identification and mitigation methods for UWB devices [32]. Their proposed method achieved recall and accuracy of 100.00% and 96.41% in identifying the NLOS environment. Cui et al. utilized capsule networks (CapsNet) to classify LOS and NLOS scenarios for UWB-based positioning systems [33]. Their method achieved an accuracy of 94.63% with a 94.74 recall rate. Cung et al. utilized different machine learning methods to identify NLOS conditions in UWB localization, and they achieved a higher overall accuracy of 91.9% using the random forest algorithm [27]. Liu et al. proposed a CNN-GRU-based indoor NLOS/LOS identification neural network to identify the NLOS scenario in an indoor environment [34]. Their proposed method can reach up to 97% accuracy in identifying NLOS and LOS channel propagation in an indoor environment. Musa et al. utilized decision tree machine learning algorithms to detect and mitigate NLOS channel propagation for UWB-based indoor tracking [35]. They tested their model for different NLOS scenarios and achieved an average accuracy of 90.13% with a 91.33% recall rate. Table 12 shows the comparison of the different NLOS identification methods with the proposed method. Our proposed method achieved an accuracy of 98.78% with a 98.17% recall rate. Therefore, it can be said that the proposed method can accurately identify different NLOS scenarios for UWB devices.

Table 12. The comparison of NLOS identification accuracy between different available solutions found in the literature and our proposed method.

Method	Recall	Accuracy
FCE [14]	93.90	96.41
CNN-Stack LSTM [31]	-	82.14
Fresnel zones-prior knowledge [32]	100	82
CapsNet [33]	94.74	94.63
Random forest [27]	-	91.9
CNN-GRU [34]	-	97
Decision tree [35]	91.33	90.13
Proposed	98.17	98.78

We have also compared the mitigated range accuracy with the available NLOS mitigation methods found in the literature to evaluate the performance of our proposed method, as detailed in Table 13. Simone et al. proposed a representation learning model (REMnet) to mitigate NLOS range error prior to positioning using UWB devices. Their method produced a significant improvement in the NLOS range error mitigation, with a mean absolute error of 5.71 cm [30]. Dong et al. proposed NLOS mitigation using the Fresnel zones-prior knowledge method, achieving an accuracy of 10.778 cm in the NLOS environment [32]. Another approach, which uses subdivided NLOS data combined with MIPL-B, achieved a mitigated error of 5.57 cm [36]. A method that involves NLOS/LOS identification followed by error correction reported an error reduction to 10.00 cm [37]. Additionally, a self-supervised deep learning range correction (DLRC) technique showed an improvement, with a mitigated error of 14.681 cm [38]. Barral et al. utilized various machine learning algorithms to identify and mitigate the UWB range measurement in an NLOS environment, achieving the highest reported accuracy of less than 20 cm [39]. Our proposed method has demonstrated a significant reduction in the NLOS effect in UWB-based range measurements, achieving a mean error of 5.30 cm. Based on these results, it can be concluded that our proposed method is effective and can be implemented in real-time UWB range measurement devices to reduce the NLOS effect in range measurements.

Table 13. The comparison of NLOS mitigated accuracy between different available solutions found in the literature and our proposed method.

Method	NLOS Mitigated Error (cm)	
REMnet [30]	5.71	
Fresnel zones-prior knowledge [32]	10.778	
Subdivided NLOS data + MIPL-B [36]	5.57	
NLOS/LOS identification + error correction [37]	10.00	
Self-supervised DLRC [38]	14.681	
Bayesian filter [40]	0.74 (wood), 7.21 (metal)	
Machine learning [39]	<20	
Proposed	5.30	

A potential limitation of the proposed model lies in the increased computational complexity introduced by the spatial–temporal attention mechanism, which may affect its feasibility for deployment on very-low-power devices. Additionally, attention mechanisms may introduce biases by overemphasizing specific features while potentially neglecting others, especially in datasets with imbalanced distributions or high noise levels. To address these challenges, optimization techniques such as model pruning and quantization can be applied to reduce computational demands. Furthermore, we can introduce regularization techniques, and training on diverse and well-balanced datasets can help mitigate biases and improve generalization across various scenarios. We can also explore antenna design, such as a compact triband implantable antenna with superior size, bandwidth, and SAR values, and a 5G wideband MIMO antenna for body-centric networks with high isolation and stable on-body performance to enhance wireless communication in biomedical and body area network applications, which can complement the proposed model's adaptability in real-world scenarios [41,42].

6. Conclusions

This paper proposes machine learning-based LOS and NLOS identification and mitigation methods to reduce range measurement error in both scenarios. A GP-enhanced non-linear filter is proposed to mitigate the bias of LOS range measurement. The standard deviation of the range measurement for both LOS and NLOS scenarios is mitigated using the min-max removal and the moving average filter. In addition, the NLOS identification method is proposed using the RSSI signal acquired from the UWB range measurement. The Conv-BLSTM method is utilized to identify four common obstacles that can be found in the indoor environment, such as wood, metal, pedestrians, and concrete walls. A spatial–temporal attention module is proposed to improve the performance of the model. Moreover, the uncertainty estimation method is introduced into the proposed model to calculate the epistemic and aleatoric uncertainty. The direct mitigation method is proposed to mitigate the range bias caused by NLOS channel propagation. An extensive experiment was performed to evaluate the performance of the proposed system. The proposed system achieved an accuracy of 3.75 cm in the LOS environment and 5.30 cm in the NLOS environment, with 98.78% NLOS channel propagation identification accuracy.

Our proposed model demonstrates strong potential for real-world applications, such as real-time NLOS classification in autonomous systems and indoor navigation. However, practical deployment may face challenges, including hardware constraints on low-power devices and the need for adaptability to diverse environmental conditions. In the future, we would like to focus on optimizing the model for computational efficiency and validating its performance across varied real-world scenarios to enhance its practicality and robustness. Additionally, we plan to explore other deep learning-based methods, such as graph neural networks and transformer-based architectures to further enhance the feature extraction and improve the model's performance in challenging scenarios. The effect of room temperature and voltage on the UWB range measurements can be explored to acquire more information on the LOS and NLOS range bias.

Author Contributions: Conceptualization, A.S.M.S.S., A.H. and S.A.; Data curation, H.S.K.; Formal analysis, E.M., L.M.D., H.S.K., M.M.P.P. and A.H.; Investigation, H.S.K. and A.H.; Methodology, A.S.M.S.S. and S.A.; Software, A.S.M.S.S.; Supervision, H.S.K. and A.H.; Validation, E.M., L.M.D. and H.S.K.; Writing—original draft, A.S.M.S.S. and S.A.; Writing—review and editing, A.H. and S.A. All authors have read and agreed to the published version of the manuscript.

Funding: This work was supported in part by the National Research Foundation of Korea (NRF) Grant by the Korean Government through MSIT under Grant 2022R1F1A1063662, and in part by the Institute of Information and Communications Technology Planning and Evaluation (IITP) Grant by the Korean Government through the Ministry of Science and Information Communication Technology (MSIT) under Grant 2022-0-00331. This research was also supported by the Seoul R&BD Program (IC230014) through the Seoul Business Agency.

Data Availability Statement: All data used to support the findings of this study are included within the article.

Conflicts of Interest: The authors declare no conflicts of interest.

References

- 1. Zafari, F.; Gkelias, A.; Leung, K.K. A survey of indoor localization systems and technologies. *IEEE Commun. Surv. Tutor.* **2019**, 21, 2568–2599. [CrossRef]
- 2. Asaad, S.M.; Potrus, M.Y.; Ghafoor, K.Z.; Maghdid, H.S.; Mulahuwaish, A. Improving positioning accuracy using optimization approaches: A survey, research challenges and future perspectives. *Wirel. Pers. Commun.* **2021**, 122, 3393–3409. [CrossRef]
- 3. Cheng, B.; Cui, L.; Jia, W.; Zhao, W.; Gerhard, P.H. Multiple region of interest coverage in camera sensor networks for tele-intensive care units. *IEEE Trans. Ind. Inform.* **2016**, 12, 2331–2341. [CrossRef]
- 4. Zorn, S.; Rose, R.; Goetz, A.; Weigel, R. A novel technique for mobile phone localization for search and rescue applications. In Proceedings of the 2010 International Conference on Indoor Positioning and Indoor Navigation, Zurich, Switzerland, 15–17 September 2010; pp. 1–4.
- 5. Jo, K.; Chu, K.; Sunwoo, M. GPS-bias correction for precise localization of autonomous vehicles. In Proceedings of the 2013 IEEE Intelligent Vehicles Symposium (IV), Gold Coast, Australia, 23–26 June 2013; pp. 636–641.
- 6. Stahlke, M.; Kram, S.; Mutschler, C.; Mahr, T. NLOS detection using UWB channel impulse responses and convolutional neural networks. In Proceedings of the 2020 International Conference on Localization and GNSS (ICL-GNSS), Tampere, Finland, 2–4 June 2020; pp. 1–6.
- 7. Wen, W.W.; Zhang, G.; Hsu, L.T. GNSS NLOS exclusion based on dynamic object detection using LiDAR point cloud. *IEEE Trans. Intell. Transp. Syst.* **2019**, 22, 853–862. [CrossRef]
- 8. Gezici, S.; Tian, Z.; Giannakis, G.B.; Kobayashi, H.; Molisch, A.F.; Poor, H.V.; Sahinoglu, Z. Localization via ultra-wideband radios: A look at positioning aspects for future sensor networks. *IEEE Signal Process. Mag.* **2005**, 22, 70–84. [CrossRef]
- 9. Fontana, R.J. Recent system applications of short-pulse ultra-wideband (UWB) technology. *IEEE Trans. Microw. Theory Technol.* **2004**, 52, 2087–2104. [CrossRef]
- 10. Alarifi, A.; Al-Salman, A.; Alsaleh, M.; Alnafessah, A.; Al-Hadhrami, S.; Al-Ammar, M.A.; Al-Khalifa, H.S. Ultra wideband indoor positioning technologies: Analysis and recent advances. *Sensors* **2016**, *16*, 707. [CrossRef]
- 11. D'Amico, A.A.; Mengali, U.; Taponecco, L. Cramer-Rao bound for clock drift in UWB ranging systems. *IEEE Wirel. Commun. Lett.* **2013**, 2, 591–594. [CrossRef]
- 12. DecaWave Ltd. DW1000 User Manual. Available online: https://thetoolchain.com/mirror/dw1000/dw1000_user_manual_v2.0 5.pdf (accessed on 24 March 2024).
- 13. De Angelis, A.; Nilsson, J.; Skog, I.; Peter, H.; Carbone, P. Indoor positioning by ultrawide band radio aided inertial navigation. *Metrol. Meas. Syst.* **2010**, *17*, 447–460. [CrossRef]
- 14. Yu, K.; Wen, K.; Li, Y.; Zhang, S.; Zhang, K. A novel NLOS mitigation algorithm for UWB localization in harsh indoor environments. *IEEE Trans. Veh. Technol.* **2018**, *68*, *686–699*. [CrossRef]
- 15. Fofana, N.I.; Van den Bossche, A.; Dalcé, R.; Val, T. An original correction method for indoor ultra wide band ranging-based localisation system. In *Ad-Hoc, Mobile, and Wireless Networks, Proceedings of the 15th International Conference, ADHOC-NOW* 2016, *Lille, France, 4–6 July* 2016; Proceedings 15; Springer International Publishing: Berlin/Heidelberg, Germany, 2016; pp. 79–92.
- 16. Van den Bossche, A.; Dalce, R.; Fofana, I.; Val, T. DecaDuino: An open framework for Wireless Time-of-Flight ranging systems. In Proceedings of the 2016 Wireless Days (WD), Toulouse, France, 23–25 March 2016; pp. 1–7.
- 17. Molina Martel, F.; Sidorenko, J.; Bodensteiner, C.; Arens, M. Augmented reality and UWB technology fusion: Localization of objects with head mounted displays. In Proceedings of the 31st International Technical Meeting of the Satellite Division of the Institute of Navigation (ION GNSS+ 2018), Miami, FL, USA, 24–28 September 2018; pp. 685–692.
- 18. Dotlic, I.; Connell, A.; McLaughlin, M. Ranging methods utilizing carrier frequency offset estimation. In Proceedings of the 2018 15th Workshop on Positioning, Navigation and Communications (WPNC), Bremen, Germany, 25–26 October 2018; pp. 1–6.

- 19. Zhang, Q.; Zhao, D.; Zuo, S.; Zhang, T.; Ma, D. A low complexity NLOS error mitigation method in UWB localization. In Proceedings of the 2015 IEEE/CIC International Conference on Communications in China (ICCC), Shenzhen, China, 2–4 November 2015; pp. 1–5.
- Schroeder, J.; Galler, S.; Kyamakya, K.; Jobmann, K. NLOS detection algorithms for ultra-wideband localization. In Proceedings of the 2007 4th Workshop on Positioning, Navigation and Communication, Hannover, Germany, 22 March 2007; pp. 159–166.
- 21. Borras, J.; Hatrack, P.; Mandayam, N.B. Decision theoretic framework for NLOS identification. In Proceedings of the VTC'98: 48th IEEE Vehicular Technology Conference. Pathway to Global Wireless Revolution (Cat. No. 98CH36151), Ottawa, ON, Canada, 21 May 1998; Volume 2, pp. 1583–1587.
- 22. Lakhzouri, A.; Lohan, E.S.; Hamila, R.; Renfors, M. Extended Kalman filter channel estimation for line-of-sight detection in WCDMA mobile positioning. *EURASIP J. Adv. Signal Process.* **2003**, 2003, 514932. [CrossRef]
- 23. Shi, X.; Chew, Y.H.; Yuen, C.; Yang, Z. A RSS-EKF localization method using HMM-based LOS/NLOS channel identification. In Proceedings of the 2014 IEEE International Conference on Communications (ICC), Sydney, Australia, 10–14 June 2014; pp. 160–165.
- 24. Casas, R.; Marco, A.; Guerrero, J.J.; Falco, J. Robust estimator for non-line-of-sight error mitigation in indoor localization. *EURASIP J. Adv. Signal Process.* **2006**, 2006, 043429. [CrossRef]
- 25. Wymeersch, H.; Maranò, S.; Gifford, W.M.; Win, M.Z. A machine learning approach to ranging error mitigation for UWB localization. *IEEE Trans. Commun.* **2012**, *60*, 1719–1728. [CrossRef]
- 26. Van Nguyen, T.; Jeong, Y.; Shin, H.; Win, M.Z. Machine learning for wideband localization. *IEEE J. Sel. Areas Commun.* **2015**, 33, 1357–1380. [CrossRef]
- 27. Sang, C.L.; Steinhagen, B.; Homburg, J.D.; Adams, M.; Hesse, M.; Rückert, U. Identification of NLOS and multi-path conditions in UWB localization using machine learning methods. *Appl. Sci.* **2020**, *10*, 3980. [CrossRef]
- 28. Tian, Q.; Kevin, I.; Wang, K.; Salcic, Z. Human body shadowing effect on UWB-based ranging system for pedestrian tracking. *IEEE Trans. Instrum. Meas.* **2018**, *68*, 4028–4037. [CrossRef]
- 29. Gal, Y.; Ghahramani, Z. Dropout as a bayesian approximation: Representing model uncertainty in deep learning. In *Proceedings of the Proceedings of the 33rd International Conference on International Conference on Machine Learning, New York, NY, USA, 19–24 June 2016*; pp. 1050–1059.
- 30. Angarano, S.; Mazzia, V.; Salvetti, F.; Fantin, G.; Chiaberge, M. Robust ultra-wideband range error mitigation with deep learning at the edge. *Eng. Appl. Artif. Intell.* **2021**, *102*, 104278. [CrossRef]
- 31. Jiang, C.; Shen, J.; Chen, S.; Chen, Y.; Liu, D.; Bo, Y. UWB NLOS/LOS classification using deep learning method. *IEEE Commun. Lett.* **2020**, 24, 2226–2230. [CrossRef]
- 32. Dong, M. A low-cost NLOS identification and mitigation method for UWB ranging in static and dynamic environments. *IEEE Commun. Lett.* **2021**, 25, 2420–2424. [CrossRef]
- 33. Cui, Z.; Liu, T.; Tian, S.; Xu, R.; Cheng, J. Non-line-of-sight identification for UWB positioning using capsule networks. *IEEE Commun. Lett.* **2020**, *24*, 2187–2190. [CrossRef]
- 34. Liu, Q.; Yin, Z.; Zhao, Y.; Wu, Z.; Wu, M. UWB LOS/NLOS identification in multiple indoor environments using deep learning methods. *Phys. Commun.* **2022**, *52*, 101695. [CrossRef]
- 35. Musa, A.; Nugraha, G.D.; Han, H.; Choi, D.; Seo, S.; Kim, J. A decision tree-based NLOS detection method for the UWB indoor location tracking accuracy improvement. *Int. J. Commun. Syst.* **2019**, 32, e3997. [CrossRef]
- 36. Deng, B.; Xu, T.; Yan, M. UWB NLOS Identification and Mitigation Based on Gramian Angular Field and Parallel Deep Learning Model. *IEEE Sens. J.* 2023, 23, 28513–28525. [CrossRef]
- 37. Yang, H.; Wang, Y.; Seow, C.K.; Sun, M.; Si, M.; Huang, L. UWB sensor-based indoor LOS/NLOS localization with support vector machine learning. *IEEE Sens. J.* 2023, 23, 2988–3004. [CrossRef]
- 38. Yang, B.; Li, J.; Shao, Z.; Zhang, H. Self-supervised deep location and ranging error correction for UWB localization. *IEEE Sens. J.* **2023**, 23, 9549–9559. [CrossRef]
- 39. Barral, V.; Escudero, C.J.; García-Naya, J.A.; Maneiro-Catoira, R. NLOS identification and mitigation using low-cost UWB devices. Sensors 2019, 19, 3464. [CrossRef]
- 40. Xin, J.; Gao, K.; Shan, M.; Yan, B.; Liu, D. A Bayesian filtering approach for error mitigation in ultra-wideband ranging. *Sensors* **2019**, *19*, 440. [CrossRef]
- 41. Gupta, A.; Kumar, V.; Bansal, S.; Alsharif, M.H.; Jahid, A.; Cho, H.-S. A Miniaturized Tri-Band Implantable Antenna for ISM/WMTS/Lower UWB/Wi-Fi Frequencies. *Sensors* **2023**, 23, 6989. [CrossRef]
- 42. Gupta, A.; Kumari, M.; Sharma, M.; Alsharif, M.H.; Uthansakul, P.; Uthansakul, M.; Bansal, S. 8-port MIMO Antenna at 27 GHz for n261 Band and Exploring for Body Centric Communication. *PLoS ONE* **2024**, *19*, e0305524. [CrossRef]

Disclaimer/Publisher's Note: The statements, opinions and data contained in all publications are solely those of the individual author(s) and contributor(s) and not of MDPI and/or the editor(s). MDPI and/or the editor(s) disclaim responsibility for any injury to people or property resulting from any ideas, methods, instructions or products referred to in the content.

MDPI AG Grosspeteranlage 5 4052 Basel Switzerland Tel.: +41 61 683 77 34

Mathematics Editorial Office E-mail: mathematics@mdpi.com www.mdpi.com/journal/mathematics



Disclaimer/Publisher's Note: The title and front matter of this reprint are at the discretion of the Guest Editors. The publisher is not responsible for their content or any associated concerns. The statements, opinions and data contained in all individual articles are solely those of the individual Editors and contributors and not of MDPI. MDPI disclaims responsibility for any injury to people or property resulting from any ideas, methods, instructions or products referred to in the content.



